

**Orbital angular momentum of  
electron states with reduced  
rotational symmetry**

Michael Gordon Mousley

Doctor of Philosophy

University of York

Physics

July 2017

# Abstract

Vortex states are interesting fundamental quantum states whilst also finding many uses in photon optics. In 2010, propagating electron vortices were experimentally produced for the first time leading to the emergence of the field of electron phase shaping. This thesis details the production of electron states containing orbital angular momentum which produce a C-shaped intensity in the focal plane. This C-shaped intensity has a diameter of approximately 10 nm and can be used to lithographically pattern nanometre scale split rings. The broken rotational symmetry also allows rotations to be viewed. The design theory and orbital angular momentum analysis of the C-shaped states is presented. Experimental results of the first production of C-shaped electrons are then shown. The C-shaped electron beams have been applied to lithographic patterning and future potential applications of C-shapes for both electrons and photons are discussed. Photons have been shown to be able to couple total angular momentum, both spin and orbital contributions, to the orbital motion of two dimensional plasmon modes in chiral structures. The similar transfer of orbital angular momentum between propagating electron and plasmon modes has not yet been shown. This thesis provides the design of two dimensional spiral structures to support plasmon oscillations containing orbital angular momentum. Simulated electromagnetic fields show the addition of a spiralling boundary can allow eigenmodes with orbital angular momentum. In addition, the first analysis and electron energy loss experimental investigation of free space electron states containing OAM with flat chiral thin film structures supporting two dimensional surface plasmon modes is presented, showing some initial evidence of an energy signal dependent on the sign of topological charge.

# Contents

<b>Abstract</b>	<b>ii</b>
<b>List of figures</b>	<b>xii</b>
<b>Acknowledgements</b>	<b>xiii</b>
<b>Author's Declaration</b>	<b>xiv</b>
<b>1 Introduction</b>	<b>1</b>
1.1 Electron microscopy history and recent developments . . . . .	1
1.2 Introduction to waves . . . . .	3
1.3 Geometric ray optics for lenses . . . . .	4
1.4 Fourier optics . . . . .	5
1.5 Wave optics . . . . .	7
1.5.1 Fraunhofer diffraction . . . . .	8
1.5.2 Fresnel diffraction . . . . .	9
1.6 Gouy phase . . . . .	10
1.7 Astigmatism . . . . .	12
1.8 Vortex physics . . . . .	13
1.9 Fourier Transform Truncated Bessel Beam modes (FT-TBBs)	16
1.10 Quantum waves . . . . .	19
1.10.1 Quantum phase vortices . . . . .	20
1.11 Optical trapping of particles and atoms . . . . .	21
1.12 Transmission electron microscopy (TEM) . . . . .	23
1.13 Inelastic scattering and EELS . . . . .	25
1.14 Plasmonics . . . . .	27
1.14.1 Surface plasmons . . . . .	28
1.15 Energy transfer to plasmon modes . . . . .	30
1.16 Thesis contribution and outline . . . . .	31
<b>2 Literature review</b>	<b>33</b>
2.1 Literature review: experimental . . . . .	33
2.1.1 Direct phase masks . . . . .	33

2.1.2	Amplitude masks . . . . .	35
2.1.3	Phase contrast masks . . . . .	38
2.1.4	Magnetic field vortex creation . . . . .	39
2.1.5	Measuring OAM . . . . .	40
2.1.6	Sample interactions . . . . .	41
2.1.7	Other phase shaping . . . . .	43
2.1.8	OAM exchange with a sample . . . . .	43
2.1.9	Modelling . . . . .	46
2.1.10	STEM EELS and plasmons with OAM . . . . .	47
2.1.11	Chiral interactions during TEM EELS . . . . .	48
2.1.12	Previous vortices with openings . . . . .	50
<b>3</b>	<b>Methods</b>	<b>52</b>
3.1	The JEOL 2200 FS Microscope . . . . .	52
3.2	Holographic reconstruction . . . . .	55
3.3	Focused Ion Beam Milling . . . . .	57
3.4	Electron beam lithography (EBL) . . . . .	58
3.5	Cathodoluminescence . . . . .	58
3.6	Simulation Methods . . . . .	59
3.6.1	Iterative Fourier transform algorithm to find a phase mask . . . . .	59
3.7	Boundary element method overview . . . . .	61
<b>4</b>	<b>C theory</b>	<b>64</b>
4.1	C shape theory . . . . .	64
4.1.1	C-shaped intensity . . . . .	64
4.1.2	Control equation derivation . . . . .	67
4.1.2.1	Controlling Fourier plane intensities . . . . .	73
4.1.3	Astigmatism effect on C shape . . . . .	74
4.1.4	Fresnel propagation simulations . . . . .	77
4.1.4.1	Simulated vortex trajectories . . . . .	79
4.1.5	Iterative Fourier transform algorithm comparison . . . . .	84
4.1.6	Low intensity in the gap . . . . .	85
4.1.7	Comparison propagation of fractional and helico con- ical beams . . . . .	88
4.1.8	Interference around the C . . . . .	89
4.1.9	OAM analysis . . . . .	92
4.1.9.1	Numerical and analytical integration . . . . .	92
4.1.9.2	Mode decomposition . . . . .	95

4.1.9.3	Effects of astigmatism on mode decomposition . . . . .	99
4.1.10	Dual C-shapes . . . . .	103
4.1.10.1	Dual C-shapes OAM . . . . .	107
4.1.11	Potential applications . . . . .	108
4.1.11.1	Optical trapping . . . . .	108
4.1.11.2	Measuring rotations of vortex electron states	112
4.1.12	Chapter summary . . . . .	112
<b>5</b>	<b>C experimental</b>	<b>114</b>
5.1	Condenser Pt Foil amplitude mask . . . . .	114
5.1.1	Amplitude within the gap . . . . .	117
5.1.2	Pt mask propagation . . . . .	120
5.1.3	Iterative phase retrieval . . . . .	120
5.2	TEM mode phase retrieval . . . . .	124
5.2.1	Phase retrieval on NBD focal plane intensity . . . . .	128
5.2.2	Phase retrieval of NBD propagation series . . . . .	130
5.2.3	Lithography of C shape and energy filtered imaging .	133
5.3	Phase contrast masks . . . . .	137
5.3.1	Phase contrast mask for a C with $\alpha = 22.5^\circ$ . . . . .	141
5.3.2	Phase contrast for a C with $\alpha = 45^\circ$ . . . . .	143
5.3.3	Phase contrast mask for a C defined with an angular co-ordinate rotation . . . . .	145
5.3.4	C shapes produced with a blazed phase contrast mask	148
5.4	A C-shaped electron produced by a direct phase mask . . . . .	149
5.5	Chapter summary . . . . .	152
<b>6</b>	<b>Simulation of 2D chiral plasmon vortex modes</b>	<b>153</b>
6.1	Nanodisk simulations with COMSOL . . . . .	154
6.2	Chiral plasmon spiral simulations with COMSOL . . . . .	157
6.3	MNPBEM simulations . . . . .	161
6.4	Chapter summary . . . . .	171
<b>7</b>	<b>EELS experimental</b>	<b>172</b>
7.1	EELS studies . . . . .	172
7.1.1	STEM EELS of nanoshapes . . . . .	173
7.1.2	STEM EELS of spiral island structures . . . . .	175
7.1.3	Cathodoluminescence experimental results . . . . .	184
7.1.4	Atomic force microscopy of spiral structures . . . . .	190
7.1.5	The nature of the recorded energy losses . . . . .	191

7.1.6	Chirality dependent EELS signals . . . . .	192
7.1.6.1	EELS from a pinhole mask integer vortex . . . . .	193
7.1.6.2	EELS using a C-shaped electron . . . . .	195
7.1.6.3	Background difference signals . . . . .	197
7.1.6.4	Point spread function recorded without a sample . . . . .	200
7.1.7	Chapter summary . . . . .	203
<b>8</b>	<b>Conclusions</b>	<b>204</b>
8.0.8	Future prospects . . . . .	205
<b>A</b>	<b>Appendix</b>	<b>207</b>
A.1	Discussion of potential causes of STEM EELS signal . . . . .	207
A.1.1	Ruled out causes of intensity difference between 3eV and 5eV . . . . .	207
A.1.1.1	Potential explanations of EELS . . . . .	212
A.1.1.2	Direct background subtraction . . . . .	213
A.1.1.3	Richardson-Lucy Matlab . . . . .	213
A.1.1.4	Richardson lucy hyperspy . . . . .	222
A.1.2	Fourier Deconvolution reconvolution . . . . .	222
A.2	IFTA implementation for beam shaping . . . . .	227
A.3	Iterative phase retrieval with function seeding . . . . .	228
A.4	EBL of Al structures . . . . .	230
A.5	ImageSurfer visualisation . . . . .	231
	<b>Bibliography</b>	<b>232</b>

# List of Figures

1.1	Action of a lens . . . . .	4
1.2	Local spatial frequency for plane wave . . . . .	6
1.3	Aperture screen geometry . . . . .	7
1.4	Fraunhofer diffraction ray diagram . . . . .	9
1.5	Phase delay responsible for Gouy phase . . . . .	11
1.6	Astigmatic focus schematic . . . . .	13
1.7	Vortex and plane wave wavefronts . . . . .	14
1.8	Surface normal vectors for a vortex . . . . .	14
1.9	Integer vortex scatter diagram . . . . .	15
1.10	Truncated Bessel Beam phase and amplitude . . . . .	17
1.11	Vortex decomposition into FT-TBB modes . . . . .	18
1.12	Optical trapping forces . . . . .	22
1.13	Electron lens schematic . . . . .	24
1.14	TEM mode schematic . . . . .	25
1.15	Electron trajectories in an energy filter . . . . .	26
1.16	Standard plasmon dispersion plot for Aluminium . . . . .	29
2.1	literature review phase masks . . . . .	34
2.2	literature review amplitude masks . . . . .	35
2.3	2nd literature review amplitude masks . . . . .	37
2.4	literature review magnetic field vortices . . . . .	40
2.5	literature review measuring OAM . . . . .	41
2.6	literature review surface plasmon vortices . . . . .	48
2.7	literature review previous openings . . . . .	51
3.1	2200fs TEM lens schematic . . . . .	53
3.2	TEM and NBD ray diagrams . . . . .	54
3.3	TEM mode ray diagrams low magnification, TEM and spectrum modes . . . . .	55
3.4	Holographic mask method schematic . . . . .	57
3.5	IFTA theory schematic . . . . .	60
4.1	Mask plane phase and fourier plane intensity for a vortex and C beam . . . . .	66

4.2	Scatter diagrams of phase gradients from local spatial frequency analysis $\alpha = 45^\circ$ . . . . .	68
4.3	Scatter diagram of phase gradients from local spatial frequency analysis $\alpha = 0^\circ$ . . . . .	69
4.4	C shape control contour plot of $l$ and $c$ in $\alpha, D$ space . . . . .	71
4.5	Scatter diagrams of phase gradients from local spatial frequency analysis Fresnel . . . . .	72
4.6	Fourier plane amplitude and phase for C beams . . . . .	73
4.7	Magnification of phases from figure 4.6 . . . . .	74
4.8	Astigmatic phase and amplitude distributions for vortex and C shape . . . . .	75
4.9	Astigmatic effect on superposition . . . . .	76
4.10	Camera length calculations diagram . . . . .	78
4.11	$l=9$ vortex simulated propagation . . . . .	80
4.12	Simulated propagation for a C beam and results of an iterative algorithm . . . . .	82
4.13	Propagation of $l=8$ and $l=9$ superposition . . . . .	83
4.14	Iterative algorithm target intensity distribution . . . . .	84
4.15	C shape radial and azimuthal intensity distributions . . . . .	86
4.16	Overlay of phase gradients and intensity for C shape . . . . .	87
4.17	Helico-conical and fractional topological charge rendering . . . . .	88
4.18	Azimuthal intensity plots for C shapes of different angles . . . . .	90
4.19	Azimuthal intensity plots for C shapes of different size . . . . .	91
4.20	Numerical OAM as a function of opening angle . . . . .	93
4.21	Numerical OAM of C shapes as a function of integration radius . . . . .	94
4.22	Numerical and analytical OAM expectation value . . . . .	95
4.23	LG mode decomposition of $l = 4$ vortex . . . . .	96
4.24	Mode decomposition of C into LG modes . . . . .	97
4.25	LG mode C decomposition . . . . .	97
4.26	$l=4$ spiral harmonic and Fourier vortex decompositions . . . . .	99
4.27	$l=9$ decomposition in to spiral harmonics with and without astigmatism . . . . .	100
4.28	$l=9$ decomposition in to Fourier vortices with astigmatism . . . . .	101
4.29	C shape OAM decompositions, spiral harmonics and Fourier vortex modes . . . . .	101
4.30	Truncated bessel beam decomposition of a C shape . . . . .	102
4.31	Iterative results decomposition . . . . .	102
4.32	Dual C phase mask and Fourier plane distributions . . . . .	103
4.33	Intensity for a dual C shape with large opening angle . . . . .	104

4.34	A rendering of a dual C beam propagation . . . . .	105
4.35	Dual C shape nodal line geometry . . . . .	106
4.36	Numerical OAM analysis of a dual C-shaped beam . . . . .	108
4.37	C-shaped atom trapping diagrams . . . . .	109
4.38	C trapping schematic . . . . .	110
5.1	Pt foil mask schematic . . . . .	114
5.2	SEM images of the Pt foil mask . . . . .	115
5.3	Experimental Fourier plane intensity from Pt mask . . . . .	116
5.4	Azimuthal intensity variation comparison . . . . .	118
5.5	Line plots of the gap intensity . . . . .	119
5.6	Pt foil experimental propagation series rendering . . . . .	120
5.7	Vortex trajectories comparison for ideal simulation and re- trieved phase . . . . .	122
5.8	Mode decomposition of retrieved phase from simulated input	123
5.9	Mode decomposition of retrieved phase from simulated ideal $l = 1$ vortex input . . . . .	123
5.10	TEM mode C shape phase retrieval . . . . .	125
5.11	TEM C phase retrieval propagation series . . . . .	126
5.12	An alternate view of figure 5.11 . . . . .	127
5.13	Comparison between retrieved and simulated vortex trajec- tories . . . . .	127
5.14	NBD mode phase retrieval results Fourier plane . . . . .	129
5.15	NBD phase retrieval propagation series . . . . .	130
5.16	External vortices not shown in figure 5.15 . . . . .	131
5.17	simulated vortex trajectory for large defocus . . . . .	132
5.18	Electron lithography results . . . . .	134
5.19	C shape patterning lineplot . . . . .	135
5.20	Energy filtered images of patterned $AlF_3$ film showing Al build up . . . . .	136
5.21	Energy filtered images of patterned $AlF_3$ film showing hole .	137
5.22	schematic of the Silicon nitride phasemasks . . . . .	138
5.23	Phase mask thickness maps from EFTEM images . . . . .	138
5.24	1D grating fourier transforms . . . . .	139
5.25	Bar width effect on diffraction patterns . . . . .	140
5.26	Phase contrast effect on diffraction patterns . . . . .	140
5.27	Silicon Nitride phase mask experimental intensity . . . . .	141
5.28	Azimuthal intensity comparison for simulation and experi- ment, $\alpha = 22.5$ . . . . .	142
5.29	Silicon nitride phase mask $\alpha = 45^\circ$ C shape . . . . .	144

5.30	$\alpha = 45^\circ$ C shape experimental intensity propagation series . . .	145
5.31	Phase mask rotated opening angle experimental results . . .	146
5.32	Experimental intensity propagation series from mask in figure 5.31 . . . . .	147
5.33	Results for a phasemask with blazed C shape design . . . . .	148
5.34	Direct phase mask experimental results . . . . .	150
5.35	Direct phase mask simulation . . . . .	151
6.1	Mode comparison with published energies . . . . .	154
6.2	Mode distributions for a nanodisk . . . . .	155
6.3	A breathing mode found for an Al disk which matches published energy . . . . .	155
6.4	The eigenmodes found for a 100nm Al nanodisk . . . . .	156
6.5	Mode decompositions for the modes found for a 100nm Al nanodisk . . . . .	157
6.6	Eigenmodes found for an $l = 1$ spiral . . . . .	158
6.7	OAM mode decomposition for an $l = 1$ spiral . . . . .	159
6.8	$l = 3$ spiral, $l = \pm 1$ dipole mode COMSOL fields . . . . .	159
6.9	$l = 3$ spiral, $l = \pm 1$ dipole mode, COMSOL OAM decompositions . . . . .	160
6.10	$l = 4$ spiral $l = \pm 1$ dipole mode COMSOL fields . . . . .	161
6.11	$l = 4$ spiral $l = \pm 1$ dipole mode COMSOL decompositions . . . . .	161
6.12	MNPBEM calculated EELS for spirals of increasing step size . . . . .	162
6.13	MNPBEM calculated $E_z$ fields . . . . .	163
6.14	MNPBEM calculated $E_z$ fields . . . . .	163
6.15	MNPBEM calculated $E_z$ fields . . . . .	164
6.16	MNPBEM calculated $E_z$ fields . . . . .	165
6.17	Mode decomposition for fields calculated for MNPBEM . . . . .	165
6.18	Numerical OAM for fields calculated by MNPBEM . . . . .	166
6.19	Induced E field for an $l = 4$ spiral island . . . . .	167
6.20	Simulated EELS spectra for an $l = 4$ spiral island . . . . .	168
6.21	The amplitude and phase of simulated induced E fields for an $l = 3$ spiral island . . . . .	169
6.22	Simulated induced E field for an off axis incident electron beam . . . . .	170
7.1	Schematic diagram of spiral island sample . . . . .	173
7.2	STEM EELS maps at 2.5eV for a nanosquare, nanodisk, nanorods and a corner . . . . .	174
7.3	The argument maxima-minima difference for bessel functions . . . . .	174

7.4	STEM experimental spiral gap measurements . . . . .	177
7.5	experimental STEM EELS intensity at 3eV for an $l = 1$ spiral	178
7.6	Simulated STEM EELS intensity at 3eV for an $l = 1$ spiral .	179
7.7	Experimental STEM EELS intensity at 3eV for an $l = 2$ spiral	179
7.8	Simulated STEM EELS intensity at 3eV for an $l = 2$ spiral .	180
7.9	Experimental STEM EELS intensity at 3eV for an $l = 3$ spiral	180
7.10	Simulated STEM EELS intensity at 3eV for an $l = 3$ spiral .	181
7.11	Experimental STEM EELS intensity at 4eV for an $l = 4$ spiral	181
7.12	Simulated STEM EELS intensity at 3eV for an $l = 4$ spiral .	182
7.13	Experimental STEM EELS intensity at 3eV for an $l = 5$ spiral	182
7.14	Simulated STEM EELS intensity at 3eV for an $l = 5$ spiral .	183
7.15	SEM images of structures produced by FIB . . . . .	185
7.16	Cathodoluminescence of structures 1 to 4 . . . . .	186
7.17	Cathodoluminescence of structures 5 to 11 . . . . .	186
7.18	Cathodoluminescence image . . . . .	187
7.19	SEM images of structures produced by EBL . . . . .	187
7.20	Cathodoluminescence of structures produced by EBL . . . .	188
7.21	Cathodoluminescence of structures produced by EBL. . . . .	188
7.22	Cathodoluminescence of silver structures . . . . .	189
7.23	AFM surface height of a structure produced by FIB . . . . .	190
7.24	AFM surface height of a structure produced by EBL . . . . .	191
7.25	EELS experiment schematic lens diagram . . . . .	193
7.26	Pinhole mask . . . . .	194
7.27	Pinhole mask EELS difference signal . . . . .	195
7.28	Al spiral C-shaped EELS . . . . .	196
7.29	Al spiral C-shaped EELS difference signal . . . . .	197
7.30	Al background C beam EELS difference signal . . . . .	198
7.31	A zoomed in view of the graph in figure 7.30 . . . . .	198
7.32	A C beam EELS difference signal for a nanodisk . . . . .	199
7.33	A zoomed in view of figure 7.32 . . . . .	199
7.34	EELS without a sample . . . . .	200
7.35	A zoomed in view of figure 7.34 . . . . .	201
7.36	The measured C beam EELS difference signals normalised to the zero loss peak . . . . .	201
7.37	The measured C beam EELS difference signals normalised to the summation up to 27eV . . . . .	202
A.1	C beam EELS comparison with $l = 0$ and a circular aperture	208
A.2	A zoomed in view of figure A.1 . . . . .	208

A.3	The effect of astigmatism on the measure C beam EELS difference signal . . . . .	209
A.4	The effect of defocus on the measured C beam EELS difference signals normalised to the zlp . . . . .	209
A.5	The effect of defocus on the measured C beam EELS difference signals normalised to the summation of intensities . . .	210
A.6	EELS recorded for +C and -C at different values of tilt . . .	210
A.7	EELS recorded for +C and -C at different values of tilt for Silicon Nitride membrane on top . . . . .	211
A.8	A zoomed in view of figure A.7 . . . . .	211
A.9	Measured full width half maximum values for zero loss peaks of different C orders . . . . .	212
A.10	EELS produced by direct subtraction of the Silicon nitride background . . . . .	214
A.11	Richardson-Lucy (RL) deconvolution of psf with psf 781 . .	215
A.12	RL deconvolution of 12sept 37 (-C on $l = 4$ spiral) with psf 781 . . . . .	216
A.13	RL deconvolution of 12sept sets with psf in matlab its 1 . .	217
A.14	RL deconvolution of 12sept sets with psf in matlab its 2 . .	217
A.15	RL deconvolution of 12sept sets with psf in matlab its 3 . .	218
A.16	RL deconvolution of 12sept set 37 (-C on $l = 4$ spiral) with 11 oct no sample PSF . . . . .	219
A.17	RL deconvolution with 1 iteration . . . . .	220
A.18	RL deconvolution with 2 iterations . . . . .	220
A.19	RL deconvolution with 3 iterations . . . . .	221
A.20	Hyperspy deconvolutions using RL 5 iterations 11th oct psf .	222
A.21	Hyperspy deconvolutions using RL 5 iterations 11th oct psf on flipped substrate . . . . .	223
A.22	Reconvolutions with gauss widths 25,30,35,40,45 . . . . .	224
A.23	Width 2 (equivalent to 30 ) reconvolutions from 12th sept psf	225
A.24	Reconvolutions from 12th sept psf . . . . .	225
A.25	Reconvolutions from 11th oct no sample psf . . . . .	226
A.26	IFTA beam shaping flowchart . . . . .	228
A.27	IFTA phase retrieval flowchart . . . . .	229
A.28	Image surfer software screenshot . . . . .	231

# Acknowledgements

I have thoroughly enjoyed my time at York during my PhD studies and I would like to express my gratitude to my supervisors Professor Yuan and Professor Babiker for their encouragement and guidance throughout my project. I have been extremely lucky to have had the opportunity to visit and present at multiple conferences over the years, giving me a chance to experience the reality of research and find out the latest developments. If anything, I have become even more fascinated with Physics, even the parts I did not think too deeply on during my undergraduate degree. I can attribute this to the stimulating atmosphere at the University of York and the enthusiasm for research of both my supervisors. During the start of my project I received help from Dr Gnanavel Thirunavukkarasu during multiple electron microscope sessions, I am grateful for his guidance and introduction to electron microscopy. In addition, being in charge of the JEOL 2200FS used in this thesis, Dr Leonardo Lari was always ready to help out during experiments if any problems arose and I would like to express my thanks for that. As well as staff at York, I have received help from two people from the University of Leeds: Dr Michael Ward helped me during focused ion beam sessions and Dr Mark Rosamond produced the thin Aluminium structures via electron beam lithography. I would like to thank them both for their efforts which ultimately enabled the experiments to proceed. Finally, it would be remiss of me not to mention the Octopush team at York ,who run underwater hockey games during the academic terms. Those sessions offered a much needed break from my studies and allowed me to form many new friendships, whilst playing a sport, which I did not know existed until I was perusing the list of clubs available at the University, when I arrived back in 2013.

# Author's Declaration

I declare that this thesis is a presentation of original work and I am the sole author. This work has not previously been presented for an award at this, or any other, University. All sources are acknowledged as References. The project goals were decided based upon discussions with my two supervisors Professor Jun Yuan and Professor Mohamed Babiker, who also aided in the interpretation of the results. The pinhole mask described in the final chapter was designed and test by Dr Yuanjie Yang and Professor Jun Yuan. The experimental data for the  $l = 5$  spiral structure was gained at the University of Manchester by Professor Jun Yuan, but all of the subsequent analysis was performed by myself. Publications including work from this thesis:

1. *C-shaped electron beams : design, experimental production and application.*  
M.Mousley, G.Thirunavukkarasu, M.Babiker, J.Yuan.  
Proc. SPIE 9581, Laser Beam Shaping XVI, 95810C (August 25, 2015); DOI:10.1117/12.2187859;
2. *Robust and adjustable C-shaped electron vortex beams*  
M.Mousley, G.Thirunavukkarasu, M.Babiker, J.Yuan New Journal of Physics, Volume 19, June 2017. DOI:10.1088/1367-2630/aa6e3c
3. *Normal modes and mode transformation of pure electron vortex beams*  
G. Thirunavukkarasu, M. Mousley, M. Babiker, J. Yuan Philosophical Transactions: Mathematical, Physical and Engineering Sciences, 375, 2087, 28 Feb 2017. DOI:10.1098/rsta.2015.0438

# Chapter 1

## Introduction

### 1.1 Electron microscopy history and recent developments

Electron microscopy (EM) built upon cathode ray technologies which had previously utilised magnetic fields to control electron trajectories [1, 2]. Ernst Ruska and Max Knoll [1] realised that magnetic fields could also be used to focus electrons and these could then be used for imaging in a transmission electron microscope (TEM). This was in direct analogy to the use of glass lenses to control photons in light microscopy. Since their creation in 1931, electron microscopes have become a key scientific tool for gaining insight into many fundamental processes occurring on length scales below the resolution limit of photon microscopy ( on the order of 100 nm). The utility of these new microscopes was acknowledged by the Nobel prize committee and the 1986 nobel prize in physics was awards partly to Ernst Ruska "for his fundamental work in electron optics, and for the design of the first electron microscope" [2] . Initially the resolution was poor by todays standards, an initial proof of principle prototype only managed 14.4 x magnification , increasing to 12,000 in 1933 [3]. This magnification increased with the introduction of scanning TEM (STEM) mode which uses a small focused probe. When raster scanned over a sample in STEM mode this focused probe allowed an increase to angstrom resolution, making atoms visible in the electron microscope [4]. In 1997 it was shown that the invention and development of aberration correctors allows the spheri-

cal aberrations in a beam to be overcome and forms very small probes in TEM and STEM mode [5]. Sub angstrom resolution was then reported. The field of electron microscopy continues to advance today, with the latest superSTEM 3 microscope capable of resolutions below 0.7 angstrom at 100kV [6]. In analogy to glass causing diffraction through a prism, energy filters using magnetic fields were developed with the capability to spread an electron beam, separating different energies (see figure 1.15) , and in addition to spatial image resolution the energy resolution of spectra has also improved greatly with current TEM systems capable of achieving 15meV energy resolution (e.g. SuperSTEM3 [7]). However progress in resolution (spatial and energy) has plateaued with each new advance taking much more effort. Due to this limitation researchers in the field of electron microscopy are constantly looking for new ways to utilise electrons to interrogate samples to provide scientists with more information. Some recent developments include ultrafast TEM[8] using pulsed lasers to interact with the sample and then using a second delayed laser pulse to produce very short electron wavepackets which will interact with the sample at a set time delay from the excitation. This allows pump probe EM experiments to analyse dynamical processes with very high temporal resolution as well as spatial resolution in pump probe type experiments. The production of large plasmonic fields in metal structures when excited by a laser can also be used to compress the electron pulse further[9]. In addition to improving the data produced by the microscope, with the increase in computational abilities there are many new data analysis methods being developed. Like many fields in science, there is currently a trend towards analysis of large data sets in microscopy one example being the 3d tomographical reconstruction from images recorded with the sample tilted to different angles [10]. Originally EM was only conducted with the sample in the vacuum of the main electron column and subject to the temperature and pressure of the column however there are new experiments being conducted utilising pressure and temperature control in addition to some experiments allowing the introduction of gas to the sample chamber whilst imaging [11].

A very recent field of research, and the focus of this thesis is the control of the probe electron phase, specifically to produce electron vortex beams. These beams are electrons propagating in free space which also have orbital angular momentum (OAM), usually associated with the bound states of an atom. The OAM is related to circulation of the electron and means each vortex state has an accompanying magnetic field much like a current loop or solenoid. These vortex electrons can in theory provide magnetic

contrast in electron microscope images which is not available to beams without OAM. The vortex electrons also have the possibility of controlling nanoscale particles in a similar manner to optical traps . This introductory chapter will cover the foundational physics required for the description of electron vortex experiments. This thesis concerns electron optics, as such it will be useful to summarise some key concepts in optics in general, which apply to both light (photon) optics and electron optics.

## 1.2 Introduction to waves

The standard pedagogical example for wave propagation is the one dimensional classical mechanical wave on a string. In this case kinetic energy is transferred from one part of the string to another via a coupling due to the tension acting between positions on the string. The motion of one part of the string is linked to the neighbouring sections in such a way that energy is transferred along the string without transferring mass in the direction of wave propagation. The displacement of the string in this basic example is described by the familiar sinusoidal wave. Each collection of constant phase positions is a series of points separated by the wavelength of the oscillation. In two dimensions, such as mechanical waves at the surface of water, these isophase points become isophase lines equally spaced by the wavelength and in three dimensions, such as sound waves, the isophase collections are surfaces. When modelling the waves as plane waves these surfaces are flat planes separated by the wavelength along the normal to the planes. By applying a Fourier transformation any arbitrary three dimensional wavefront,  $f(\mathbf{r})$  of position  $\mathbf{r}$ , can be decomposed into the basis set of monochromatic plane waves, with wavevector  $k$ , following the equation

$$F(\mathbf{k}) = \int f(\mathbf{r}) \exp^{i\mathbf{k}\cdot\mathbf{r}} d\mathbf{r} \quad (1.1)$$

Whilst plane waves offer a simple basis set, each function has an infinite extent and as such plane waves can never physically be produced. A commonly used alternative is to describe a beam with an amplitude envelope, such as Gaussian beams. In this case the intensity is no longer constant and the wave can be normalised.

Within this classical wave model oscillations at one point in space affect the oscillations of neighbouring points in space. The local phase defines how much of a single sinusoidal oscillation the oscillation has reached locally, with respect to the surrounding oscillations. The two properties of note for any wave oscillation are its amplitude and phase. If two positions are in phase they have always completed the same amount of an oscillation.

### 1.3 Geometric ray optics for lenses

The concept of a ray is a basic model for describing how wave-based phenomena will behave in an optical system. Ray diagrams, such as those in figure 1.1, show trajectories of waves with straight arrows and optical systems can be shown with multiple arrows, following different paths between points. This method simplifies the action of a lens into a geometric operation mapping intensity on the lens to intensity in an image and ignores the phase of the incident wave. It can be applied to simple imaging and is applicable to incoherent illumination, where the image only relies on the the amplitude of the wave travelling through the optical system.

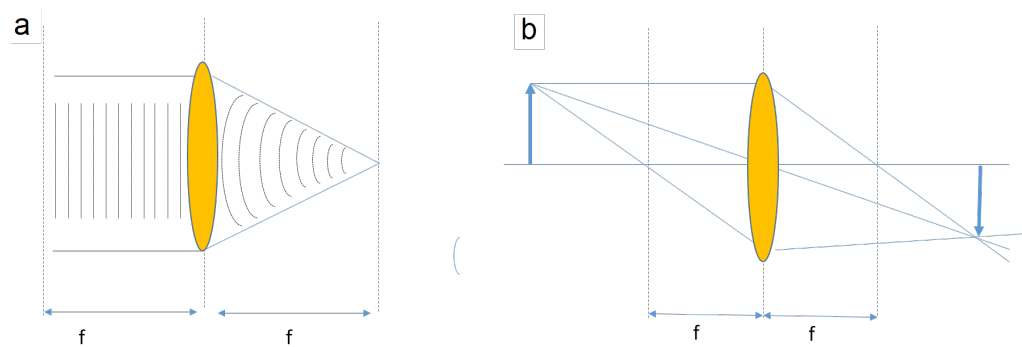


Figure 1.1: *Ray diagrams for lens focusing and imaging, where  $f$  is the focal length showing a) the action of a lens on a plane wave allowing Fourier optics and b) image formation*

## 1.4 Fourier optics

In ray optics [12] when a plane wave encounters a lens, the part of the wave at the thicker center of the lens suffers a larger phase delay than the positions at the edges, as such the phasefront is curved so that the energy in the wave is transferred to a single point in the focal plane as shown in figure 1.1.

This means that the wave in the front focal plane (the same side as the object, left side in figure 1.1) is the Fourier transform of the wave in the back focal plane (same side as the image, right in figure 1.1) . The same analysis applies when considering point sources in the back focal plane which will produce plane waves in the front focal plane. This type of ray tracing analysis can be applied to explaining simple image formation as shown in figure 1.1 b, where the object arrow on the left of the lens produces a smaller image arrow on the right of the lens. This image is formed at the plane where two rays meet, the first of which is the parallel ray which is directed through the central point of the focal plane, the second is the ray travelling through the center of the lens which continues without diversion. Where these two meet all the intensity from the tip of the object arrow is brought back to focus at the tip of the image arrow.

The Fourier transform relationship between the front and back focal planes is the basis of local spatial frequency analysis when applied to a phase distribution. In this analysis the local normal of a phase front is considered to represent a contribution from a plane wave pointing along the normal. When a plane wave is focused the transverse gradient of the phase will determine the transverse component of the normal to the phasefront, as shown in figure 1.2. The Fourier plane intensity of a plane wave can be predicted by plotting the value of the transverse phase gradient as a dot in reciprocal space. This can be understood by considering a monochromatic plane wave travelling directly into a lens, with the wavevector parallel to the lens optical axis. The image formed in the Fourier plane will be a focused spot, corresponding to a wavevector with no transverse components, which is centered at and defines the origin. When the plane wave is tilted the spot will move depending on the direction of tilt. Figure 1.2 shows this effect for a tilted plane wave, (a) shows a plot of the phase distribution and the arrow highlights the phase gradient, (b) now considers the wavefront (isophase surface) as such the coloured phase gradient in (a) now corresponds to a

distance along propagation of the phase front, the phase gradient is the local surface normal to the isophase surface. Figure 1.2 c shows the spot produced by the phase distribution in (a) is shifted from the origin in the  $k_x$  direction, by an amount corresponding to the size of the phase gradient (i.e. the amount of tilt). When the wavefront incident on the focusing lens is not a plane wave the contributions from many different local phase gradients build up multiple spots in the predicted Fourier plane intensity.

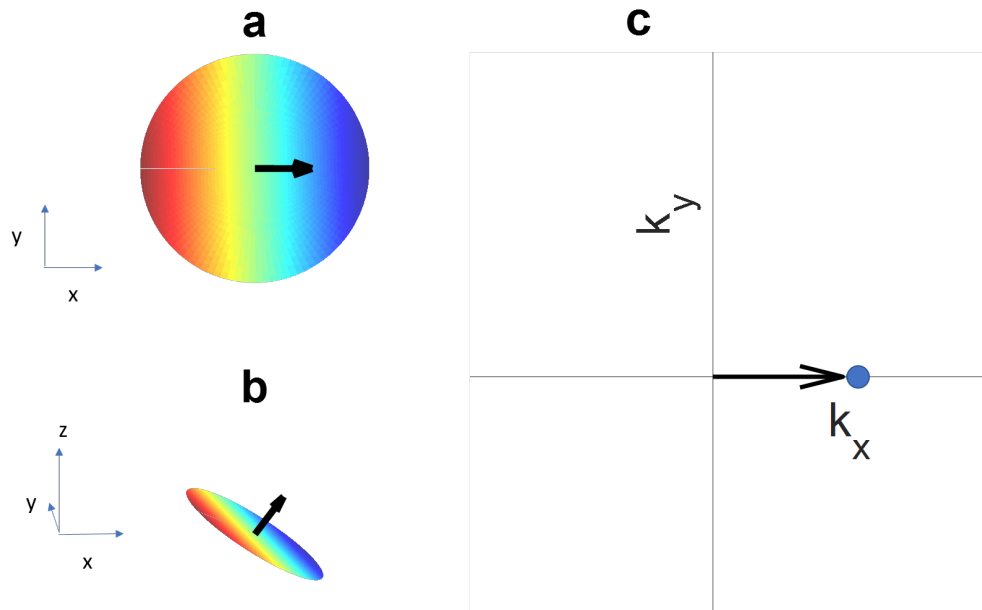


Figure 1.2: *Applying a local spatial frequency analysis, calculating the local phase gradient of a tilted plane wave a) colour represents phase and the black arrow shows the 2D phase gradient. b) the surface normal to the isophase surface where colour now represents distance along propagation c) the plane wave in (a) contributes a single spot (blue circle) at the end of the black arrow in reciprocal space.*

When sending a non-planewave through a lens the varying local phase gradients can be considered as causing spots of intensity to appear in the focal plane at positions corresponding to the local phase surface normals of the non-planewave which is incident on the lens. This is a simplified model and does not account for the phase differences between contributions from different points which may end up at the same focal plane position. As such any interference effects are not captured by this geometric ray model.

## 1.5 Wave optics

In contrast to the ray model a wave optics description can be used to predict the intensity in experiments involving wave phenomena, whilst including interference effects by considering phase terms. This model uses the Huygens Fresnel principle [12] where each local oscillation is viewed as a source of secondary complex waves, following the equation

$$E(\mathbf{d}, t) = \frac{E_0}{|\mathbf{d}|} \exp i(\mathbf{k} \cdot \mathbf{d} - \omega t). \quad (1.2)$$

where  $\mathbf{k}$  is the wavevector and  $\mathbf{d}$  is the displacement vector from the source,

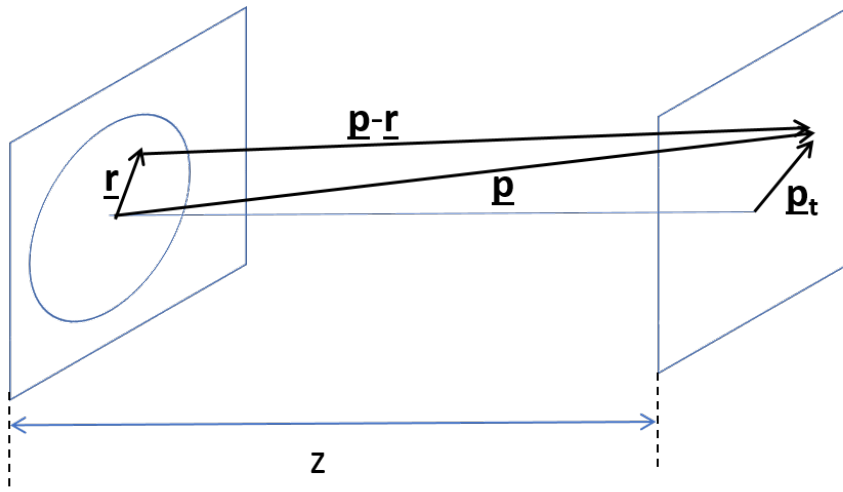


Figure 1.3: *The field at a position  $\mathbf{p}$  caused by a source in the aperture plane at position  $\mathbf{r}$  can be described by considering the total vector separating the two,  $\mathbf{p}-\mathbf{r}$*

$\omega$  is the waves frequency and  $t$  is the time at which the field is measured. The overall wave can then be described by the summation of the entire collection of complex secondary waves. This means the diffraction pattern at a position  $\mathbf{p}$  at a plane after an aperture ( as shown in figure 1.3) can be expressed as a integration of infinitely many individual sources over the aperture area

$$E(\mathbf{p}) = \exp i\omega t \int \frac{E_{ap}(\mathbf{r})}{|\mathbf{p} - \mathbf{r}|} \exp i(\mathbf{k} \cdot (\mathbf{p} - \mathbf{r})) dA \quad (1.3)$$

where  $\mathbf{p}$  and  $\mathbf{r}$  are shown in figure 1.3 along with  $z$ , the distance between the measurement plane which contains  $\mathbf{p}$  and is parallel to the aperture

plane. This wavelet analysis can be used to derive different integral equations describing the wavefield after an aperture. There are two distinct regions where approximations to 1.3 can be taken [12]. The far field where curvature of the wavefront can be ignored, known as the Fraunhofer regime and the near field where the curvature of the wavefront must be taken into account, known as the Fresnel regime.

### 1.5.1 Fraunhofer diffraction

Considering the limit of the separation,  $z$  between aperture and screen,  $z \rightarrow \infty$ , in the far field Fraunhofer case, the distance  $|\mathbf{p} - \mathbf{r}|$  is predominantly  $z$ . This means the main variation is taken to be mostly from the exponential and so the factor  $1/|\mathbf{p} - \mathbf{r}|$  is considered to be approximately constant over the aperture and is taken outside the integral. Thus from the aperture field  $E_{ap}$ , the screen plane field  $E(p)$  can be approximated by

$$E_{fraun}(p) = \frac{\exp i\omega t}{|\mathbf{p} - \mathbf{r}|} \int E_{ap}(\mathbf{r}) \exp i(\mathbf{k} \cdot (\mathbf{p} - \mathbf{r})) dA \quad (1.4)$$

the angular spread of light coming from the aperture and reaching the screen reduces until the light at point  $p$  is due to rays travelling from the aperture at the same angle. This can be experimentally achieved by placing the screen in the back focal plane of a focusing lens with the aperture in the front focal plane. The lens imparts a phase distribution such that all wavelet source rays travel towards the center of a circle, and so we only need to consider the phase delay of each wavelet source in reaching the lens. In this picture the phase difference  $\mathbf{k} \cdot (\mathbf{p} - \mathbf{r})$  across the mask will depend on the path length difference  $\delta = r \sin(\theta)$ , as shown in figure 1.4, causing a phase delay  $|\mathbf{k}| \sin(\theta) \hat{\mathbf{k}}_t \cdot \mathbf{r}$  where  $\hat{\mathbf{k}}_t$  is the transverse unit vector of  $\mathbf{k}$ .

Due to the mapping of a single angle onto a single point when  $z \rightarrow \infty$ , the transverse component of  $\mathbf{p}$ ,  $\mathbf{p}_t$  in the screen plane corresponds to the transverse reciprocal space wavevector component  $|\mathbf{k}| \sin(\theta) \hat{\mathbf{k}}_t$ . This relationship means that the summation of  $|\mathbf{k}| \sin(\theta) \hat{\mathbf{k}}_t \cdot \mathbf{r}$  terms is equivalent to a summation of  $\mathbf{p}_t \cdot \mathbf{r}$ .

However in real space the physical size of  $\mathbf{p}_t$  depends upon the focal length  $f$  through  $|p_t| = f \tan(\theta)$  this shows that a larger focal length

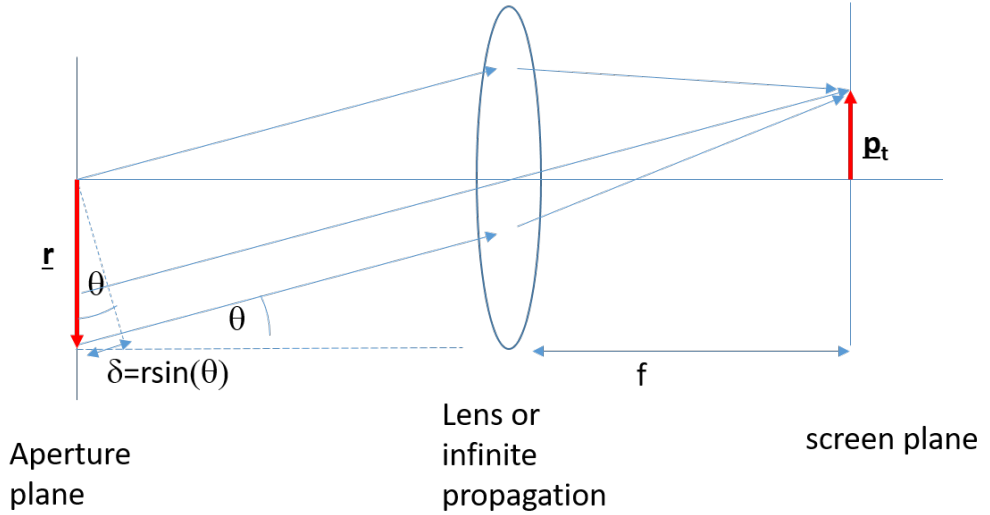


Figure 1.4: When considering diffraction from an aperture, collected onto a screen by a lens, plane waves will be collected to a point on the screen if it is placed in the focal plane of the lens.  $a$  labels the path length difference, which is a function of position in the aperture plane.

increases the physical image size, through a simple magnification, but the position  $\mathbf{p}_t$  still represents the same incident wavevector on the lens. The optical system is then characterised by this angular mapping, in electron microscopy the effective focal length is called the 'camera length'. Within the paraxial (small angle) approximation,  $\sin(\theta) \approx \tan(\theta)$ , meaning that an integration of  $k \sin(\theta) \cdot r$  terms with respect to  $r$  is equivalent to an integration of  $k \tan(\theta) \cdot r = (k/f) \times \mathbf{p}_t \cdot \mathbf{r}$  terms. This means in the field can be calculated by considering each position  $\mathbf{r}$  as contributing a term  $|k|(|\mathbf{p}_t|/f) \hat{\mathbf{p}}_t \cdot \mathbf{r} = (k/f) \mathbf{p}_t \cdot \mathbf{r}$ . This means the total field as  $z \rightarrow \infty$  is expressed as

$$E_{\text{Fraun}}(\mathbf{p}_t) = \frac{\exp i\omega t}{|\mathbf{p} - \mathbf{r}|} \int E_{\text{ap}}(\mathbf{r}) \exp i((|k|/f)(\mathbf{p}_t \cdot \mathbf{r}) dA \quad (1.5)$$

, which is only valid at large  $z$  and for small angles where  $\sin(\theta) \approx \tan(\theta) \approx \theta$ . This is proportional to the Fourier transform of the aperture field.

## 1.5.2 Fresnel diffraction

For small angles the separation  $\mathbf{r}_{rp} = \mathbf{p} - \mathbf{r}$ , in the denominator outside the integral of equation 1.3 is approximately equal to  $z$ . The phase delay of

each wavelet contribution depends on the term  $|\mathbf{p} - \mathbf{r}| = \sqrt{R^2 + z^2}$  where  $R = |\mathbf{p}_t - \mathbf{r}|$  with subscript  $t$  representing a transverse component. This square root can be approximated, to first order terms, using a Taylor series expansion as  $z(1 + \frac{R^2}{2z})$ . This means the field at a plane  $z$  away from a known field distribution  $E_0$  is

$$E(\mathbf{p}_t) = \frac{\exp(ikz)}{z} \int \frac{E(r)}{z} \exp(i(\pi/\lambda z)|\mathbf{p}_t - \mathbf{r}|^2) dA \quad (1.6)$$

Mathematically the integral in 1.6 is equivalent to convolution of the aperture field,  $E(r)$  with a propagator function  $F_{prop}(z, \mathbf{r}) \equiv \exp(i\frac{\pi}{\lambda z}|\mathbf{r}|^2)$ . This means the Fourier transform of the Fresnel propagation equation can be expressed in reciprocal space as a product of the two separate Fourier transforms.

$$G_p(k) = FT_r(k) \times FT_p(\mathbf{k}) \quad (1.7)$$

where  $FT_r$  is the Fourier transform of the aperture field  $E(r)$  and  $FT_p$  is the Fourier transform of  $F_{prop}(z, \mathbf{r})$ . This can be shown to be equal to [13]

$$FT_p(z, \mathbf{k}) = \exp(i\pi\lambda z|\mathbf{k}|^2) \quad (1.8)$$

Thus the field at a distance  $z$  away from a known field can be expressed via the equation

$$E(p) = \frac{\exp(ikz)}{z} FT(G_p(k)) \quad (1.9)$$

where  $FT$  denotes the Fourier transform. When calculating the Fresnel propagation close the Fourier plane from an apertured mask, the mask plane is the Fourier transform of the diffraction (Fourier) plane, as such when simulating propagation the mask function can be used as  $G_p(k)$  in equation 1.9.

## 1.6 Gouy phase

When focusing a wave the energy density increases and then after the focal plane the energy density decreased, as the wavefronts expand outward.

This is shown schematically in figure 1.5 a This physical process can be described with a Laguerre-Gaussian function,

$$LG_{p,l} = e^{ik_z z} \frac{N}{\sqrt{z_R^2 + z^2}} L_p^l \left( \frac{2\rho^2}{\omega^2(z)} \right) \frac{e^{il\phi}}{w(z)} \left[ \frac{\rho}{w(z)} \right]^l \times \exp \left( i \frac{k_z \rho^2 z}{2(z_R^2 + z^2)} - \frac{\rho^2}{w^2} - i\delta_{Gouy} \right) \quad (1.10)$$

where the  $l$  is the azimuthal quantum number which determines the OAM and  $p$  is the radial quantum number and determines the number of nodes as the radius is increased, the Gouy phase term is defined by  $\delta_{Gouy} = [2p + l + \arctan(\frac{z}{Z_R})]$ . This  $\delta_{Gouy}$  leads to an extra phase where  $z_R$  is the rayleigh length defined as the distance away from focus at which the intensity is  $1/e$  of its maximum value. This is extra Gouy phase is related to the

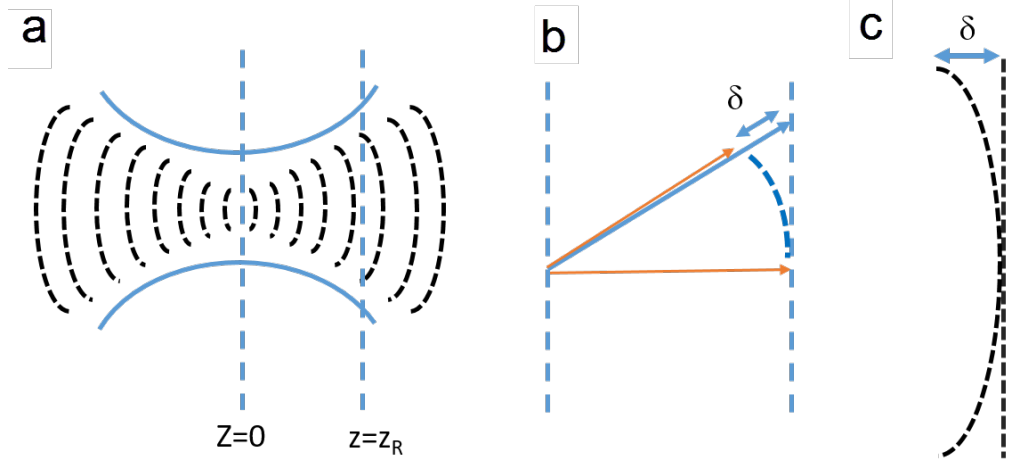


Figure 1.5: a) a schematic of the focusing of wavefronts showing a cross section of a focused spherical wave. Black lines are isophase lines, solid blue lines mark the top and bottom of the volume in which the highest intensity is.  $Z_R$  is the distance at which the maximum intensity falls to  $1/e$  of the maximum intensity at  $z = 0$  b) A plane wave wavevector (blue arrow) at an angle to a second plane wave wave vector (orange arrow), the first will need to travel further to reach the same distance in the direction of the second plane wave, suffering a phase delay  $\delta$ . c) A similar position dependent phase delay  $\delta$  is also present when a plane wave wavefront is curved, which occurs whilst focusing.

uncertainty principle [14]. Any finite wave must necessarily be composed of multiple plane waves. This can be clarified by noting that for a wave to be finite there must be an uncertainty in the position which is less than infinity, as such the corresponding uncertainty in momentum (i.e. the wavevectors of the plane waves) must be non zero. As explained by Feng and Winful [14], by focusing a wave with a lens the spread of the intensity is decreased and so is the uncertainty in the position. This leads to an increase in the spread of the component wavevectors which produce the total wave. Any second plane wave at an angle to a first will undergo more oscillations when travelling the same distance in the direction parallel to the first wavevector, as shown in figure 1.5 a. Therefore by increasing the uncertainty in the modulus of the transverse wavevector components producing the total wavefront, a lens transfers more intensity to wave components travelling at higher angles to the forward wave propagation direction and increases the phase gained upon propagation.

## 1.7 Astigmatism

When forming an image physical systems can suffer from imperfections which can cause distortions to the image, these are known as aberrations. One key aberration which is experienced in many imaging systems including electron microscopes is astigmatism [15]. When producing physical optical components it is likely they will not be perfectly symmetric, if an optical lens or magnetic lens field has a slightly cylindrical curvature rather than a spherical curvature then the wavefronts leave the lens with different radii of curvature along two perpendicular directions as shown in figure 1.6 (firstly along the height of the cylindrical distortion and then perpendicularly around the curvature of the cylinder). This distortion is what is meant by the term astigmatism, it means rays dispersed along the horizontal axis (sagittal) are brought into focus at a different point along the propagation direction to those dispersed along the vertical axis (tangential), as shown in figure 1.6. This causes circular details to be imaged as ovals. The effect of astigmatism can be mathematically represented as an extra phase term  $\chi(\rho, \phi)$  added to the ideal phase following the equation  $\chi(\rho, \phi) = 2\pi A\rho^2 \cos^2(\phi)$  where  $(\rho, \phi)$  are polar coordinates and  $A$  is an amplitude determining the strength of the astigmatism. The distortion could

also be measured with an ellipticity of a circle defined as  $\frac{a-b}{a}$  for an ellipse of large horizontal radius  $a$  and short vertical radius  $b$ .

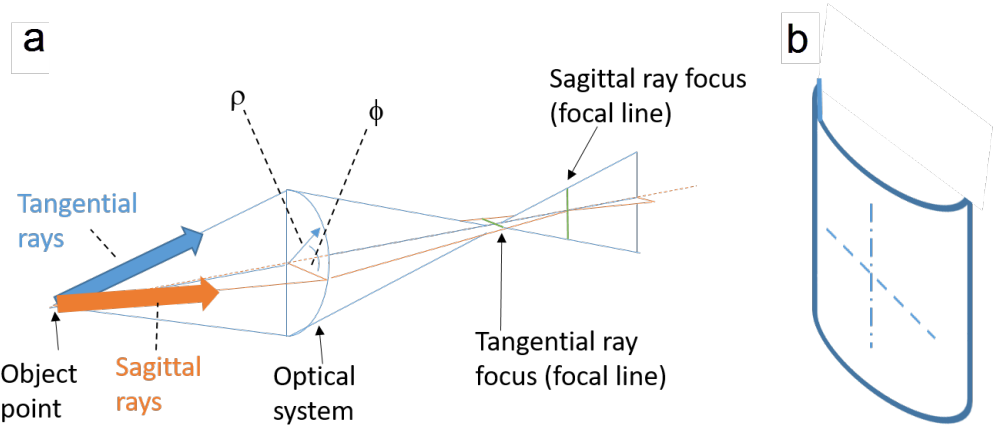


Figure 1.6: *a) In an astigmatic optical system the tangential rays (vertical spread) and the sagittal rays (horizontal spread) are brought to focus at in planes located at two different distances along the beam axis. b) a cylindrical curvature causes two different radii of curvature along the height (dashed-dotted line) and the curve (dashed line).*

## 1.8 Vortex physics

A complex field given by  $A \exp(i\chi)$  has an amplitude  $A$  and a phase  $\chi$ . If the phase  $\chi$  is proportional to the circular polar angular coordinate  $\phi$  this means that the phase must increase as you circulate the axis. As such there is a singularity at  $\rho = 0$  where  $\phi$  and so  $\chi$  is undefined. If such a complex function is associated with a travelling wave oscillation then the corresponding wavefronts produced are twisted (see figure 1.7). These twisted vortex states can offer an alternative complete basis set of functions as they themselves are a combination of plane waves. Through the combination of plane waves travelling in all directions on a circle in the transverse plane the vortex beam has a circulation associated with it. Each vortex mode can be considered to be a combination of plane waves with a constant transverse amplitude as shown by the phase surface normals in figure 1.8.

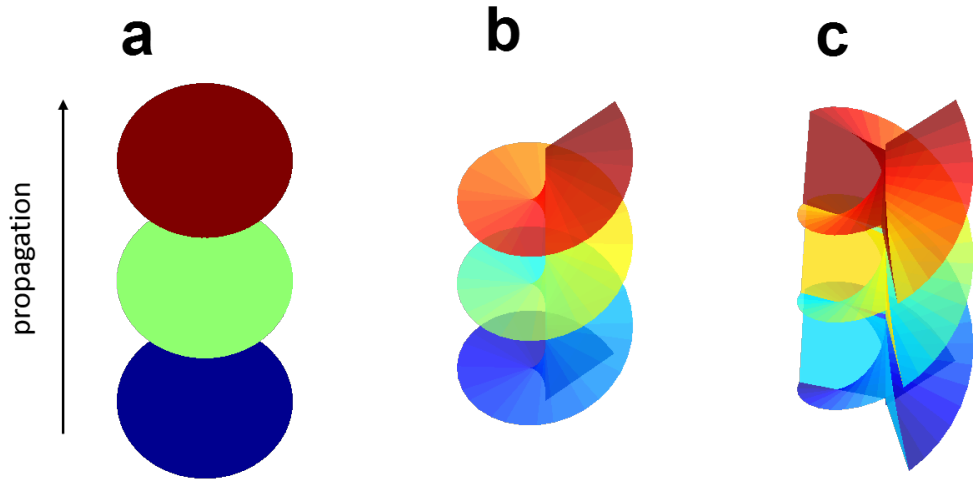


Figure 1.7: *Flat isophase fronts of a plane wave (a) form stacks of non intersecting planes at different propagation distances. When the phase is twisted in beams with topological charge  $l=1$  (b) each sheet is deformed such that it meets the neighbouring sheets to form a spiralling ramp of equal phase. For  $l=3$  (c) there are 3 lines along which neighbouring planes meet. Colour shows the distance along propagation of the isosurface.*



Figure 1.8: *A side on view with propagation upwards (left) and a top down view with propagation out of the page (right) of a vortex isophase surface. Colour represents distance along propagation and arrows show the local surface normal vector.*

By considering these local normals to the phasefront, local spatial frequency analysis ([16]) can explain the ring distribution of a vortex beam. As discussed in section 1.3, each normal contributes a point of intensity in the focal plane. As shown by the right image in figure 1.8, these points

will cover all angles and all have an identical radius, as such the intensity distribution in the Fourier plane of a vortex phase will be a ring. By plotting out Fourier plane points from local phase gradients sampled around an apertured vortex phase function the Fourier plane intensity can be predicted (see figure 1.9). Areas of higher density of points in these scatter diagrams correspond to higher Fourier plane intensities, colours distinguish between phase gradients at different radii on the mask.

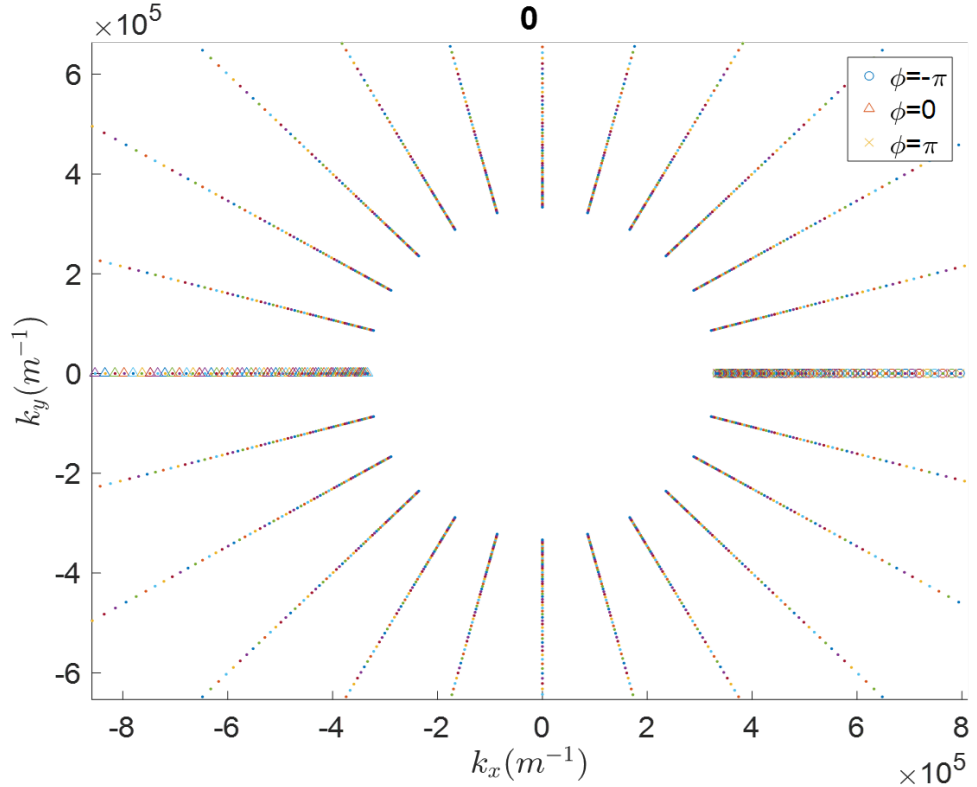


Figure 1.9: *The scatter diagram from a local spatial frequency analysis of an  $l = 1$  vortex. The local gradients at constant radius form rings of points in the reciprocal plane scatter diagram. Different colours are gradients measured at different radii. Gradients are sampled at a discrete collection of angles, producing the separate radial lines.*

It must be noted here that this ignores any interference effect between rays coming from different parts of the vortex phase distribution, this shows up particularly for non-integer vortex states. In this case the phase gradients would still point in the same direction but the discontinuity in the phase creates a region of low intensity which is not captured by

the simple geometric ray analysis. However this analysis provides a useful rational for understanding the implications of varying the mask plane phase and explaining the breaking of the symmetry seen for C-shaped intensity as will be discussed later in this thesis. In general it is simplest to choose basis functions which match the symmetry of the physical system, this means vortex beams are useful basis functions for problems with cylindrical symmetry, especially those containing phase singularities.

## 1.9 Fourier Transform Truncated Bessel Beam modes (FT-TBBs)

To describe phase structured beams produced by apertured masks, it is useful to define a basis set of functions which are themselves produced by an apertured mask. As such one can consider an apertured Bessel function[17],  $\psi$ , with a vortex phase term following the equation

$$\psi(\rho, \phi)_{p,l} = N_{p,l} A(\rho) J_l(k_{p,l} \rho) e^{il\phi} \quad (1.11)$$

where  $N_{p,l}$  is a constant normalisation factor,  $l$  is the azimuthal index of the mode and  $p$  is the radial index. The phase term ( $k_{p,l} \rho_{max}$ ) is the argument at the  $(p+1)^{th}$  zero of the Bessel function, and the aperture  $A(\rho) = 1$  for  $\rho < \rho_{max}$  and 0 elsewhere. The normalisation factor can be calculated by applying the two identities

$$\int_0^{\rho_{max}} (J_l(k_{p,l} \rho))^2 \rho d\rho = \frac{(J_{l+1}(k_{p,l} \rho_{max}))^2}{2} \quad (1.12)$$

and

$$\int_0^{2\pi} e^{im\phi} e^{in\phi} d\phi = 2\pi \delta_{mn} \quad (1.13)$$

this means  $N_{pl} = \frac{1}{\sqrt{2\pi} J_{l+1}(k_{p,l} \rho_{max})}$ .

Taking the Fourier transform of this function can then define the FT-TBB modes,  $U_{p,l}$ , as

$$U_{p,l}(\mathbf{k}, \phi_k) = FT(\psi(\rho, \phi)_{p,l}) = \int \psi(\rho, \phi) e^{i\mathbf{k} \cdot \boldsymbol{\rho}} d\boldsymbol{\rho} \quad (1.14)$$

This can be rewritten using the jacobi-Anger relationship

$$e^{i\mathbf{k} \cdot \boldsymbol{\rho}} = e^{i|\mathbf{k}||\boldsymbol{\rho}|\cos(\theta-\phi)} = \sum_{n=-\infty}^{\infty} i^n J_n(k\rho) e^{in(\phi-\theta)} \quad (1.15)$$

where  $\theta$  and  $\phi$  are the in plane azimuthal angles of vectors  $\mathbf{k}$  and  $\boldsymbol{\rho}$  respectively.  $k$  and  $\rho$  are the modulus of the wavevectors  $\mathbf{k}$  and  $\boldsymbol{\rho}$  respectively. Application of identity 1.15 gives

$$U_{p,l}(k, \phi_k) = \int_0^{2\pi} d\phi \int_0^{\rho_{max}} (\psi(\rho, \phi)_{p,l}) \sum_{n=-\infty}^{\infty} i^n J_n(k\rho) e^{in(\phi-\theta)} \rho d\rho \quad (1.16)$$

Using the relation 1.13 the integral becomes

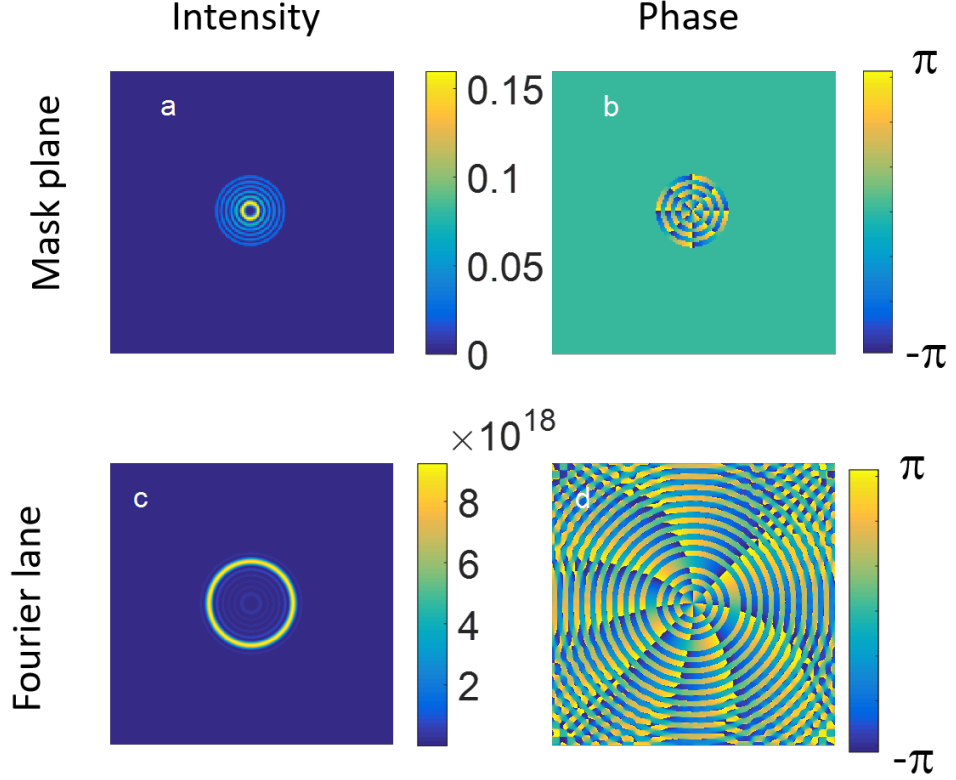


Figure 1.10: The amplitude (a,c) and phase (b,d) of a  $l = 4$   $p = 5$  Bessel mode for the Truncated Bessel mask function (a,b) and the Fourier transform of the mask function (c,d). The mask aperture boundary was set to the  $p + 1^{th}$  zero of the Bessel function.

$$U_{p,l}(k, \theta) = N_{pl} i^l e^{il\theta} \int_0^{\rho_{max}} (J_l(k\rho) J_l(k_{p,l}\rho)) \rho d\rho \quad (1.17)$$

the identity

$$\int_0^a (J_l(k_1\rho) J_l(k_2\rho)) \rho d\rho = \frac{a}{k_1^2 - k_2^2} [k_2 J_l(k_1 a) J_l'(k_2 a) - k_1 J_l(k_2 a) J_l'(k_1 a)] \quad (1.18)$$

can then be applied to calculate the FT-TBB modes as

$$U_{p,l}(k, \theta) = N_{pl} i^l e^{il\theta} \frac{\rho_{max}}{k^2 - k_{p,l}^2} [k_{p,l} J_l(ka) J'_l(k_{p,l}a) - k J_l(k_{p,l}a) J'_l(ka)] \quad (1.19)$$

Alternatively the Fourier transform can be evaluated numerically as shown in figure 1.10 for the example of  $U_{5,4}$ , these modes .

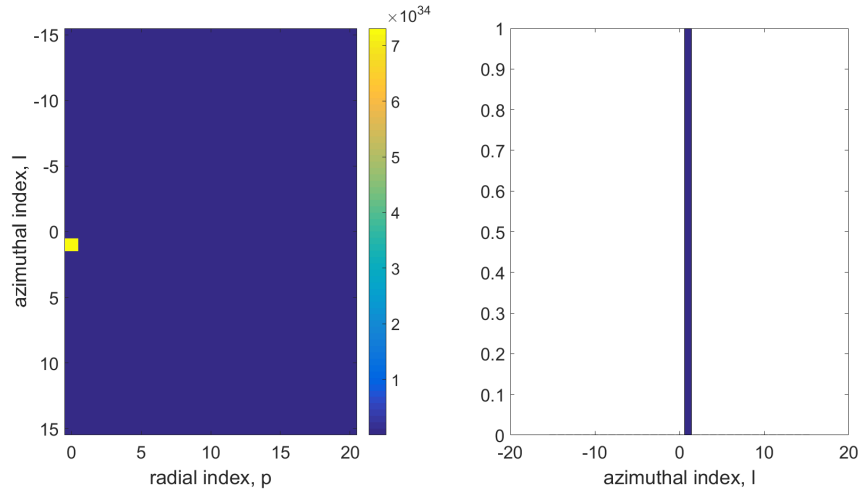


Figure 1.11: A decomposition of an  $l = 1$  vortex function into FT-TBB modes, using the edge of the aperture as a zero in the Bessel function. left: a full map of  $l$  and  $p$  values. right: the normalised intensities after summation over  $p$  as a function of  $l$ .

These TBB and FT-TBB modes offer alternative circularly symmetric basis sets with which to decompose fields instead of Laguerre-Gauss modes or Bessel functions. Due to the requirement of using an aperture in a physical experiment these basis sets are useful when describing diffraction experiments through an aperture in an electron microscope [17]. Figure 1.11 shows the decomposition of an  $l = 1$  integer vortex function into FT-TBB modes, the x axis corresponds to the radial index,  $p$  and the y axis is the azimuthal index,  $l$ , the intensity goes from blue to yellow showing the major component is the  $l = 1, p = 1$  FT-TBB mode (i.e. the mask radius is the first zero in the Bessel function), as expected. Alternatively the argument  $(k_{p,l}\rho_{max})$  could also be defined as the  $p + 1^{th}$  maximum or minimum in the Bessel function, this would give a second set of TBB and FT-TBB modes. Unless stated otherwise the condition of a Bessel function zero at the boundary at  $\rho_{max}$  will be used in this thesis.

## 1.10 Quantum waves

The Schrodinger equation, (equation 1.20), describes the link between the spatial and temporal variations in a quantum wavefunction,  $\psi$  and is a very useful mathematical description to predict quantum experiments.

$$\frac{-\hbar^2}{2m}(\nabla^2 + V)\Psi = -i\hbar\partial\Psi/\partial t \quad (1.20)$$

When considering the quantum entities as harmonic waves with wavefunctions dependent on a term  $e^{i\omega t}$  then the schrodinger equation can be expressed in a time independent form.

$$\left(-i\frac{\hbar^2}{2m}\nabla^2 + [V - \hbar\omega]\right)\Psi = 0 \quad (1.21)$$

These harmonic solutions have an identical mathematical description to classical waves, except that instead of  $|\Psi(\mathbf{r})|$  determining the amplitude of displacement, it now determines the probability of interacting with the quantum entity at position  $\mathbf{r}$ . By analogy with descriptions of classical waves, quantum phenomena can be predicted with wave-like solutions to the time independent Schrodinger equation. As will be shown this is a very useful method for describing the diffraction experiments with freely propagating electron waves conducted in this thesis. The square brackets of equation 1.10 contains the difference between the energy of the electron and the background potential  $V$ . This difference determines the wavevector of the electron compared to a free space electron with the same energy. Thus when encountering a potential well compared to a free electron (i.e.  $V < 0$ ) the square bracketed term ( $V - \hbar\omega$ ) becomes ( $-|V| - \hbar\omega$ ). The wavevector depends on the equation  $k = \sqrt{2mE}/\hbar$  where the total energy  $E = V - \hbar\omega$  is related to the square bracketed term. In a potential well the increased ( $-|V| - \hbar\omega$ ) term means the wavevector is increased compared to a free space electron which has escaped the well. Due to this effect the potential of a solid can act as a potential well and increase the wavevector of an electron travelling through the medium. In a similar manner to light travelling through the glass of a lens this means some materials can act as a phase object for electrons, slowing the electron down and compressing the wavelength. This effect will be used later on to produce phase masks out of Silicon nitride membranes.

### 1.10.1 Quantum phase vortices

When predicting experimental results involving quantum entities the wave model can be used to describe the transfer of energy from one point to another. In contrast to a classical wave, for the case of electrons, mass is also transferred. The wave model allows recorded intensities to be explained in terms of interferences. This means photons and electrons can effectively be cancelled out or excluded from regions of space depending upon the experimental conditions. The simplest example of this is the double slit experiment where the measured intensity on a screen has bright fringes and dark fringes, regardless of whether the incident quantum phenomena is laser light [12], single photons [18] or single electrons [19]. Within a wave description of quantum phenomena the relative distribution of phases determines where energy (or mass) are transported. So a complex wave amplitude tells you about the probability of where a quantum particle is and the complex phase tells you about how it is moving. In this framework optical experiments involving photons or electron can be viewed as a quantum mechanical measurement where a complex wavefunction propagates towards the measurement device (usually a CCD or similar sensor) and upon meeting the device the wavefunction collapses to produce a single measurement (i.e. a count on a CCD sensor) an image is then built upon over time of many individual wavefunction collapses. It is this mechanism through which the double slit interference fringes become visible. The electron based experiments described in this thesis rely on this idea of multiple counts of a set of electrons, building up a statistical picture of the complex wavefunction. However it must be noted that these measurements can only directly record the amplitude (where the particle was). It is only by using specialised experimental set ups (such as biprisms [20]) and applying prior knowledge that the phase can be extracted from these amplitude measurements. These were not available in the microscopes used in this project, however algorithms will be used to calculate approximations to the phase of the wave, these will be described in the appendix chapter A section A.2.

Vortex states have long been known for classical waves in nature, for example, tornadoes or whirlpools and are related to circulation around a point. In these cases the central node corresponds to zero mechanical flow, hence the calmness in the 'eye of the storm'. The twisted nature of physical wavefronts was first experimentally described by Nye and Berry [21] when the reflections of ultrasound from a rough surface was analysed, in

order to explain experimental data of radio waves reflected by the Antarctic ice sheets. It was not until 1992 when Allen et al applied a similar description to light and realised that vortex photons could carry orbital angular momentum [22]. The advent of laser technology allowed coherent light sources to produce photons suitable for interference experiments and optical vortices have since found applications in diverse fields including, optical particle trapping and manipulation[23], astronomy [24] and data transfer for communications [25].

Within the Copenhagen interpretation of quantum physics particles can be described by complex functions and as such the phenomena associated with other waves and the maths of phase vortices can be applied to electrons. This was achieved in the first explicit theoretical description of freely propagating electron vortices as allowed solutions to the schrodinger equation[26], carrying OAM. The development of nanoscale manufacturing has now made it possible to produce structures on the nanometer scale, which is close enough to the wavelength of electrons (of the order of picometers for 200keV) such that the structures can interact with electrons and alter the phase of the electron. This allowed the beginning of the field of experimental electron vortex research. Since its beginning around 2010 there has been a lot of fundamental progress in experimental production and theoretical understanding of electron vortices, which will be described in section 2.

## 1.11 Optical trapping of particles and atoms

Photon vortices can be used to manipulate the motion of transparent particles such as silica spheres [27] or small atoms [28]. As explained in 1970 by Ashkin [27], for transparent particles there are two main forces present during the interaction with a photon. Firstly there is the transfer of momentum in the direction of propagation, known as the radiation or scattering force, this pushes the particles along the direction the light is travelling in. Secondly the light undergoes refraction when travelling through the particle and the exchange of momentum, as shown in figure 1.12, leads to a restoring force acting towards regions of high intensity, following the local intensity gradient, due to this it is known as the gradient force.

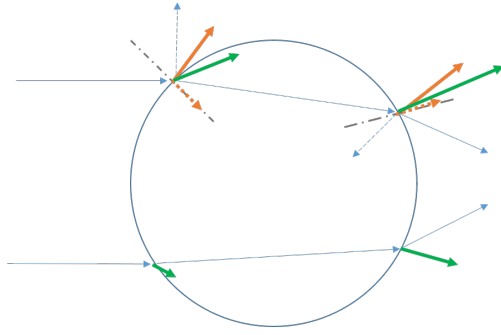


Figure 1.12: *A particle within a laser beam path will experience net forces (green arrows) corresponding to momentum transfer between incoming photons (leftmost blue arrows) and the refracted (solid blue arrows) and reflected (dashed arrows) photon paths. The resultant forces are shown in dashed orange arrows for the reflection and solid orange for the refraction. The combination of both orange arrows gives the net green arrows. If the lower intensity is weaker than the higher then the forces at the top will be larger (represented by larger solid green arrows), moving the particle upwards towards the higher intensity region.*

Figure 1.12 shows the forces responsible for the momentum transfer during the refraction of light inside a transparent dielectric sphere. There are two sets of forces acting on the sphere as the light enters and exits the sphere. The first forces shown by dashed orange arrows in figure 1.12 are from the reflection of light from the boundaries and point along the normal to the surface (shown in grey dash-dot lines). These dashed orange lines have a net force along the direction of propagation. The second set of forces are due to the transmission of the light, these are shown as bold orange arrows. For a uniform intensity the net radial force (component of green arrows in figure 1.12 transverse to propagation) will be zero. However, for an uneven intensity the half of the sphere in the more intensity region will experience a greater set of forces (shown by larger green arrows in the upper section in figure 1.12) and as such the net force will act towards regions of high intensity. It was shown in 1986 [29] that for a tightly focused beam this leads to a trapping force along the propagation axis as well as in the transverse plane. When the light distribution contains an azimuthal phase gradient the scattering force will gain an azimuthal component, allowing the vortex beam to impart a torque on the trapped particle, creating a trap known as an 'optical spanner', [30].

Similar trapping effects can be achieved when trapping atoms however the physical nature of the force is slightly different, this was initially discussed in terms of a simple standing wave by Letokhov [31] and the furthered to describe a trapping geometry by Ashkin [32]. There is a scattering force which can be viewed as due to absorption and subsequent spontaneous emission of photons. There is also a dipole force which is related to the average induced dipole moment of the atom. The potential energy of a dipole moment  $d$  in an electric field  $E$  is given by  $d \cdot E$  thus the force experienced by a dipole is given by the gradient in this potential and as such is related to the direction of  $\nabla \cdot E$ . However the dipole force can be aligned with this direction or in the opposite direction depending on whether the laser frequency is above or below resonance. As explained by Chu [33] this is related to the phase relation between the driving oscillations of the laser field and the response oscillations of the dipole moment of the atom. If the atom is viewed as an oscillating dipole acting as a harmonic oscillator, then when driven below the transition frequency (red detuned) then the atom will respond in phase with the Electric field, the interaction energy will be lower and the force will be towards positions of high  $E$  intensity. However alternatively, when the laser is above the atom transition the atom dipole will oscillate out of phase and the force will be away from areas of high  $E$  intensity.

## 1.12 Transmission electron microscopy (TEM)

The lenses in an electron microscope are coils of wire, inside a polepiece, which is shown in figure 1.13. This structure is designed to focus the magnetic field induced by the coil and produce an inhomogeneous magnetic field which deflects electron trajectories at larger radii to a greater extent, acting to focus the electron wave, just like a glass lens does for light. These magnetic lenses can be used to manipulate the complex waves of the beam electrons following the wave optics theory introduced in section 1.5. The ray diagram for a TEM imaging mode is shown in figure 1.14, here the condenser lens forms a demagnified image of the condenser aperture, to be used to illuminate the sample plane from which an image is formed. The diffraction plane of the condenser aperture shown in figure 1.14 allows the production of vortex electrons to be understood as similar to a double slit diffraction with light with the diffraction plane being the Fourier transform

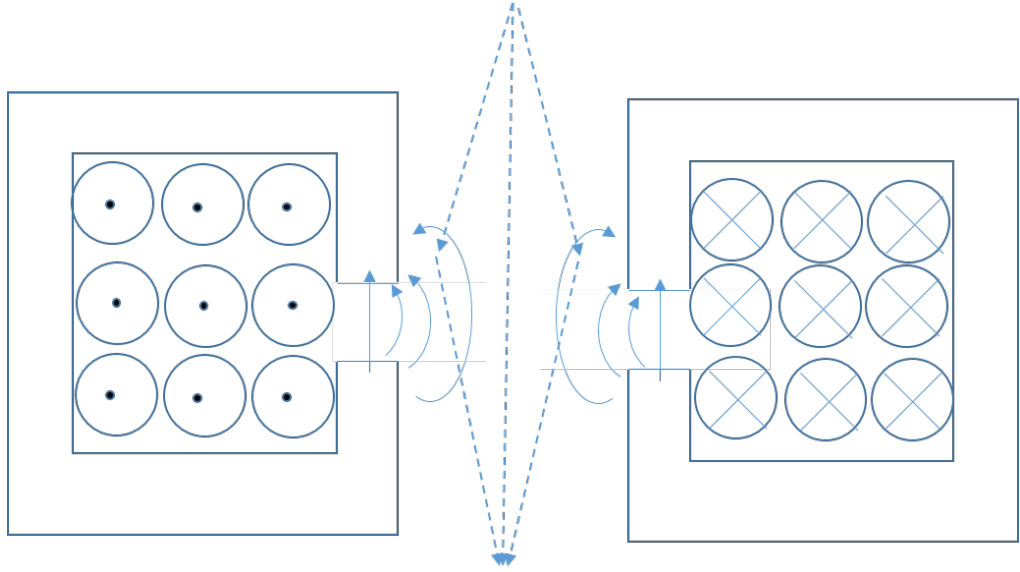


Figure 1.13: *A schematic diagram of an electron lens, the circles represent cross sections through a coil of wire with current going into (crosses) or out of (dots) the page. The square outline shows the cross section through a magnetic polepiece. The solid blue arrows are the magnetic flux lines which leak out of the gap in the polepiece causing an inhomogeneous magnetic field which acts as a focusing lens for the electrons. Dashed blue lines show the electron trajectories are focused back to a point.*

of the field in the condenser aperture. However the electrons take the place of photons and magnetic fields take the place of the electric potential of the glass lenses. During Lorentz imaging, electrons can be used to image the magnetic induction of a sample by using the fact that electrons are deflected by magnetic induction [34]. At a domain wall the direction of deflection changes and this can be made to produce a variation in recorded intensity. The two main methods are Fresnel and Foucault. In the Fresnel method the image is recorded with the objective lens turned off as usually this causes a large magnetic field which magnetises the sample to saturation (completely magnetised aligned with the field). By relying on lens fields away from the sample an image can be formed without saturating the sample. When defocusing this image the varying deflection cause electron intensity to either build up or decrease along domain walls depending on whether the deflections are moving towards or away from each other respectively. Alternatively in Foucault mode an aperture is placed in the

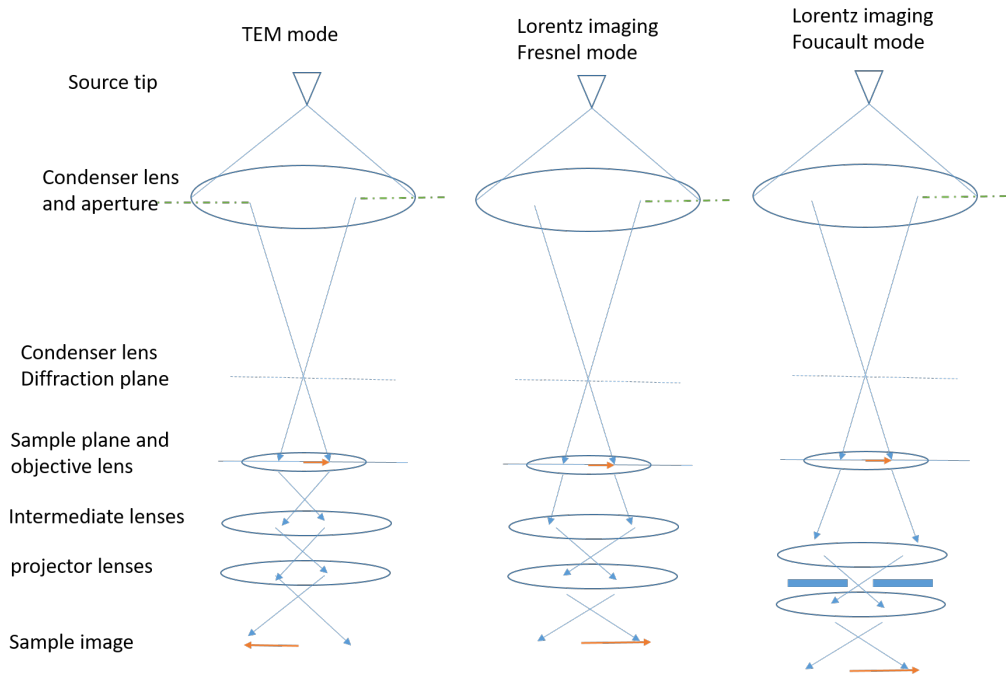


Figure 1.14: *A schematic ray diagram of the lenses in TEM mode imaging. A defocused source image is used to illuminate the sample from which a sample image is formed by the imaging system.*

Fourier plane of the sample plane to then form an image only from (or with a majority of) deflected electrons. In a similar method to dark field imaging where a ring detector records intensity at high angles, the Foucault method allows areas of high deflection (and so high magnetic field) to be recorded. Whilst these two modes of Lorentz imaging require either working with a defocus or a specialised aperture experimental set up to control the angles collected, vortex beams offer the potential to be developed into a magnetic imaging tool which can be used at focus and one long term goal would be to allow images to be collected more similarly to a standard TEM images.

## 1.13 Inelastic scattering and EELS

A simple example of a dispersive scattering experiment is when white light is refracted through a prism. Light waves of different wavelengths (different energies) take different paths through the prism and thus leave the prism travelling at different angles. In a similar manner the electrons leaving

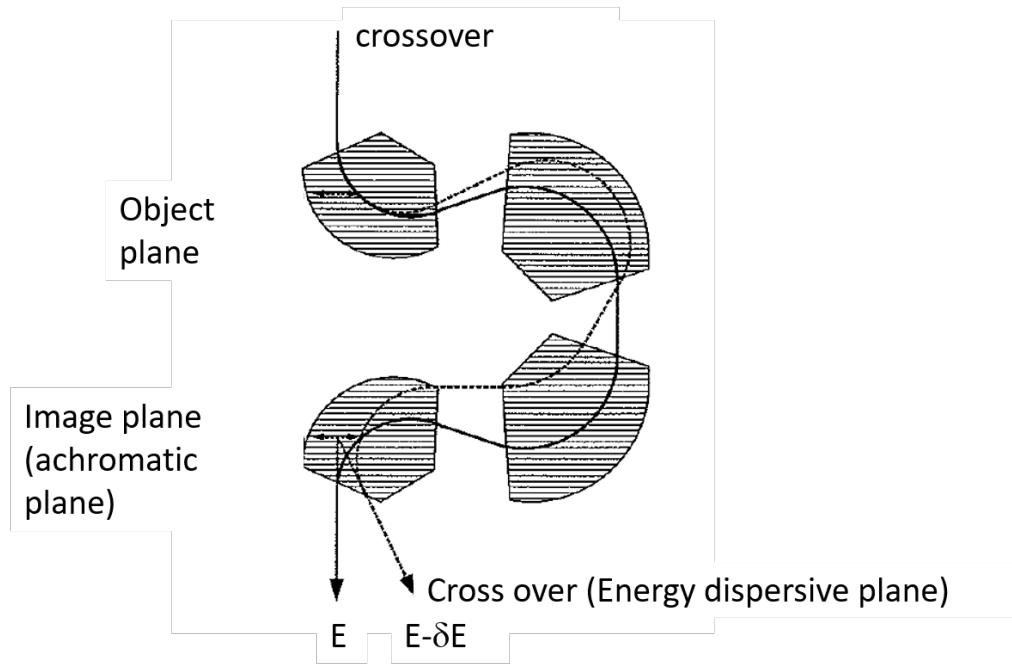


Figure 1.15: *Electron trajectories for different energies when travelling through filter lenses, which act like a prism on the electron beam. Different energies exit the filter at different angles. Image adapted from York Nanocentre 2200 handbook.*

a sample can be considered as a mix of different energies. The spread of energies is larger than before the sample due to some electrons losing energy through inelastic scattering processes during the interaction with the sample. Following the same overall principle as a prism's effect on light, correctly designed magnetic fields can cause electrons travelling at different velocities (with different energies) to follow different paths (an example of these filter lenses is shown in figure 1.15). This allows electrons to be separated depending on their energies, forming an energy loss spectrum, during electron energy loss spectroscopy (EELS). The current state of the art energy resolution can be achieved by using an energy filter before the sample (called a monochromator) and the superSTEM facility in the UK can achieve an energy resolution of 15 meV on their superSTEM3 TEM machine [6]. The JEOL 2200 FS microscope used in this project has an energy filter which can provide a zero loss peak (intensity representing electrons with 0 energy loss), with a full width half maximum of between 1-1.5eV. It is this width which determines the resolution as all peaks are convoluted with the spread of the zero loss peak. One of the ways in which the work in this thesis could be furthered would be the study of similar

structures as chapter 7 but on the superSTEM3 machine or a microscope with a resolution better than 1eV.

Angular broadening of the source (a finite spread in incoming angles) will cause spreading perpendicular to the dispersion axis. Alternatively a slit in the spectrum plane can be used to select only electrons within a certain energy loss window, these selected electrons can then be used to form an energy filtered TEM (EFTEM) image. EFTEM can be used to calculate the thickness of a material in terms of the electrons mean free path when travelling through the material following the log ratio equation [35]

$$t/L = \log_e(I_t/I_0) \quad (1.22)$$

where  $t$  is the thickness of the material,  $L$  is the mean free path of the electron due to inelastic scattering,  $I_0$  is the integrated intensity of the zero loss peak and  $I_t$  is the integrated intensity of the whole spectrum.

Alternatively in STEM mode an EELS spectrum can be acquired at multiple positions across the sample producing STEM EELS maps. This produces datacubes with a stack of images equivalent to energy filtering around successive energies. The technique can be used for elemental analysis (L,K transition edges) at higher energies but has also been shown to give information on surface plasmon modes. [36] This energy loss to surface plasmons can be modelled as a transfer of a virtual photon from the electron to the surface plasmon oscillation. Alternatively the energy loss can be viewed as the work done by the electron in travelling against the electric field of the plasmon which the electron induced in the sample. The energy transfer to plasmon modes will be discussed further after an initial description of surface plasmons.

## 1.14 Plasmonics

Maxwell's equations describe the creation and propagation of Electric and magnetic fields by charges and currents. The dielectric constant describes a materials response to changes in the electric field and as such can measure how much material resists the flow of electro magnetic waves in that medium. Maxwell's equations predict the requirement of boundary conditions between two different materials, for zero divergence of the magnetic

field the tangential magnetic field component must be continuous and for no net surface currents the tangential displacement field must be constant. This means that unlike free space when an electromagnetic wave encounters a boundary there will only be certain modes of oscillation which the electric field can undergo, one such mode of oscillation is the surface plasmon.

### 1.14.1 Surface plasmons

Surface plasmons are the energy quanta of surface charge density oscillations which are coupled to oscillations in the local electromagnetic field. These are solutions to Maxwell's equations which are allowed at the interface of a dielectric and a metal[37]. The analytical dispersion for surface plasmon waves at the interface between non-magnetic materials, 1 and 2, with corresponding dielectric constants  $\epsilon_1$  and  $\epsilon_2$  can be shown to follow equation 1.23. [38][37][39]

$$k_{sp} = \frac{\omega}{c} \left( \frac{\epsilon_1 \epsilon_2}{\epsilon_1 + \epsilon_2} \right)^{1/2} \quad (1.23)$$

where  $\omega$  is the frequency of plasma oscillation,  $k_{sp}$  is the wavevector and  $c$  is the speed of light in a vacuum. The dispersion for a  $Si_3N_4/Al$  interface has been calculated using equation 1.23 with values for  $\epsilon$  taken from Palik [40] and is shown in figure 1.16. This calculation uses the convention of choosing a real frequency and imaginary wavevector which results in the observed back bending as discussed by Archambault et al. [41]

The states on the plasmon dispersion curve shown in figure 1.16 occur for much larger wavevectors (smaller wavelengths) than for free space light. This causes a momentum mismatch between photons and surface plasmons. To overcome this various mechanisms have been devised to couple incident photons to plasmons. These include using a periodic variation in the surface to create a grating using a resonance effect with a periodicity which defines modes carrying a momentum matching the missing momentum. Alternatively a double interface can be used as shown in the upper inset of figure 1.16, material 3 is chosen such that the photon dispersion line intersects the surface plasmon dispersion at the interface between materials 1 and 2. This intersection means the light can be angled in such a way that the projection of the wavevector onto a first interface (2-3 interface in upper inset of figure 1.16) surface matches the modes defined by equation

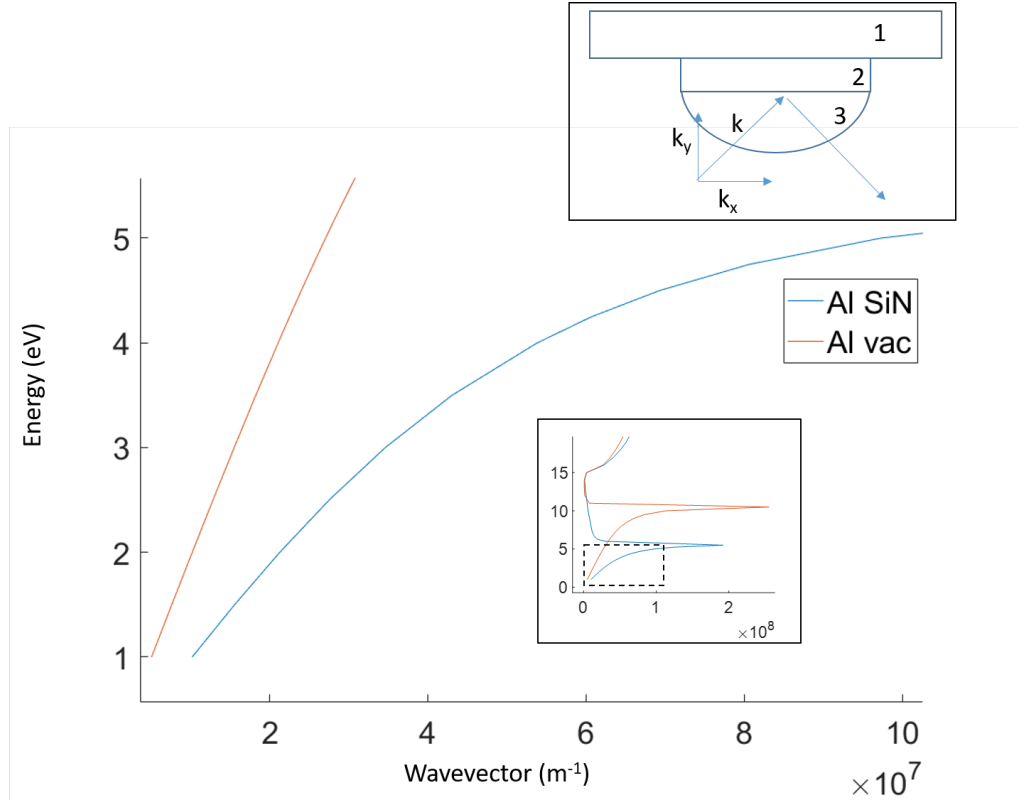


Figure 1.16: *The standard calculated dispersion for SiN/Al (blue) and Al/Vacuum interfaces (red). Upper inset: a multi interface can be used to couple light in medium 3 into surface plasmons between mediums 1 and*

1.23 for a second interface (1-2 interface in figure 1.16). This is known as the attenuated total reflection method [? ]. By matching the momentum, it is possible for these quasi particles to couple to light and allow the energy in a photon to be confined to regions much smaller than its free space wavelength. Due to this 'shrinking' of length scales associated with light, plasmonics is an active area of research with many varied applications in fields such as metamaterials, surface enhanced spectroscopies and plasmon enhanced light harvesting (see references within [42] and [43]) . In addition electrons can transfer energy to these charge density oscillations as they pass through thin metallic films as initially described by Ritchie [44]. It has been shown that chiral structures in thin films can support plasmons which carry orbital angular momentum [45]. The exchange of orbital angular momentum between vortex electrons and these plasmon modes has not yet been shown experimentally.

## 1.15 Energy transfer to plasmon modes

Electrons can be modelled as providing a pulse of electric field as they pass through a sample, this time varying E field can be decomposed into harmonic oscillations of different frequencies. As such a passing electron can be viewed as a white light source and can couple to all frequencies. The energy loss of an electron can be related to the work done in moving against the electric field which is induced in the sample, following the integral

$$\Delta E = e \int dt \mathbf{v} \cdot \mathbf{E}_{ind}(\mathbf{r}_e(t), t) \quad (1.24)$$

where  $e$  is the charge on an electron,  $\mathbf{v}$  is the velocity of the electron and  $\mathbf{E}_{ind}$  is the induced electric field in the sample due to the travelling electron. The integral with respect to time integrates along the parameterised electron trajectory  $\mathbf{r}_e(t)$  and the total energy lost includes energy at all frequencies. This can be rewritten as an integral over frequency

$$\Delta E = \int d\omega \hbar\omega \Gamma_{EELS}(\omega) \quad (1.25)$$

where

$$\Gamma_{EELS}(\omega) = \frac{e}{\pi\hbar\omega} \int dt \text{Re}[\exp^{-i\omega t} \mathbf{v} \cdot \mathbf{E}_{ind}(\mathbf{r}_e(t), t)] \quad (1.26)$$

is the probability of energy loss at a particular frequency  $\omega$ . The EELS problem now only requires solving for the induced field in the sample. This is related to the boundaries of the sample as it is these which distinguish the finite structure from a continuous homogeneous medium. The fields inside the structure are completely determined by the value of the surface charges at the boundaries. Continuity at the boundary of transverse E field means that these induced boundary charges need to follow an eigenvalue equation [46] [47]

$$2\pi\lambda_i\sigma_i(s) = \oint ds' F(s, s')\sigma_i(s') \quad (1.27)$$

here  $\sigma_i(s)$  is a surface charge eigenfunction,  $F(s, s')$  is the normal derivative of the free space greens function. Greens functions summarise effects from one position to another. In this case it is the electric field at test position  $\mathbf{s}'$  caused by a surface charge at source position  $\mathbf{s}$ . Equation 1.27 thus states that the electric fields caused by all other points,  $s'$ , of the eigenmode charge

distribution add up to create a scalar amount of the eigenmode charge distribution at  $s$ . In this way eigenmodes are the charge distributions which map back onto themselves and can be thought of as 'self re-enforcing'.

It has been shown [46] that the eigenvalue,  $\lambda_i$ , only relies on the geometry of the boundary. The particular frequency at which solutions are found is then dependent on the material dielectric response described by  $\epsilon_i(\omega)$  where  $i = 1, 2$  corresponds to materials either side of the boundary. This link is expressed through the equation

$$\lambda_i = \frac{\epsilon_1(\omega) + \epsilon_2(\omega)}{\epsilon_1(\omega) - \epsilon_2(\omega)} \quad (1.28)$$

The total induced charge can be written as a summation of supported eigenmodes at different frequencies .

The probability of energy loss is proportional to the local density of plasmon mode states available, this is related to both the amplitude of the eigenmode fields and the dielectric response of the material at the eigenfrequencies. Thus EELS can be seen to measure the local density of states (LDOS), reflecting both the combined amplitude of the supported modes and the polarisability of the material at the corresponding mode frequencies. Approximating a thin film as a homogeneous dielectric material the EELS maps can be seen to reflect the underlying geometry of the LDOS. If there is only one dominant mode in a particular energy range then the EELS map will show the distribution of electric field for that mode. When there are multiple modes within the energy range of the EELS map then the intensity will be a weighted combination of each mode distribution. As such care needs to be given when evaluating EELS maps and deciding on whether the intensity is from a single or multiple modes of Electric field oscillation. It is here where numerical simulation of single modes can vastly aids the interpretation of EELS intensity maps, as has previously been shown, for example, with nanotriangles [48].

## 1.16 Thesis contribution and outline

As will be shown in chapter 2, the majority of the literature concerning electron vortex research has focused on integer vortices. This thesis focuses on using electron phase shaping methods to produce a new vortex beam formed

from a superposition of integer vortex states. This beam forms a C-shape when focused and carries fractional orbital angular momentum. This beam has not been described before in the photon or electron vortex literature, as such this thesis represents the first time the beam has been analysed and experimentally produced for electrons inside a TEM. Chapter 2 will also show that OAM transfer has been shown experimentally for interactions between incident photons and plasmons in chiral structures. Many of these experiments use circularly polarised light and the conversion of spin angular momentum to orbital angular momentum during the photon-plasmon interaction. In contrast to photon optics, the transfer of OAM from freely propagating probe electron vortices with plasmon modes has theoretically been described [49] however there is a lack of experimental evidence of such an interaction with only one arXiv paper . In their paper, Harvey et al investigate and describe interactions with 3D plasmon systems [50] where interactions between separated spheres in a chiral arrangement is responsible for determining the OAM of the localised plasmon mode. A weak difference in the EELS spectra recorded from different vortex beams occurs around 3.5eV which the authors attribute to OAM dependent coupling to a chiral plasmon mode delocalised over the arrangement of particles. Similarly to the 3D arrangement of particles the interaction of electrons with flat 2D chiral plasmon modes and possible OAM transfer has been looked at theoretically but only in one paper by Ugarte and Ducati [51] and experimental results have not been published. This thesis investigated the interaction of electron vortices with flat chiral structures which in contrast to reference [51] have broken rotational symmetry. In chapter 6, the plasmon modes in flat chiral structures are simulated. The addition of chirality to a nanodisk will be shown to produce chirality in the plasmon eigenmodes and induced electric fields, giving the plasmon modes OAM . Descriptions of a similar effect have only been discussed previously for slits in continuous metal films and not for isolated spirals . Finally, chapter 7 investigates the interaction of C-shaped beams as well as integer vortices with 2D plasmon modes. Conclusions and possible future work are then discussed. Finally, an appendix is included to give details of analysis of energy loss spectra as well as the iterative algorithm used in this thesis. This thesis represents the first experimental investigation of the interactions between travelling electrons with OAM and 2D plasmon modes containing OAM. The theory for these interactions has also not yet been calculated, but is not included in this thesis, and is left open as an area for future research.

# Chapter 2

## Literature review

### 2.1 Literature review: experimental

Since the first theory paper explicitly describing electron vortex wavepacket solutions was published in 2007 [26], attempting to experimentally control the phase of electrons, mostly to form vortex states, has been an active area of research. The first part of this review chapter will describe the main methods and experiments which have been used to produce phase controlled electrons in a TEM. These include; amplitude contrast masks, phase contrast masks, direct phase masks, and the application of magnetic fields. The second part of this review section describes interactions with samples both experimental and simulated, including TEM based experiments interacting with plasmons and previous work done involving transfer of OAM between photons and plasmons. Finally previous papers showing states with phase vortices containing an opening are described.

#### 2.1.1 Direct phase masks

The first vortex type electron beam reported was actually with an approximation to a direct phase mask where graphite sheets had randomly stacked to produce a height which increased stepwise around a point [52] figure 2.1 a. This was shown to lead to a fork dislocation when the transmitted beam was interfered with a reference plane wave and proved electron beams with

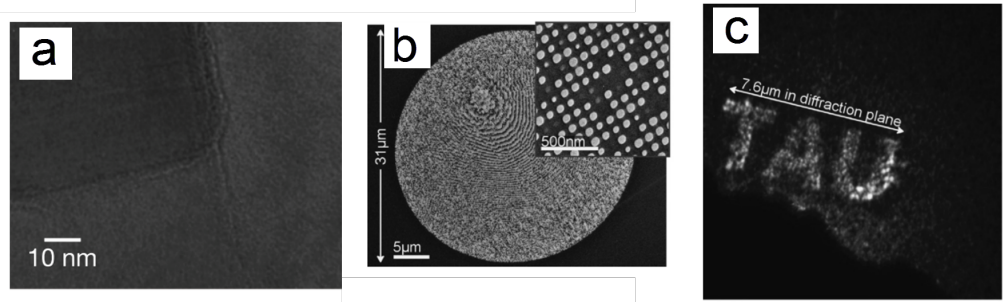


Figure 2.1: *a) Stacked graphite sheets used as a phase mask in [52]. b) The pixellated Silicon Nitride phase mask from [53] c) the Fourier plane intensity distribution produced by the mask in b)*

a central phase singularity could be experimentally produced. Recently progress in focused ion beam milling technology has allowed more precise control over the thickness of substrates, allowing direct modification to the phase of the electron wavefront. Shiloh et al[53] have shown a linear azimuthal phase ramp creating vortex beams, and have used very fine (60nm diameter) pixels of varying thickness (figure 2.1 b) to successfully imprint a Fourier transform of arbitrary patterns (figure 2.1 c) onto a phase mask. Whilst this does highlight the ability to manipulate the spatial phase dependence directly, the vortex beams produced in this paper are still not ideally symmetric, highlighting the difficulty of achieving an exact  $2\pi$  phase change around the centre. There will always be a physical limitation that real surface gradients cannot be infinitely large, as such there will be an inner cut off radius below which the gradient will be above the maximum resolution of the production method.

A recent improvement in producing a spiral phase plate for electrons is the used of focused electron beam induced deposition to precisely control the thickness of a deposited  $SiO_2$  layer from a tetraethyl orthosilicate (TEOS) precursor [54]. After this spiral had been built up a platinum block was deposited in the center of the spiral to block the non diffracted beam caused by inability of the physical production process to produce the ultimately infinite gradients required at the central region. The mask was finally carbon coated to limit the effects of sample charging under the electron beam illumination. This was placed in the sample plane and the far field diffraction pattern was imaged in diffraction mode. It appears that a vortex was successfully generated with an estimated 60%  $l = 1$  in its

OAM mode decomposition. However even with this advanced production technique the phase step was still only 0.8 of the full  $2\pi$  required for an  $l = 1$  beam. The drawbacks are that this type of phase mask only works at a particular energy and being a physical mask it can degrade with use.

### 2.1.2 Amplitude masks

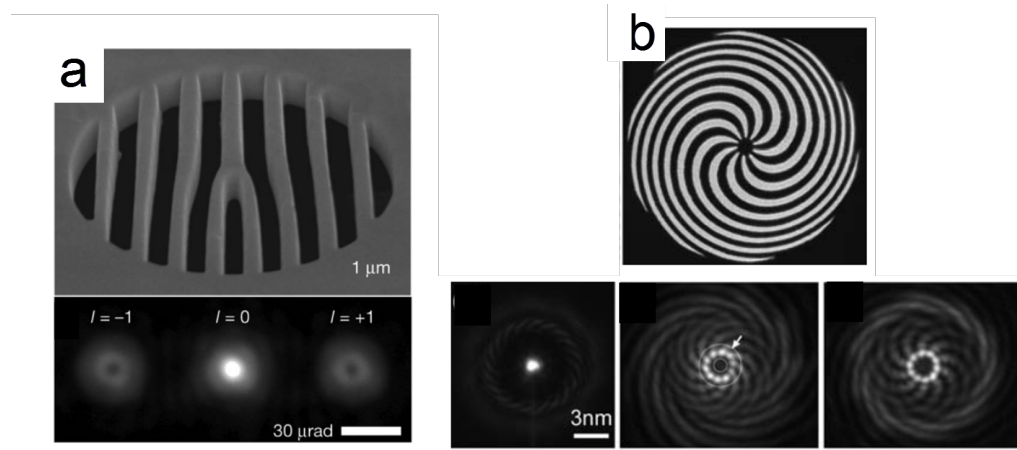


Figure 2.2: *a) the mask and fourier plane intensity from [55]. b) The mask and vortex beams produced in reference [56].*

The simplicity of only requiring binary control on the structure of amplitude diffraction masks has meant that these are the type which have been used for many electron vortex experiments. The first was in 2010 by Verbeeck et al. [57] (figure 2.2 a, where the experiment used a Pt foil roughly 100nm thick and focused ion beam (FIB) milling to create 2.5 $\mu\text{m}$  and 5 $\mu\text{m}$  diameter binarised hologram gratings. These successfully demonstrated the expected far field diffraction pattern with a central zeroth order beam and two side beams with a ring shaped intensity distribution (figure 2.2 a).

The mask was then used as an analyser whilst placed after an Fe sample. The beam from the sample underwent diffraction into different vortex orders and EELS spectra were gained for the +1 and -1 orders individually by using the energy filter entrance aperture. The difference between these two spectra was show an EMCD signal resembling the X-ray Magnetic Circular Dichroism (XMCD) from the  $L_{2,3}$  spin polarised

transition in the Fe crystal. This is a key result which highlighted the possible magnetic interactions vortex beams offer, however the results are still not fully understood and there has not been any further reproduction of these types of signal. In 2011 Verbeeck placed the same grating mask in the condenser aperture of a TEM and produced smaller vortex beams with a diameter of  $1.2\text{\AA}$  at focus, in the sample plane [58]. This is shown to be of a similar scale in intensity and phase distribution to atomic p orbital and highlights the possibility of probing vortex beam interactions with atomic resolution.

Hologram masks created from the interference of a spherical wave have also been successfully produced (figure 2.2 b). For these masks the intensity measured at a plane is a sum of many different orders each focused by a different amount. The patterns produced are thus not ideal rings but as Saitoh et al. show they appear as interference fringes around a circle with intensity spiralling outward [59] (figure 2.2 b). The aim of separating orders along the z axis is to be able to switch which OAM value has the highest peak intensity simply by changing the z defocus. For interactions depending on intensity, Z axis separation also prevents other orders from interacting with large samples during TEM by ensuring they are out of focus at the sample plane.

Verbeeck experimentally showed that these vortex probes from spiral masks can successfully be used in a STEM set up to give  $1.413\text{\AA}$  resolution [60]. This shows that even with current technology, electron vortex probes have the potential for real world atomic scale applications.

Amplitude masks have allowed very large values of OAM to be experimentally shown, this is one of the most important properties of electron vortex beams as they are freely propagating and unlike atomic bound states can have an arbitrarily large OAM. The spiral mask in [59] showed OAM up to  $90\hbar$  per electron. McMorran et al have managed to show some intensity in a 4th order  $100\hbar$  OAM from a fork dislocation mask made from Gold supported by a Silicon Nitride membrane, however the relative intensity was very low and the images do not show full rings (figure 2.3 a).[61]

In addition to the potential applications in STEM imaging and probing chiral transitions, amplitude masks have been used to measure induced rotations of electron vortex states. Larmor rotations due to Zeeman

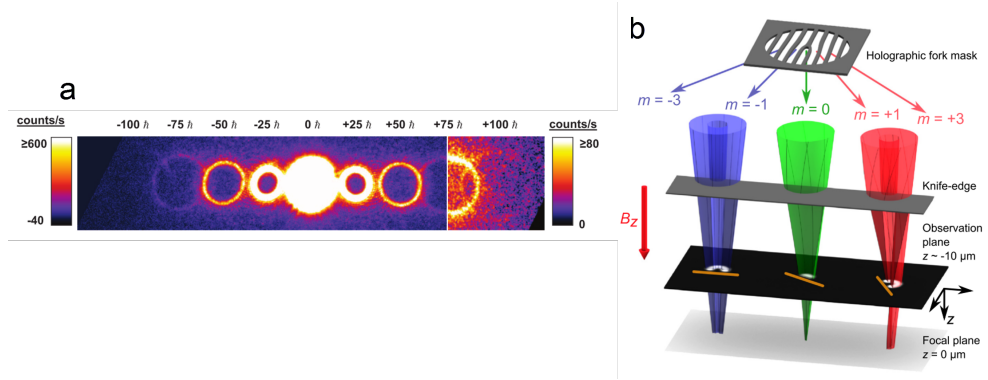


Figure 2.3: *a) The large OAM electron vortex beams produced in [61]. b) the knife edge diffraction experimental set up used in [62]*

coupling of OAM to a magnetic field have been experimentally demonstrated by Guzzinati et al. and have been predicted [63] and visualised separately to the rotations due to the Gouy phase [64]. An amplitude contrast hologram mask was used to create a superposition of topological charges and the intensity pattern of the superposition experimentally shows distinct Gouy and Larmor rotations. The Larmor rotations are objective lens field dependent rotations explained by classical cyclotron orbits but can also be explained by quantum Zeeman phase difference between opposite  $l$  values (as mentioned in [65]). Larmor rotations were produced by altering the objective imaging lens strength, a stronger B field in the lens created a rotation of the entire final image. As a separate effect Gouy rotations of superpositions are due to the  $l$  dependence of the Gouy phase. This was achieved by changing what plane was being imaged by the imaging lens by varying the condenser lens strength. Building upon these results the same group went on to measure the rotational frequency of different topological charges when the radius of the electron ring is matched to the Landau level (natural states encircling a magnetic flux) [62]. This showed varying rotational frequencies depending upon the topological charge (figure 2.3 b), theoretically this is due to the link between velocity and phase gradients in addition to the magnetic moment of the vortex aligning with or against the magnetic field [63]. When the beam waist is equivalent to the magnetic length  $\sqrt{\hbar/m_e\Omega}$  (where the Larmor frequency  $\Omega = |eB_z/2m|$ ), this leads to only 3 allowed rotational frequencies, zero, Larmor or cyclotron (double Larmor) frequencies. This experiment highlights the interactions with magnetic fields which only electron vortices can show, thus separat-

ing them from photon vortices, and increasing our understanding of vortex beam propagation in a TEM column.

### 2.1.3 Phase contrast masks

Phase contrast masks are produced by using the binarised holograms described in chapter 3, section 3.2, to produce two different thickness values determined by the binary hologram. These type of masks act as phase objects and should produce higher transmitted intensities, due to allowing the entire electron beam through all of the mask aperture. In addition, if the phase contrast is  $\pi$  radians, there will be reduced zeroth order intensity due to destructive interference between intensity from thick and thin parts of the mask. A key paper showing the use of phase contrast holography is by Grillo et al [66], who successfully produce a blazed diffraction grating based on an  $l=1$  hologram. The blazed grating has a saw-tooth thickness profile which adds an additional phase change across the mask, this diverts intensity into a non zero order side beam, dependent on the saw-tooth angle. The group successfully diverted intensity into the  $m=1$  side beam. This technique promises to be useful in increasing the signal to noise ratio of experiments relying on single values of topological charge. Recently in a paper by Hossein et al the same group managed to use electron beam lithography to produce very fine structures on phase contrast masks produced by the high resolution EBL resist Hydroxysilsesquioxane (HSQ). With these masks an OAM of approximately  $1000\hbar$  was obtained [67]. This is a huge step towards amplifying interactions between incident vortex electron magnetic moments and magnetic samples, which is required if electron vortices are to become routine scientific tools.

Phase contrast holography has also been used to produce Bessel beams using a mask with thickness variations to show phase contrast [68]. These masks were FIB milled with very narrow 100nm periodicity on a  $10\mu\text{m}$  diameter area. The beams produced showed minimal variation in transverse distribution over 0.4m of effective propagation distance, and show the production of 'non diffracting' electron beams showing the wave physics known for optical vortices [69]. This increased stability upon propagation could allow electron vortex probes to be less susceptible to changes in height and also allow interaction with thicker samples.

### 2.1.4 Magnetic field vortex creation

In addition to the interaction with the inner electrostatic potential, magnetic fields can also alter an electrons phase and have been shown to produce electron vortices. One approach utilises the aberration correctors present in a TEM to create an  $\exp(il\phi)$  phase dependence but selects a ring shaped region from this using an annular aperture and then views the diffraction pattern of this [70] (figure 2.4 a). This is an experimental approximation to the idealised infinitely narrow delta ring of an exact Bessel function Fourier transform. The ring aperture blocked sections where the radial dependence of the aberrations distorted the phase from an azimuthal gradient. Whilst this is in theory a promising technique as it can be applied to all correctors currently installed in TEM machines the resulting vortex state is not very pure. The paper claims the rings of a Bessel function are visible however the intensity is broken up into spots and the central vortex ring is not well defined showing the electron is not in a pure OAM  $l=1$  state. Indeed the paper calculates a decomposition of the Fourier series used to approximate an  $l=1$  state and shows contributions from  $l$  values between -5 and 5, caused by a non-linear azimuthal phase gradient. Although it is shown that 65% of the transmitted beam intensity is in the  $l=1$  state compared to 17% for an amplitude hologram, in the current state the probes formed by this method would not be as useful for atomic resolution applications due to distortions. A second technique, also based upon magnetic fields, uses a very thin magnetic needle placed in the path of the electron beam [71] (figure 2.4 b). The field surrounding the needle is a physical approximation to a magnetic monopole with flux lines spreading radially outward from the tip. A magnetic monopole flux causes an aharanov bohm phase shift creating the  $\exp(il\phi)$  phase dependence in the beam. The approximate monopole field cannot create an exact  $2\pi$  phase change due to flux lines re-entering the needle within the aperture. The needle also blocks some of the beam and so the beam produced appears as a beam with fractional topological charge, having a radial nodal line in the intensity distribution (figure 2.4 b). This method offers much higher beam intensity than the popular amplitude masks and the possibility of the vortex to heal itself as it propagates is mentioned, however this relies on working out of focus and would most likely not be suited to atomic sized probes.

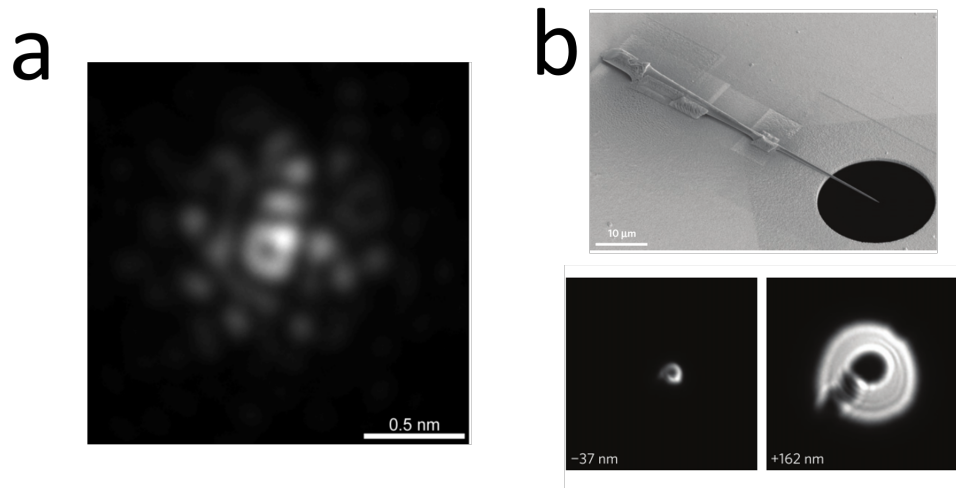


Figure 2.4: *The electron vortex intensity formed by aberration correctors in [70]. b) the magnetic needle and vortex intensity presented in [71].*

### 2.1.5 Measuring OAM

To gain more information about a specimen (e.g. magnetic information or available electron transitions) a method for measuring the OAM of the electron will be required. To achieve this, experiments involving two amplitude masks have been conducted where the second mask is used as an analyser of the beams produced by the first. Saitoh has used the same spiral mask mentioned above in an experiment to produce electron vortex beams which were then analysed by a forked mask [72] (figure 2.5). The diffraction pattern from the final forked mask showed a ring of dots at each order, the zeroth central ring having a number of dots equal to the input pattern. The +1 and -1 side beams had either one more or one less dot respectively, showing that diffraction from the second mask transfers OAM between each side of the mask (each side gains OAM in opposite directions). It is suggested that moving a pinhole between diffraction orders will allow an analyser to be made where intensity is only found once the pinhole is over the order corresponding to total loss of OAM from the incoming beam (i.e the -1 order for an  $l=1$  incoming beam).

Guzzinatti et al have also investigated some possible OAM measurement methods [73], these include methods which utilise a secondary structured mask (a diffraction amplitude mask, triangular aperture and a

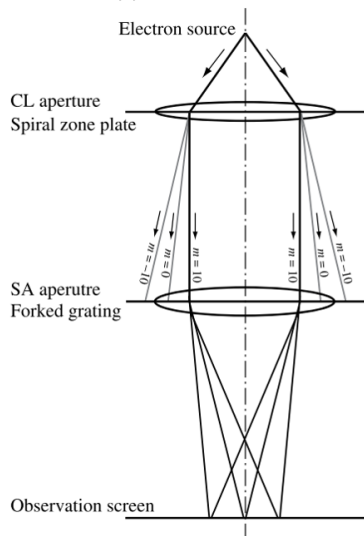


Figure 2.5: *The experimental set up used to measure OAM of electron vortices produced with a spiral mask from [72].*

knife edge) for the electron vortex to diffract from. The intensity distribution after the mask is then characteristic of the topological charge. This work has recently been furthered by Clark et al. [74] where the diffraction pattern from a multihole aperture was analysed with a computer algorithm to give an OAM spectrum of the vortex state.

This initial analysis method is limited by aliasing produced by the necessity for a finite number of holes and frequency information limitations due to sampling. A secondary method, also investigated by Thirunavukkarasu et al [17] , involves an astigmatic deformation of the vortex beam which creates intensity fringes, the number of which shows the topological charge of the undeformed beam. This has the benefit of being able to be applied by the corrector lenses currently installed in many TEM machines and the effect could be removed once the OAM measurement has been done.

## 2.1.6 Sample interactions

Propagation of vortices after interaction with a non-circular aperture was investigated theoretically and experimentally by Clark et al. [75]. They showed that vortex antivortex pairs can be created by diffraction from edges and the topological charge of the incident beam can be found by counting the number of lobes in the diffracted intensity . Higher order off

axis vortices were found to split up upon propagation however the central vortex splitting only occurs when the topological charge is greater than half of the rotational symmetry order of the aperture . It has been shown that rotations of particles is possible with vortex electrons [76] [77]. Verbeeck et al showed elastic and inelastic scattering causes angular momentum to be transferred to Au particles on  $Si_3N_4$  membrane approximately  $3nm$  diameter particle from  $3nm$  diameter vortex. The direction of rotation depends upon sign of topological charge. Elastic transfer of OAM is caused by the radiation force arising from the local phase gradient in the beam .

Juchtmans et al have shown that by analysing the OAM content of the first order Laue zone, produced by an incident plane wave electron beam after diffraction from a chiral crystal , it would be possible to determine the crystal chirality[78]. This was a theoretical study utilising multislice simulations and is yet to be shown experimentally. Further to this Juchtmans et al. considered instead an incident vortex electron being scattered by a chiral array of scatterers as would be found in a chiral crystal [79]. Through analytic derivation, multislice simulations and experimental diffraction it was shown that the symmetry of higher order diffraction zones reveal the crystal chirality. This provides another application for electron vortices as a scientific tool.

Juchtsman et al have shown that due to the complex phase term the Fourier transform of vortex phase does not have to be centrosymmetric as it would for a solely real function [80]. The diffraction pattern from oppositely charge vortices follows an inversion of intensity from  $-k$  to  $k$  which in 2 dimensions means that the amplitudes for  $+/- 1$  are rotated by  $\pi$  compared to one another. This rotational symmetry of the first order diffraction intensities means that higher order diffraction spots would need to be used to see variations due to interactions which vary with the chirality of the incident vortex beam.

When assessing the feasibility of measuring chiral dichroism from the interaction with the  $L_{2,3}$  of a ferromagnetic atom, it was predicted that the difference signal for vortices of opposite chirality is does not survive past  $1nm$  distance from the atom [81]. As such the authors suggest that chiral dichorism will not be observable with current microscope technology unless the particles are below  $2nm$  diameter. This is supported by the lack of difference in experimental EELS recorded for a thin film Fe sample.

### 2.1.7 Other phase shaping

By placing a magnetised needle across an aperture the phase of an incoming electron beam has been shaped such that there is a  $\pi$  phase change between opposite halves of the aperture[82]. When interacting with 200nm long metallic rods the EELS recorded is shown to depend upon whether the probing electron is unstructured or structured. This is explained by an increased probability of exciting plasmon modes when the phase of the incoming electron matches the phase distribution of the plasmon mode. This is experimentally verified by altering the incoming electron probe and also the orientation of the plasmonic structure relative to the incident electron beam.

Two biprisms were used to produce an intensity grid in an electron microscope image [83]. Through comparison with theoretical amplitudes the presence of a grid of phase vortices was presumed. The observed patterns showed similar patterns to different phase offsets between the two outputs of the biprisms however the spatial variation of this phase was not explained as the paper only wanted to show the experimental results. If correct these arrays of vortices could be used to analyse larger samples without needing to align a single vortex beam exactly, with the array increasing the overlap with structures and potentially increasing the probability of any chirality dependent interaction.

### 2.1.8 OAM exchange with a sample

Despite being a fascinating fundamental physical phenomenon in its own right, one major goal of investigating vortex beams is to add extra utility to the TEM allowing more information to be gained from samples. This is mostly focused on magnetic contrast in images reliant on interactions of spin in the sample with the magnetic moment of the electron vortex states. To achieve this an understanding of the interaction of vortex beams with atoms and crystals is required and has been studied by various groups.

The first experimental results of vortex-sample interactions came from a key paper by verbeeck et al. [57] This paper was also the first to experimentally produce vortex beams via a holographic amplitude contrast

mask. The mask was placed after a magnetic Fe sample, the electron energy loss spectroscopy (EELS) spectra were then recorded for the  $l=+1$  and  $l=-1$  separately and a difference spectra was gained showing an energy loss magnetic chiral dichroic (EMCD) signal. This matched the  $L_{2,3}$  dichroic signal seen for Fe between oppositely circularly polarised photons in X-ray magnetic circular dichroism (XMCD) however the explanation for these results is still not clear. The basis of such a dichroic signal is that each electron vortex is associated with a circulation of charge and so a corresponding magnetic field and this can be aligned or against the local spins in the sample, thus causing differing interaction strengths and different energy loss probabilities.

In an attempt to gain a better understanding of Verbeeck's dichroic signal and sample interactions in general, Lloyd et al. derived a transition matrix for the interaction of a vortex Bessel beam with a hydrogenic atom [84]. This was conducted within the dipole approximation, such that the distance from the electron vortex beam to the atom is considered as much larger than the atomic electron orbital and thus the vortex electron effectively sees the electron and nucleus as a dipole. Schattsneider et al. commented on this paper in [85] questioning the use of an approximation that the distance between the internal electron and the atomic centre is much smaller than the distance between the vortex electron and the atomic centre (dipole approximation). They stated that the final state need not be of integer topological charge or an eigenstate of OAM and so OAM exchange does not always occur with quantised transfer of  $\hbar$  OAM. This is cleared up by a reply from Lloyd et al. [86] explaining the dipole approximation is a first order expansion of the electron-atom polarisation field and that the assumption will be valid even when the distance from the nucleus approaches that of the atomic electron due to the first order term still being the largest term. The aim of the first paper was not to state that all transfer is quantised, only to show theoretically that quantised OAM transfer *can* occur between vortex beam and atomic electron.

The initial paper by Lloyd et al, [84], showed there are 3 types of transition possible which transfer quantised amounts of OAM ; from the electron vortex or atomic centre to the atomic electron, the reverse process, from the atomic electron to the vortex beam or atomic centre and finally one which involves the transfer from the vortex beam to the internal atomic electron state. These are dipole transitions which are not possible

for optical vortices interacting with the same atom. These interactions offer a possible explanation for the dichroic signal found by Verbeeck et al. Which could be due to different density of final states for different topological charge, in magnetic materials.

A paper aimed at explaining chiral specific effects by Yuan et al., [87] describes the expansion of a Bessel vortex beam in off axis co-ordinates, effectively how off an axis atom 'sees' the vortex beam. This is actually as a superposition of different topological charges. Using this type of expansion a new transition matrix is gained with an operator including a term dependent on the integral of  $1/Q^2$  where  $Q$  is the scattering wavevector. This operator is shown to lead to selection rules agreeing with the previous findings that OAM can be transferred in quantised amounts of  $\hbar$ . The expansion into off axis components shows that variations in the amount of topological charge  $l$  do not always mean interactions resulting in an exchange of  $l$  OAM, as these interactions most likely occurred off axis. Forbidden transition probabilities actually peak off axis and so could contribute more than expected from a purely on axis consideration in real samples. The effect of these off axis forbidden transitions should be minimised by well focused probes, but will still need to be considered if vortex beams are to be used experimentally.

In addition to OAM transfer to atomic nuclei or individual electrons, the transfer of OAM from vortex electrons to chiral plasmon oscillations has been theoretically studied by Asenjo-Garcia and Garcia de Abajo [49]. This paper used a Greens tensor analysis for a chiral arrangement of 4 metallic nanospheres,  $30nm$  diameter separated by  $5nm$  gaps. They assume the spheres are small enough to apply a scalar electric polarisability but large enough to model with a local classical theory. Their calculations predict the possibility of a 10% difference in intensity between opposite chirality of vortex beam, when recording EELS over the chiral arrangement of particles. The chiral interaction is due to the electron vortex being a chiral entity and thus the interaction with substrates of two different chiralities represents two distinct physical situations. Each vortex electron can be thought of as acting like a current loop with its own magnetic moment, this can interact with the magnetic properties in the sample, in this case the circulating plasmon current.

### 2.1.9 Modelling

Due to the difficulty of producing pure high intensity vortex states computer simulations are a valuable tool for gaining an understanding of how electron vortex beams will behave when interacted with a sample. Multislice simulations involve condensing atomic potentials into slices (projections a set distance along propagation), the electron wavefunction then interacts with this 2d potential slice and then undergoes free space Fresnel propagation until it meets the next slice. Multislice simulations have been used to simulate the effect of propagating vortex electron Bessel beams through an Fe BCC crystal [88]. Modelling magnetic interactions is still computationally difficult and so these simulations only investigate the effect of the electrostatic potential in the sample.

The phase at the exit plane of a 200Å thick crystal shows the vortex structure is strongly affected by the crystal potential and is sensitive to the beam position relative to atomic columns. The vortex phase structure is channelled along atomic columns (which agrees with Lubk et al. [89]), meaning close to atoms the phase structure is distorted more than inbetween atomic columns. However when directly on an atomic column the local azimuthal phase gradient appears to be maintained within a small radius of the atomic column. Due to the OAM exchange occurring between the vortex beam and the crystal the expectation value of OAM is no longer constant and oscillates as the beam propagates through the sample. The propagation dynamics of the phase distribution of vortex beams were studied by Lubk et al. [89], where vortex nodes were mapped out as they propagated. It was found that small perturbations for  $l=1$  beams only lead to a shifting or tilting of the nodal line, whilst for higher orders multiple first order beams are created. Vortex beams were found to be attracted to the positive coulomb potential of atomic columns. These effects lead to three key features of the simulated vortex node maps: 1) the creation of vortex-antivortex pairs either along the direction of propagation or in rings around the main vortex, 2) off centre vortex nodes will circulate an atomic column and 3) the splitting of  $l > 1$  modes can create higher orders as long as total winding number is conserved from the creation of opposite topological charges. The channeling along atomic columns is due to the similarity between the vortex phase and intensity distribution and that of the atomic 2p states (specifically a combination of Px and Py orbitals), as shown in simulations by Xin et al the ring intensity structure of on axis

vortex states can persist for much larger propagation distances than the equivalent off axis [90] .

Juchtmans has also shown that a spiral phase plate of topological charge  $-m$  could potentially map the local  $m$  component by cancelling out the  $+m$  phase and creating on axis intensity [91]. The  $-m$  topological charge is added by a spiral phase plate in the Fourier plane and then the transform of this produces an intensity with an on axis value determined by the coefficient of the  $+m$  component. The image formed has intensity related to the local  $m$  component taken with respect to an axis centered at that point. As has been discussed, there are currently multiple ways of producing electron vortex beams each with its advantages , binary amplitude masks are simple to produce but split intensity into unwanted orders, phase contrast masks could increase the intensity ending up in the vortex beams but are much harder to produce. Direct phase masks or altering the phase with magnetic fields offer the possibility of a purer, brighter vortex beam however their implementation is very difficult and the ideal pure vortex probe has yet to be produced in an easy, reproducible way.

### **2.1.10 STEM EELS and plasmons with OAM**

STEM EELS has proved to be a very useful tool for analysing plasmon modes in thin metal films at nanometre scales, providing experimental evidence for non-dipolar plasmon breathing modes which cannot couple to EM radiation and as such are 'dark' and not observable when interacting with photons [92, 48]. Previous studies of Aluminium structures have shown the size dependence of small nanodisks follow a standard plasmon dispersion when using the fitting of integer half wavelengths to the diameter. Schmidt et al have suggested a universal dispersion [93] for straight edges and nanodisks constructed from edge modes and breathing modes, similar to the plasmon breathing modes found for silver nanodisks by Schmidt previously in 2012. However the edge modes do not appear to follow the predicted dispersion relation when assuming a simple standing wave model either along the edge of a nano rod or around the circumference of a nanodisk.

Much like other wave phenomena surface plasmon oscillations can be travelling waves (often referred to as surface plasmon polaritons, SPPs) or standing waves (called localised surface plasmons, LSPs) and

these standing waves are produced when multiple travelling waves interfere. [94]

### 2.1.11 Chiral interactions during TEM EELS

It has recently been shown that 2D plasmon states can carry OAM. Kim et al. excited plasmons with laser irradiation and then measured the induced plasmon field with scanning near field optical microscopy (SNOM) and have shown coupling of photon SAM to plasmon OAM [45] (figure 2.6). This highlighted the capability of plasmonic lenses to exhibit chiral interactions with left and right hand circularly polarised light .

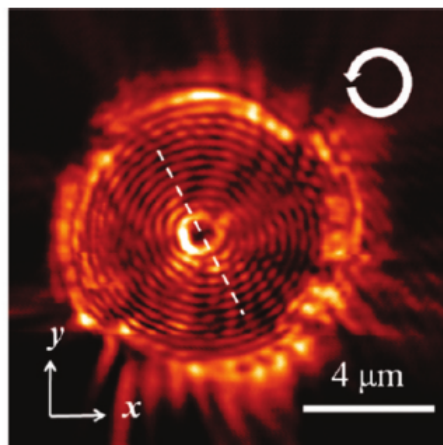


Figure 2.6: *The recorded SNOM intensity measurement of a plasmon mode with OAM from [45].*

Gorodetski et al . have shown that the OAM of incident photons survives transformation into a plasmon mode, propagation through an aperture and subsequent reemission as a photon mode [95]. This was achieved by measuring the transmitted intensity of right and left circularly polarised vortex photon beams after interaction with a plasmonic lens. Similarly Yu et al. showed different vortex beams produce different intensities after interaction with a plasmon mode and by matching the amplitude with that predicted for different vortex states they showed experimental evidence for the conservation of OAM throughout the interaction. Although direct measurement of the phase of plasmon modes has not been achieved, the interaction of plasmon vortex modes with gold particles has been shown by Shen et al. [96]. The particles were diffused in water above a plasmonic

structure designed to produce a vortex plasmonic near field proportional to the incident laser topological charge. The particles were recorded rotating at a rate dependent on the incident topological charge.

Entanglement of orbital angular momentum states has also been shown to survive when one photon of an entangled pair undergoes the conversion from photon to plasmon and back to a photon again [97]. Following these experiments, the interaction and possible transfer of OAM between an incident electron and a 2D plasmon mode is an untested avenue of research. There has been one study of the interaction of vortex electrons with a three dimensional arrangement of aluminium nanoparticles of roughly  $100nm$  diameter. An arXiv paper [50] reports a difference in energy loss around  $3.5eV$  for vortex electrons of opposite chirality. Ugarte and Ducati have theoretically modelled the interaction of electron vortex beams with surface plasmons of varying rotational symmetry [98]. They approached the problem by considering an ensemble of classical electron trajectories distributed around a ring and found that there can be an enhancement of energy loss to surface plasmons if the phase of the vortex matches the phase distribution of the plasmon mode. As such an  $l = 1$  vortex beam can also excite a plasmon mode if focused onto a position corresponding to a node, so that the phase of the plasmon mode undergoes a  $\pi$  change either side of the vortex probe.

This work builds upon previous findings by investigating the effect of a spiralling boundary, which reduces the rotational symmetry disks, going beyond the triangles studied in [98], it is shown that the EELS maps produced have a features which differ from what would be predicted by the standard dispersion relation for reflection and interference from a straight boundary. The interaction between photons and spiral plasmonic lens structures have previously been studied [45]. However these use a laser of approximately  $660nm$ , exciting low energy plasmons and only those plasmons with a frequency matching the incident laser wavelength. The size of the structures is also fairly large compared to the wavelength ( $8\mu m$  diameter) such that with a long decay length ( $430\mu m$ ) multiple oscillations are seen in the recorded SNOM (scanning nearfield optical microscopy) field. In contrast to these studies, in this chapter EELS is used to study structures of dimensions much closer to the wavelength of surface plasmon and multiple plasmon wavelengths can be excited by the incident beam electron.

This thesis involved measuring the energy loss of electrons carrying OAM after interacting with isolated thin metallic film structures designed to sustain plasmon modes with OAM. In the following chapters the plasmon modes present in Aluminium thin film structures are mapped by means of STEM EELS. After this the TEM EELS are compared for opposite signs of C-shaped beam after interaction with the Aluminium structures.

### 2.1.12 Previous vortices with openings

Previous work in the field of photon vortices has studied fractional OAM [99] [100][101] [102]. This has been both theoretical [99] and experimental [102]. The main findings have been that fractional OAM is associated with lines of vortices of alternating charge, producing a low intensity opening in an otherwise circular ring. The OAM carried by such fractional vortices has been shown to follow a step profile when plotting OAM against topological charge. The fractional OAM states are generally considered unstable and the intensity breaks up upon propagation, although one study showed by carefully controlling the Gouy phase of individual integer vortex components the fractional state can be stabilised [103]. Previous work has mostly concentrated on the wavefunction directly after phase modification [100] [99], and then propagation from this plane is considered [102], with only a few papers looking explicitly at the Fourier plane, for example [104] [105]. In common with the latter set of papers this thesis concerns the wavefunction in the Fourier plane of the phase modification and the Fresnel propagation before and after this Fourier plane. Fractional optical vortex states have successfully transferred angular momentum to  $3.1\mu\text{m}$  diameter spherical latex particles [106], proving the OAM associated with fractional states is not merely a theoretical idea. Furthering this an array of fractional OAM vortices was used to achieve optical sorting of polymer microparticles (refractive index of 1.59) with diameters of  $3.1\mu\text{m}$  and  $1.5\mu\text{m}$ . The two different sizes experienced two distinctly different alterations to their trajectories providing the basis for optical particle sorting [107].

Extending the work on fractional optical vortices, Alonzo produced helico conical beams by including radial phase gradients in the phase profile [16], from which the Fourier transform produces the intensity. The intensity in these types of beam has been seen to spiral [16][108][109][110].

Studies of fractional vortex states has shown that the branch cut used to define the phase discontinuity is a parameter which defined the quantum state [102] such that different branch cut orientations are no longer identical states. This chapter describes how the idea of using an alternative branch cut (i.e. a phase range of  $-\pi$  to  $\pi$ ) can be applied to the use of radial phase gradients. This allows the formation of more symmetric C-shaped intensity structures, of which the size and opening angle can be easily controlled. This control can be explained using a local spatial frequency analysis using the method shown by Alonzo et al [16]. A selection of previously described

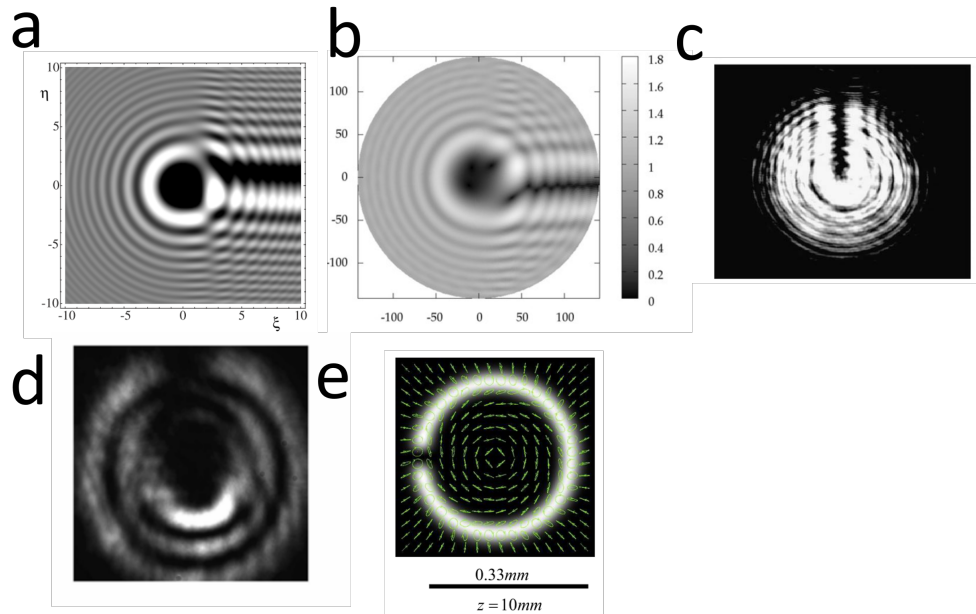


Figure 2.7: *Fractional OAM modes taken from references [99], [102], [111], [103] and [112]*

states with an opening are shown in figure 2.7. As can be seen most of the simulated (figure 2.7 a,b) and experimental results ( figure 2.7 c,d) show a narrow opening and multiple rings of intensity. The closest to a C shape is the error function 'erf-G' beams described by Fadeyeva [104] (figure 2.7 e) however this paper focuses more on the polarisation state of the beam, the beam has a much more complicated phase structure due to the use of error functions and there is no discussion of controlling the opening angle size. The beam also appears to break up from the C like shape as it propagates. For these reasons the C-shaped beams described in this thesis represent a furthering of the field going beyond the C like states produced previously.

# Chapter 3

## Methods

The main experimental method used for the results in the thesis was electron microscopy, either transmission or scanning, the details of the microscope used are given below. In addition, brief descriptions of techniques, apparatus and simulation methods is given in this section. Focused Ion Beam milling (FIB) was used to produce the amplitude and phase masks shown in chapter 5 and some of the spiral structures shown in chapter 7. Iterative Fourier transform algorithm (IFTA) methods were used to calculate an example phase which produces a C like shape for comparison with the C-shaped beams. IFTA methods were also applied to experimental data to retrieve estimates of the phase associated with the measured intensity. The boundary element method (BEM) and Finite element method were used to simulate the electromagnetic eigenmodes supported by the metal structures described in chapters 6 and 7. Electron beam lithography (EBL) was used to produce a grid of structures which were then analysed by Electron Energy loss spectroscopy (EELS) and Cathodoluminescence (CL) in chapter 7. Both EELS and CL were used to look for evidence of energy loss characteristic of surface plasmon modes.

### 3.1 The JEOL 2200 FS Microscope

The microscope used in the experimental sections of this thesis was a JEOL 2200FS with aberration correction at the University of York Nanocenter.

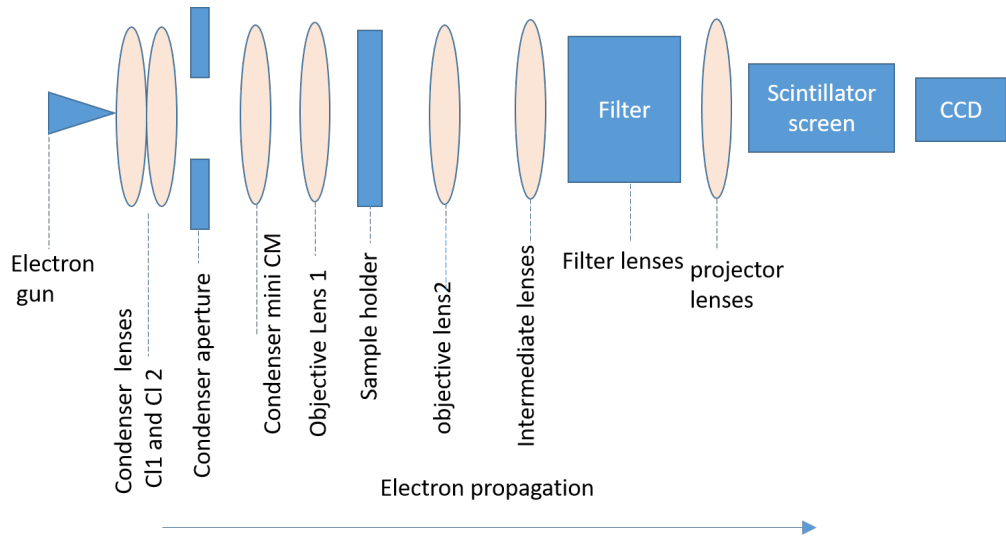


Figure 3.1: A schematic of the main lenses and apertures in the 2200 microscope.

The main lenses and apertures are shown schematically in figure 3.1. During beam shaping experiments diffraction masks were placed in the 2mm condenser aperture holder or the 3mm sample plane holder. The ray diagrams for 3 different convergence angles along with nano beam diffraction (NBD) mode are shown in figure 3.2. In figure 3.2, Cl1 and Cl2 are the condenser lenses close to the condenser aperture, CM is the condenser mini lens, which is used to alter the angle of incidence on the sample. Diffraction masks were placed in the condenser aperture (if 2mm) and also inserted as a sample into the sample holder plane (if 3mm). To vary the defocus of the condenser aperture mask diffraction pattern the condenser lens was varied, during TEM mode. In addition to TEM mode the illumination can be changed to a very small spot, useful for recording diffraction from a well defined area, for this application the microscope can be operated in NBD mode (figure 3.2) in this case weaker lens currents are used, in the condenser lens 2 (Cl2 in figure 3.2) and condenser lens mini (CM in figure 3.2), this reduces the effect of lens aberrations, increasing the coherence of the illumination and allows a smaller spot size to be produced. In section 5.2.1 NBD mode is used to produce a C-shaped probes and shows more fine structure. In TEM mode this sample plane is illuminated with plane waves (or the diffraction pattern of the condenser aperture mask) and it is this plane whose image is formed onto the CCD at the 'end' of the microscope column. For the sample plane masks the TEM was changed to low magnification mode (see figure 3.3). In figure 3.3 IL1,IL2,IL3 and IL4 are

the intermediate lenses inbetween the sample and the spectrometer, PL1 and PL2 are the final projector lenses which form the image recorded by the CCD. The two post-sample plane apertures shown are the selected area aperture and the EELS spectrometer entrance aperture. In low mag mode the Objective lens is turned off reducing the overall magnification however the sample plane is still the conjugate plane to the CCD image. To vary the defocus of the sample plane mask the first intermediate lens 'IL1' was varied in this low magnification mode . In spectrum mode the filter lenses are used to disperse electrons according to their energy and it is this dispersion plane (labelled spectrum plane in figure 3.3) which is imaged onto the CCD. In this way the probability of losing a certain energy is recorded by imaging the intensity of electrons after travelling through the filter.

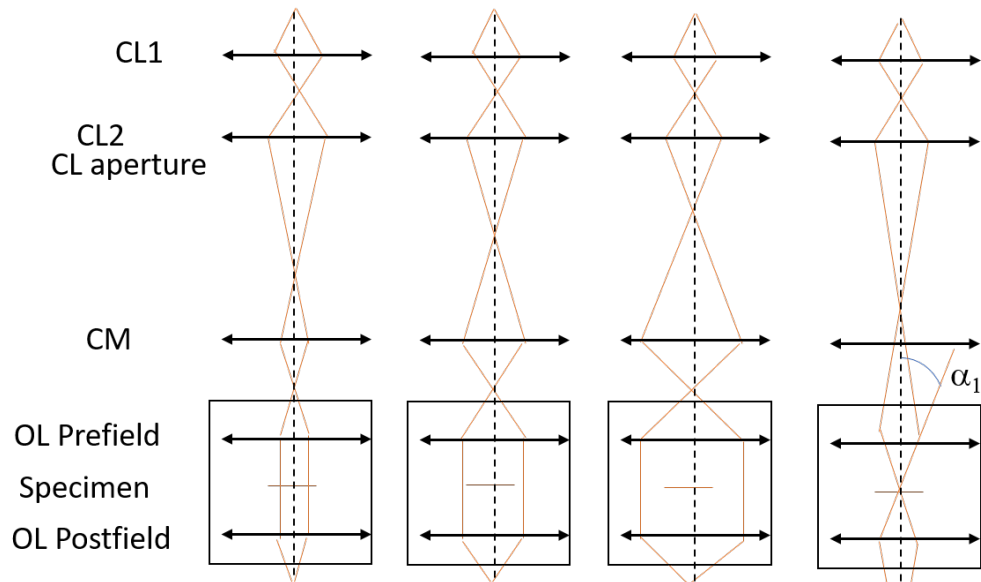


Figure 3.2: *Illumination ray diagram for TEM mode and NBD mode. Image taken from York Nanocentre 2200 handbook. CL1, CL2 are condenser lenses, CM is the condenser mini lens. OL prefield and OL postfield are ways of modelling the optical effect of the objective lens.  $\alpha$  is the angle of rays entering the objective lens.*

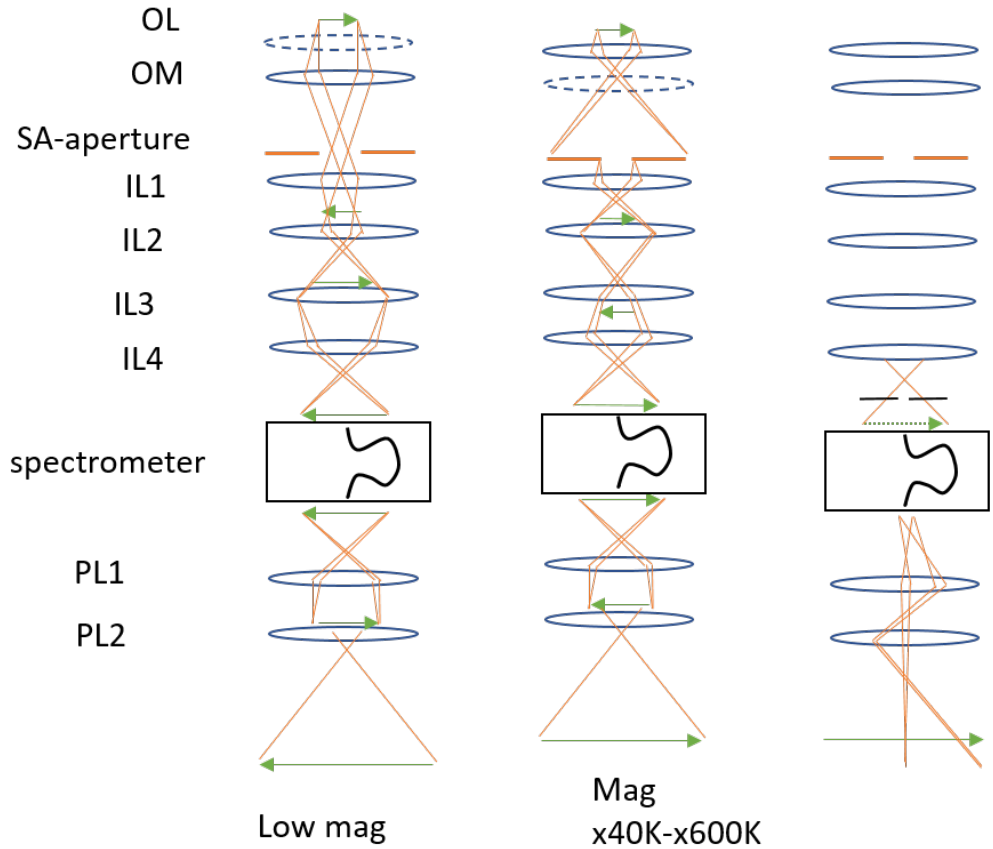


Figure 3.3: Ray diagrams of the 3 main microscope modes used in this thesis, low magnification, TEM mode (40,000-600,000 times magnification) and spectrum mode. Image taken from York Nanocentre 2200 handbook.

## 3.2 Holographic reconstruction

Holographic reconstruction is a way of imparting a desired phase distribution onto an incoming wave. This utilises the fact that the intensity in an interference pattern between two complex fields  $A_1 \exp(i\phi_1)$  and  $A_2 \exp(i\phi_2)$  is determined by the phase difference  $(\phi_1 - \phi_2)$  and amplitudes ( $A_1$  and  $A_2$ ) as shown below.

$$\begin{aligned}
& |A_1 \exp(i\phi_1) + A_2 \exp(i\phi_2)|^2 = \\
& |A_1 \cos(\phi_1) + A_2 \cos(\phi_2) + i * (A_1 \sin(\phi_1) + A_2 \sin(\phi_2))|^2 \\
& = A_1^2 \cos^2(\phi_1) + A_2^2 \cos^2(\phi_2) + 2A_1 A_2 \cos(\phi_1) \cos(\phi_2) + \\
& \quad A_1^2 \sin^2(\phi_1) - A_2^2 \sin^2(\phi_2) + 2A_1 A_2 \sin(\phi_1) \sin(\phi_2) \\
& = A_1^2 + A_2^2 + 2A_1 A_2 \cos(\phi_1 - \phi_2)
\end{aligned}$$

To use this interference effect, the interference pattern of a target phase distribution and an angled plane wave is calculated. The resulting amplitude distribution can be imprinted onto a plane wave, via the use of an amplitude mask with the same amplitude distribution. The field after the mask is then a combination of the input plane wave and fields with the target phase distribution travelling at an angle. The mask made in this manner can be thought of as the combination of modes, when illuminating the mask you excite this combination of modes. If the interference pattern is binarised ( as being above or below a threshold value) then multiple higher order modes are produced too. This can be rationalised by considering that to form a straight edge, like a top-hat function, many larger frequencies are required compared to a single sine wave oscillation. An example of a simple holographic reconstruction mask is a linear grating. This is calculated by the interference of two plane waves travelling at an angle to one another. When illuminated with a plane wave the field after the mask contains other plane waves travelling at an angle, thus producing the well known diffraction spots in the far field [113] (see figure 3.4). The diffraction angles are determined by the ratio of the slit width  $d$  to the wavelength  $\lambda$  by  $\Phi = \lambda/d$ , which for the electron experiments described here gives angles of the order of  $2.5E - 12/1E - 7 = 2.5E - 5rad = 25\mu rad$ . As described in section 1.3, by looking at the far field of the field after the mask you are visualising the Fourier transform of that field. This allows fields which are travelling at different angles to be separated. This is one of the methods which is used in this thesis to produce the phase structured electron states in the subsequent chapters. When discussing this experimental set up the 'mask plane' refers to the field just after the input wave has interacted with the mask being used. Alternatively the 'Fourier plane' or 'diffraction plane' is in the focal plane of a lens system performing a Fourier transform of the mask plane field. In practice, the interference pattern is calculated numerically to produce a computer generated hologram (CGH) mask.

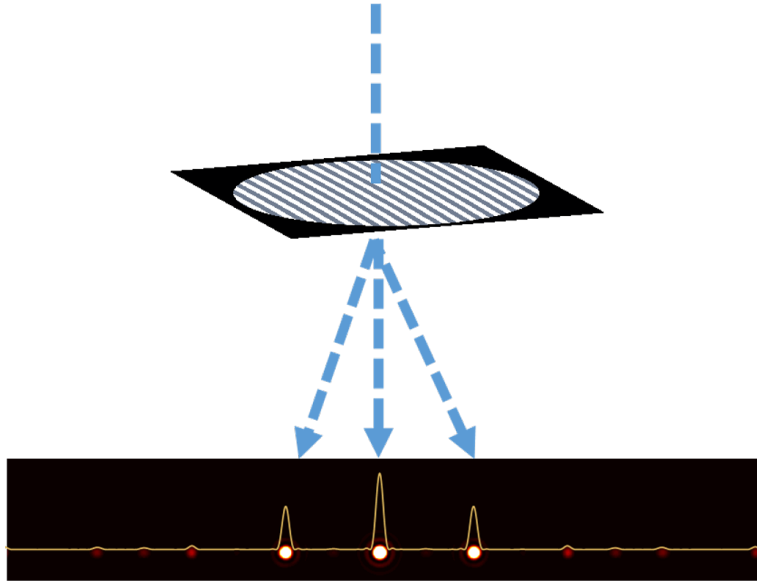


Figure 3.4: A schematic diagram of diffraction pattern intensity from a plane wave on a linear diffraction grating. Energy is distributed between the three main diffraction orders (+1, 0, -1). The yellow line plot is an intensity profile through the diffraction orders.

### 3.3 Focused Ion Beam Milling

In a similar way to electrons, larger more massive particles can be ionised and focused by magnetic or electric fields using analogies with photon optics [114]. This is utilised in a focused ion beam (FIB) milling machine to accelerate and focus a source of ions, for example  $Ga^+$ , to a spot on a sample. When the  $Ga^+$  ions hit the sample, they can impart enough energy to cause sputtering and remove atoms from the sample wherever the beam is focused, milling at very small scales. In addition to sputtering, the incident ions can cause emission of secondary ions or electrons, which can be used for imaging in a similar manner to scanning electron microscopy. The lenses allow scanning of the focused beam to pattern samples, this is a useful method for producing structure on the nanometer scale for certain samples. It is best suited to conductive metals which can dissipate any charge build up from the bombarding ions. However if needed an electron beam can be used to flood the sample with negative charge to help alleviate any positive charge built up during FIB milling.

## 3.4 Electron beam lithography (EBL)

In lithography a resist is a material which can undergo local changes in physical properties, such as solubility in a particular solvent. This allows areas to be defined which can be removed by such a solvent. Any areas left can be used to block deposition of material in the pattern which was defined on the resist. During electron beam lithography (EBL) electron optics can be used to scan a focused electron beam over a resist which will react to illumination by electrons and change its properties [115]. A first work up step will remove some of the sample leaving either the exposed region (negative resist) or unexposed region (positive resist) [116]. A top metal layer is then deposited over the resist whilst still leaving some of the resist accessible. A final work up step removes the resist which was initially left, lifting off the metal which was on the resist left after the first work up. This leaves behind a metal layer with the pattern determined by the electron beam. Due to the small sizes an electron beam can be focused to this is a useful high throughput method for controlling structure on the nm scale. Researchers are constantly searching for new resists which can achieve higher resolution patterns when interacting with ion beams. One of the most widely used resists is polymethyl methacrylate (PMMA), which has achieved resolutions of the order of 5nm (40nm PMMA resist layer, 30keV beamline dose of  $1.2 - 1.3nCm^{-1}$  [116]). This has been pushed further to 3-4nm by ultrasonic agitation during the work up process. However the highest resolutions have been produced for isolated structures and PMMA still has a problem of instability and pattern collapse when producing dense features. Due to its limitations alternatives to PMMA are being searched for with a recent higher resolution resist Hydroxysilsequioxane (HSQ) becoming popular [116].

## 3.5 Cathodoluminescence

In a scanning electron microscope it is possible to include a collection mirror above the sample to collect any photons emitted after electron excitation, known as cathodoluminescence (CL)[117]. The energy of these photons can be related to transitions between excited states from the sample of radiative modes excited in the sample. The SEM used for this project used a

hemispherical curved mirror to collect the intensity onto a CCD. The system can produce either CL images or spectra. When forming CL images the incident electron is focused to a spot and any photon emitted are collected into a photomultiplier tube which amplifies the incoming photon into an electrical signal by a cascade of photoelectron emission. Filters can be used to select different wavelength ranges. Similarly to STEM the focused spot is scanned across the sample and at each point the emitted photon intensity is recorded thus building up an image of local photon emission at each point. Alternatively the collection time can be increased such that the focused spot covers all of the sample multiple times, any emitted photons during this collection window can be collected into a spectrometer, which separates out photons from the entire sample area depending on their energies by using a diffraction grating to produce a spectrum.

## 3.6 Simulation Methods

### 3.6.1 Iterative Fourier transform algorithm to find a phase mask

For a Fourier pair of planes, real and reciprocal, when an amplitude is known in the reciprocal plane, the amplitude and phase required in the real plane to form such an amplitude can be found by iteratively applying a Fourier transform to complex functions in both planes. After each transform the new phase is used to define the next function, using the desired amplitude, gradually this should find the phase and amplitude in the real plane which produces the best match in the reciprocal plane to the known amplitude. The algorithm used followed the Gerchberg-Saxton method [118][53]. A flow chart for this method is shown in the appendix in section A.2. The assumption behind this method is that Fourier transforming a similar phase distribution to the actual solution will reach a distribution more similar to the actual solution. By imposing an amplitude condition on each new phase the algorithm restricts the solutions it explores to those similar to the recorded intensity and the true phase solution. The amplitude condition allows the algorithm to explore the possible solutions as shown in figure 3.5, where each point on the real and reciprocal space planes represents a different complex function.

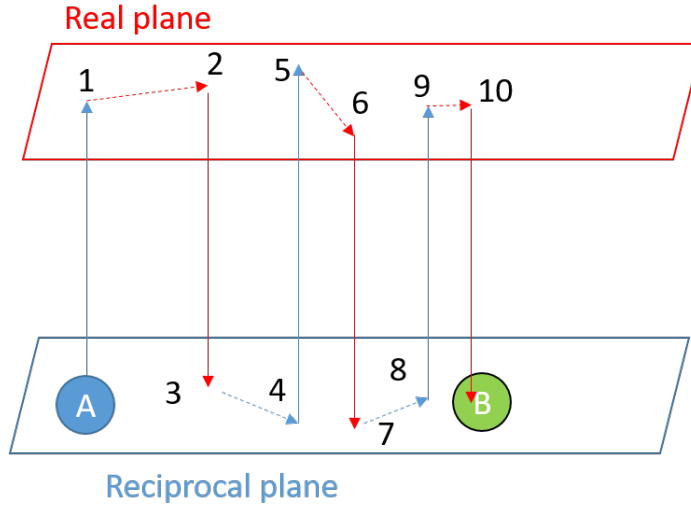


Figure 3.5: *By imposing boundary conditions (represented by dashed arrows) after each transformation (represented by solid arrows) an initial guess A can be moved closer to the true solution B, during an iterative Fourier transform algorithm.*

The known reciprocal space intensity combined with a constant phase is used as the initial reciprocal space guess, shown as circle A. By performing a Fourier transform (shown as vertical blue arrow) an initial real space solution is gained, shown as point 1. However if Fourier transformed, the initial reciprocal plane guess will be returned to, by imposing an amplitude onto the Fourier transform you alter the real space solution guess, this is shown as a red dotted arrow changing initial Fourier transform guess point 1 to a different guess, point 2. This involves selecting only intensity within an aperture. By Fourier transforming this reduced range (shown as a solid red arrow from 2 to 3) the reciprocal solution moves closer to the true reciprocal solution, shown as circle B. This is because the solution the algorithm is designed to solve for a mask which only uses intensity within an aperture, any intensity outside of the aperture represents deviations from the final solution. Finally a new guess of the reciprocal space complex function is gained by imposing an amplitude condition in the reciprocal plane (shown as a dashed blue arrow from 3 to 4). This will have a similar function to the real plane aperture, selecting only those contributions we want in the final solution. Repetition of this sequence, should result in the amplitude conditions being smaller changes to the overall functions (shown with decreasing arrow size). This allows a pair of points in real and reciprocal space to be found which satisfy the amplitude conditions in both

planes and reproduce the known intensity in the real plane. This method can either be used to solve for the real space phase distribution required to form a desired reciprocal space intensity (beam shaping, appendix section A.2 ) or it can retrieve the phase of a reciprocal complex function when the reciprocal plane intensity and real plane amplitude are known (phase retrieval, appendix section A.3).

The details of the IFTA algorithm used are in appendix chapter A section A.3. Iterative algorithms can often get stuck in a local state where the solution error does not decrease enough, going back and forth between multiple unsatisfactory solutions. When performing phase retrieval the algorithm was improved to include a method known as charge flipping [119]. This was used with the threshold value of  $1.2\zeta$  where  $\zeta$  is the standard deviation of the mask amplitude distribution. The charge flipping method works as follows, instead of an ideal circular aperture binary mask, an amplitude mask with a sign of  $\pm 1$  depending on whether the calculated amplitude in step 2. is above or below the  $1.2\zeta$  threshold. This replacement of the binary circular aperture occurs for a series of 10 iterations out of every 100 after which the previously described aperture condition is used for another 90 iterations. Adding in this extra variation allows the algorithm to explore more possible solutions whilst reducing the potential for the algorithm to get stuck in an unsatisfactory local minimum. This iterative algorithm, when used for phase retrieval, will converge on the complex function which best matches the experimental amplitude. The application of this phase retrieval algorithm to experimentally produced C-shaped vortex intensity is shown in chapter 5, in section 5.1.3.

### 3.7 Boundary element method overview

To simulate electromagnetic fields Maxwells equations need to be solved numerically. When using the Boundary element method (BEM) this is achieved via a Greens function formalism, where the function  $G$  represents the field created by a single point charge. The field inside a homogeneous dielectric environment can then be described by the summation of effects from any externally applied fields,  $\phi_{ext}$ , and the integrated effects of source charge terms  $\sigma$ , distributed over the boundary between two different materials with dielectric constants  $\epsilon_1$  and  $\epsilon_2$ . By applying the conditions of

continuous parallel electric field and continuity of normal dielectric displacement field across the boundary, a boundary integral equation can be formed. To compute this integral it is approximated by a summation of individual elements which, within the quasi-static approximation ( which assumes that the dimensions considered are much smaller than the wavelength of light being used), yields equation 3.1, linking the surface charge at point  $i$  to contributions from points  $j$ . [120]

$$\Lambda\sigma_i + \sum_j \left(\frac{\partial G}{\partial n}\right)_{ij}\sigma_j = -\left(\frac{\partial\phi_{ext}}{\partial n}\right)_i \quad (3.1)$$

where

$$\Lambda = 2\pi \frac{\epsilon_2 + \epsilon_1}{\epsilon_2 - \epsilon_1} \quad (3.2)$$

and  $n$  is the outer surface normal vector.

When the quasistatic approximation does not apply, the full maxwell equations must be solved and this leads to a more complicated version of( 3.1) with multiple equations, however the principle is the same. Eigenvalue equation (3.1) can then be solved by matrix inversion. To achieve this the surface is split into a grid of elements joined by nodes. The field value at each node relies on the effect of the fields from all other nodes in the sample thus equation 3.1 is a collection of simultaneous equations from Maxwell's equations, using neighbouring nodes to calculate derivatives. The inputs for the simulation consist of the dimensions of the geometry to be solved, parameters controlling the mesh production and optical constants defining the materials. The MNPBEM (Magnetic Nano Particle BEM) toolkit [121] then utilises the built in MATLAB function 'mldivide.m' . This function checks the matrix for symmetries which could reduce computation time if none of these checks are true then the default method is the LU solver, which applies Lower -upper (LU) decomposition, thus allowing the inverse of the matrix to be calculated.([122]) Once the surface charges have been solved for (the eigenvector) then the fields can be calculated. The MNPBEM toolbox also allows for the inclusion of a line current as a  $\phi_{ext}$  and can thus model interactions with an electron beam [123]. The probability of energy loss (per unit of transferred energy) can be calculated by evaluating 3.3, where  $\Gamma_{bulk}(\omega)$  is the probability of energy loss at frequency  $\omega$  during propagation through a lossy medium and is proportional to the imaginary term  $\Im[-1/\epsilon(\omega)]$  within the quasistatic approximation.

$$\Gamma_{EELS}(\omega) = \frac{e}{\pi\hbar\omega} \int \Re[e^{-i\omega t} \mathbf{v} \cdot \mathbf{E}_{ind}(\mathbf{r}(t), \omega)] dt + \Gamma_{bulk}(\omega) \quad (3.3)$$

In 3.3 the  $\Re$  is the real part, the integral calculates the work done by the electron, with velocity  $\boldsymbol{\nu}$ , in moving against the electric field induced in the sample,  $\boldsymbol{E}_{ind}$ , and can thus predict the energy loss probability.

# Chapter 4

## C theory

### 4.1 C shape theory

#### 4.1.1 C-shaped intensity

The theory behind producing a C-shape will now be presented. A C-shaped vortex state removes the rotational symmetry of the standard annular integer vortex and allows rotations of the intensity to be viewed as well as allowing the production of split-ring structures via lithography. Throughout this section the intensity produced by a phase alteration will be considered where the intensity is in the diffraction plane ("Fourier plane") of the phase alteration plane ("mask plane"). The fields in the mask and Fourier planes form a two dimensional Fourier transform pair. Both planes are perpendicular to the overall propagation direction along the beam axis. When the mask plane phase includes a product term of the form  $\rho\phi$ , where  $(\rho, \phi)$  are circular polar coordinates in the perpendicular planes, the phase distribution in the mask plane contains a radial phase gradient. For helico-conical beams, [108], this has been shown to produce a Fourier plane intensity with spirals instead of the vortex rings produced by solely azimuthal  $\phi$  dependent phases of integer vortex beams [55]. This can be explained by considering a simple geometric ray model where every point on the phase surface in the mask plane provides a contribution with a transverse wavevector equal to the transverse component of the surface normal vector of the mask phase surface. This is known as a local spatial frequency analysis [16], each spatial

frequency is directly mapped onto a point of intensity in the Fourier plane. For an  $l = 1$  vortex these phase gradients point in the direction of the local azimuthal unit vector. For helico-conical beams these phase gradient vectors are now off set by an additional radial vector component which increases as you increase the azimuthal angle value. An additional parameter which was not varied in the previous studies of helico-conical beams was the distribution of angles used in the definition of  $\phi$ , which in turn varies the spatial variation in the size and sign of the contribution from the additional  $\rho\phi$  term. In addition to this, the helico-conical paper was limited to only integer coefficients in front of the topological charge and mixed  $\rho\phi$  terms. Furthermore only differences, not summations, between these terms were considered. Thus, by choosing summations of fractional topological charges for symmetric  $|\psi|$  distributions new types of intensity distribution and wavefunctions have been explored in this thesis. A C-shaped intensity distribution can be produced by using the mask plane phase distribution,  $U$ , of equation 4.1, where  $m$  and  $c$  are dimensionless non-integer constant coefficients,  $\rho_0$  is the aperture radius,  $\bar{\rho} = \rho/\rho_0$  is the scaled radius and  $\phi_0$  is the offset from a  $0 \leq \phi \leq 2\pi$  range of angles for the definition of  $\phi$  values. An example of a phase mask using equation 4.1 is shown in the lower left of figure 4.1.

$$U = (m + c\bar{\rho})(\phi - \phi_0) \quad (4.1)$$

Two key properties of the phase function (4.1) which determine the intensity pattern produced are the range of angles used and whether a summation or difference is used when combining the  $m\phi$  and  $c\rho\phi$  terms. Previously shown helico-conical beams are reproduced by using an angle defined between 0 and  $2\pi$  ( $\phi_0 = 0$ ) and by taking a difference between the two terms  $m$  and  $c\rho$  ( $c < 0$ ). Using a symmetric range of values for the polar angle ( $-\pi \leq \phi \leq \pi$ , i.e.  $\phi_0 = \pi$ ) along with a summation ( $c > 0$ ), the intensity can be made to create a C shape (shown in figure 4.1). The gap in the C-shape can be understood by returning to a local spatial frequency analysis. Each point from the mask phase contributes a wavevector, governed by its local phase gradient, which can be represented by a dot in k space placed at the end of the vectors projection on the  $k_x, k_y$  Fourier plane. The phase discontinuity in the mask plane removes any phase gradient pointing solely along the azimuthal unitvector at  $\phi - \phi_0 = -\pi$  or  $\phi - \phi_0 = \pi$ . Either side of the discontinuity there is an additional

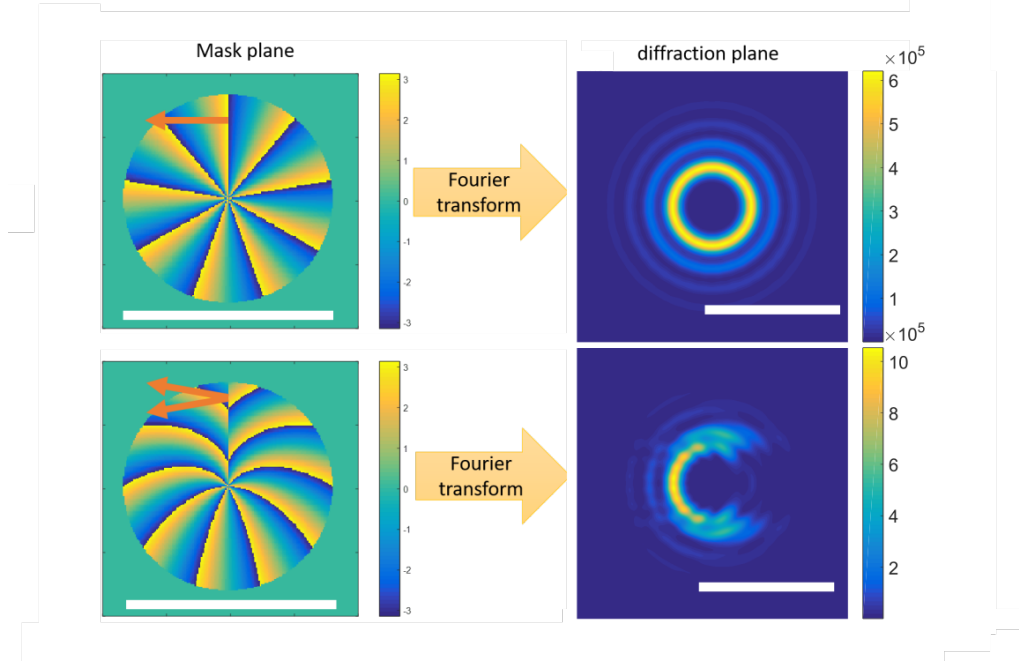


Figure 4.1: *The mask plane phase and Fourier plane intensities for an  $l=9$  integer vortex (top) and an  $\alpha = 45, D = 10$  C-shaped beam (bottom). The mask plane scale bar is  $30\mu\text{m}$  and the scalebar on the Fourier plane is  $2.5 \times 10^5 \text{m}^{-1}$ . The orange arrows on the mask plane phase indicate the local direction of largest phase gradient, at either side of the discontinuity which only differ when radial phase components are added.*

wavevector (phase gradient) component either in the positive or negative radial direction as shown in figure 4.1 by the orange arrows on the phase distributions. There are two arrows as one is for the phase gradient to the left and one is for the phase gradient to the right of the discontinuity. This means there are missing phase gradients, between the directions of the two orange arrows there are no phase gradients with those angles. Thus the ring in the integer vortex is split open to form a C, the missing local phase gradients corresponding to those points in the Fourier plane with low intensity. The phase gradient is predominantly in the  $\hat{\phi}$  direction and as such the Fourier space opening in the C is rotated  $90^\circ$  from the real space mask discontinuity. As will be shown, analysis of the derivative of the phase allows equations to be derived, linking the predicted shape opening angle and radius to the mask parameters  $m$  and  $c$ .

### 4.1.2 Control equation derivation

To predict the intensity distribution we initially require the phase gradient as a function of polar coordinates,  $\nabla U(\rho, \phi)$ . Depending on how the sign of the phase is defined, a mask plane phase gradient along a vector  $\hat{r}$  could correspond to wavevectors travelling along  $\hat{r}$  or  $-\hat{r}$ , however due to the mirror symmetry of the C shape it is not important which convention is used. The following calculations consider a mapping of a positive gradient onto a positive wavevector. The gradients of the mask plane phase distribution with respect to radial and angular coordinates  $(\rho, \phi)$  can be calculated as

$$\frac{\partial U}{\partial \rho} = c(\phi - \phi_0) \quad (4.2)$$

$$\frac{\partial U}{\partial \phi} = (m + c\rho) \quad (4.3)$$

$$\nabla U = \frac{\partial U}{\partial \rho} \hat{\rho} + \frac{1}{\rho} \frac{\partial U}{\partial \phi} \hat{\phi} = (c(\phi - \phi_0)) \hat{\rho} + \left(\frac{1}{\rho}(m + c\rho)\right) \hat{\phi} \quad (4.4)$$

Two useful limits can be used to define the C shape produced when  $0 < \phi < 2\pi$  and  $\phi_0 = \pi$ . Firstly, for  $\phi = \pi$ ,

$$\nabla U = \left(\frac{m}{\rho} + c\right) \hat{\phi} \quad (4.5)$$

this produces a dot in the scatter plot of figure 4.2 directly opposite the C opening, representing a gradient pointing solely in the  $\hat{\phi}$  direction. Smaller phase gradients occur for larger radii in the mask plane, as such the smallest point on the scatter plot will be from positions where  $\bar{\rho} = 1$ . This can be used to define a distance characterising the size of the C shape, by looking at the smallest inner value for the gradient which gives  $D = m + c$  as the radial dimension of the C shape size, as shown by the distance between the green dashed lines in figure 4.2. The second useful limit is for  $\phi - \pi = \pm\pi$ , where the scatter plot points create the opening in the C shape. Here,

$$\nabla U = \pm c\rho \hat{\rho} + \left(\frac{m}{\rho} + c\right) \hat{\phi} \quad (4.6)$$

The additional contribution in the  $\hat{\rho}$  direction leads to a redirecting of phase gradients away from the  $\hat{\phi}$  direction. This causes an absence of phase gradients pointing solely along  $\hat{\phi}$  and it is this effect which causes the opening in the C-shaped beam, when compared to the full ring of the

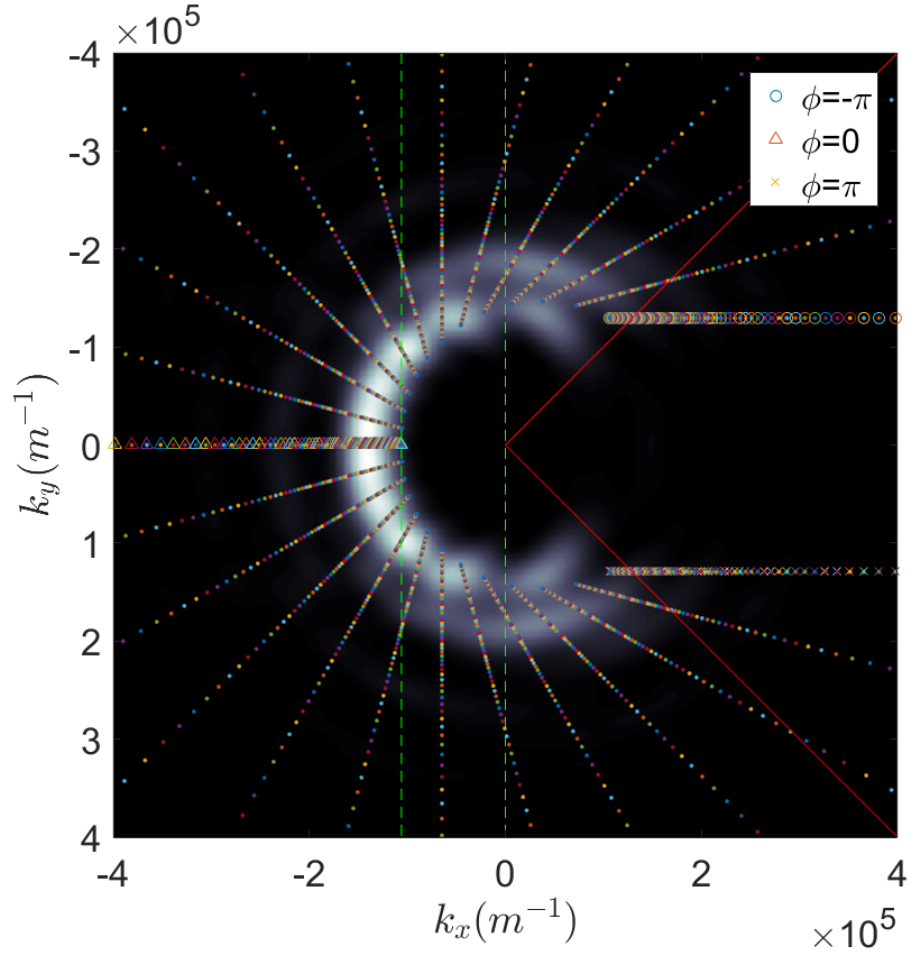


Figure 4.2: Markers are Fourier plane points representing local spatial frequency analysis of mask plane phase gradients, the different coloured groups are phase gradients from constant mask plane radius. The phase gradient points from key mask plane angular co ordinates are shown by circles ( $\phi = -\pi$ ), triangles ( $\phi = 0$ ) and crosses ( $\phi = +\pi$ ). The greyscale colour is the corresponding Fourier plane intensity. The 2 characterisation parameters  $\alpha$  and  $D$  are also shown with the distance between the dotted green lines and angle between the red lines respectively ,  $\alpha = 45^\circ, m = 6.1161, c = 3.8839$ .

integer vortex (figure 4.3). For  $\phi - \pi = \pm\pi$  the reciprocal space phase gradient vectors satisfy  $\hat{\rho} = k_y$  and  $\hat{\phi} = k_x$ , as such the angle can be found by using the equation

$$\alpha = \tan^{-1}\left(\frac{c\pi}{\left(\frac{m}{\rho_{cut}} + c\right)}\right) \quad (4.7)$$

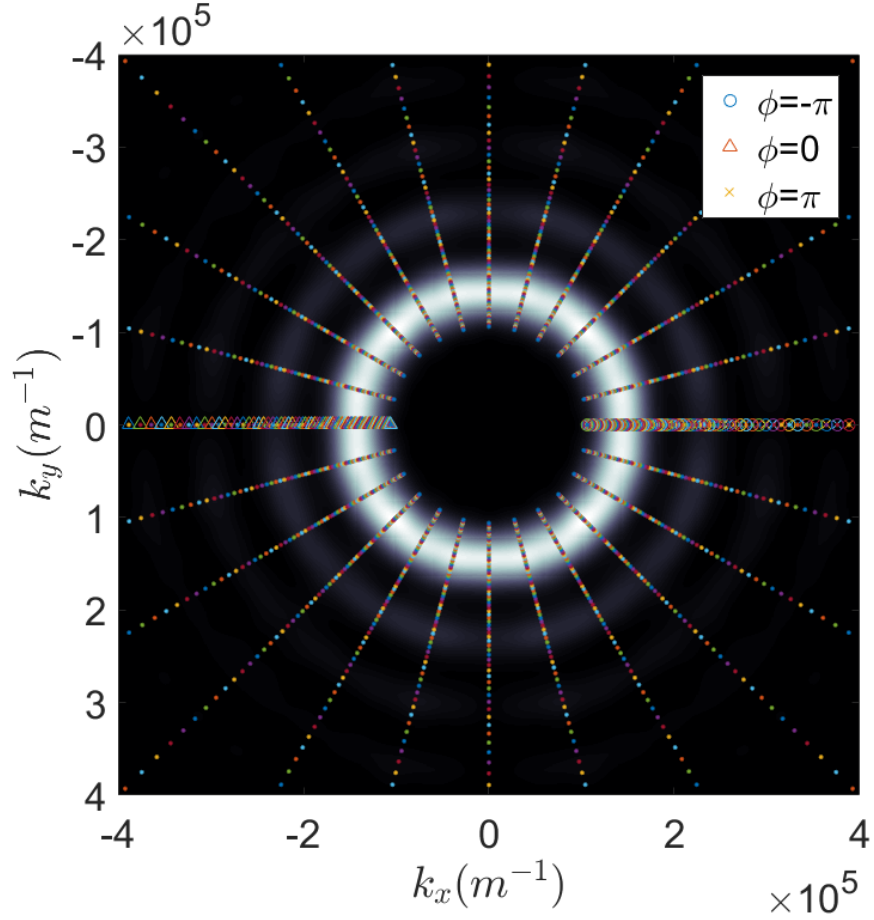


Figure 4.3: *Markers are Fourier plane points representing local spatial frequency analysis of mask plane phase gradients, The different coloured groups are phase gradients from constant mask plane radius. The phase gradient points from key mask plane angular co ordinates are shown by circles ( $\phi = -\pi$ ), triangles ( $\phi = 0$ ) and crosses ( $\phi = +\pi$ ). The greyscale colour is the corresponding Fourier plane intensity. ( $\alpha = 0^\circ$ ,  $m = 10$ ,  $c = 0$ ).*

where a decision must be made for which scatter plot position is used to measure the angle. This in effect is choosing a corresponding mask plane radius which produces that scatter plot point. This parameter is labelled  $\rho_{cut}$  and as will be described the optimum value will depend on where you decide to measure the opening angle from.

For a given half angle of opening  $\alpha$ ,  $m$  and  $c$  must satisfy for

$$\phi_0 = \pi$$

$$\alpha = (\tan^{-1}(\frac{\phi_0}{\frac{m}{\bar{\rho}_{cut}c} + 1})) \quad (4.8)$$

$$C_{cut} \equiv 1/\bar{\rho}_{cut} \quad (4.9)$$

$$C_{cut} \frac{m}{c} = \frac{\pi}{\tan(\alpha)} - 1 \quad (4.10)$$

$$C_{\alpha} \equiv \frac{\pi}{\tan(\alpha)} - 1 \quad (4.11)$$

$$\frac{m}{c} = \frac{C_{\alpha}}{C_{cut}} \quad (4.12)$$

Through the two dimensionless parameters  $C_{\alpha}$  and  $C_{cut}$ , equation 4.12 defines a curve in the  $(m, c)$  plane, on which the pairs of  $m$  and  $c$  must lie for a desired angle. Moving along the curve satisfying (4.12) will keep the angle  $\alpha$  constant whilst varying the size,  $D$  of the C shape (shown by path A in figure 4.4). By using the relationship 4.12,  $D$  can be written as

$$D = \left| \frac{\partial \psi}{\partial x} \right|_{\phi=0} = |-m - c| = m(1 + \frac{c}{m}) = m(1 + \frac{C_{cut}}{C_{\alpha}}) \quad (4.13)$$

and so pairs of  $m$  and  $c$  can be determined for a given set of  $\alpha, D$  and  $C_{cut}$  from

$$m = D(1 + \frac{C_{cut}}{C_{\alpha}})^{-1} \quad (4.14)$$

$$c = \frac{C_{cut}m}{C_{\alpha}} = \frac{C_{cut}}{C_{\alpha}} D(1 + \frac{C_{cut}}{C_{\alpha}})^{-1} = D(\frac{C_{\alpha}}{C_{cut}} + 1)^{-1} \quad (4.15)$$

from which is can be deduced that

$$(4.16)$$

$$m + c = D([(1 + \frac{C_{cut}}{C_{\alpha}})^{-1} + (\frac{C_{\alpha}}{C_{cut}} + 1)^{-1}]) = D \quad (4.17)$$

$$(1 + \frac{C_{cut}}{C_{\alpha}})^{-1} + (\frac{C_{\alpha}}{C_{cut}} + 1)^{-1} = 1 \quad (4.18)$$

the control parameters  $\alpha$  and  $D$  are labelled on figure 4.2.  $C_{cut}$  is a fitting parameter, by comparisons of simulated focal plane intensities, from a range of  $C_{cut}$  values, it was judged by eye that a value of 1.36 gave a good match with the predicted angle. This parameter was then used for the production of the masks early on in the experimental work. For future experiments, this method could be made more robust by plotting out the azimuthal intensity and defining the ends of the C shape by looking where the intensity goes below a threshold value. When using the  $C_{cut}$  value of 1.36 to design a C shape for an angle of  $\alpha = 45$ , the intensity is 0.0764 of

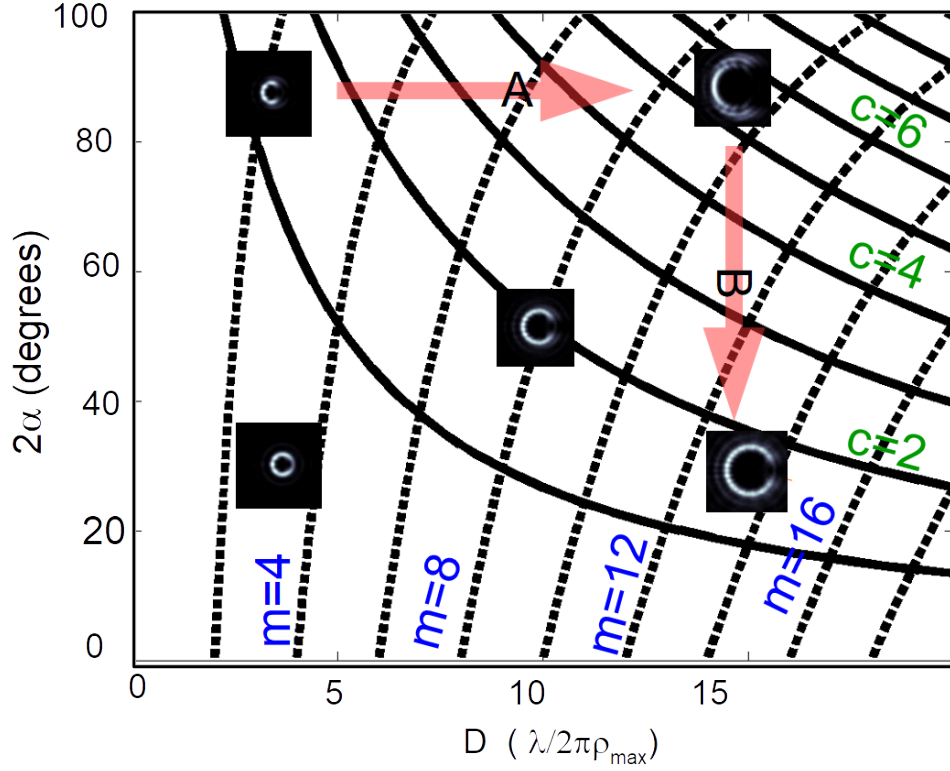


Figure 4.4: A contour plot showing values of  $m$  and  $c$  constants which produce opening angle ( $\alpha$ ) and size ( $D$ ) parameter pairs. The opening angle and size of the C shape can be independently controlled by using simple variations of  $m$  and  $c$  values. Path A represents a collection of  $(m, c)$  values which give a constant opening angle of  $2\alpha = 90$  for  $D = 5$  to  $D = 15$  whilst path B shows a constant size of  $D = 15$  and varying opening angle of  $2\alpha = 90$  to  $2\alpha = 30$ .

the maximum intensity. This occurs as the intensity is increasing out of the gap ( an intensity plot is given along with a more detailed discussion in section 4.1.6). With hindsight the  $C_{cut}$  value should have been more rigorously defined, the aim of this experiment was to show that C-shaped electrons could be produced and that the opening angle could be varied and a precise definition of how to measure the opening angle was not required. If C-shaped beams are applied to processes with a natural intensity threshold with which to define the ends of the C shape required then  $C_{cut}$  could easily be changed and the methodology of this chapter could be applied to control the C shape, as such the conclusions of this theory chapter are completely valid. The ability to control the C shape described by equations 4.14 and 4.18 is shown in figure 4.4 by overlaying different C shapes onto the  $(\alpha, D)$

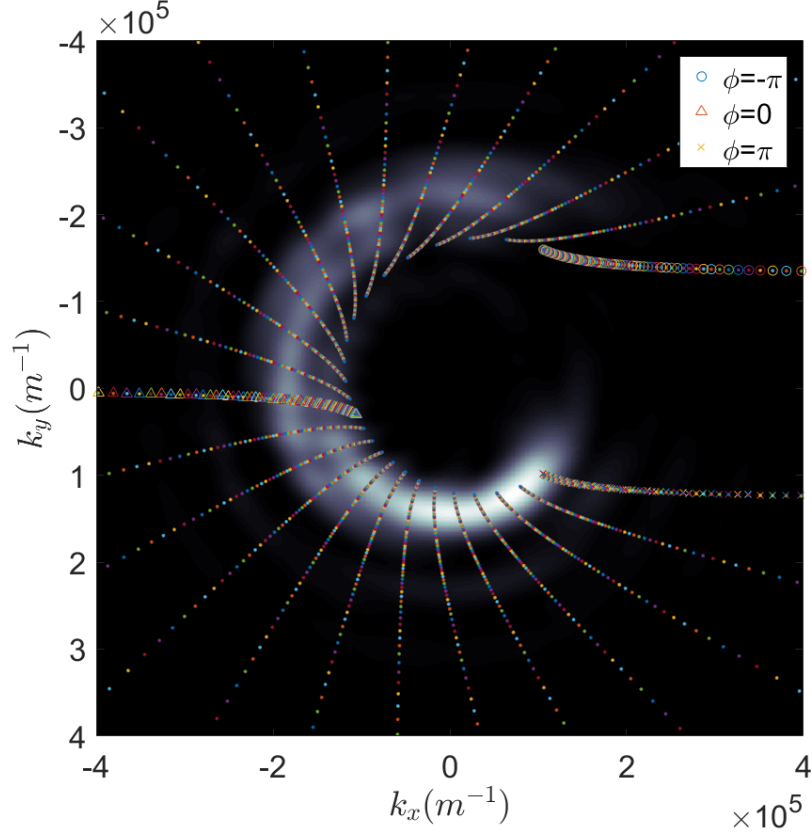


Figure 4.5: Markers are Fourier plane points representing local spatial frequency analysis of mask plane phase gradients, including Fresnel propagator phase terms. The different coloured groups are phase gradients from constant mask plane radius. The phase gradient points from key mask plane angular co ordinates are shown by circles ( $\phi = -\pi$ ), triangles ( $\phi = 0$ ) and crosses ( $\phi = +\pi$ ). The greyscale colour is the corresponding Fourier plane intensity. The propagation distance is  $10\delta z$  where  $\delta z = L^2\lambda_e/(2\pi R_{max})^2$ .  $L = 0.016m$  is the camera length,  $\lambda_e = 2.5 \times 10^{-12}m$  is the electron wavelength and  $R_{max} = 15 \times 10^{-6}m$  is the aperture radius.

plane. One can collect  $(\partial\psi/\partial x, \partial\psi/\partial y)$  Fourier plane co ordinates from sampled  $(\bar{\rho}, \phi)$  mask plane. Representing each image plane co ordinate as a dot adds some intensity produced by the local phase gradient in the mask plane point. Showing many of these dots from evenly sample positions on the mask plane allows the shape of the Fourier transform intensity to be predicted. An additional Fresnel term can be added to the local spatial frequency derivation to predict the intensity away from focus too ( figure 4.5). As described in chapter 1 section 1.5.2, this Fresnel term only affects

the radial phase gradients such that

$$U = (m + c\bar{\rho})(\phi - \phi_0) + (\pi\bar{\rho}^2\lambda z) \quad (4.19)$$

$$\frac{\partial U}{\partial \bar{\rho}} = c(\phi - \phi_0) + 2\pi\bar{\rho}\lambda z \quad (4.20)$$

where  $\lambda$  is the electron wavelength and  $z$  is the defocus distance from the Fourier plane.

#### 4.1.2.1 Controlling Fourier plane intensities

Using the equations derived in the previous sections it is now possible to show the control of the Fourier plane intensity structure using the parameters  $\alpha$  and  $D$ . When the defocus value is 0 the Fresnel propagator goes to a factor of 1 and thus the at focus intensity distribution is the direct Fourier transform of the mask plane wavefunction. Figure 4.6 shows examples where the analytic control equations of section 4.1.2 have been used to produce simulated intensities with a controlled opening angle and size.

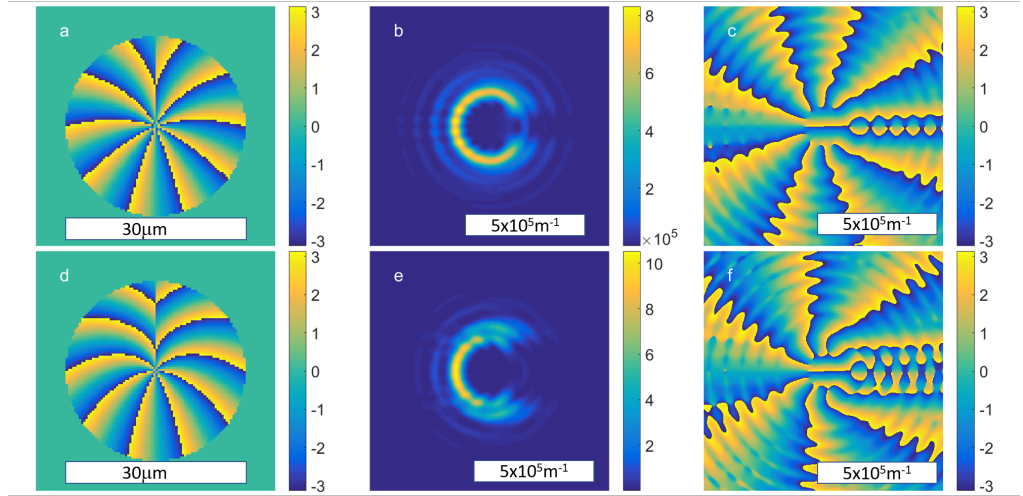


Figure 4.6: The Fourier plane amplitude (a,c) and phase (b,d) for  $m=1.7119$   $c=8.2881$  (a,b) and  $m=3.8839$   $c=6.1161$  (c,d) for a mask of radius  $15\mu\text{m}$ . Axes are from  $-5 \times 10^5\text{m}^{-1}$  to  $5 \times 10^5\text{m}^{-1}$

This plot shows that the gap in the at focus intensity is due to the build up of vortex anti vortex pairs along a radial line from the center. The increase of the ratio  $m/c$  causes more vortex anti vortex pairs to stack up above and below this radial line thus opening the C gap to larger angles (as can be seen in figures 4.6 f and 4.7 b ). This ability to produce larger

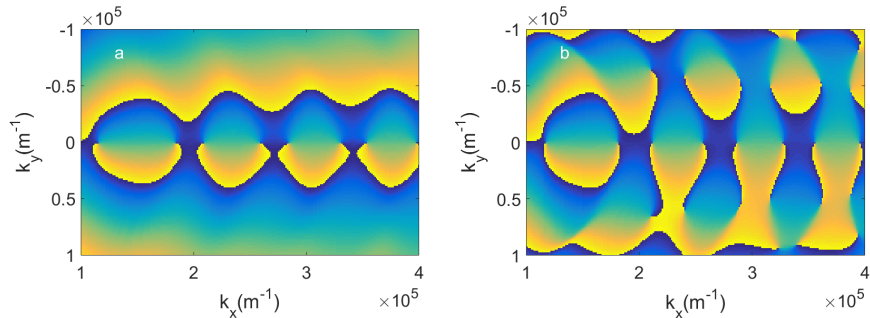


Figure 4.7: A magnification of the the phase distribution in the gap of the same C shapes as in figure 4.6. a)  $m=1.7119$   $c=8.2881$  and b)  $m=3.8839$   $c=6.1161$  .

opening angles is shown in figure 4.4 along with the ability to independently control the size of the C shape. When angles above  $2\alpha = 100^\circ$  are used the C shape begins to form a cusp and the intensity becomes much more concentrated half way around the C curve, with oscillations in intensity around the curve due to interference between different OAM mode components. This type of intensity oscillation for larger  $\alpha$  angles can be seen with a comparison of the two ends of path B in figure 4.4.

### 4.1.3 Astigmatism effect on C shape

When the phase in the mask plane has an astigmatism term  $\chi = 2\pi A\bar{\rho}^2 \cos^2(\phi + \phi_a)$  added to the phase structure, the C shape produced is distorted.  $A$  is a constant which determines the strength of astigmatism and  $\phi_a$  is an angle determining the offset between the astigmatic axis and the phase distribution. For a circularly symmetric vortex the direction of the astigmatic axes would not alter the intensity pattern, except for a simple rotation. For the C-shape intensity however the alignment of the astigmatic axis with the opening also varies the intensity pattern observed. As shown in figure 4.8 vortices of opposite OAM are distorted along different directions for the same astigmatic phase alteration. The patterns produced in the focal plane of such astigmatic integer vortex phase masks produce chiral intensity patterns which are related to one another by a reflection and a

rotation of  $90^\circ$ . The ideal circle is now compressed along an axis, the direction of this compression depends upon the axis of astigmatism (determined by  $\phi_a$ ) and the sign of the topological charge. When the same procedure is applied to C-shaped beams the compression axis for one order is parallel to the opening (C image in fig 4.8) whilst for the opposite sign C it is perpendicular to the opening (D in fig 4.8). The distorted C-shapes produced in this way are 2D chiral intensity patterns. In general the effect of the astigmatic phase deforms positive and negative C-shaped diffraction orders into different shapes however, for C-shapes the astigmatic intensity produced by a positive diffraction order is the mirror image of the intensity from a negative diffraction order only when  $\phi_a = 0$ . In this case the relative deformations of the waves phase fronts are mirror images of one another.

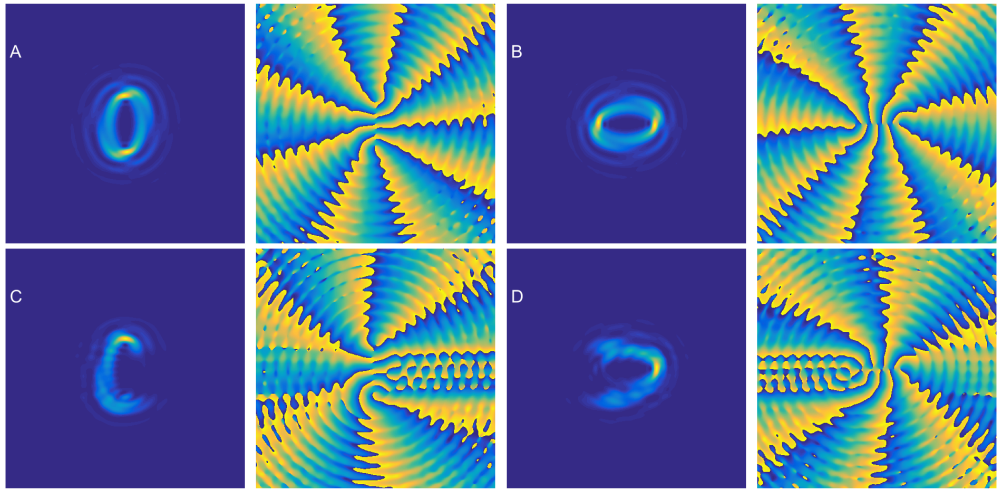


Figure 4.8: *Amplitude (left) and phase (right) distributions for astigmatic beams with  $A = -0.8$  for: A)  $m = 0, c = +9$ , B)  $m = 0, c = -9$  C)  $m = 3.889, c = 6.1161$ , D)  $m = -3.889, c = -6.1161$ . The astigmatic axis is set to  $45^\circ$  to the vertical. There is mirror symmetry for integer topological charge but there is no longer any symmetry between the  $\pm$  diffraction orders for the C-shaped beam.*

The lack of mirror symmetry for the intensities produced when applying an astigmatic phase to the mask plane can be explained by considering the effect of a phase delay. Opposite diffraction orders will be mirror images of one another in the plane which cuts the mask phase discontinuity. The mirror symmetry of opposite topological charges necessarily inverts phase gradients normal to the mirror plane. This can be

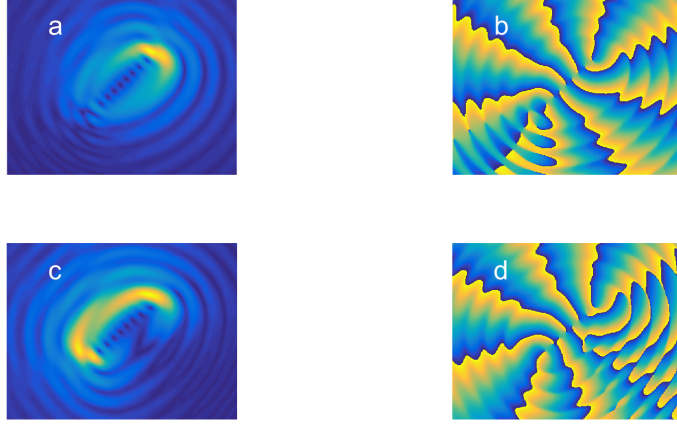


Figure 4.9: When adding astigmatism ( $A=1$ ) to a 50:50 superposition of  $l=8$  and  $l=9$  the Fourier plane intensity pattern depends on the relative phase offset between the two modes. The amplitude (a,c) and phase (b,d) for a phase offset of 1.1541 rad (a,b) and 2.6928 rad (c,d).

explored expressing each C shape as a summation of integer vortex beams with amplitudes  $A_m$  and phase offsets  $\theta_m$ .

$$C_+ = \sum_m A_m e^{im\phi} e^{i\theta_m} \quad (4.21)$$

$$C_- = \sum_{m'} A_{m'} e^{im'\phi} e^{i\theta_{m'}} \quad (4.22)$$

$$= C_{+mir} = \sum_m A_m e^{-im\phi} e^{i\theta_m} \quad (4.23)$$

where the subscript *mir* implies reflecting in the mirror plane, and similarly the Fourier transforms form a mirror pair

$$FT(C_+)(\mathbf{k}) = FT(C_-)(\mathbf{k}_{mir}) \quad (4.24)$$

and opposite C shapes are related by a reflection. However when imposing an astigmatic phase  $\chi$  on the Fourier transforms, which is the same for each beam

$$FT[C'_+(\mathbf{k})] = FT[C_+(\mathbf{k})e^{i\chi(\mathbf{k})}] \quad (4.25)$$

$$FT[C'_-(\mathbf{k})] = FT[C_-(\mathbf{k})e^{i\chi(\mathbf{k})}] \quad (4.26)$$

$$FT[C'_-(\mathbf{k}_{mir})] = FT[C_+(\mathbf{k})e^{i\chi(\mathbf{k}_{mir})}] \quad (4.27)$$

and now the beams are in general no longer conjugate versions of each other and the mirror symmetry is broken. A special case occurs when the additional phase distribution has the same symmetry as the initial phase i.e.

$\chi(\mathbf{k}) = \chi(\mathbf{k}_{mir})$ . For integer vortex states the rotational symmetry means that the discontinuity can always be rotated to match the astigmatism, as such the astigmatic integer vortices of opposite topological charge will be related by a reflection. This can only occur for one orientation of the astigmatic phase ( $\phi_a=0$ ) for C-shaped beams and fractional vortices.

A simpler situation is shown in figure 4.9 when a combination of  $l = 8$  and  $l = 9$  integer vortices are Fourier transformed, including astigmatism. There is a phase delay included between the two modes in the mask plane. By varying this phase delay the type of intensity pattern can be altered as shown for a phase delay of 1.1541 rad and 2.6928 rad. Including a phase delay alters the angle of the line along which the phase of the  $l = 8$  will be equivalent to the phase of the  $l = 9$  mode. It is the angle between this line and the astigmatic axis which will determine the pattern caused in the focal plane and for C beams of opposite order this is different except for when the astigmatic axis is aligned with the phase discontinuity in the mask plane.

#### 4.1.4 Fresnel propagation simulations

To calculate the propagation of a wavefront over short distances relative to the wavelength of radiation used close to focus, the Fresnel principle can be applied, where each point on the wavefront is considered to be a source of spherical waves. The wavefront at a distance further along the propagation axis is then defined by the integral of all the contributions from wavefront oscillations which occurred previously in time. As was shown in chapter 1 section 1.5.2 a Fresnel type analysis leads to the equation for a propagated wave

$$\psi(x, y, z + dz) = FT_{\perp}(FT_{\perp}(\psi) \times \exp(i\pi\lambda(k_{\perp})^2 dz) \quad (4.28)$$

where  $FT_{\perp}$  is the two dimensional Fourier transform in the plane perpendicular to propagation and,  $k_z \approx k_0$  from the paraxial approximation. Simulations can predict the intensities found at specific angles, however experimentally these angles will be mapped to distances depending on the effective camera length, following a right angled triangle with the camera length as the adjacent side and the distance as the opposite side.

Using experimental data the camera length of the microscope used (2200fs in TEM mode) was calculated to be  $0.016m$  when forming an image from the condenser aperture onto the sample plane. The method to find the camera length was to record the intensity distribution of a linear grating and C-shaped mask. The recorded separation,  $d$ , of the +1 and -1 orders, were then compared with with the calculated angles  $\theta$  (found in the paraxial approximation from the wavevectors). This method follows the diagram shown in figure 4.10. The effective camera length  $L$ , is then calculated

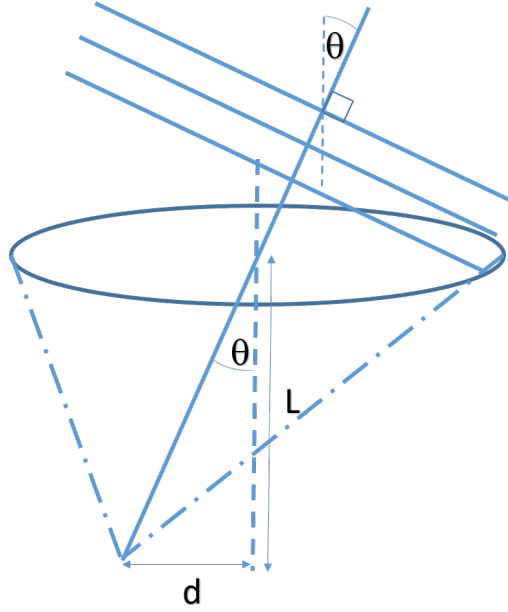


Figure 4.10: A plane wave incident on a lens, at an angle  $\theta$  to the lens optical axis, will be focused by a an optical system to a point in the focal plane with a distance from the beam axis , $d$ , dependent on the effective focal length, known as the camera length, of the lens system,  $L$ .

using right angled triangles and the equation  $L = d/\sin(\theta)$ . In simulations a separation of  $1.65E - 6$  radians (found by dividing the wavenumber by  $1/\lambda_0$ ), was experimentally measured (for the condenser aperture amplitude mask) as  $26.56nm$  this gives a camera length of  $26.56E - 9/\sin(1.65E - 6) = 0.016m$ . Using a camera length of  $0.016m$  the simulated propagation can be calibrated to reflect the distances predicted for the experiments in chapter 5. To compare different optical systems, the distance from focus is commonly transformed into normalised units[124] [125]

$$b = 2\pi N \frac{z/L}{1 + z/L} \quad (4.29)$$

where  $N = R_{max}^2/\lambda L$  is the Fresnel number of the optical system,  $R_{max}$  is the aperture radius and  $z$  is the propagation distance from the focal plane . As such in the simulation defocus value range in the simulations was  $\pm 30\delta f$  where

$$\delta f = L/2\pi N = L^2\lambda_e/(2\pi R_{max}^2) \quad (4.30)$$

By using a scale of  $\delta f$  the normalised units are then the  $z/\delta f$  multiplied by a  $1/(1 + z/L)$  factor. For the the TEM mode experimental conditions of chapter 5 equates to  $\pm 13.58\mu m$  above and below focus.

#### 4.1.4.1 Simulated vortex trajectories

It is interesting and illuminating to investigate the trajectory of phase singularities in the simulated propagation. Phase singularities are found by applying the following algorithm in the matlab code:

1. Check if the phase at the current pixel and the pixel to the left has a difference of more than  $\pi$ .
2. Check if the phase at the current pixel and the pixel above has a difference of more than  $\pi$ .
3. Set any pixels for which step 1 and step 2 are true to 1 , set all other pixels to 0. This forms lines from the pixels with a value of 1.
4. Use MATLAB built in code to find the endpoints of the lines produced by step 3

This algorithm produces a binary array for each defocus value with dots at each phase singularity. To save memory by working with a single array (which helps when visualising the data), this binary array of phase singularities ( $PS$ ) can be added to the normalised intensity of the complex wavefunction,  $NI$ , (normalised to maximum intensity pixel at focus) to give the total intensity image ( $TI$  following the equation

$$TI = 0.5NI + 0.5PS \quad (4.31)$$

This produces an image ( $TI$ ) with the phase singularities overlapped onto the intensity distributions. The intensity is normalised by

dividing by the maximum intensity for the image corresponding to a defocus of 0. These overlapped images are then saved together in a tiff stack file. This can be rendered by ImageSurfer2 software [126], as described in appendix chapter A section A.5 . Below are renderings of initially an  $l = 9$  vortex shown in figure 4.11 and then the C-shaped beam propagation shown in figure 4.12 formed by the method described above. Figure 4.11 a

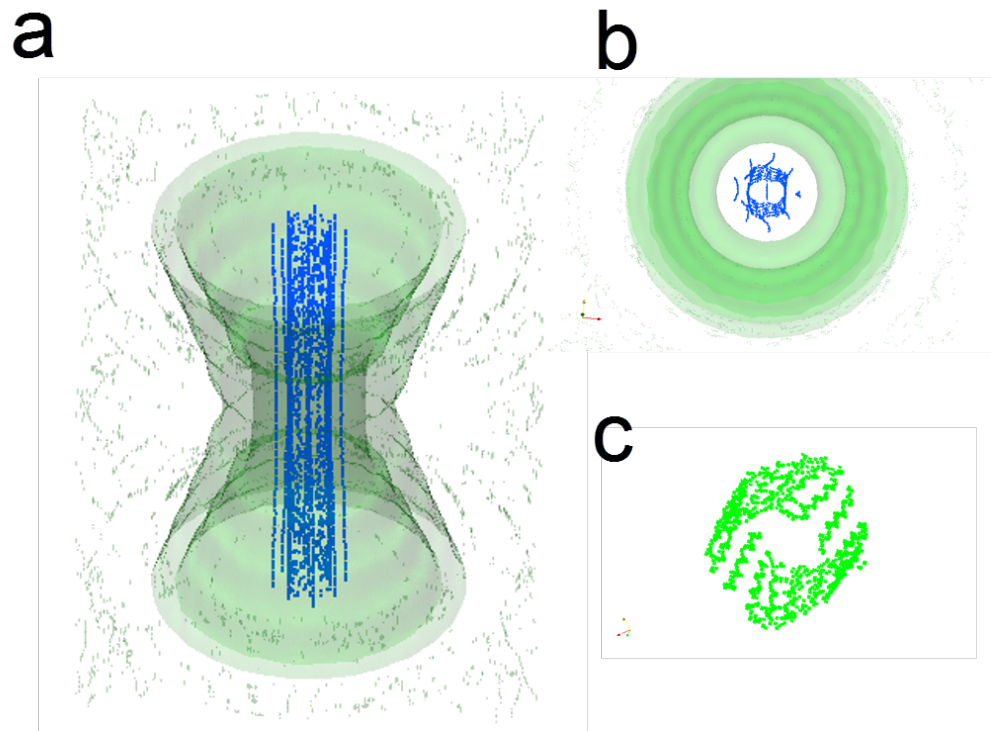


Figure 4.11: *The simulated propagation of an  $l = 9$  vortex, the transparent green volume is the high intensity region (i.e. the vortex ring). The blue lines are the nodal lines tracing phase singularities and the green dots outside the volume are phase singularities outside the vortex ring. a) a side on view with propagation up and down. b) a top down view along the propagation direction. c) The collection of phase singularities which are visible in (a) and (b) inside the ring, but which can be considered as artefacts of the simulation, they form pairs which come together to annihilate each other only to reform at larger  $z$ .*

shows a side on view of the propagation of an  $l = 9$  vortex beam, the beam propagation direction is vertically downwards on the page. The green volumes for a structure which has circular cross sections of increasing radius away from focus. The blue lines correspond to phase singularities. Figure

4.11 b shows a view along the propagation direction, here it can be seen that there is an outer collection of 8 blue lines with one central line, all of which slowly rotate causing a projection onto the end on view which is a small curved line. The presence of separate  $l = 1$  phase singularities is consistent with previous findings that higher order  $l > 1$  vortices are unstable upon propagation and break up into multiple  $l = 1$  vortices [127]. There is also an inner collection of blue lines which oscillate more and figure 4.11 c shows the spatial distribution of this collection on its own looking at a slight angle, mostly along propagation. These form pairs of opposite topological charge which constantly form and then annihilate along the propagation direction and do not add any OAM to the beam. These pairs are artefacts of the simulation and are related to the use of an aperture, which restricts the high frequency components reducing the Fourier plane phase gradients possible as well as the limited resolution of the arrays. This  $l = 9$  simulation acts as a check for the simulation procedure for Fresnel diffraction and shows that the method does not add any additional OAM and captures the focusing trends of the ideal vortex. Figure 4.12 shows the focal plane phase and intensities as well as the propagation renderings for both a C shaped beam and a 'non-vortex' beam found via iterative methods. Figure 4.12 c presents a similar rendering for a C-shaped beam. In figure 4.12 c the green volume highlights regions of highest intensity and blue or red lines show the position and trajectories of phase singularities. It can be seen that there is also a collection of phase singularities (blue lines in figure 4.12 c ) which propagate along with the beam and that the opening is maintained throughout propagation whilst undergoing a slow rotation. This rotation can be explained by considering the varying Gouy phase that each individual OAM component in the C beam will have. Any arbitrary field can be described by decomposing into a basis set of vortex states with different OAM. When one OAM component gains a larger phase than another, the angles for which the two destructively interfere rotates, thus rotating the low intensity gap. This is similar to the analysis of superpositions of vortex modes as shown by Baumann et al.[128] This is the same effect shown by the application of an astigmatic phase in figure 4.9, where altering the phase delay causes a rotation of the area of low intensity in the Fourier plane. The full analysis of the OAM components present, in a C-shaped Fourier plane function, will be shown in section 4.1.9.2. The slow rotation of mode combinations can be seen for an example of an equal mix of  $l = 9$  and  $l = 8$  in figure 4.13. For this mixture, at focus, there is a C like shape however this is not maintained for the same propagation

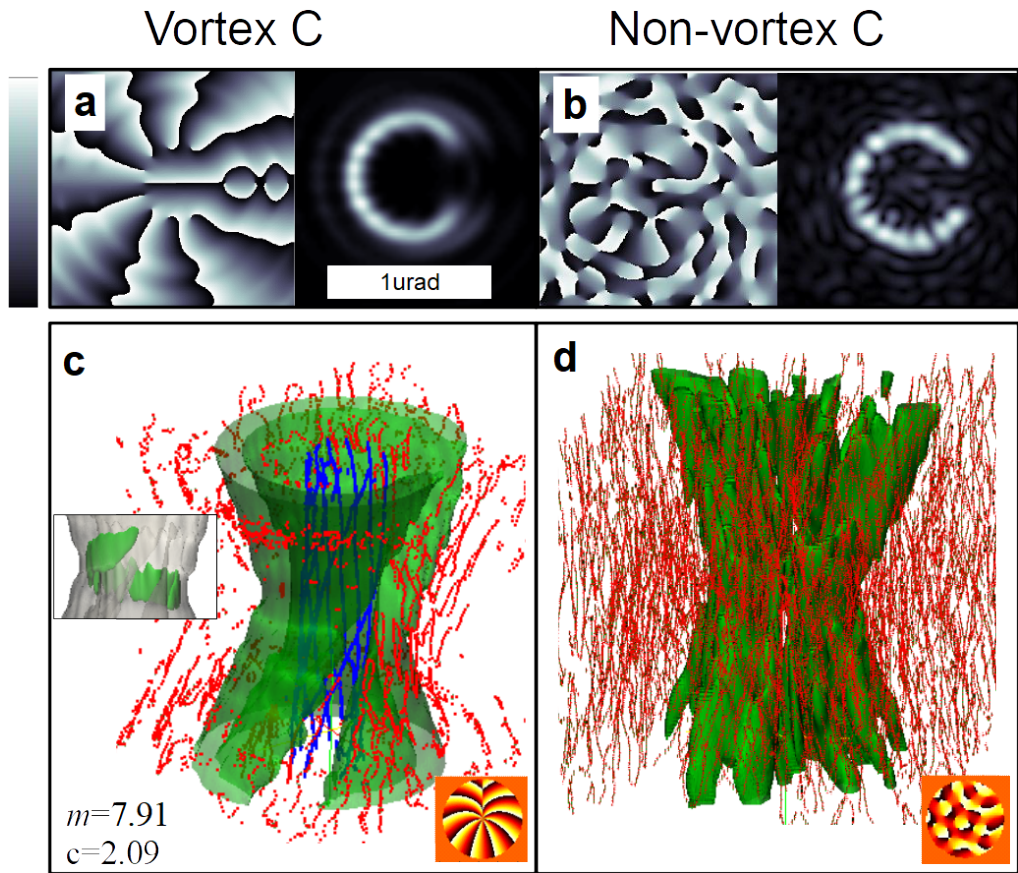


Figure 4.12: *At focus phase and intensities (a and b) with simulated propagation (c and d) for a vortex C beam (left) and the non vortex iterative algorithm result (right). (Scale bar in i applies to i and ii and is 1  $\mu$ rad, calculated for a mask of 30  $\mu$ m and an electron wavelength of 2.5 pm traveling  $\pm 13.58 \mu$ m either side of the focal plane). In c and d the propagation is vertically downwards, the green volumes show regions of high intensity in c) this shows a gap which rotates whilst in d) the intensity disperses away from the focal plane. The blue or red lines are positions of phase singularities, in c) a group shown in blue travel along with the C shape giving it OAM , however no such group is found amongst the numerous phase singularities in d.*

distance as in figure 4.12. This shows that the specific combination of components with varied OAM is what allows the C beam to maintain the gap as it propagates.

As can be seen from figure 4.12 there are a collection of vortex nodal lines that propagate along with the C beam which are indicative

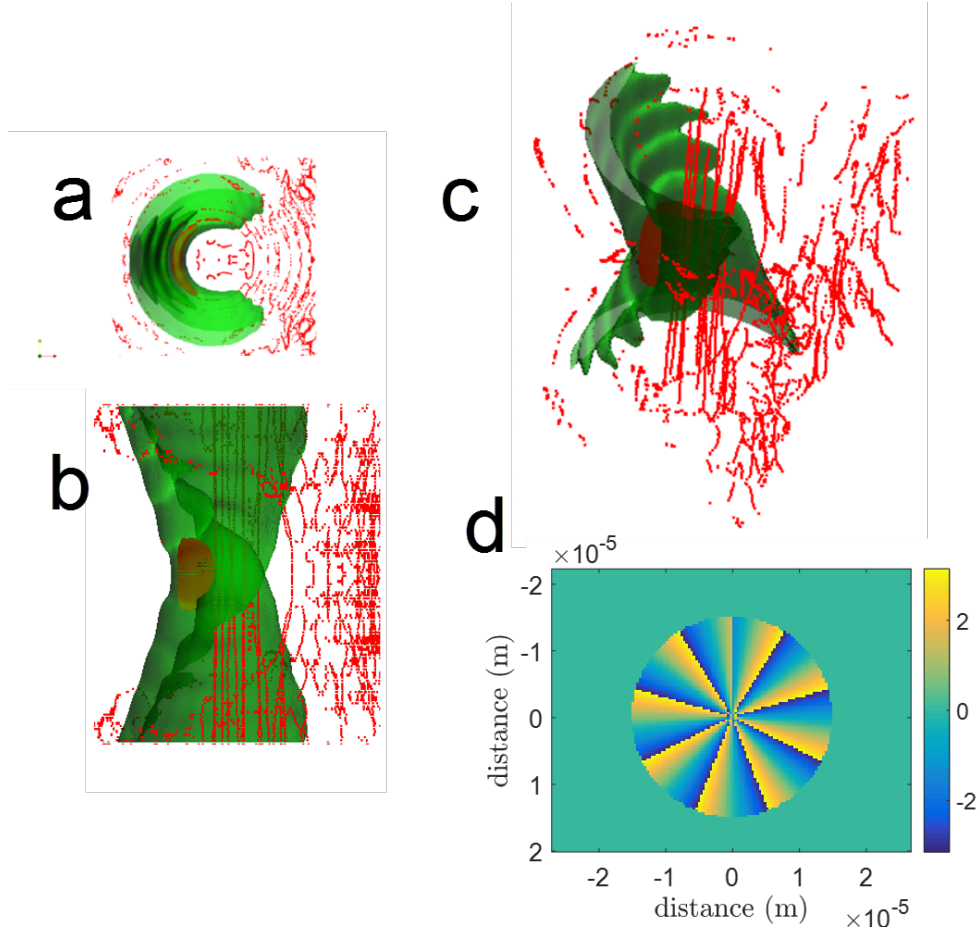


Figure 4.13: *The propagation of an equal mixture of  $l = 8$  and  $l = 9$  vortices at the mask plane. The green volumes are high intensity regions and the red lines are phase singularities. The red inner volume is the highest intensity region. a) a view along the beam axis b) a side on view and c) an angled side on view. d) the phase mask used to produce the mixture.*

of the presence of OAM within the beam. This collection of nodal lines appears to allow the C-shaped intensity to remain intact during propagation as is the case for other beams containing OAM and phase singularities such as Bessel beams. The physical mechanism by which this is achieved is unclear and presents an interesting starting point for future theoretical research. The main section of the gap is caused by one vortex moving to a further radius than the others and thus reducing the intensity in the gap section of the ring.

### 4.1.5 Iterative Fourier transform algorithm comparison

The analysis in sections 4.1.4 and 4.1.9 has also been applied to the results of an iterative Fourier transform algorithm (IFTA) method (see section 3.6.1). The IFTA method uses a target intensity distribution  $I_t = (R < C_{out})(R > C_{in})(|\phi| > \pi/4)(1 - (|\frac{R-R_{av}}{diff}|)^2)$  where  $C_{in}$  and  $C_{out}$  are inner and outer radii,  $R_{av} = (C_{out} + C_{in})/2$  and  $R_{diff} = (C_{out} - C_{in})/2$ . This target intensity is shown in figure 4.14 and is used in the iterative algorithm detailed below.

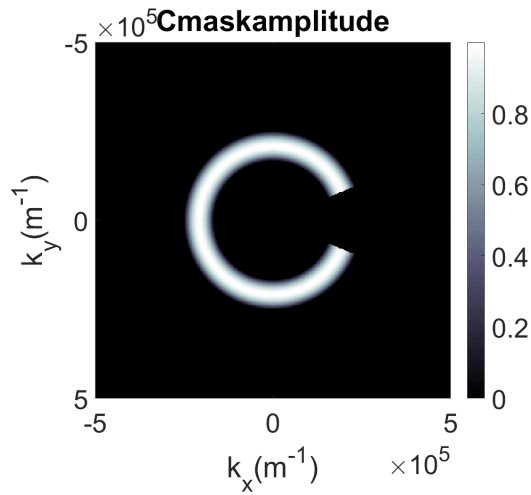


Figure 4.14: *The target intensity distribution used for the iterative Fourier transform algorithm.*

This was applied to a C-shaped intensity distribution by using an input intensity defined for step 1 by  $(R - R_{Av})/(R_{out} - R_{in})$  where  $R_{av} = (R_{out} + R_{in})/2$  (this is shown in figure 4.14). The parameter used to check the convergence of the algorithm was  $\sum |I_{res} - I_{tar}|$  where  $I_{res}$  and  $I_{tar}$  are the squared amplitudes of the complex fields in the current result field and the target field respectively. The code was ran for 2000 iterations above which this fitting error parameter did not significantly decrease. Using the methods described in sections 4.1.4 and 4.1.9 the resulting mask can be put into the MATLAB code used for the analysis of C-shapes and the propagation of the beam around focus can be compared to the C-shape described earlier.

The main findings when analysing the C-shaped intensity are that this C-shaped wave has predictable OAM, a controllable opening angle and

shows a slow rotation upon propagation. There are several key differences between the C-shape and the 'non-vortex' IFTA results as can be seen by a comparison of figure 4.12 c and d. The iterative method produces an intensity (green regions) which spreads out within shorter distances away from focus and breaks up without maintaining a similar intensity pattern. For the C-shape there are core phase singularities which are not present in the iterative method these could be responsible for the reduced spreading by some form of self-reinforcement however the exact physical mechanism by which this is achieved is unclear.

#### 4.1.6 Low intensity in the gap

The low intensity in the gap of the C shape is shown in figure 4.15, there is a clear peak in the azimuthal and radial plots at low intensity. This is also shown experimentally with a line of higher intensity connecting either side of the large gap within the overall comparably low intensity region. (see figure 5.5 in chapter 5). The sections of alternating intensity visible in figure 4.15 can be explained by looking at the phase gradients. These are shown in figure 4.16, where the direction of the local phase gradient is shown by the arrows, the length representing the amplitude of the phase gradient. The alternating vortex-antivortex structure creates alternating areas of high and low intensity where the combination of alternating circulation directions either aligns with or against the overall circulation of the full C shape. This is shown in the relatively long or short phase gradient arrows. Phase gradients will determine how electron probability density flows, as such the longer phase gradients act to 'funnel' intensity away from areas of flatter phase, thus creating the higher intensity channels linking the top and bottom of the C shape.

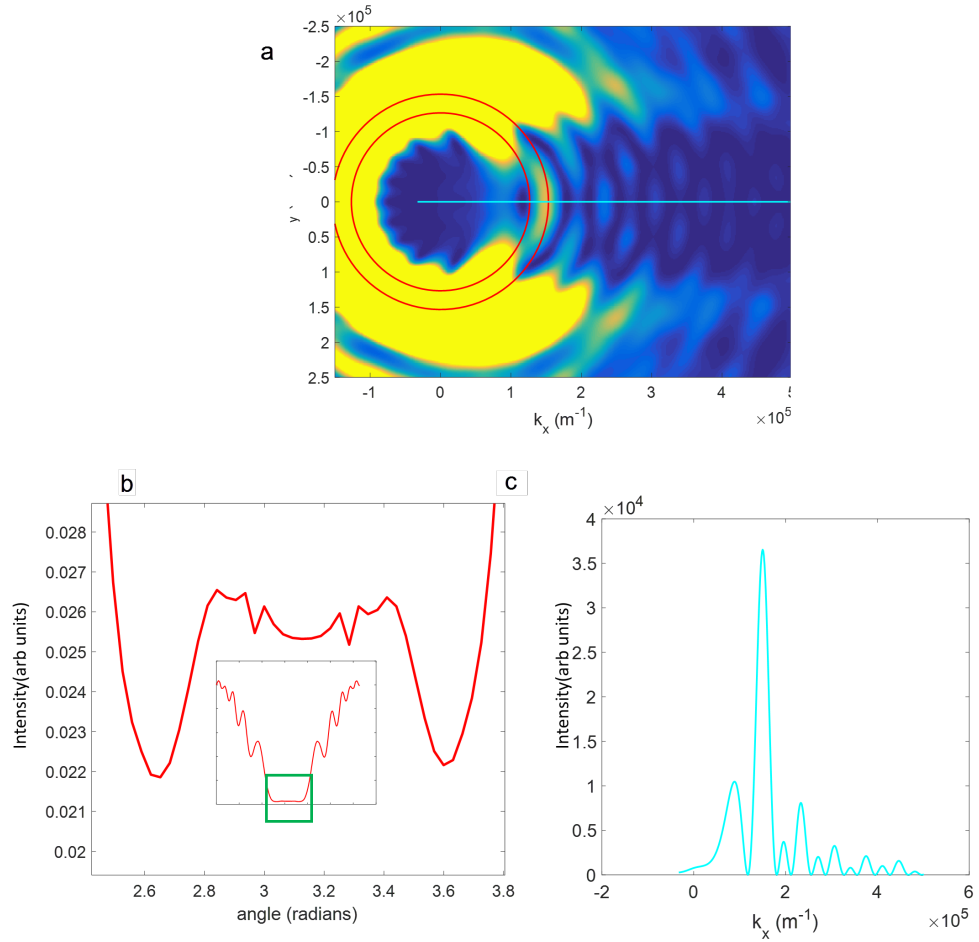


Figure 4.15: radial and azimuthal intensity distributions from a simulated C-shaped intensity distribution. a) Intensity distribution with azimuthal summation boundaries (red) and radial path (cyan). b) Angular intensity summed between the circular boundaries (inset shows entire  $2\pi$  range whilst main figure focuses on the gap area highlighted by the dashed green box). c) Radial intensity line plot along the cyan radial path.

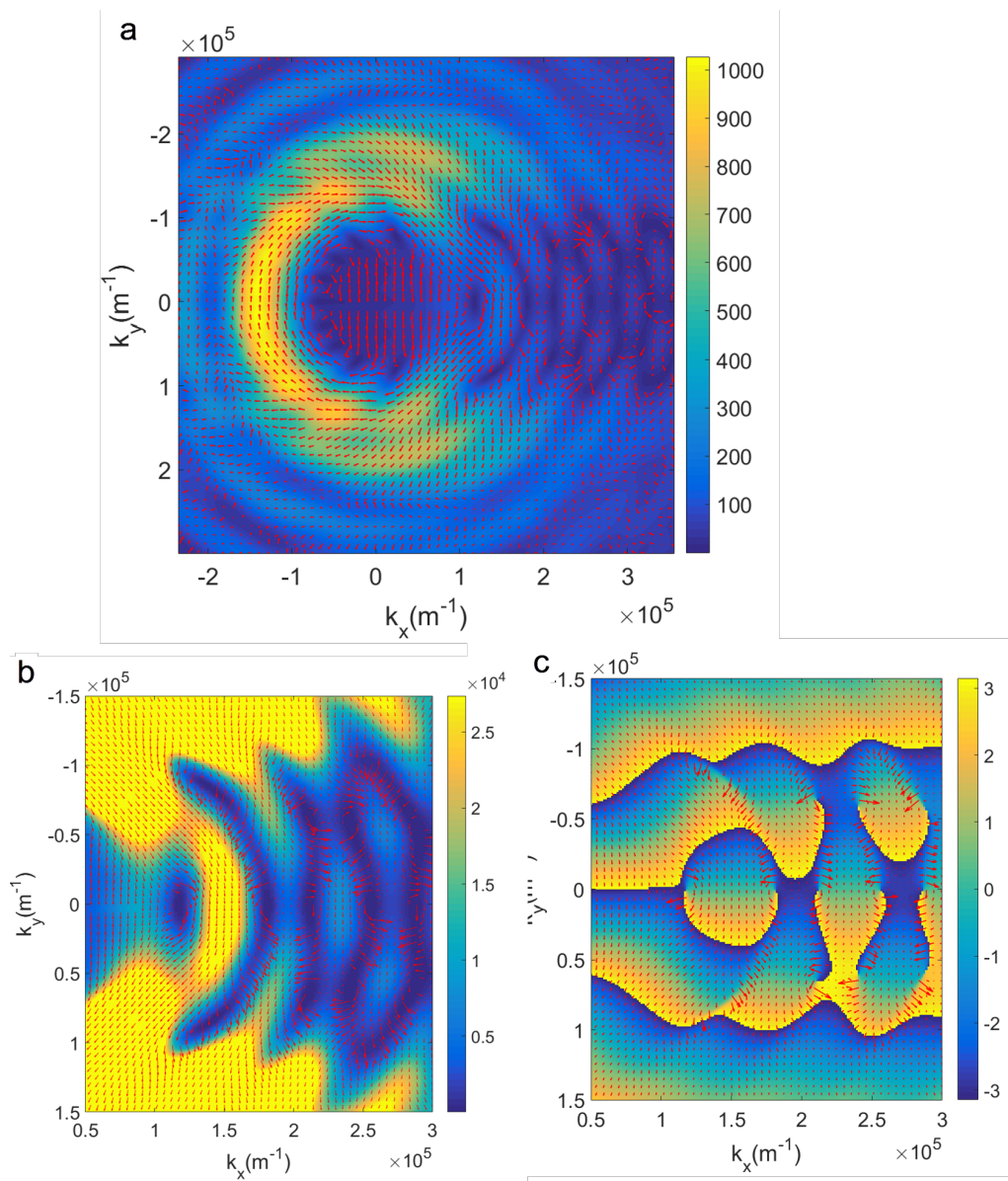


Figure 4.16: An overlay of phase gradients (arrows) with the simulated intensity (a,b) and phase distribution(c).

### 4.1.7 Comparison propagation of fractional and helico conical beams

Figure 4.17 shows simulated propagation for a fractional vortex with topological charge  $l = 8.5$  and a helico-conical beam [16] defined with  $m = 3$  and  $c = -3$ , in equation 4.1 and an angle defined between  $0$  and  $2\pi$ . The fractional vortex shows an opening away from focus in a spiral like shape and has a well defined set of vortices (blue and turquoise lines in figure 4.17) however at focus there is a high intensity instead of a low intensity gap. Conversely whilst the helico-conical beam does have a large opening and is a spiral at focus, it lacks a clear set of vortices with only one vortex (blue dots) following the beam center and the intensity is less constant as the beam propagates. By comparison, the C-shaped beam shown in figure 4.12 combines the well defined set of vortices, propagation stability and large opening size even at focus. These properties distinguish the C beam from previously published 'C-like' states as a new type of fractional vortex wavefunction.

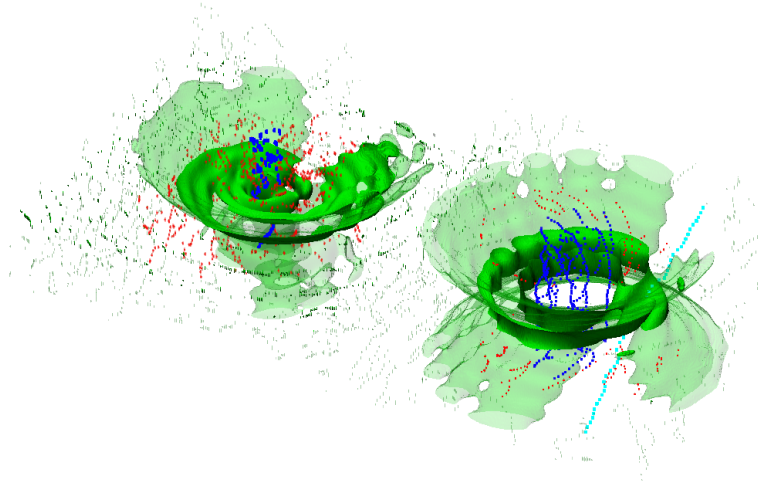


Figure 4.17: *Simulated propagation from  $-30\mu\text{m}$  to  $+30\mu\text{m}$  for helico-conical (left) and fractional topological charge  $l = 8.5$  (right). Assuming the same experimental conditions for a  $200\text{keV}$  electron with an optical system with a  $0.016\text{m}$  camera length. Green volumes enclose regions of high intensity, dots represent phase singularities. Dot colours are only for distinguishing trajectories .*

### 4.1.8 Interference around the C

As the angle  $\alpha$  or size  $D$  is increased the C shape shows an increased amount of oscillations in intensity around the arc of the intensity. This is shown in figures 4.18 and 4.19 .

In the upper part of figure 4.18 the azimuthal intensity is plotted for C shapes of increasing opening angle  $\alpha$ . The lower section shows the azimuthal images of the intensity in both  $(\rho, \phi)$  and cartesian plots for the 5 angles compared. Increasing  $\alpha$  increases the amplitude and the frequency of the oscillation in intensity around the C. This can be understood by the use of different OAM modes to create an opening, this produces a beating like interference effect between different topological charges. This effect becomes more pronounced as the opening is increased and the OAM distribution is less pure, as shown in figure 4.18. Figure 4.19 shows intensity plots for three different size of C all with  $\alpha = 22.5$ . The upper right shows the intensity plots as a function of angle, the lower shows the  $(\rho, \phi)$  intensity images and the left images are the cartesian co ordinate images. For larger D, modes of larger topological charge are used, producing larger rings which include more phase oscillations and as such the circumference increases allowing more maxima and minima to fit around the ring, shown in figure 4.19.

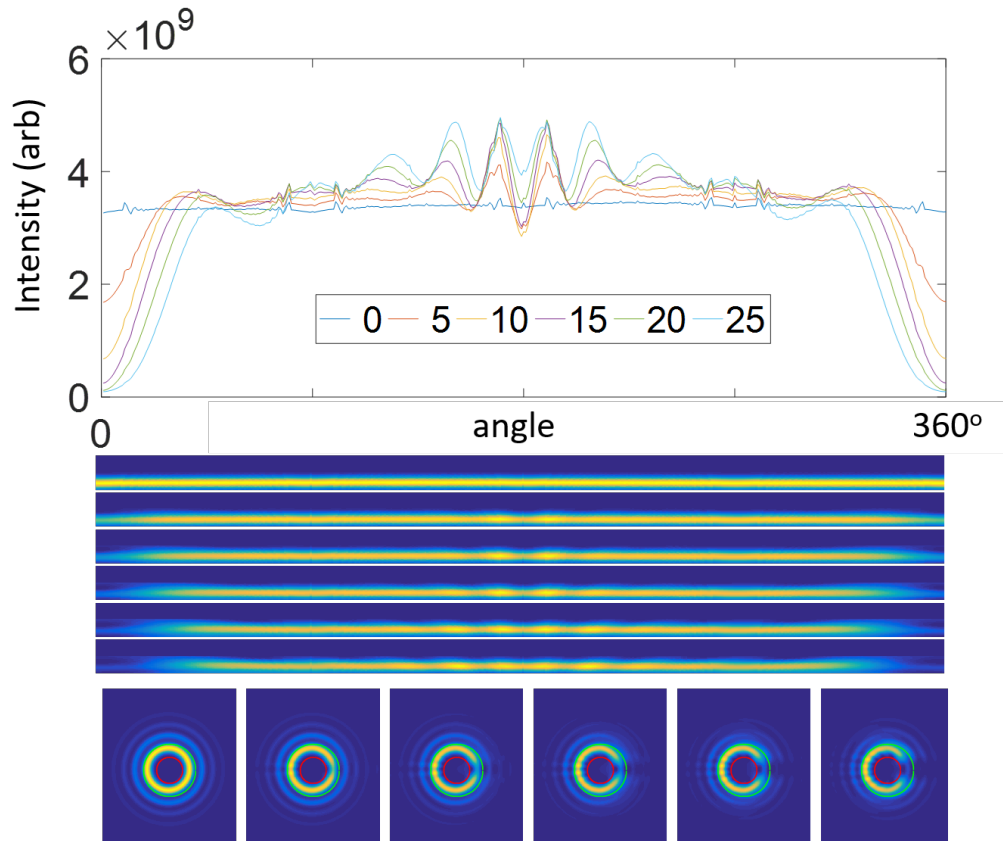


Figure 4.18: *The upper graph shows line plots of intensity found by summing the azimuthal intensity between the red and green rings in the lower C shape figures. The colour of the lineplot corresponds to the opening angle as shown in the inset key. The azimuthal intensity images in  $(\rho, \phi)$  coordinates is shown below for increasing angles (smallest opening angle on top with angle increasing for lower images), finally the cartesian co-ordinate images are shown for the 5 opening angles increasing from left to right . The intensity for the upper line plots was summed between the red and green rings on the lower cartesian images.*

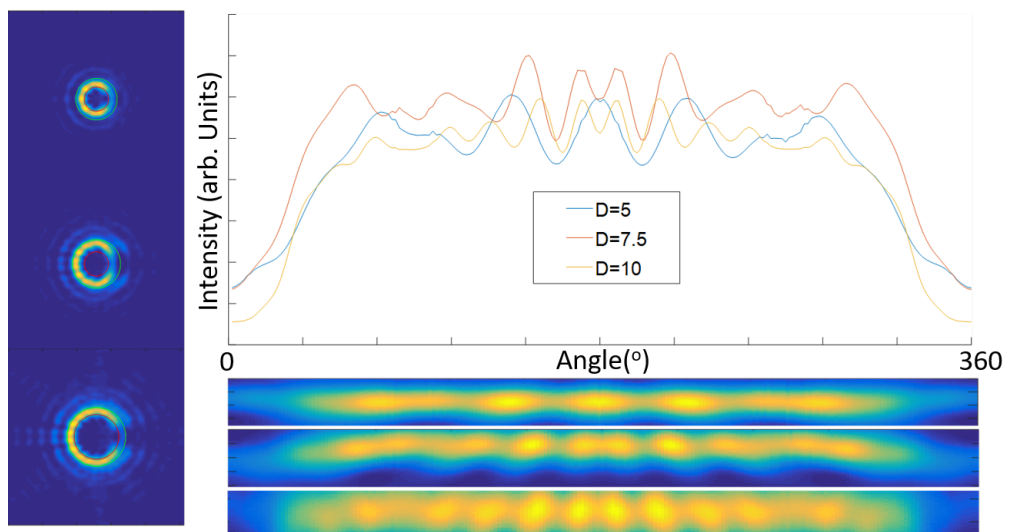


Figure 4.19: *The upper right graph shows line plots of intensity found by summing the azimuthal intensity between the red and green rings in the cartesian intensity figures to the left. The azimuthal intensity images in  $(\rho, \phi)$  co ordinate space for the radii between the green and red rings on the left images are shown below the line plots. The legend shows the value of  $D$  used.*

## 4.1.9 OAM analysis

### 4.1.9.1 Numerical and analytical integration

For vortices propagating in free space, OAM is conserved along propagation [26], so the OAM in the mask plane should be equivalent to the OAM in the Fourier plane. To check this an analytical OAM expectation value in the mask plane will be compared with a numerical integration in the Fourier plane.. The mask plane integral is as follows:

$$OAM = -i\hbar \frac{\int \psi * \frac{\partial}{\partial \phi} \psi dA}{\int \psi * \psi dA} \quad (4.32)$$

$$= \hbar \frac{\int_0^1 \int_0^{2\pi} \psi * (m + c\bar{\rho})\psi \rho_0 d\bar{\rho} \rho_0 \bar{\rho} d\phi}{\int_0^1 \int_0^{2\pi} \psi * \psi d\bar{\rho} \rho_0 \bar{\rho} d\phi} \quad (4.33)$$

$$= \hbar \frac{2\pi \rho_0^2 [m\bar{\rho}^2/2 + c\bar{\rho}^3/3]_0^1}{2\pi \rho_0^2 [\bar{\rho}^2/2]_0^1} \quad (4.34)$$

$$= \hbar [m + 2c/3] \quad (4.35)$$

This means that the  $c\rho\phi$  term only contributes 2/3 of the OAM that a  $c\phi$  term, without any radial dependence, would. To check the conservation of OAM between the mask plane and Fourier plane the amplitude and phase in the Fourier plane is required. There is not a simple analytical form for the wavefunction in the Fourier plane, however the OAM integral can be approximated by a numeric integration of the simulated wavefunction. This uses the MATLAB gradient function applied to the complex array. The OAM numeric integration of equation equation (4.32) is evaluated using the following algorithm:

1. The complex array from Fresnel propagation is used as the input wavefunction,  $\psi$
2. Calculate the complex conjugate  $\psi^*$ , using built in matlab function `conj`
3. Apply matlab gradient as  $[\nabla\psi_x, \nabla\psi_y] = \text{gradient}(\psi, dk_x)$  where  $dk_x$  is the separation of array elements in reciprocal space in the Fourier plane.

4. These gradients are then converted into azimuthal gradient components by multiplying components by the Fourier plane reciprocal space radius,  $KR$ , in  $m^{-1}$ 

$$\nabla\psi_\phi = KR. * (\nabla\psi_x\cos(\theta) - \nabla\psi_y\sin(\theta));$$
5. The integrand is formed by using these wavevectors along with  $\psi^*$  from step 2 using  $\psi^*\frac{\partial}{\partial\phi}\psi dA = \psi^*\nabla\psi_\phi(dk_x^2)$ ;
6. The integration is performed by using the function trapz in MATLAB

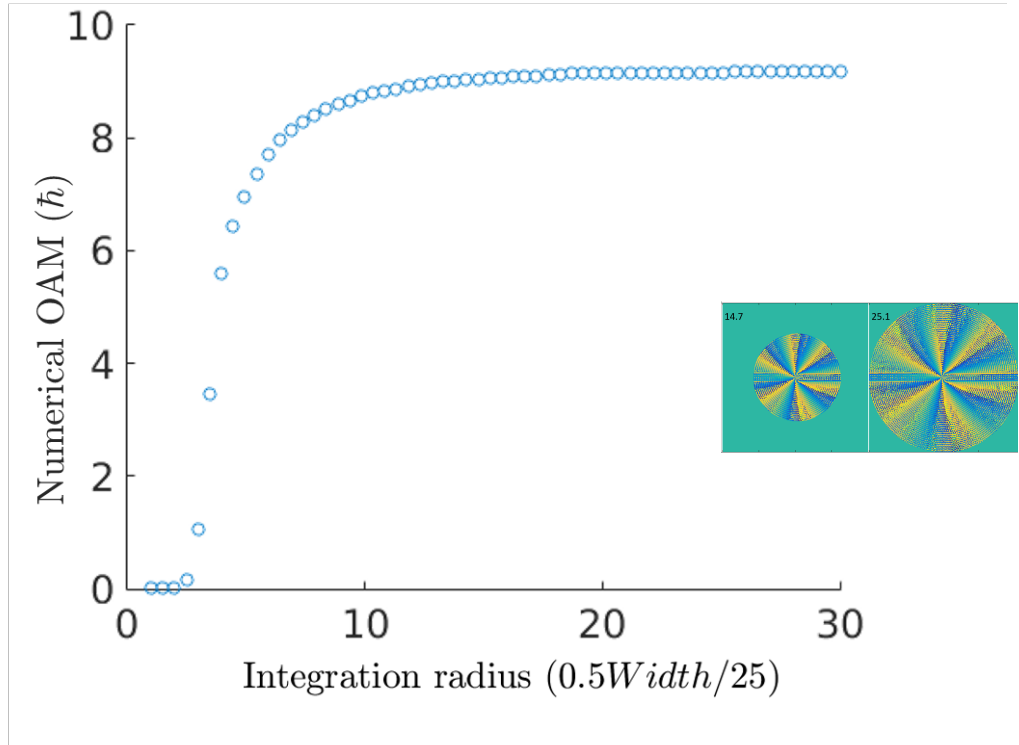


Figure 4.20: *The calculated numerically integrated OAM as a function of the integration radius in the Fourier plane for the C-shaped intensity. (inset: the integration radius for xaxis values of 14.7 (left) and 25.1 (right) ). The horizontal axis is the integration radius in units of  $(1.3653E+06/50)$  where a value of 25 indicates a circular integration radius with a diameter equal to the simulated array width (as shown in the insets). The vertical axis is predicted OAM in units of  $\hbar$ .*

An aperture is used to set the amplitude of  $\psi$  to 0 outside of a circular aperture, thus the numerical integration is only evaluated within a circular region of the Fourier plane, enclosing the C-shape. The total OAM result

depends on the exact radius of the aperture chosen, as shown in figures 4.20 and 4.21. For smaller integration radii the phase gradients are not large and the total OAM is small and close to 0. As the integration radius is increased it begins to include the azimuthal phase variations and the OAM rapidly increases up to  $> 8\hbar$  for the C shape in figure 4.20 but only  $1.4\hbar$  for the iterative result in 4.21. For both figures 4.20 and 4.21, above an integration radius of about  $10 \times 0.5/25 = 1/5$  of the array width the integration radius only includes phase oscillations which are due to the finite width of the mask plane array. These do not add significant OAM and the integrated OAM result plateaus.

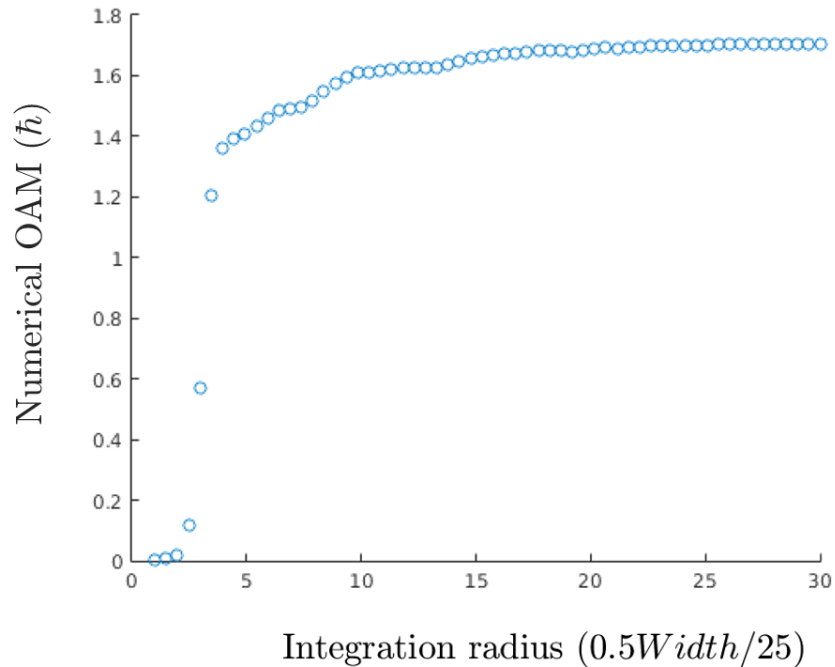


Figure 4.21: *The calculated numerically integrated OAM as a function of the integration radius in the Fourier plane for the intensity from the IFTA. The x axis scale is as defined for figure 4.20.*

There is an extremely close match between the analytic and numeric results (as shown by the matching red and blue lines in figure 4.22), providing evidence for the conservation of OAM between the mask plane and the Fourier plane which implies the conservation of OAM during propagation of the C-shaped beam.

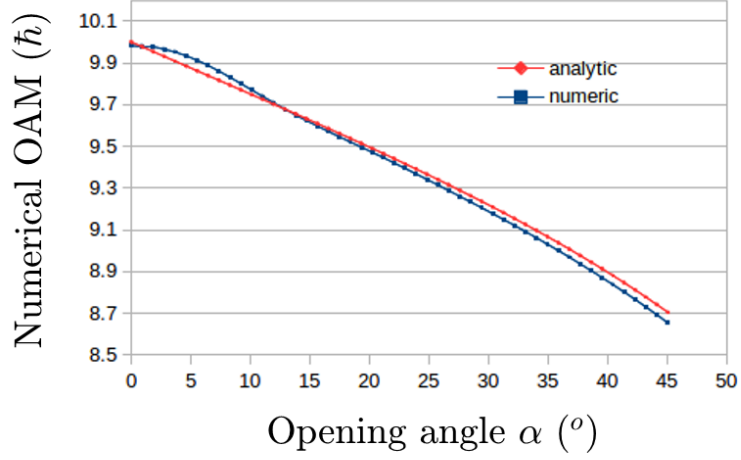


Figure 4.22: The predicted OAM from both mask plane analytic integration and Fourier plane numerical integration, as a function of opening angle.

#### 4.1.9.2 Mode decomposition

To fully characterise the C-shaped beam, one can calculate the overlap integral with Laguerre-Gaussian (LG) modes defined by the complete basis set functions

$$\begin{aligned}
 LG_{p,l} = & e^{ik_z z} \frac{N}{\sqrt{z_R^2 + z^2}} L_p^l \left( \frac{2\rho^2}{\omega^2(z)} \right) \frac{e^{il\phi}}{w(z)} \left[ \frac{\rho}{w(z)} \right]^l \\
 & \times \exp \left( i \frac{k_z \rho^2 z}{2(z_R^2 + z^2)} - \frac{\rho^2}{w^2} - i\delta_{Gouy} \right)
 \end{aligned} \tag{4.36}$$

where  $l$  is the azimuthal mode index and  $p$  is the radial mode index,  $w(z) = w_0 \sqrt{1 - \frac{z^2}{z_R^2}}$  is the distance away from the beam axis at which the intensity falls to  $1/e$  of its maximum in a transverse plane at  $z$ ,  $z_R = k_z w_0^2$ ,  $L_p^l$  is a Laguerre polynomial and  $\delta_{Gouy} = (2p + |l| + 1)\zeta$  is the Gouy phase. Using these basis set functions the overlap integrals

$$\langle LG_{p,l} | \psi \rangle = \int LG_{p,l}^* \psi dA \tag{4.37}$$

can be equated to the contribution from an OAM mode with  $l\hbar$  OAM to the overall beam state. There is however ambiguity in what value should be chosen as the beam waist  $w_0$ . The LG modes are scaled by this arbitrary parameter. In order to be completely orthogonal all the basis modes

require the same  $w_0$ . In this thesis a beam waist was chosen so that the  $l=0$  mode matched the airy disk profile produced by a circular aperture in the simulation. This ensures that all LG basis functions used to decompose the Fourier plane have the same beam waist. If enough modes of differing  $p$  values are used and the results summed over the  $p$  range then the resulting OAM decomposition as a function of  $l$  should not depend upon the beam waist used, the beam waist will, however alter the spread of  $p$  values required to form the radial mode structure [129]. A test decomposition with the beam waist defined to match the full width half maximum to a circular aperture airy function is shown for a function defined as  $e^{i4\phi}$  and indeed the only mode with a significant overlap is the  $l = 4$  as is shown in figure 4.23. A decomposition with the beam waist matched to the  $l = 0$  airy pattern is implemented in matlab and performed over a selected area in the Fourier plane defined by a circular aperture enclosing the C-shape. As can be seen from figure 4.24 and 4.25 the largest contribution comes from the  $l = 9$  LG modes with some contributions from neighbouring modes  $l = 7$  to  $l = 11$ , which decrease away from  $l = 9$ .

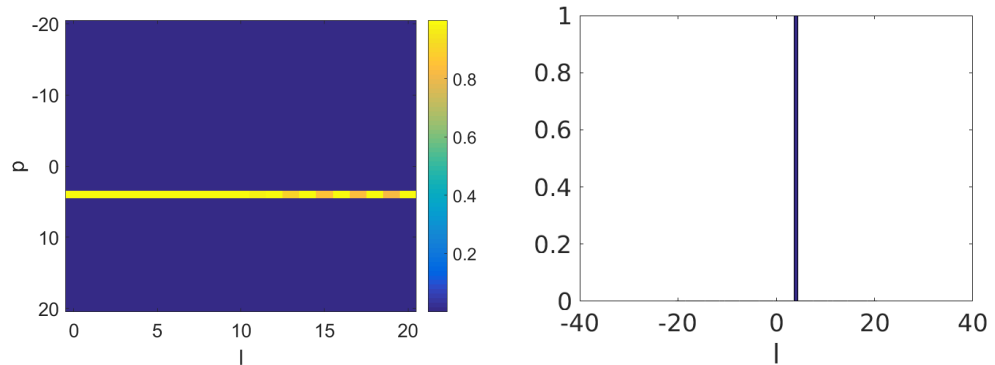


Figure 4.23: *Decomposition of  $e^{i4\phi}$  into LG modes. Left:  $(l,p)$  mode intensity Right: summation of  $p = 1$  to  $p = 20$  values for individual  $l$  values*

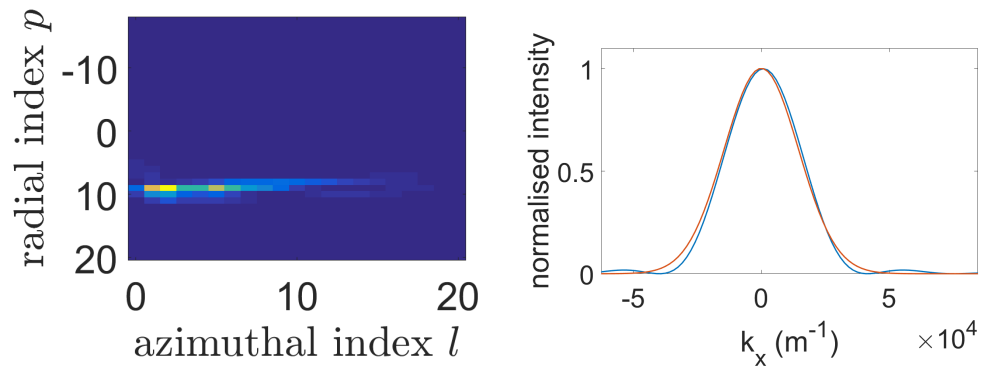


Figure 4.24: *left:  $(p,l)$  decomposition of a C shape  $l = 6.11$   $c = 3.89$ . Right: Lineplots of intensity for an fitted  $LG(0,0)$  mode (red) and an airy disk pattern (blue) from a constant phase circular aperture of the same size as the  $LG$  phase mask.*

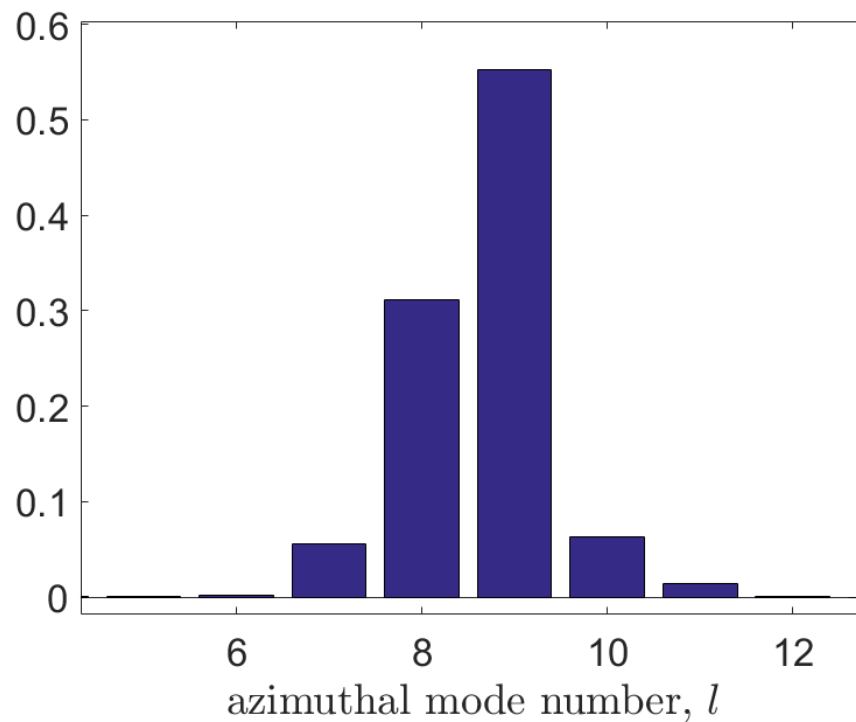


Figure 4.25: *A summation over  $p = 0$  to  $p = 20$  fitted  $LG$  mode overlap integrals giving an  $l$  OAM decomposition, for a C shape  $l = 6.11$   $c = 3.89$ .*

Two alternate basis sets can be used, spiral harmonics with a constant amplitude consisting of only a phase term  $\exp(il\phi)$  or truncated Fourier vortex modes produced by Fourier transforming a mask with a phase term  $\exp(il\phi)$  inside a circular top-hat function aperture. When using spiral harmonics for the  $n^{\text{th}}$  OAM mode, the radially varying coefficient  $a_n(k)$  can be calculated following the method of Molina-Terriza [130] by the integral

$$a_n(k) = (1/2\pi)^{1/2} \int_0^{2\pi} \psi(k, \phi_k) \exp(in\phi) d\phi \quad (4.38)$$

The power weighting of the  $n^{\text{th}}$  mode can be calculated from  $a_n(k)$  as

$$C_n = \int_0^{k_0} |a_n(\rho)|^2 k dk \quad (4.39)$$

where  $k_0$  is the upper integration limit. Ideally this would be infinity, however, in practice, to be implemented numerically the OAM decomposition is carried out for a finite  $k_0$  and a finite range of OAM harmonic terms. For the following results, the calculation is only done for  $k_0 = 12.5/\rho_{\text{max}}$ , for OAM modes between  $l = -20$  to  $l = 20$ . The weightings are then plotted as the normalised OAM distributions, defined by

$$\frac{C_n}{\sum_{n=-20}^{20} C_n} \quad (4.40)$$

From these weightings the total OAM of the field can be approximated with

$$\hbar \frac{\sum_{n=-20}^{20} n C_n}{\sum_{n=-20}^{20} C_n} \quad (4.41)$$

To compare these basis sets an  $l = 4$  mode of each basis set has been decomposed into the two other basis sets. Decomposing a  $l = 4$  spiral harmonic into Fourier vortex modes produces the distribution shown in figure 4.26 left whilst decomposing an  $l = 4$  Fourier vortex into spiral harmonics is shown in figure 4.26 right. These show there is a strong similarity between the spiral harmonics and Fourier vortex function but a broader range of Fourier vortex modes are required to form a spiral harmonic than the range of spiral harmonics required to form a Fourier vortex. This does show however that by forming a vortex in the Fourier plane, even with an ideal phase mask there will be contributions from spiral harmonics other than the value of  $l$  for which the mask is designed.

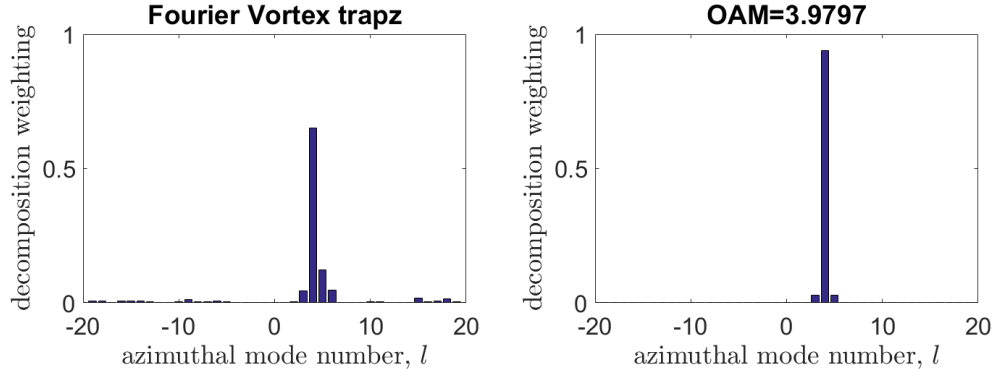


Figure 4.26: *left: an  $l = 4$  spiral harmonic decomposed into Fourier vortex modes right: an  $l = 4$  Fourier vortex decomposed into spiral harmonics.*

#### 4.1.9.3 Effects of astigmatism on mode decomposition

As is shown in the spiral harmonic decomposition of figure 4.27 and the Fourier vortex decomposition of 4.28, by adding astigmatism to an ideal  $l = 9$  vortex the mode decomposition shows contributions from a wider spread of  $l$  values at lower intensities. This can be rationalised by considering transforming a circle into an oval, in some sections the curvature is decreased and in others the curvature is increased. These varying curvatures mean the phase profile is compressed in some sections and stretched in others, thus requiring higher or lower phase gradients respectively.

When decomposing a C-shaped intensity ( $l = 6.11, c = 3.89$ ) into spiral harmonics the decomposition shows a spread of modes concentrated between  $l = 5$  and  $l = 11$  with a peak at  $l = 9$  (figure 4.29 a). The OAM approximated within the modes  $l = -20$  to  $l = 20$  is 8.5299 (from equation 4.41). This is close to the total mask plane OAM analytically calculated by equation 4.35. Similarly a decomposition into Fourier vortex modes peaks at  $l = 9$  with mode visible contributions between  $l = 7$  and  $l = 11$  (figure 4.29 b). The radial dependence of the amplitude of Fourier vortex functions means the weighting for the  $l = 9$  mode is a larger fraction of the total summation of modes between  $l = -20$  and  $l = 20$ .

The Fourier Transform Bessel beams (FTBBs) described in section 1.9 can also be used as a convenient basis set to decompose the C-shaped beam. When applying the same methods as LG modes and summing over  $p = 0$  to  $p = 20$  for different  $l$  modes the decomposition shown

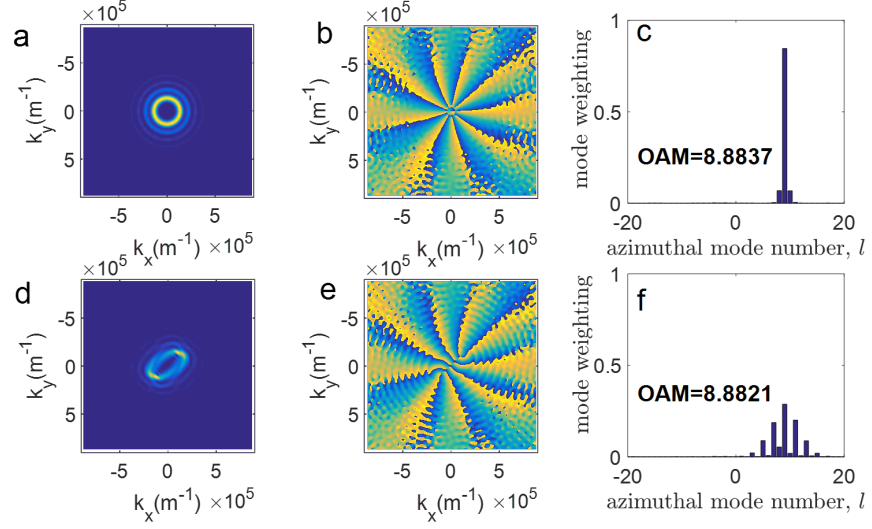


Figure 4.27: *amplitude (a,d), phase (b,e) and decomposition into spiral harmonics (c,f) of an  $l = 9$  without (a,b,c) and with (d,e,f) astigmatism ( $\chi$  with  $A = 1$ ). OAM expectation, found from weighted summation of mode OAM, is shown in (c) and (f).*

in figure 4.30 was obtained. Similarly to the previous 3 basis set functions the dominant contributions are from  $l = 9$  and  $l = 10$  with larger contributions from  $l < 7$  values than spherical harmonics or Fourier vortex modes. All 4 decomposition methods show that even for a large opening angle of  $2\alpha = 90^\circ$  the C-shaped beam is constructed from a narrow range of states. This appears to allow the intensity and vortex structure to be fairly stable upon propagation, compared to modes with a wider range of OAM basis functions. This point will be shown in section 4.1.5 with a comparison between the two types of state. However as has been discussed only mixing  $l = 8$  and  $l = 9$  modes does not form a closed gap, thus it is the specific combination and phase offsets of the narrow range which gives the C shape its characteristic slowly rotating gap.

The iterative method produces many phase singularities in the intensity, these make an assessment of nature of OAM of such a beam difficult. The total OAM present in the beam is less than the equivalent C-shape and many of the nodal lines form loops within the volume not adding to the OAM in the focal plane. OAM mode decompositions of the iterative result show it contains contributions from many different modes both positive and negative as shown in figure 4.31. These will cancel each other out, explaining the low calculated total OAM.

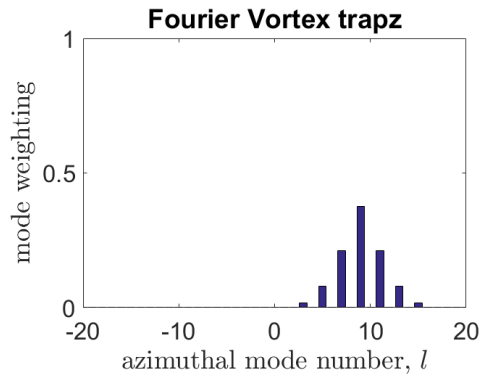


Figure 4.28: *decomposition of  $l=9$  into Fourier vortices with astigmatism ( $\chi$  with  $A = 1$ )*

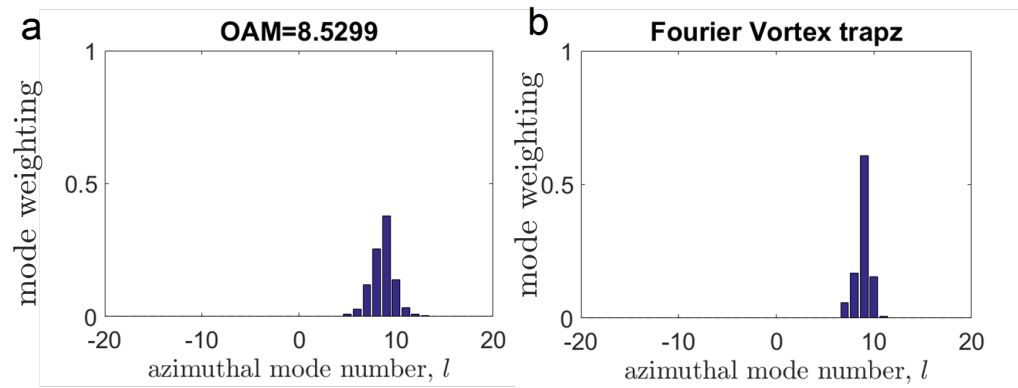


Figure 4.29: *a) decomposition of a  $C \alpha = 45$ ,  $m = 6.11$ ,  $c = 3.89$  with spiral harmonics. b) a decompositon of  $C \alpha = 45$ ,  $m = 6.11$ ,  $c = 3.89$  with Fourier vortex modes.*

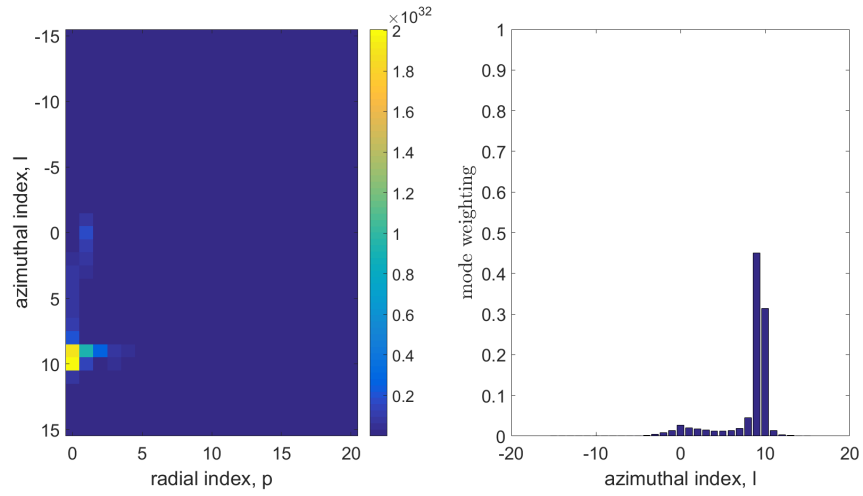


Figure 4.30: A decomposition for a C shape  $m = 6.11$   $c = 3.89$ , using truncated FT-TBB modes. The full  $p, l$  dependence (left) and summations over  $p$  modes (right).

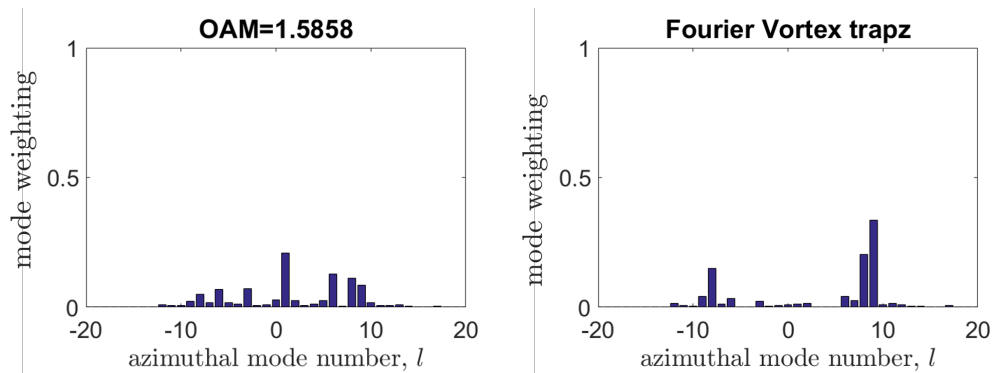


Figure 4.31: OAM decompositions of the result of an iterative algorithm (shown in figure 4.12), using spherical harmonics (left) and Fourier plane vortices (right).

#### 4.1.10 Dual C-shapes

Split ring resonators with two split rings facing in opposite directions have been used in the study of left handed materials (see for example Smith et al. [131]), as such the production of Dual C shapes could offer a one step method for the production of such multiple split ring structures if used in EBL . Cheng-Shan et al. [132] have shown that 2 different vortex rings can be encoded on the same phase mask, in a similar way a phase mask with two different C-shapes encoded into the inner radii ( $R < R_0/2$ ) and outer radii ( $R > R_0/2$ ) of the mask can be used. This will produce 2 C-shapes in the diffraction plane, one inside the other. The opening angle, size and rotation can all be independently controlled as described in section 4.1.2.

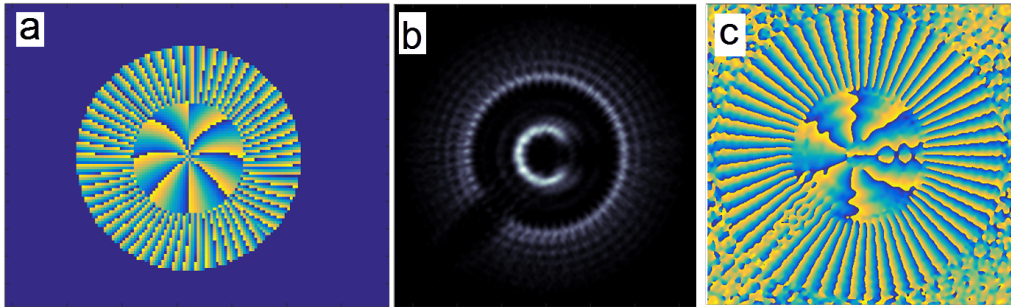


Figure 4.32: *a) Phase mask (diameter  $30\mu\text{m}$  with 2 separate radial sections used to produce a dual C-shape b) Fourier transform amplitude for the phase mask in (a) c) Fourier transform phase for the phase mask in (a) . Both C-shapes can have the size, opening angle and relative orientation altered independently.(for (b) and (c) the window size is  $6.8\mu\text{rad}$  for a  $200\text{keV}$  beam in an imaging system with a camera length of  $16\text{mm}$ .)*

In figure 4.32 the inner C-shape has a size of  $D = 10$  and an opening angle of  $45^\circ$  the larger C-shape has a size of  $D = 60$  and opening angle of  $10^\circ$  and the opening direction is rotated  $135^\circ$  from the inner C. There are certain limitations on the quality of the dual C-shapes. If the C-shape radii are too similar then they will overlap and there will only be one distinct shape. The same limits are present as for single C-shapes with large sizes giving a more broken intensity around the ring. At very large opening angles the outer C-shape can interfere with the inner C as shown in figure 4.33. Upon propagation both C-shapes show the properties described in section 4.1.4 with a rotating opening caused by a collection of

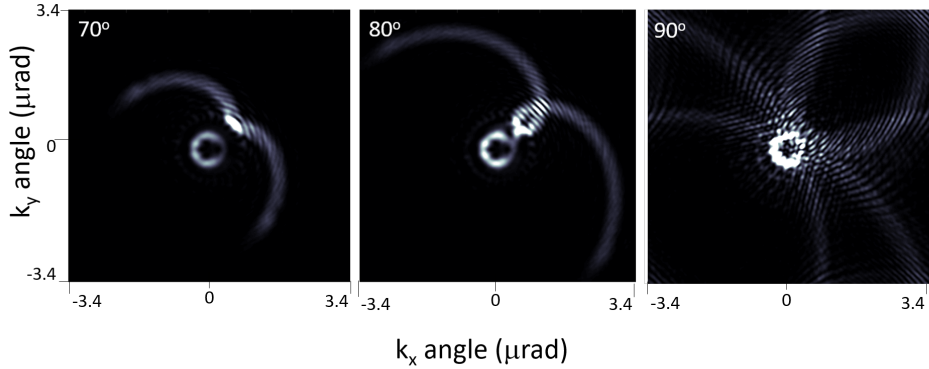


Figure 4.33: *A larger opening angle causes a cusp which interferes with the inner C. The dual C-shape Fourier plane intensity is shown for an outer C with half opening angles of  $70^\circ$ ,  $80^\circ$  and  $90^\circ$ . The window size for all three images is  $6.8\mu\text{rad}$  for a  $200\text{keV}$  beam in an imaging system with a camera length of  $16\text{mm}$ .*

nodal loops and lines along with a collection of nodal lines travelling inside the C-shape and slowly rotating (see figure 4.34).

The loops are easier to see and occupy less propagation distance for the inner C whilst the nodal lines form larger loops and more complicated connections at larger radii. The nodal lines at larger radii rotate through a similar but slightly larger angle for the same propagation distance this can be seen by the relative angles formed by the openings in figure 4.35. This means when considering how the phase singularities move along the propagation direction, the outer phase vortices are rotating at a similar angular rate and so a larger absolute rate as shown by the angle of travel on the side on images in figure 4.35.

The two C-shapes are closest together when the smaller C is encoded on the inner part of the mask. This is because larger spatial frequencies occur in the inner part of a phase mask encoding OAM. This means the intensity from the inner section contributes to Fourier plane intensity at larger radii than it would have in the outer phase mask, similarly the outer phase mask contributes to smaller Fourier plane radii than if it was encoded on the inner. These two effects bring the intensities closer together in the Fourier plane.

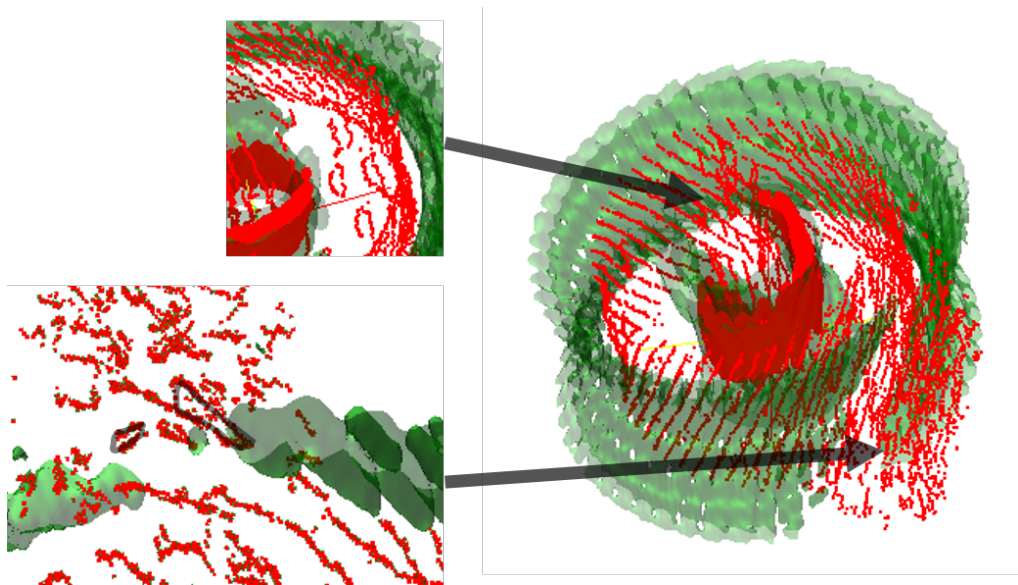


Figure 4.34: *Both openings in the dual C-shape are caused by the collection of phase singularities along nodal lines which can form loops as shown in the insets, in the lower inset 2 loops have been highlighted with a transparent black line. The camera is angled such that the propagation direction is downwards and slightly into the page*

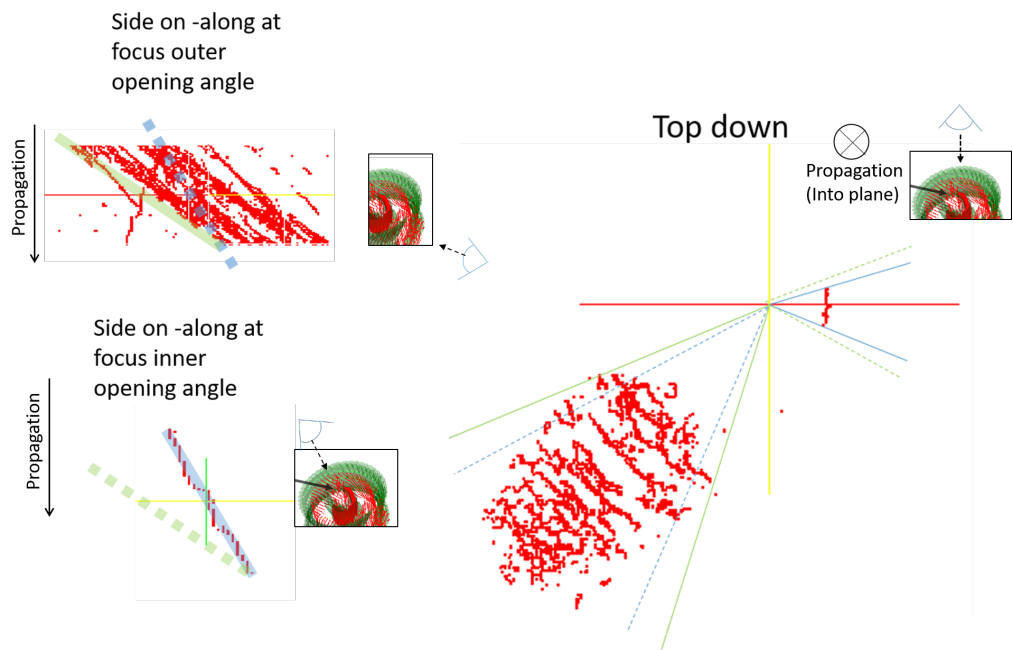


Figure 4.35: *geometry of nodal lines in dual C shape beam, blue lines highlight the angle for the inner C phase vortices and green lines highlight the angles for the outer C phase vortices. a) a view perpendicular to beam propagation, looking into outer opening. b) the view parallel to propagation. c) a view perpendicular to propagation looking into inner gap.*

#### 4.1.10.1 Dual C-shapes OAM

When performing a numerical integration analysis of the OAM content of the dual C intensity distribution, there are 2 clear steps whilst increasing the integration radius as the successive C-shapes are included (figure 4.36). The inner values are  $m = 6.11$  and  $c = 3.89$  whilst for the outer the values are  $m = 55.51$  and  $c = 4.49$ . These would give individual predicted single C OAM (calculated for the mask plane analytical function) values of  $58.5\bar{h}$  and  $7.96\bar{h}$  however the integral of 4.32 can be evaluated for the mixed mask plane function to give equation 4.47

$$OAM = -i\hbar \frac{\int \psi * \frac{\partial}{\partial \phi} \psi dA}{\int \psi * \psi dA} \quad (4.42)$$

$$= \hbar \frac{\int_0^{1/2} \int_0^{2\pi} \psi * (m_2 + c_2\bar{\rho})\psi \rho_0 d\bar{\rho} \rho_0 \bar{\rho} d\phi}{\int_0^{1/2} \int_0^{2\pi} \psi * \psi d\bar{\rho} \rho_0 \bar{\rho} d\phi} \quad (4.43)$$

$$+ \hbar \frac{\int_{1/2}^1 \int_0^{2\pi} \psi * (m_2 + c_2\bar{\rho})\psi \rho_0 d\bar{\rho} \rho_0 \bar{\rho} d\phi}{\int_{1/2}^1 \int_0^{2\pi} \psi * \psi d\bar{\rho} \rho_0 \bar{\rho} d\phi} \quad (4.44)$$

$$= \hbar \frac{2\pi \rho_0^2 [m\bar{\rho}^2/8 + c\bar{\rho}^3/24]_0^1}{2\pi \rho_0^2 [\bar{\rho}^2/2]_0^1} \quad (4.45)$$

$$+ \hbar \frac{2\pi \rho_0^2 [m_2(1 - 1/4)\bar{\rho}^2/2 + c_2(1 - 1/8)\bar{\rho}^3/3]_0^1}{2\pi \rho_0^2 [\bar{\rho}^2/2]_0^1} \quad (4.46)$$

$$= \hbar \left[ \frac{m}{4} + \frac{c}{12} + \frac{6m_2}{4} + \frac{7C_2}{12} \right] \quad (4.47)$$

When the total integral is calculated the  $m$  and  $c$  inner mask terms (the first two in 4.47 ) provide  $1.85\bar{h}$  and the outer mask terms provide  $44.25\bar{h}$  together giving the whole state  $46.1\bar{h}$ . These values are reflected in the plateaus in the numerically calculated OAM as the integration radius is gradually increased. These plateau values are at reduced values, close to  $2\bar{h}$  and  $46\bar{h}$  instead of close to  $8\bar{h}$  and  $58\bar{h}$ . The OAM contributions from each section of the dual C mask are reduced from the individual single OAM states, due to the reduction in surface area necessitated by the presence of the other in the dual C phase mask. This is shown in figure 4.36 where a single C state the same as the inner of the dual C beam shows a much higher numerical OAM when calculated for region only containing the inner C shape.

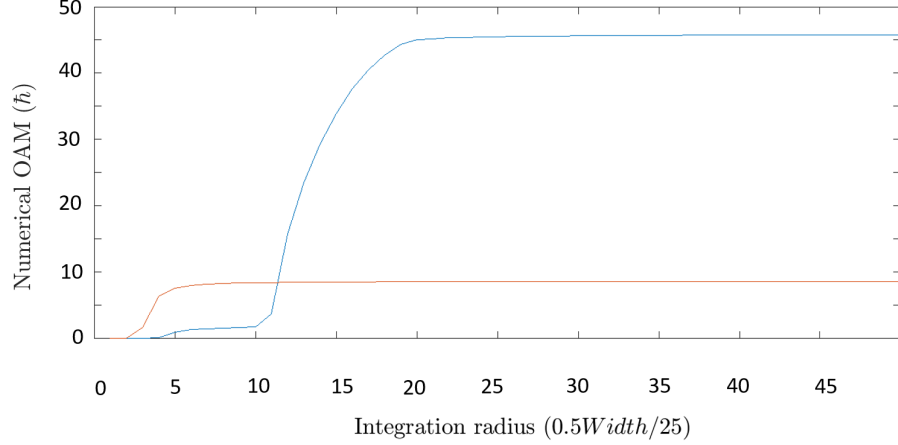


Figure 4.36: *The results of numerical OAM integration for increasing radius of integration area. The Dual C shapes show 2 plateaus one for the inner and one for the outer ring intensities however the inner OAM is lower than for a single C beam of the same type as the inner. The horizontal axis is the radius in units of  $(1.3653E+06/50)$  where a value of 25 indicates a circular integration region with a diameter equal to the simulated array width (as for figure 4.20). The vertical axis is predicted OAM.*

## 4.1.11 Potential applications

### 4.1.11.1 Optical trapping

Optical beam shaping can be achieved by using a spatial light modulator (SLM) [133], this uses a liquid crystal array to impart a designed phase change onto a laser whilst it is reflected from the device screen. The SLM can be controlled as an external screen, allowing rapid updating of the phase profile of a shaped laser beam. The ability to control the opening angle of an optical trap intensity allows applications such as dynamical adaptive particle sorting. Figure 4.37 A and B show the force distribution which would be experienced by a microparticle, calculated from intensity gradients and phase gradients. The effects at play involve trapping along the ring from the dipole potential and rotation around the ring from the optical torque associated with the OAM. Optical C-shaped beams as described in the preceding sections could be applied to laser trapping of particles and atoms. As explained in chapter 1 optical beams can be used to trap transparent particles and the intensity can be attractive or repulsive for

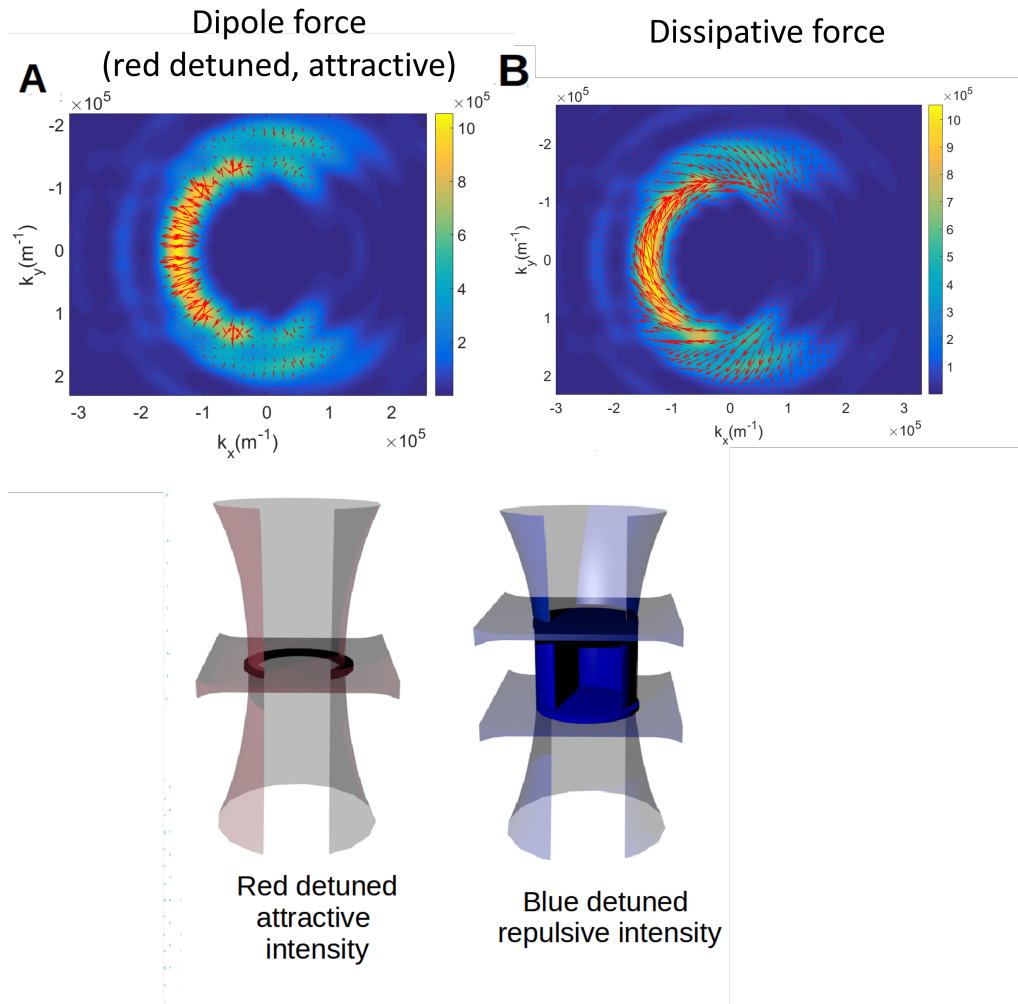


Figure 4.37: *Red and blue detuned optical traps based upon C-shaped intensities. A) the dipole force due to amplitude gradients B) the dissipative force due to phase gradients C) a C-shaped arc trap D) A C-shaped box formed from laser light.*

atoms. By combining a C-shaped beam with a single light sheet a thin C-shaped region could be created which holds and traps particles or atoms ( if laser is red detuned, as in figure 4.37 C). This could be used to confine particles or atoms to a broken ring whilst also imparting OAM to the particle (figure 4.38). In a similar manner to previous particle rotation experiments varying the gap via control of an LCD spatial light modulator, could vary the rotation speed of the particle around the bright arc.

If a particles was accelerated by an integer vortex beam a SLM could be used to quickly open a gap, potentially ejecting the particle or atom from its orbit like an optical slingshot. This would require a low friction environment but could have applications in sorting particles and light-matter interactions. C-shaped intensity could be used to sort optically trapped

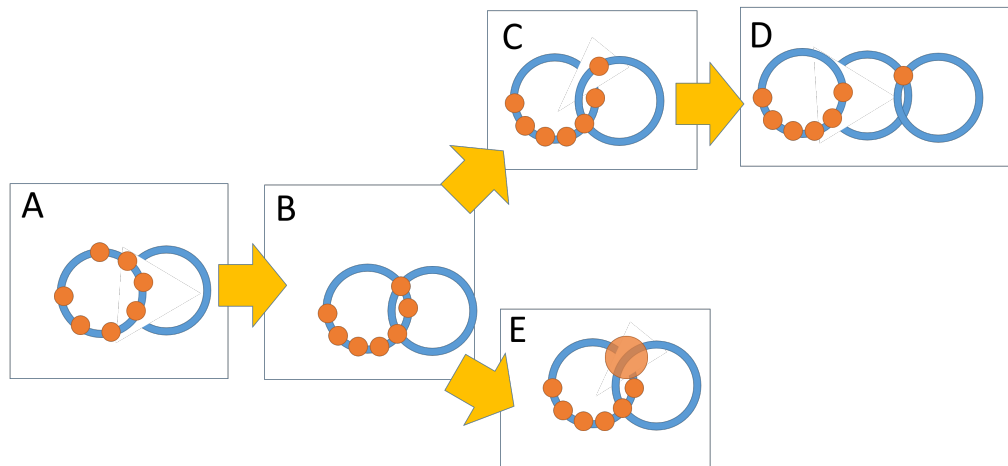


Figure 4.38: *Blue areas represent vortex ring intensity orange circles represent particles being trapped (e.g. Silica particles, or atoms) A) Particles trapped and rotating in the left vortex B) Particles stopped from rotating by right vortex C) Single particle transfer from left to right vortex D) Trapping of transferred particle by a third vortex. E) particles larger than the gap will not be transferred out of the left vortex.*

particles by size. If silica microparticles are trapped in an integer vortex beam by refraction they are confined to the bright ring and will rotate around the ring (figure 4.38 A) . If a second laser, also shaped into a vortex beam, is overlapped on the first as shown in figure 4.38 B then the intensity gradient will slow down (or stop) this rotation, potentially leading to the confinement of a particle to the position of overlapping intensity. This assumes that the two vortex beams add incoherently and extra phase offsets, potential time dependent, may be required to achieve this. If the integer

vortex beam is then gradually changed to a C-shaped beam such that the opening occurs over the particle then the particle could be transferred to the second optical trap and continue rotating in the new trap, figure 4.38 C. A third ring could be used to hold the transferred particle away from the initial left ring, figure 4.38 D. This transfer could be dependent on the size of the C with the transfer only occurring if the particle is smaller than the opening size, larger particles would be held by the intensity either side of the opening figure 4.38 E. This could lead to passive sorting of trapped particles based on size. If arrays of this arrangement were produced then the C-shaped slingshot could lead to only small particles being given a momentum kick, thus eventually separating out large collections of mixed size particles. This transfer could be cascaded between multiple rings giving selective transport of particles. If a particle is trapped between the two ends of the C by the gradient forces at the tips, as shown in figure 4.38 E, then gradually opening the C-shape could apply very small amounts of strain onto trapped particles. This sort of fine control could allow the study of very weak interactions, if two interacting entities could be pulled apart by the opening of the gap in a controlled, repeatable manner.

Adjustable C-shaped optical beams can also have interesting applications in the emergent field of atomtronics - the physics and applications of guided current due to motion of atoms. For example, if we place a light sheet beam to intersect the C-shaped beam at a right angle (see figure 4.37C), the atoms are then trapped in the high intensity regions if the frequencies of both laser beams are red-detuned from the atomic resonance[28]. A Bose-Einstein condensate trapped in such a ring circuit with a variable gap is an atomic equivalent quantum interference device[134]. Such a circuitry allows an investigation into tunnelling through the gap barrier, in a manner similar to a Josephson junction[135]. Previous experiments have used an additional laser spot to introduce a potential barrier for a Bose-Einstein condensate, however a C-shaped intensity would remove the need for this extra beam thus simplifying the experimental set up. [136].

If a trapping experiment uses a blue detuned laser to interact with an atom then the C-shaped intensity could be combined with a light sheet above and below focus to provide repulsive intensity around the sides of a 'light-box' which could have a section opened and closed by increasing and decreasing  $\alpha$  (figure 4.37 D). This could add another tool to optical

trapping experiments to allow for controlled interaction or transport of atoms.

#### **4.1.11.2 Measuring rotations of vortex electron states**

Due to the broken cylindrical symmetry of the C-shaped function rotations of the intensity distribution would be measurable, if the C interacts with magnetic fields. The C shape could thus act as a probe for local magnetic environments, offering the possibility of gaining contrast on the scale of the C shape intensity. This would offer a simplification to the experimental setup used by Guzzinatti et al [64] where a knife edge is used to break the symmetry of an integer vortex state. The theory of the interaction of these C shapes with a magnetic field has not been included in this thesis and represent a possible investigation which could continue this project. No varying rotation was seen in the experimental set up when comparing the results for opposite topological charges.

### **4.1.12 Chapter summary**

This chapter has introduced the concept of a C-shaped intensity carrying OAM due to phase vortices. This Fourier plane intensity is produced by using radial phase gradients in the mask plane. This is the first time these states have been reported and applies concepts previously applied to fractional vortex states to radial phase gradients. Initially the C-shaped state was described and explained in terms of local spatial frequency analysis from which control equations have been derived allowing the variation of opening angle and size of the C by changing two control parameters. Next the effect of astigmatism was shown to rely on the orientation of the astigmatic axis relative to the phase discontinuity in addition to the relative phases of the constituent integer OAM modes. Simulations of the phase structure of these C-shaped vortex states were analysed to track the position of the phase singularities, tracing out nodal lines of the phase vortices. The vortex structure of the C-shape contains a group of vortex lines which circulate one another, appearing to give the C-shaped state higher structural stability and OAM than a non vortex C-shape produced by an iterative algorithm. Subsequently, the OAM of the C shape was discussed, starting by describing the effect of interference of different OAM

modes producing oscillations in intensity around the C. The phase structure of the C shape was numerically integrated to give a simulated OAM. The phase structure was then decomposed into different OAM components and it was shown that the C shapes has a narrow spread of OAM modes centered around the numerically calculated OAM. Finally future developments and applications were discussed with Dual C shapes and applications in trapping and lithography. This characterisation of the C-shaped state adds to the library of known states containing phase vortices and could be used in the future to design other intensity distributions without rotational symmetry but containing OAM. Following this, chapter 5 will describe the experimental production of the C shapes introduced in this chapter.

# Chapter 5

## C experimental

To experimentally produce the C-shaped states described in chapter 4 a variety of methods were used. Holographic reconstruction was used for the amplitude contrast and phase contrast masks. However it must be noted that the analytic phase only occurs in the mask plane and the C shape is in the Fourier (diffraction) plane. All of the masks are designed to engineer the phase of the wave at the mask plane to thus produce a C in the Fourier plane.

### 5.1 Condenser Pt Foil amplitude mask

Amplitude contrast masks have sections which either block an incoming wavefront or allow it to pass through (figure 5.1), following the shape of the binarised interference pattern as described in chapter 3 section 3.2. For electrons in the TEM a thin Pt foil mask was placed in the path of a TEM electron beam (figure 5.2).



Figure 5.1: *A schematic cross section through the Pt foil amplitude mask. In this experiment the foil was  $1\mu\text{m}$  thick.*

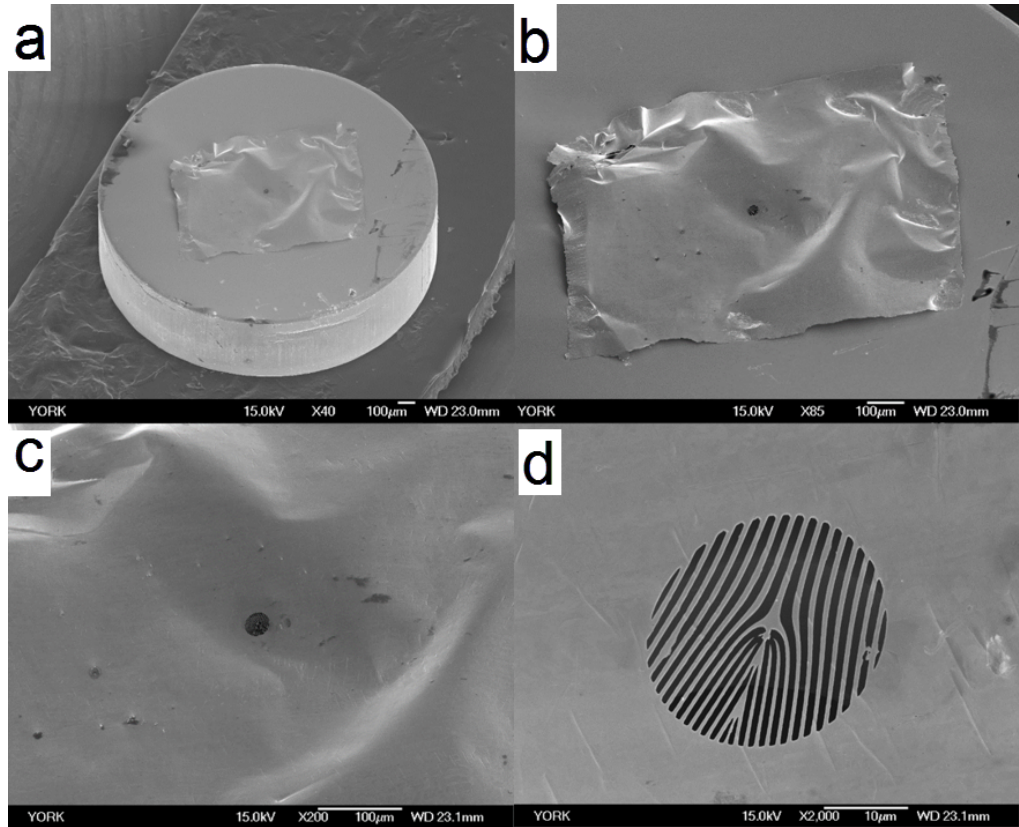


Figure 5.2: SEM images of the  $1\mu\text{m}$  Pt foil amplitude mask produced by FIB. The magnification increases from A-D , a) shows the substrate and the foil which has been attached buy spot welding, b) shows the border of the Pt foil rectangle, c) shows the central region of the film with the mask just visible, d) shows the amplitude mask in the foil film.

To make this mask,  $1\mu\text{m}$  Pt foil was attached to a Pt substrate by using an ultrasonic wire bonder without wire. The wire bonder tip vibrates rapidly, heating up the section of film it touches, effectively producing a "spot weld" in each corner of the thin Pt square (see figure 5.2 a and b). Once attached the foiled sample was place in a focused Ion beam machine where a pattern was milled into the foil with accelerated  $\text{Ga}^+$  ions. This procedure created the mask shown in figure 5.2 c and d, by using the hologram shown in figure 5.3 c . The calculated hologram shows that as the radius is increased along the discontinuity the bars and gaps spread outward signifying a larger amount of phase being covered around one full rotation, consistent with a mixed radius-azimuth product. These are not present for fractional masks with only constant azimuthal phase gradients, as shown in figure 5.3 e. The number of bars in the fork of a dislocation grating represents how many times the the two waves come in and out of

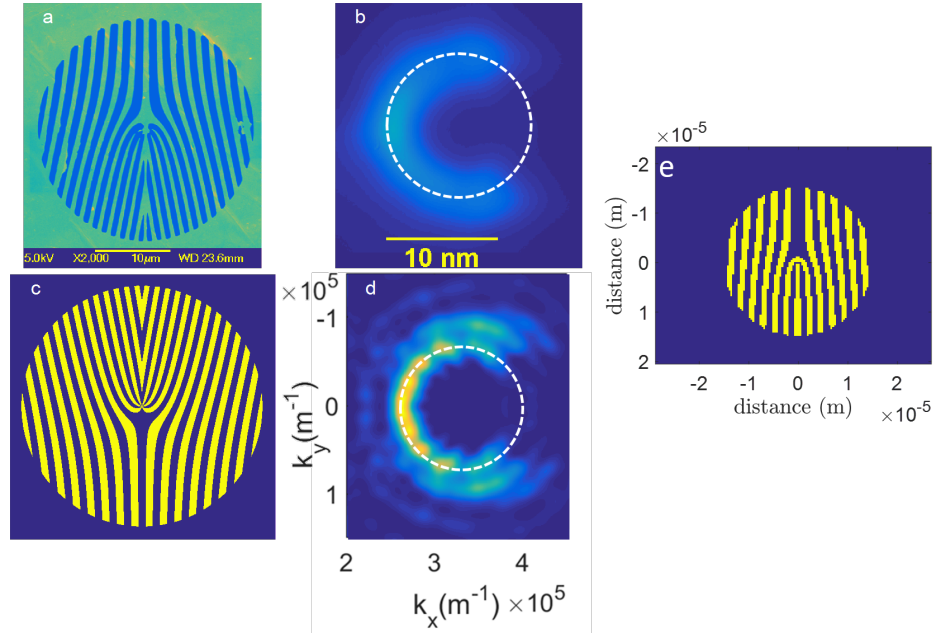


Figure 5.3: a) An SEM image of the Pt amplitude mask, b) the intensity produced in the focal plane first diffraction order at 150K magnification with 3 second exposure , c) the CGH design used to produce the mask. d) a simulated intensity distribution of the C shape which should have been produced. The simulated image is from  $2E5 \text{ m}^{-1}$  to  $4.5E5 \text{ m}^{-1}$  in  $k_x$  and  $-1.5E5 \text{ m}^{-1}$  to  $1.5E5 \text{ m}^{-1}$  in  $k_y$ .

phase, and is related to the topological charge, as such the average OAM can be estimated by counting the number of bars at small and large radii. For example figure 5.3 c shows the c mask has 8 bars close to the center but this increases to 11 at the largest radius shown by the tip of the v shape at the top of the mask discontinuity. This means the average OAM is somewhere between 8 and 11, as will be discussed later this is correct.

This mask was placed into the condenser aperture of a JEOL 2200FS microscope and the diffraction pattern of the mask was brought into focus at the sample plane by varying the condenser lens voltage. The intensity distribution produced at the first diffraction order ,at focus, is shown in figure 5.3 b. This was recorded at 150,000 times magnification with an exposure time of 3 seconds. The opening angle in the experimental intensity matches well with the simulated intensity and a comparison can be made by plotting the intensity as a function of angle (figure 5.4) tracing the intensity value around the C arc , following paths like the dashed white lines in figure 5.3 b and d . Both the experimental and simulated distri-

butions are normalised such that the maximum intensity in the C takes a value of 1. The experimental distribution can be characterised by finding the angle at which the normalised intensity in the experiment equals the normalised simulated intensity for a  $45^\circ$  opening angle. This analysis gives  $44.7^\circ$  however whilst there is definitely a strong match this value appears to be fortuitously close. The actual experimental data show a shallower intensity gradient than the simulation and, when normalised so that intensities lie between 0 and 1, the experimental line crosses the simulated line. This crossing occurs very close to the 45 degree angle, however if a comparison was made at larger or smaller angles there would be a larger difference between experiment and simulation. Looking at the finer structure, most of minima and maxima are not resolved in the experimental data however the experimental intensity does show a slight minima after the lowest intensity point when moving around the arc to the highest intensity. This experimental data shows successful control and production of an opening angle in a vortex state for a C-shaped electron.

### 5.1.1 Amplitude within the gap

As discussed in chapter 4 section 4.1.6 there are still some areas of low-intensity within the gap. The experimental intensity shows a region giving a peak in the in both radial and azimuthal intensity plots (figure 5.5) showing there is a linking intensity section between the two ends of the C shape. This is consistent with the simulated intensity (figure 4.15) which also shows a linking section of weak intensity between the upper and lower ends of the C shape. The experimental intensity represents path electron probability density can take when circulating from one tip to the other. These results show that the electron beam can be predicted by the wave model upon which the simulation is based and has some possibility to circulate and maintain orbital angular momentum.

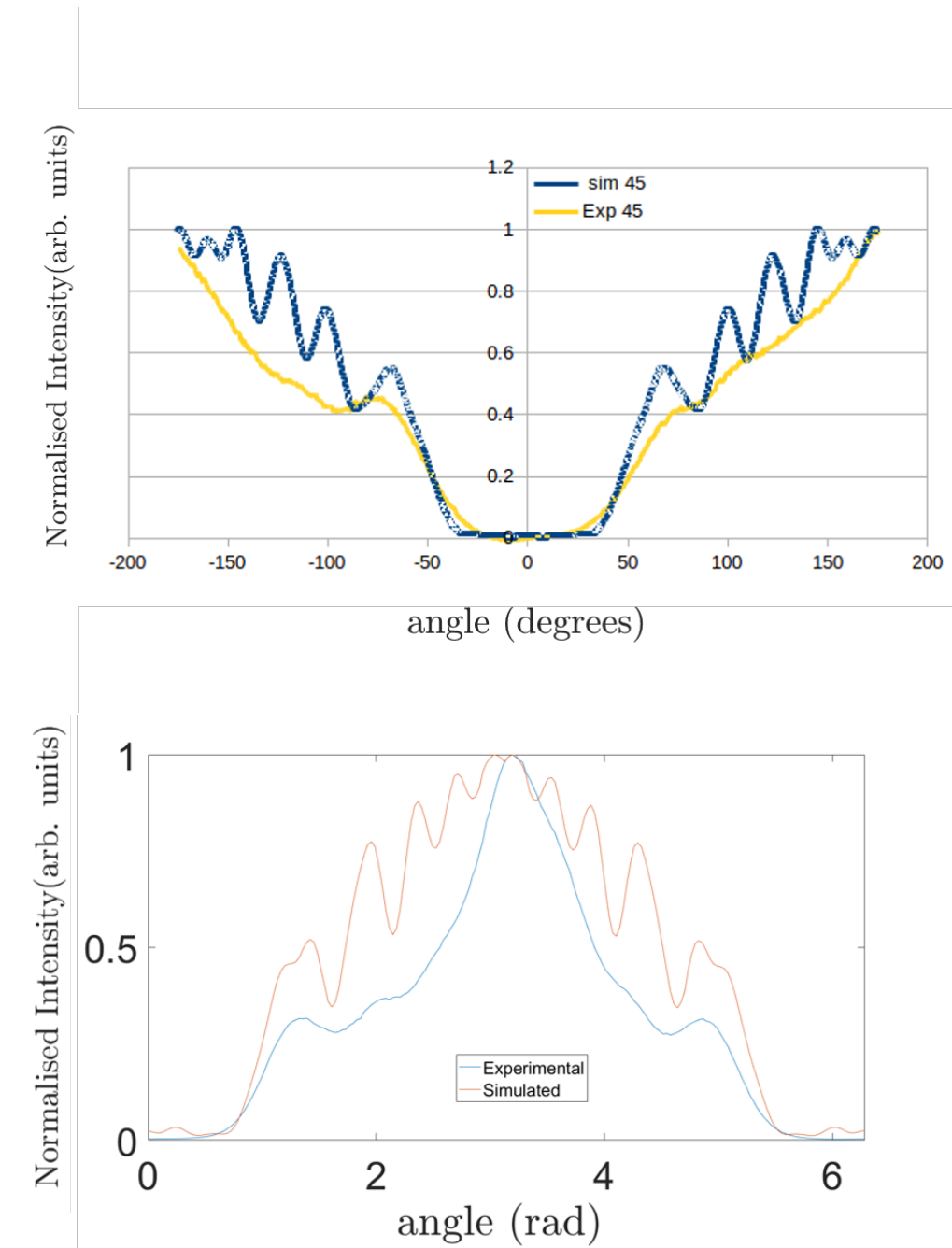


Figure 5.4: A comparison between the simulated azimuthal intensity distribution and the experimental intensity recorded. The intensities are taken around the curves as indicated by the dashed white paths in figure 5.3 b and d. The upper image compares the experimental with an ideal  $C$  from a direct phase mask, whilst the lower compares the experimental with a simulated first diffraction order. The first diffraction order (lower panel) has less oscillations in the intensity close to the highest intensity around the arc ( $\pi$  rad in lower and  $\pm 180$  degrees in upper). This is due to overlap with the zeroth order.

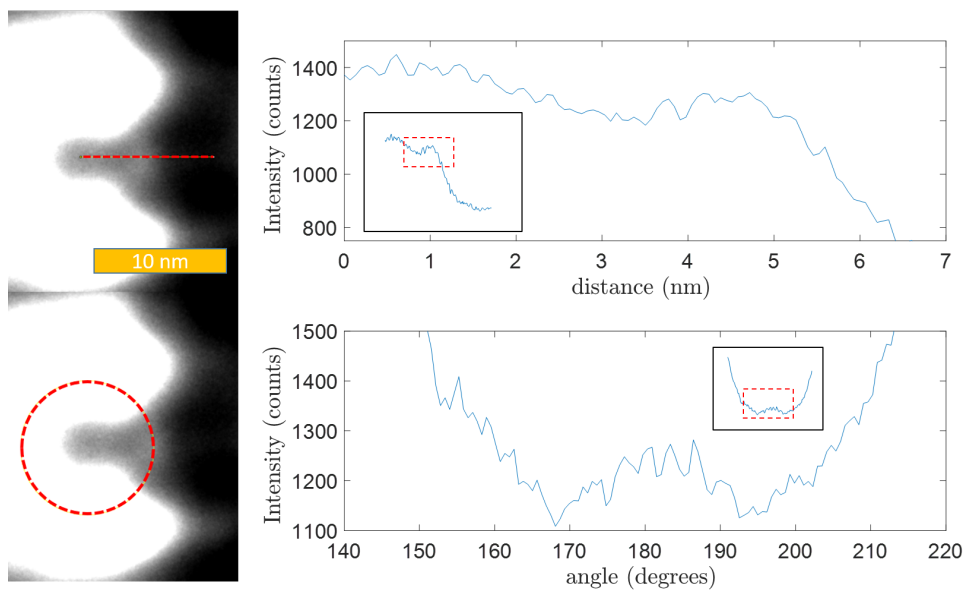


Figure 5.5: *Radial (upper) and azimuthal (lower) plots of the experimental C-shaped intensity. The line plots are intensities along the dotted red lines overlain on the experimental intensity. The orange scale bar is 10nm and applies to both upper and lower experimental images.*

### 5.1.2 Pt mask propagation

A through focus series of images was collected by varying the condenser lens strength. These are rendered in figure 5.6 by stacking the images on top of one another, ( as explained in appendix section A.5) with the green volume enclosing regions of high intensity. Figure 5.6 a shows a side on view of the first three diffraction orders showing the gap of the order closest to the camera. Figure 5.6 b shows a top down view along the propagation direction and all three diffraction orders can be seen, with the gaps on opposite sides of opposite diffraction orders. The opening is clearly shown to slowly rotate as explained in section 4.1.4.1 and shown in figure 4.12. The opposite diffraction orders rotate in opposite directions showing this is due to the varying relative Gouy phases of topological charge components with different signs, as discussed in chapter 4 section 4.1.4.1.

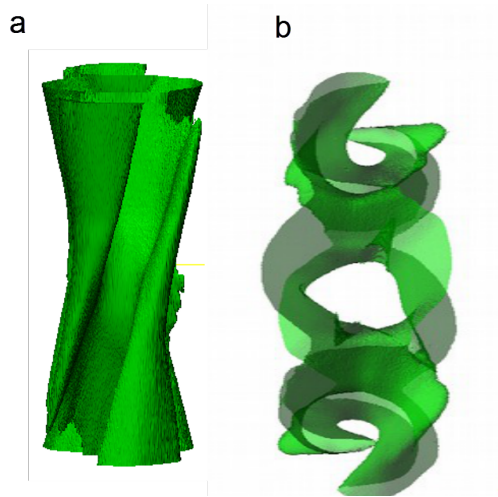


Figure 5.6: *An isosurface outlining regions of experimentally recorded high intensity for the defocus C-shaped diffraction pattern. a) side on view, perpendicular to propagation showing the rotating gap on one diffraction order. b) view along beam propagation axis showing both  $\pm 1$  and 0 diffraction orders.*

### 5.1.3 Iterative phase retrieval

The iterative method describe in section A.3 can be used for phase retrieval from an input intensity . The desired phase solution is now the phase in the Fourier plane and not the mask plane. To improve the algorithm when

applying it to a series of images , with an increasing distance from focus, the output from the previous image in the series was used as the starting guess for the next image in the series. To test out the algorithm an ideal simulated C-beam ( $\alpha = 45, D = 10$ ) was used as the input intensity image sequence. In this case for each slice the initial guess was the ideal at focus simulated C. As is shown in figure 5.7 the algorithm successfully reproduces the simulated phase singularities in the core and opening of the C shape at focus. The trajectories of the retrieved phase singularities also match extremely well with the simulated trajectories as shown by the overlapping datasets in figure 5.7. When performing the OAM mode decomposition described in section 4.1.9.2 the retrieved at focus phase gives very similar results (figure 5.8) to the ideal simulation (in chapter 4 section 4.1.9.2) showing the phase retrieval method does not introduce artefacts to the ideal dataset. However whilst the numerical OAM values for the simulated input and retrieved output match each other, 8.374 and 8.45 these do not match the ideal  $9.32\hbar$  this is due to the lower resolution required for the iterative retrieval, higher resolutions give numerical OAM much closer to the ideal prediction, however the long runtimes and memory requirements for the phase retrieval algorithm limits the resolution which is feasible.

As a second check of the algorithm a simulated input from an  $l = 1$  vortex was used, whilst still having an initial guess as an ideal C shape. Despite starting with the same high orbital angular momentum C shape as before the algorithm successfully ends up at a single central vortex line as shown in figure 5.9, proving the reliability of the algorithm.

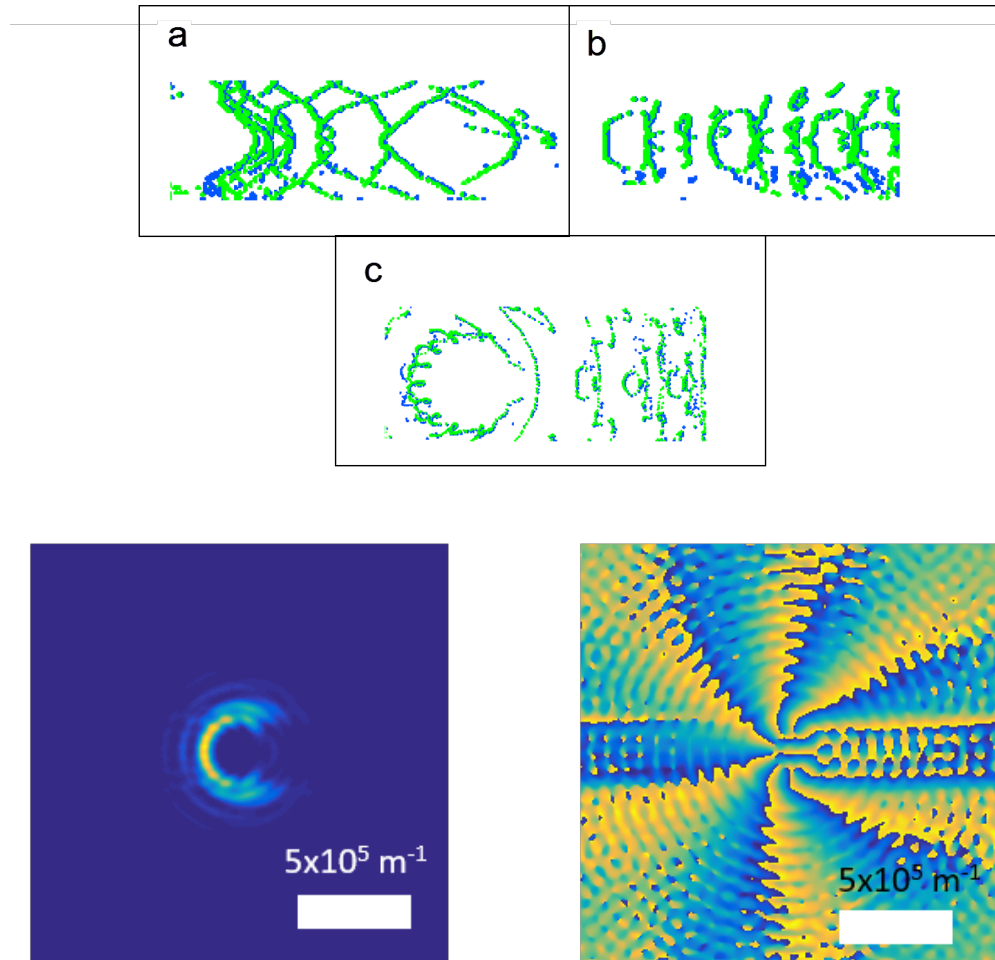


Figure 5.7: (a,b,c): For propagation along the  $z$  axis, these figures show an overlay of vortex trajectories from the ideal simulation (green points and the retrieved phase (blue points) showing a successful match. a)  $(x,z)$  plane b)  $(y,z)$  plane c)  $(x,y)$  plane (d,e): The intensity (d) and phase (e) of the wavefunction retrieved from the ideal simulated intensity at focus.

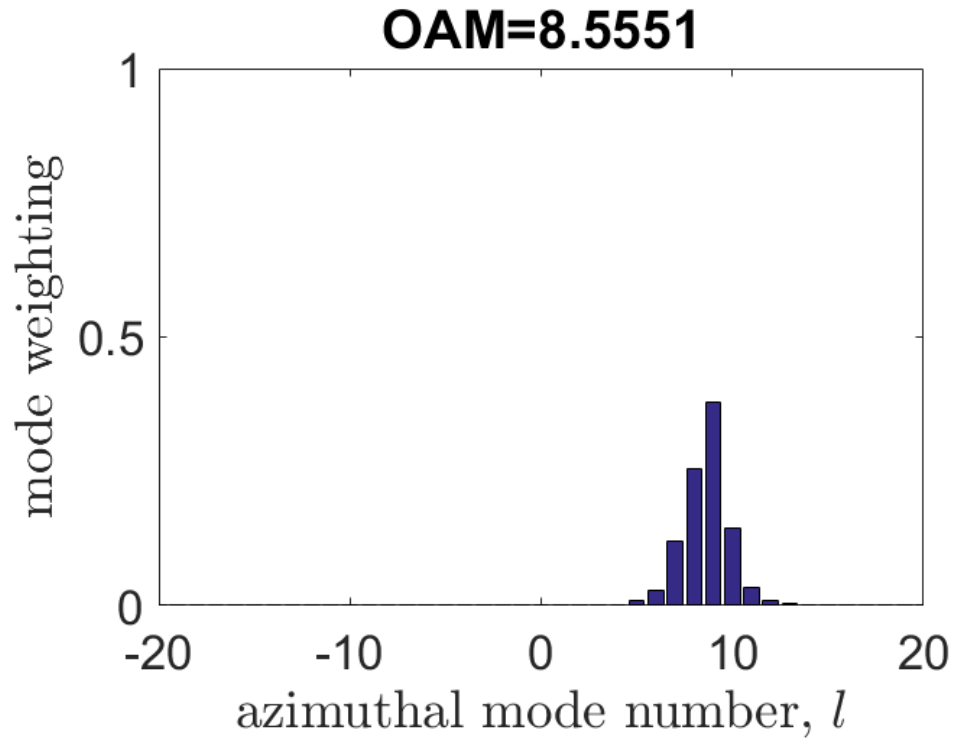


Figure 5.8: *OAM mode spiral harmonic decomposition for the phase retrieved from simulated input , OAM approximation by weighted summation is 8.55 and the numerically evaluated integral gives OAM= 8.45 )*

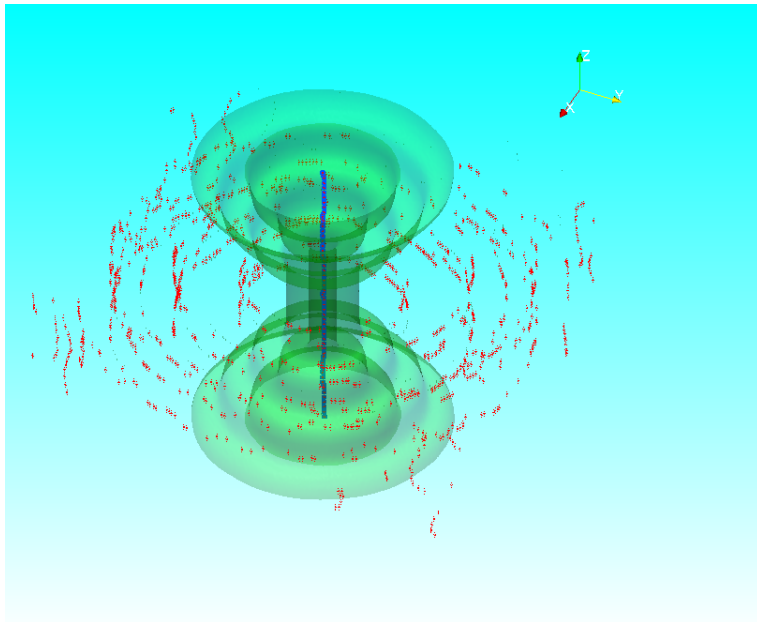


Figure 5.9: *A rendering of the retrieved wavefunction from the iterative algorithm, when applied to a simulated  $l = 1$  input. Green volumes enclose regions of high intensity and red or blue dots are phase singularities.*

## 5.2 TEM mode phase retrieval

The phase retrieval algorithm of section A.3 has been applied to experimental images, the at focus simulated wavefunction was only used as the initial guess for the central at focus experimental image. When moving outwards away from the focus the solution from the previous image is used as the initial guess for the current image. The results of this method when applied to a C formed in TEM mode are shown in Figures 5.10 to 5.12.

Figure 5.10 shows the at focus retrieved wavefunction along with its OAM decomposition. The retrieved phase shows a very similar OAM mode distribution to the ideal simulated however there are increased contributions from modes outside of the  $l = 5$  to  $l = 11$  range. This reduces the OAM approximated by coefficients to less than  $8\hbar$ . The numerically evaluated OAM expectation value is calculated as  $8.26\hbar$  for the retrieved phase, only slightly lower than that of the simulation. These results suggest the electron beam produced in TEM mode has a phase structure very similar to that of the designed C shape with only small deviations from the theory.

Figures 5.11 and 5.12 shows the rendered wavefunction propagation of the solution retrieved from the TEM experimental intensities.

Different colours are only so that different vortex lines can be distinguished when they overlap. There are a clear set of vortices which propagate and circulate with the C shape, this can be seen as the long lines in figure 5.11 and the collection of points within the grey ring in figure 5.12. However the phase retrieved contains short nodal lines which do not occur in the ideal simulation (e.g. the bright green points in the lower image of figure 5.11). These end without annihilating by meeting a vortex of opposite charge (see shorter lines in figure 5.11). This is unphysical for a phase singularity to just end, the reason for this is unknown and is most likely an artefact of the array resolution and finite arrays. Future studies with larger computing power could increase the resolution to investigate this further, seeing if these vortex lines are still present. These short lines could also show that the experimental conditions create a slightly different vortex structure when compared to the ideal simulations, as would be expected.

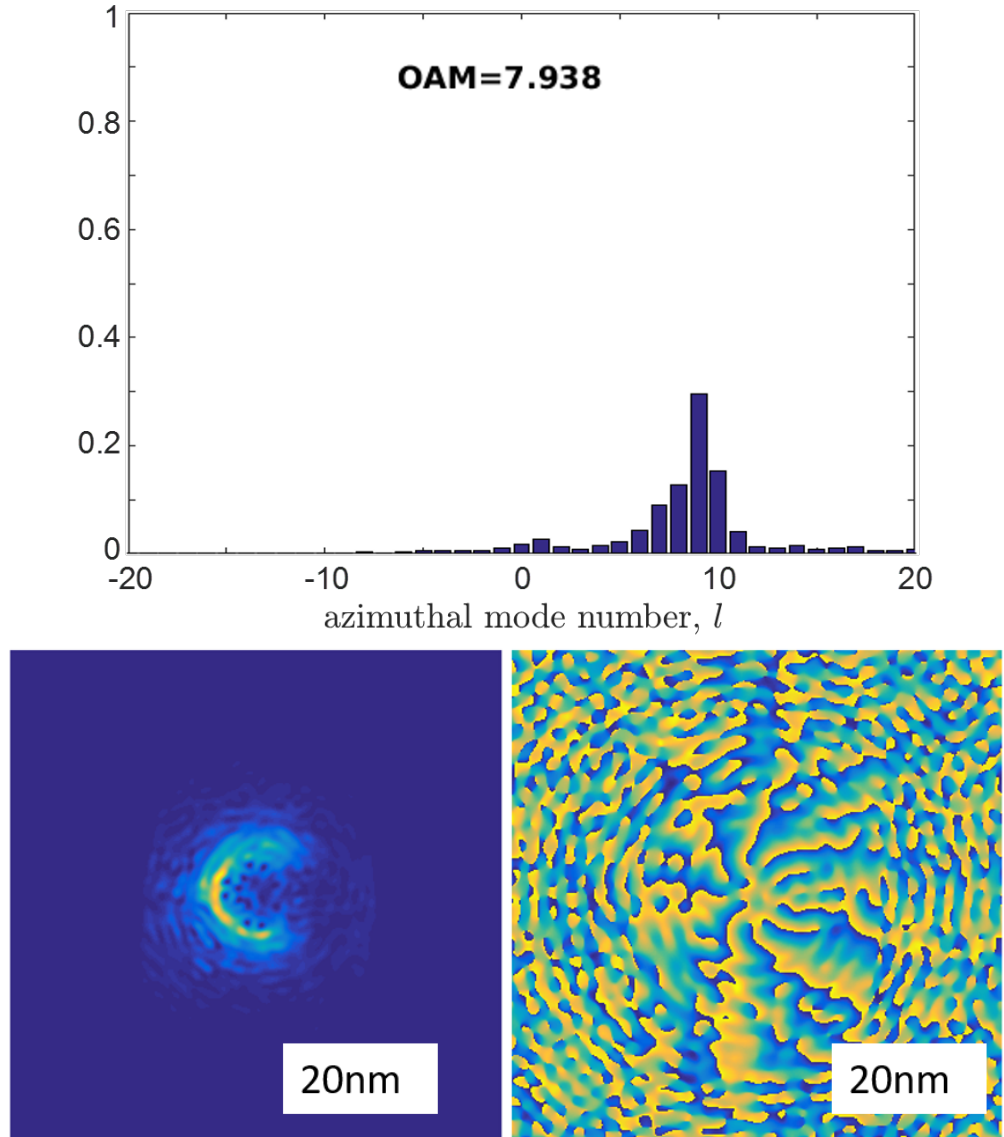


Figure 5.10: *upper: spiral harmonic decomposition lower: Phase (right) and amplitude (left) of retrieved wavefunction from TEM mode C shape using previous image as the start for each slice. The numerical OAM integral is  $8.26\hbar$ .*

A comparison of an ideal Fresnel propagation away from focus with the retrieved vortex trajectories from the experimental intensities shows a distinct mismatch (figure 5.13), this discrepancy between ideal and experimental vortex trajectories can be attributed to the inhomogeneous environment due to remaining aberrations in the TEM.

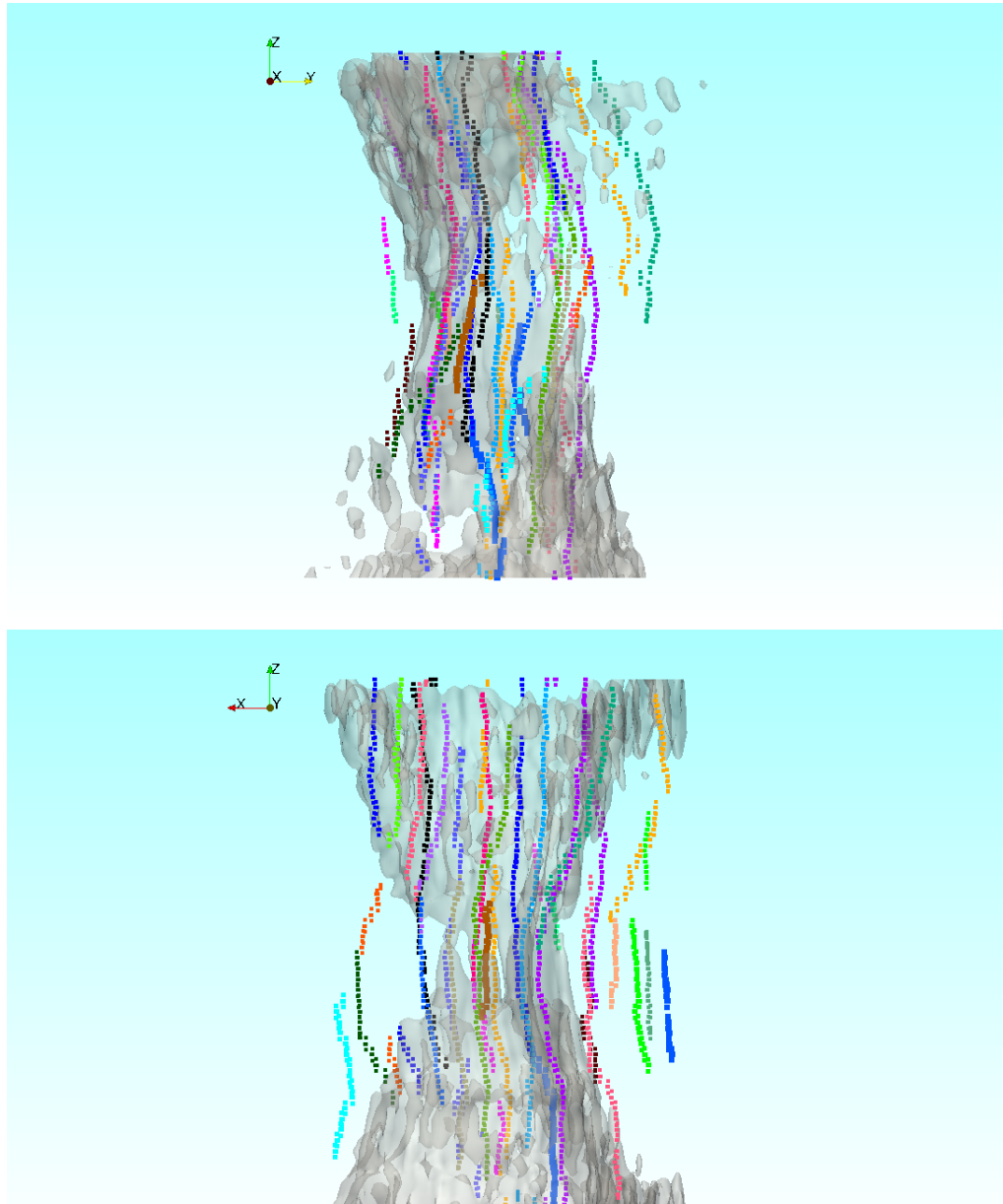


Figure 5.11: *Rendering of retrieved wavefunction using previous slice result as the initial guess, working from focus outwards. Coloured lines track vortex trajectories in the retrieved phase for the TEM mode C. The numerical OAM of the retrieved at focus phase is  $8.26 \hbar$*

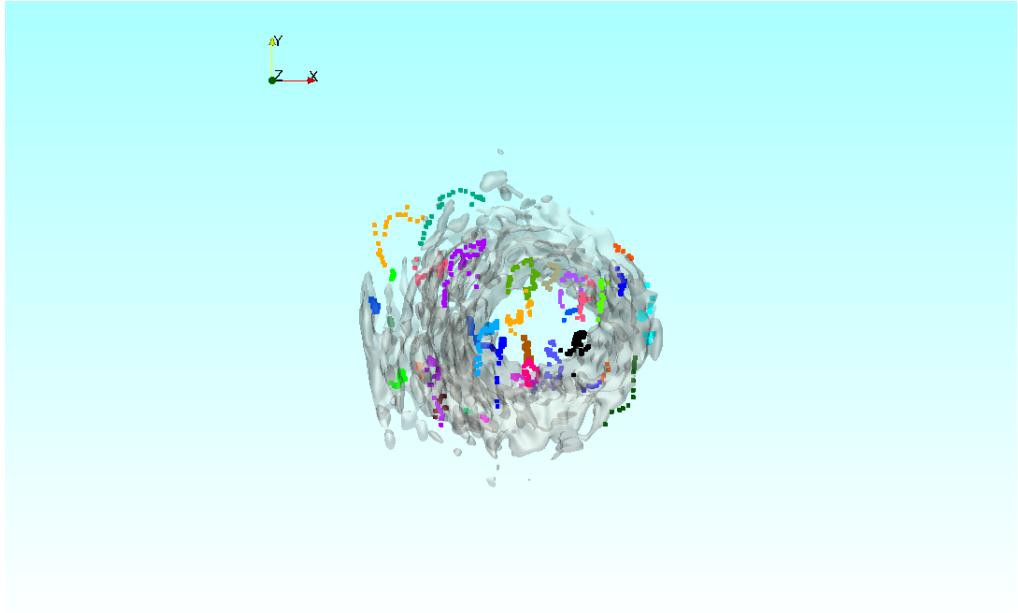


Figure 5.12: *A top down view of same distribution as figure 5.11*

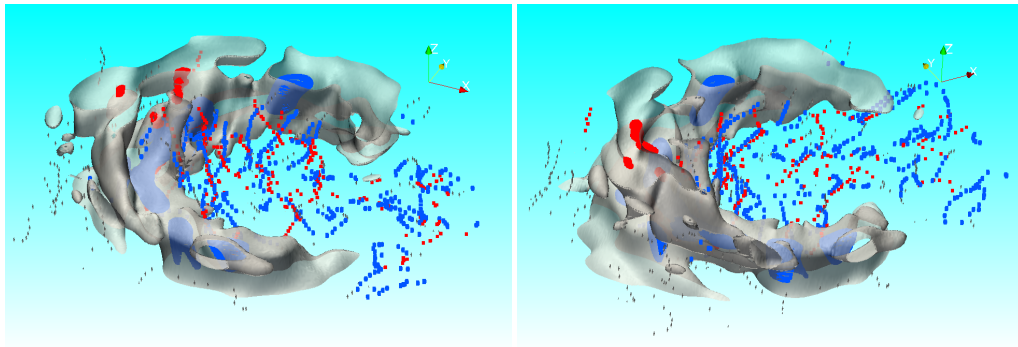


Figure 5.13: *Retrieved phase vortex trajectories from TEM mode (red) and simulated Fresnel propagation trajectories (blue) from the retrieved wavefunction at focus. The grey volume is simulated intensity. The mismatch suggests the experimental conditions still contain aberrations.*

### 5.2.1 Phase retrieval on NBD focal plane intensity

When using the nanobeam diffraction mode of the JEOL 2200 there is more fine detail in the C-shaped intensity compared to the previously shown results which were recorded in TEM mode. When using the ideal simulated C shape as an initial guess for the phase the iterations gradually deform the phase structure until a best match has been found for the measured amplitude. The phase retrieval method described in section A.3 was applied to a series of images taken in NBD mode. Figure 5.14 shows the results when using an experimental C shape recorded at 600,000 times magnification with an exposure time of 5 seconds. The retrieved phase shows vortices with a distortion from the even distribution around a ring seen in the ideal simulation. However the azimuthal phase gradient and alternating vortex anti vortex pairs survive through the iterations. The OAM mode decomposition of the retrieved phase shows significant contributions from OAM mode between  $l = 7$  and  $l = 10$  as expected, but similarly to the TEM mode there are larger contributions from outside this range. For the wavefunction retrieved from the amplitude recorded in NBD mode the spread of prominent contributions to the decomposition is larger than the ideal simulation and the numerically evaluated OAM expectation value is  $7.7\hbar$ , lower than the equivalent for the analytical  $9.32\hbar$  and ideal retrieved  $8.24\hbar$ . This reduced OAM is most likely related to the presence of aberrations which as shown for two-fold astigmatism can introduce a spread in the OAM mode decomposition. The reduced OAM could also be due to any imperfections in the mask structure. The phase retrieved and subsequent OAM analysis of the NBD mode suggests that this mode in practice does not offer a significant benefit in terms of increased OAM of the electron beam. The phase retrieval finds a wavefunction with a similar OAM spiral harmonic mode distribution and OAM from the coefficients calculated. The numerically evaluated OAM for the NBD mode is slightly lower than for the TEM mode. The reason for this is unclear, however it must be noted that the TEM mode images and NBD mode images were recorded in separate sessions over a year apart and so variations in the lens calibration in between mean it is not an ideal comparison and are a potential explanation for the unexpected variation.

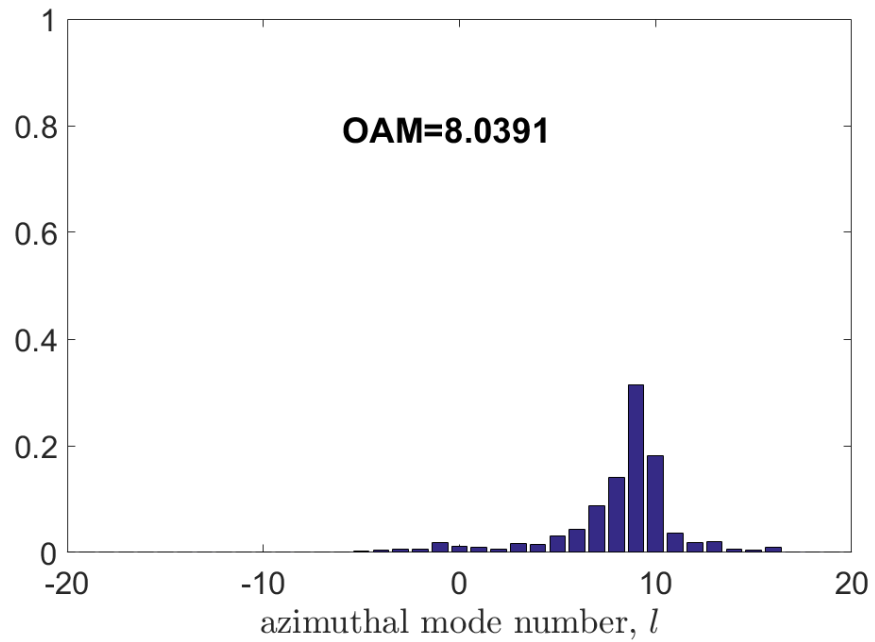
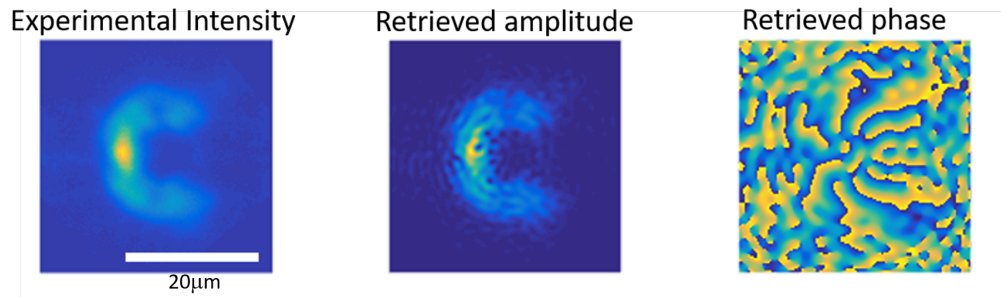


Figure 5.14: *The results of the phase retrieval algorithm when applied to a C shape produced in NBD mode with magnification 600,000 times (scale bar is 20 nm) . Top experimental input intensity (left), the retrieved intensity (center) and the retrieved phase profile (right). Bottom: the OAM mode decomposition of the retrieved phase with an approximated OAM of  $8\hbar$ . The numerical OAM integral of the retrieved function is  $7.7\hbar$ .*

## 5.2.2 Phase retrieval of NBD propagation series

To characterise the C shape produced during the NBD mode the phase retrieval was applied to a set of images recorded with different defocus. The recovered vortex trajectories are shown as coloured lines in figures 5.15 and 5.16. These phases were found by working from the focal plane

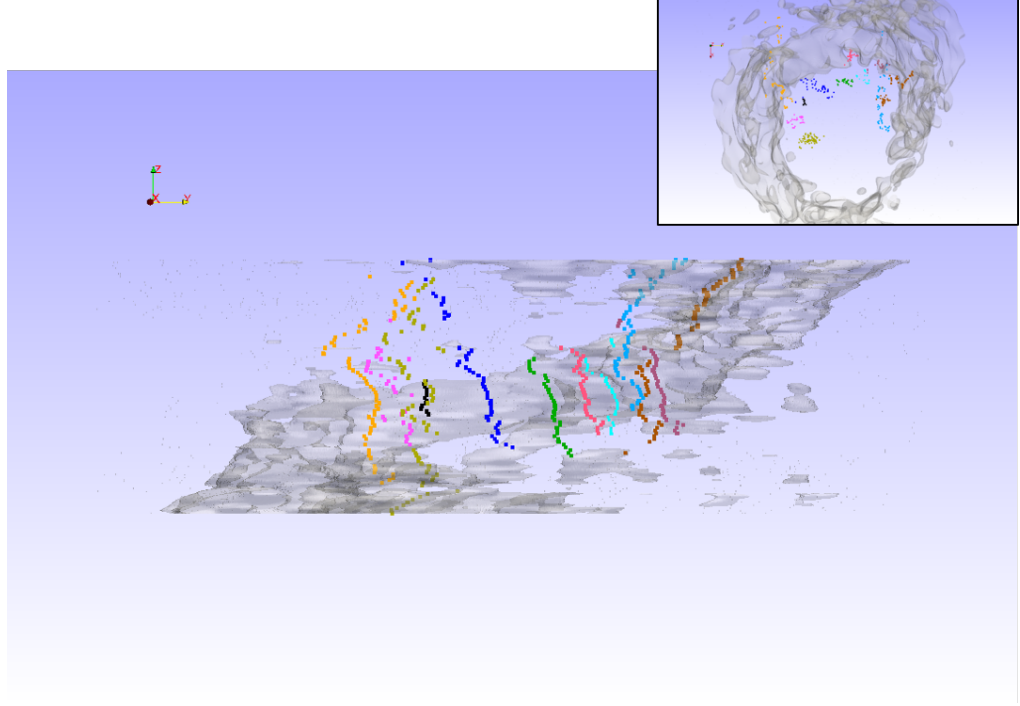


Figure 5.15: *Rendering of the retrieved wavefunction for the NBD series containing the at focus distribution in figure . Vortex trajectories which thread the central C ring have been highlighted, colour is only for distinguishing individual trajectories. (inset: a top down view along propagation)*

outwards and using the previous image's iterative result as the initial guess. At focus there are 13 main vortices found within the ring (figure 5.15) , this contrasts the ideal simulated 9 and is due to 2 extra central vortex-antivortex pairs forming inside the arc.

11 of the phase vortices are away from the gap and rotate inside the high intensity arc as they propagate. Some of these vortices are only found in the central region close to focus( black, light pink, salmon pink), whilst others have trajectories from large defocus ( yellow, dark blue, light blue, brown). These large defocus trajectories reproduce the qualitative prediction from the simulations of chapter 4 figure 4.12, with the large angle trajectories also shown in the dark blue line in figure 5.17.

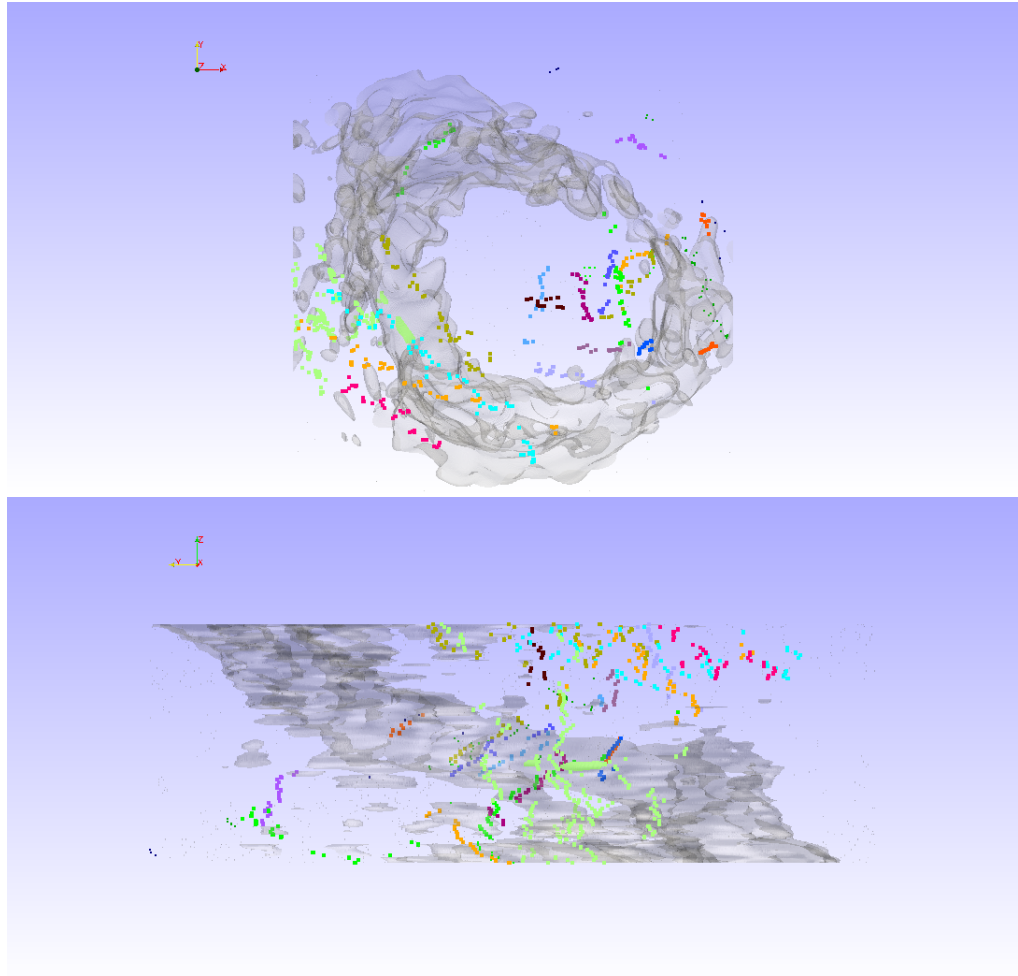


Figure 5.16: *A rendering of the external vortices not included in figure 5.15.*

The iterative algorithm also produced a phase distribution with a collection of vortices outside the C arc opposite the gap (shown in light green in figure 5.16). These were not expected from simulations the lack of these in the retrieved phase from an ideal simulated series of images shows these are not an artefact of the phase retrieval algorithm and are due to some experimental conditions not captured in the simulation. This phase retrieval analysis gives evidence for the OAM of the produced C-shaped intensities and is broadly consistent with the vortex trajectories predicted by simulations.

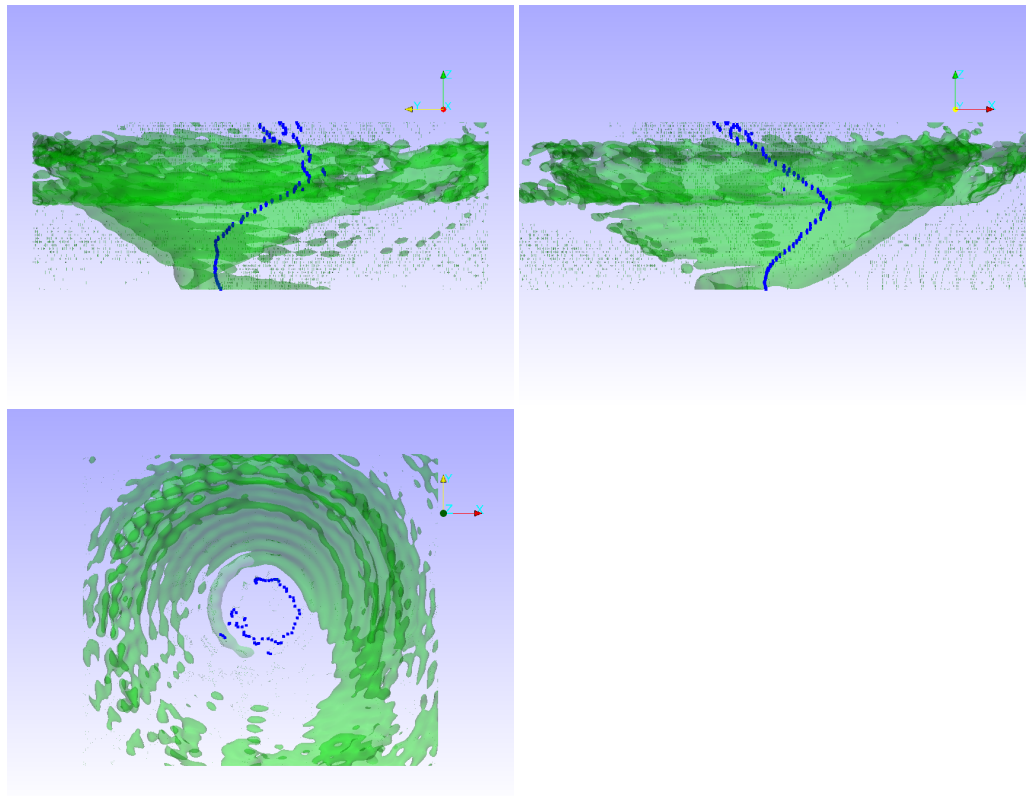


Figure 5.17: *Simulated vortex trajectories (blue dots) for large defocus of a  $\alpha = 45^\circ$  C-shaped function. The green volume encloses high intensity regions.*

### 5.2.3 Lithography of C shape and energy filtered imaging

C-shaped beam intensity could be used in the formation of split ring structures for metamaterials for light on the micron scale or for electrons at the nanometer scale. C-shaped electron vortex beams can be directly used in coherent electron beam lithography, for example, producing nanostructures by exposing direct writing electron beam resists to such beams [137]. The advantage is that no scanning beam is used, as such all the intensity interacts with ‘virgin’ resist and the achievable resolution is not limited by any previous exposures of the resist. Currently methods are being developed to utilise the electron probe in a STEM to construct materials by moving individual atoms or causing structural changes at the nanoscale [138][139]. This has mostly been limited to two dimensional patterning however experimental methods such as focused electron beam induced deposition (FEBID) have been shown to produce three dimensional spirals [140]. In this emerging field, electron intensity shaped in three dimensions will be extremely useful as it allows intensity to be defined in all three dimensions simultaneously, potentially speeding up the writing process by removing the need for separate probe positioning steps. The central left inset in Fig. 4.12 E shows the regions of high intensity which form a spiral close to the focal region. This high intensity spiral could be used to produce chiral spiral structures or spiral crystalline volumes where scanning a focused probe may otherwise be time consuming or alter the resist through its entire thickness.

The C-shaped beam produced in section 5.1 was used to lithographically imprint a C shape into a resist. This could have a benefit over scanning a focused probe in that all of the C can interact with new resist, this is important for inorganic resists such as  $AlF_3$  for which a focused probe causes beam damage around the interaction region, coating the walls surrounding the probe with metal [141]. Previous research using  $AlF_3$  has shown it can be used as a self developing resist. Under lower electron beam irradiation, the  $AlF_3$  is reduced to fluorine and Aluminium, for higher irradiation holes can be produced [142]. In 1985 it was shown by Murray et al. that holes can be produced down to  $2nm$  diameter [143] and lines of linewidths  $5nm$ . This resolution still compares favourably to modern resists [144] such as PMMA (line widths of 3-4 nm) and HSQ (line widths of 6 nm).

Using a pre-shaped probe provides a one-step stamping method, avoiding the effect of previous pixel interactions when scanning a C shape. This could find uses in the production of intricate or curved shapes such as split ring structures for metamaterials and plasmonic applications.  $AlF_3$  was chosen to test the lithographic potential of C-shaped illumination due to its self developing nature allowing instant feedback on the mechanism and not requiring transfer of the sample from the electron microscope. The  $AlF_3$  was deposited by thermal evaporation from a crucible at a rate of 1.5 – 2 angstroms per second and a thickness of approximately 50nm was achieved. A thin C-shaped hole was produced in the film as shown

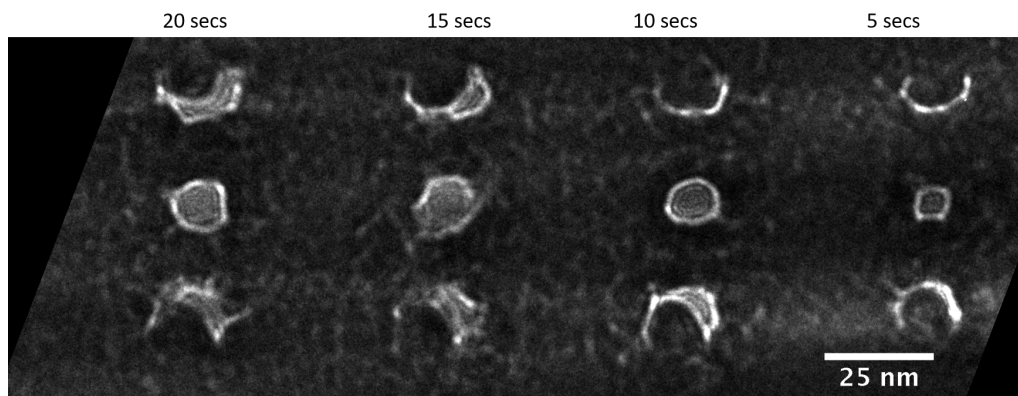


Figure 5.18: *A bright field TEM image of  $AlF_3$  substrate after illumination with C-shaped electron diffraction pattern. The three main diffraction orders produced sets of curves either side of a dot, diffraction axis is along the vertical. The horizontal bars are due to the defocused shadow of the condenser aperture bars.*

in figure 5.18, the 5 second exposure is shown in figure 5.19 along with an intensity line plot showing that the image of the patterned film shows line structure which is narrower than the image of the probe used to form it. The explanation for this C shape on the image is that the resist has been removed or reduced to decrease the thickness in the area exposed thus forming a bright section in the bright field TEM image. This suggests that the resist was only fully removed where the beam intensity was the highest, after an exposure of 5 seconds. Another brief exposure ( 10 seconds) to the electron C-shaped beam the  $AlF_3$  resist showed a section which has undergone beam induced reduction leaving behind  $Al$  metal. This is evidenced by the energy filtered TEM image around 15eV in figure 5.20 which is the bulk plasmon of  $Al$  metal. However whilst testing this method it was

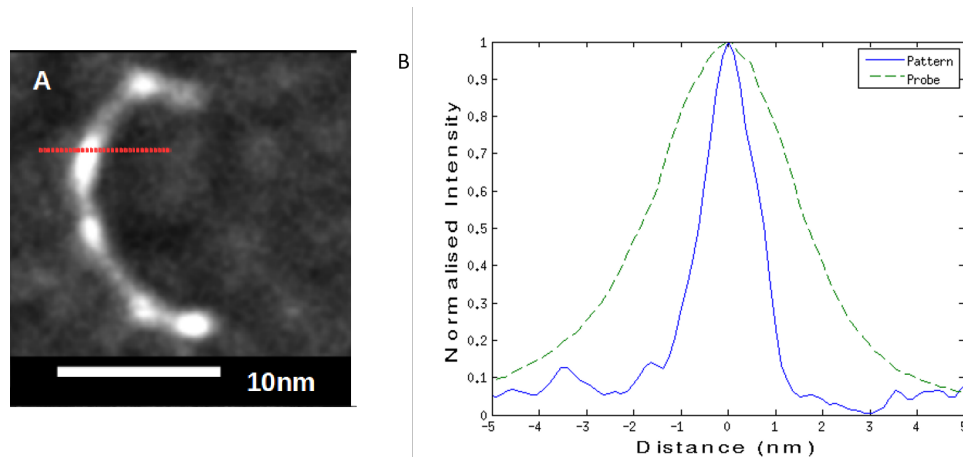


Figure 5.19: A) The 5 second Bright field TEM from figure 5.18. B) A comparison of a lineplot through the center of the 5 second exposure C shape shown in (A) with a similar lineplot of the intensity recorded of the C-shaped beam with no sample.

noticed that Al builds up in the center in addition to around the C curve. If left for longer periods of time the aluminium builds up in an outline of a C, as is shown for the energy filtered image of figure 5.21 showing the Al bulk plasmon of 15eV. These points are both evidence for Al being ejected away from the beam during the interaction, which is consistent with the findings of Nikolaichik [142] and Chen et al. [145], who discuss the build up of fluorine bubbles which then collapse, dispersing Al away from the site of reduction. This means that the thermally deposited resist used in this experiment would not be suitable for large scale repeatable production of C-shaped structures, single crystal layers of similar resists may perform better and react more uniformly. The production of a C shape after the interaction shows that this method is feasible and would just require more suitable resists and procedures to be found. This was however outside the scope of this thesis project.

In the slightly defocused image of figure 5.18 the longer exposure times show an increasing size of the central spot. The rings seen in the image can be explained by Fresnel diffraction from the small hole created by the intense central diffraction order. A similar effect on the C shapes becomes more prominent for longer exposure times suggesting the 5 second exposure does not produce a hole straight away and it is only after 10 seconds that there is a C-shaped slit through which the electron diffracts to form the oscillations associated with Fresnel rings. The patterning in  $AlF_3$

was very difficult to reproduce exactly and the interaction was not even or predictable around the C. This could be due to large grain size in the thermally deposited  $AlF_3$  and shows that a different resist would be required, one with higher homogeneity and one which is less reactive under electron beam illumination, to offer more control over the patterning interaction. In addition these feasibility tests showed that using thermally deposited  $AlF_3$  is not suitable to leave a metal deposit at sites of high intensity due to the production of a hole surrounded by aluminium instead. Whilst the success with this resist was limited, these tests show there is potential for shaped electron beams to help in lithographic patterning of nanoscale structures with features below 10nm size. The C-shaped electrons described in this chapter could potentially be adapted to producing nanoscale variation in crystal structures following the spatial spiral structure shown in figure 4.12 similar to the reported work by [138].

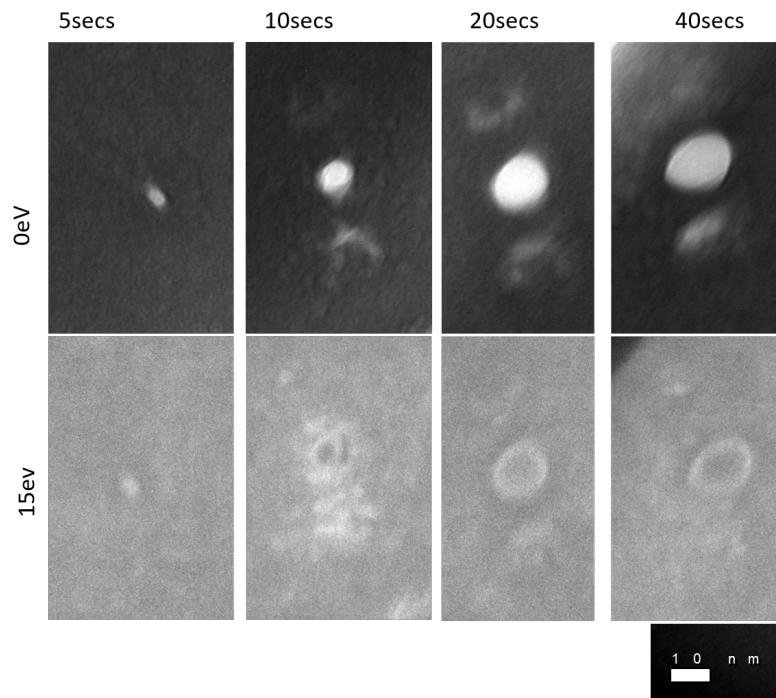


Figure 5.20: *Energy filtered TEM images of  $AlF_3$  substrate after C-shaped electron beam illumination for different exposure times. Recorded at 0eV and 15eV.*

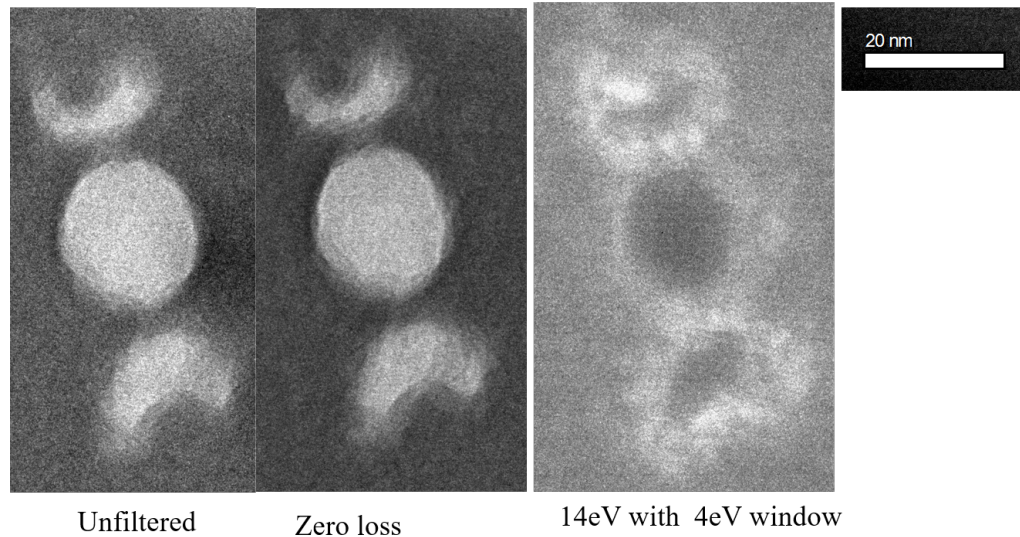


Figure 5.21: *Energy filtered TEM images of  $AlF_3$  after C-shaped electron beam illumination showing intensity around 0eV and 14 eV, revealing the build up of Al around the outside of the C shapes.*

### 5.3 Phase contrast masks

A second type of mask uses the same CGH as the amplitude contrast but now the binary values correspond to differences in thickness of transparent Silicon Nitride as shown schematically in figure 5.22. The silicon nitride membrane samples were ordered from Silson [146] and were in  $200\mu m$  thick octagonal substrates to fit the 3mm diameter aperture of the TEM sample holder, the membrane window area was  $250\mu m \times 250\mu m$ . To produce the phase contrast masks 200 nm thick Silicon nitride membrane samples were coated in approximately 50nm of Pt/Pd via plasma sputter coating. The function of this is 2 fold, to act as a conductive charge alleviation layer and to also reduce the electron intensity outside of a designated circular aperture. Initially a circular aperture was milled into the sample by removing the Pt/Pd layer and once uncovered the mask pattern was milled into the Silicon Nitride sample. The resulting phase contrast masks are shown in figure 5.23, the thickness was determined by energy filtered TEM (see chapter 1 section 1.13) to be 0.8 mean free paths (this mean free path has been estimated to be 135nm [147]). Figure 5.23 shows that the thickness profiles through the silicon nitride phase masks are closer to a sinusoidal oscillations rather than ideal binary steps.

The Silicon Nitride substrates were 3mm diameter and as such

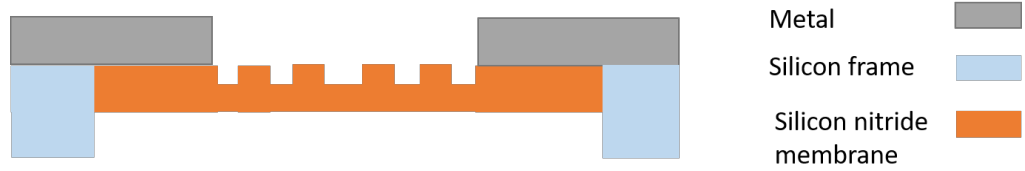


Figure 5.22: A schematic of the Silicon nitride phase masks.

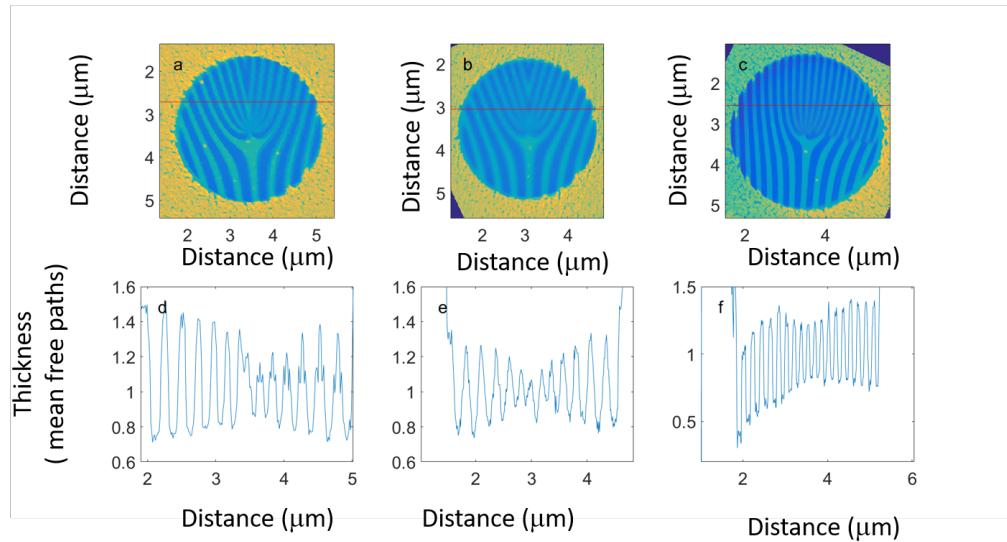


Figure 5.23: Thickness maps from EFTEM of the produced phase contrast sample plane masks. a) the mask for  $\alpha = 45$ , b) the mask for  $\alpha = 45$ , c) the mask defined with  $\alpha = \text{atan}(y/x)$  (d,e,f) Thickness plots across red lines in (a,b,c), distances are in  $\mu\text{m}$  and the thickness are in units of mean free paths.

could not fit into the 2mm condenser aperture and needed to be placed in the sample plane of the JEOL 2200 TEM. Free lens control was used during low mag mode (see chapter 1) section 3.3), lenses IL1 and IL3 were used to bring the diffraction pattern into focus on the CCD and lens IL1 was used to vary defocus. The ratio of the widths for the milled and unmilled sections of the masks produced in this manner varies from the ideal CGH. The ideal mask is produced by a binarisation procedure which distinguishes areas on the interference pattern above and below a threshold, taken to be the minimum value plus 0.5 of the range of values. If this value is higher or lower than the threshold then one set of bars will become wider and the other narrower. This relative width change produces intensity in a diffraction order at lower wavevectors (angles) than would be expected from an ideal mask as shown in figure 5.24. This can be seen for a simple

1D case in figure 5.24 and for the C shapes in figure 5.25, where the second order is not present when the step and gap widths are equal however it is present when step and gap widths are unequal.

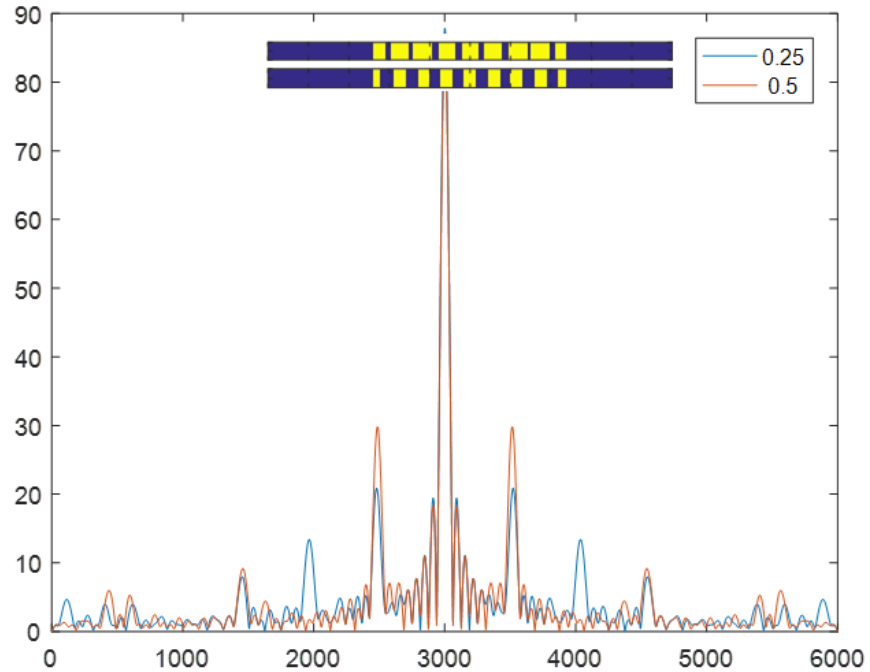


Figure 5.24: *Simulated results: Fourier transforms of two 1D phase gratings with different bar width ratios. A more uneven bar thickness ratio leads to intensity in the otherwise 'missing' second order.*

In addition to uneven barwidths, the overall phase change induced by the mask will deviate from the ideal  $\pi$  phase change. This will prevent the destructive interference possible in the ideal case and allow intensity into previously missing diffraction orders, most notably the zeroth order (see figure 5.26).

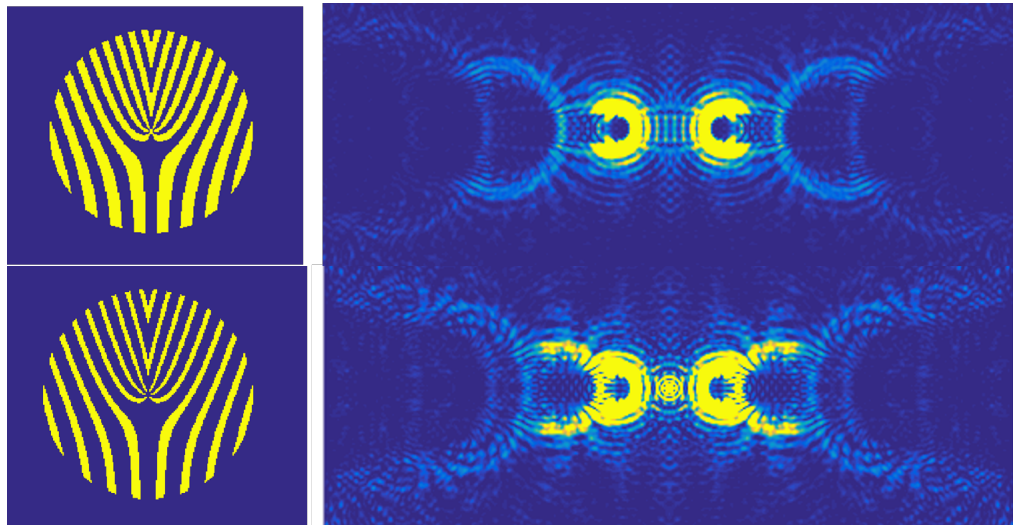


Figure 5.25: *Simulated results: The effect of varying bar thickness on the diffraction orders present in the Fourier plane. The top has equal bar widths with an average cut off value of normalised intensity of 0.5 . The lower images have a cut off value of 0.25 giving a bar width ratio of 1:3, this allows intensity at smaller wavevectors.*

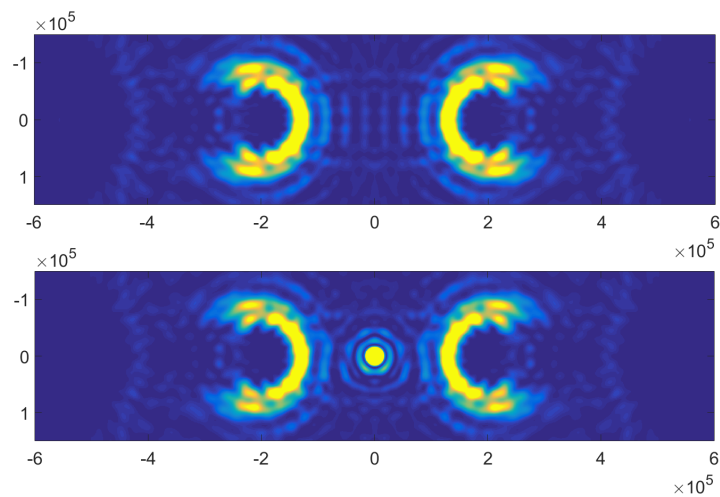


Figure 5.26: *Simulated results: The effect of varying phase contrast between binary sections on the diffraction orders present in the Fourier plane. The top has an ideal phase contrast of  $\pi$  however the lower image is formed from a mask with  $0.75\pi$ , as such the central order no longer has destructive interference.*

### 5.3.1 Phase contrast mask for a C with $\alpha = 22.5^\circ$

For the values  $m = 7.91$  and  $c = 2.09$  the predicted half opening angle is  $22.5^\circ$ . The computer generated hologram is shown along with the mask produced and the resulting electron Fourier plane diffraction pattern intensity in figure 5.27 b.

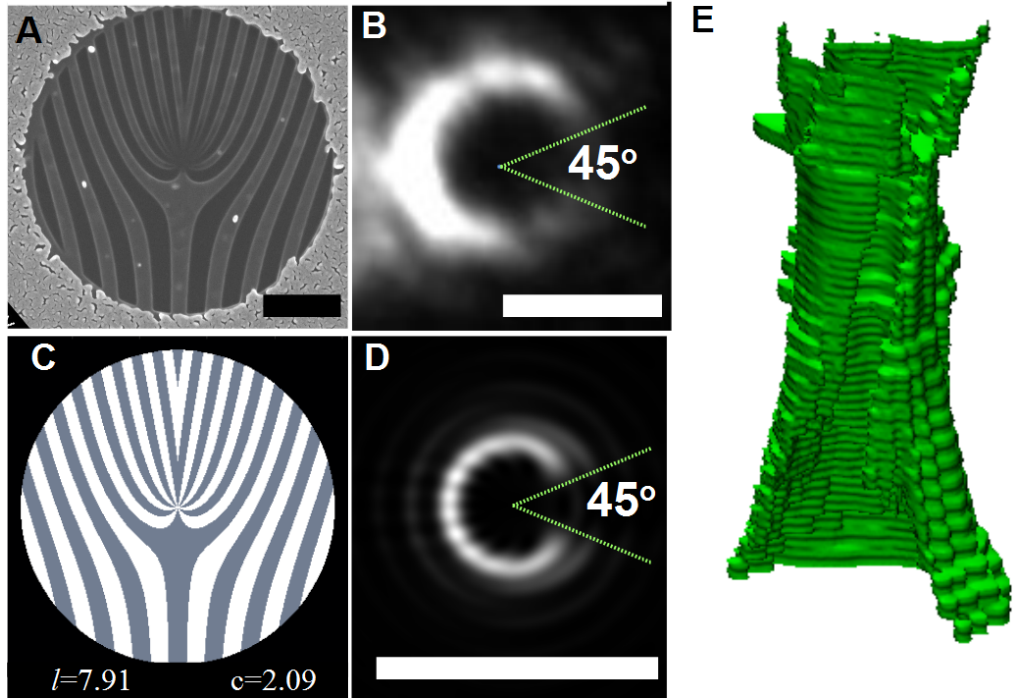


Figure 5.27: A) An SEM image of the Silicon Nitride membrane phase mask B) the Fourier plane intensity of the right 1st diffraction order C) the input hologram used to produce the mask in (A) D) the simulated C-shaped target intensity. E) A rendering showing the region of high experimental intensity as a function of propagation. Scale bars are A)  $1\mu\text{m}$ , B)  $500\mu\text{m}$  and D)  $1\mu\text{rad}$  (for a  $200\text{keV}$  electron with an optical system with a  $0.016\text{m}$  camera length).

As can be seen the angle produced experimentally matches well with the simulation however the lower part of the C-shaped structure is less intense than the upper part. The reason for this is not known however it could be related to the limitations in producing the central region of the mask which requires very fine bars, another possibility is due to imperfections in the physical mask such as remaining bits of Pt or varying thickness. The opening angle can be made more visible by varying the contrast in

the image. A comparison of the normalised azimuthal intensities, shown in figure 5.28, shows the good match between the simulated intensity opening angle and the experimentally produced intensity. The reduced intensity in the lower section of the C is shown by the lower values on the right hand side of the plot. When normalised for values between 0 and 1 the experiment is much lower than the simulation, this is potentially due to a lower efficiency than the simulation leading to a zero order of increased brightness. Overlap with this bright order thus makes the C shape intensities further away (at smaller angles towards the center of the plot) less intense relative to the peak value.

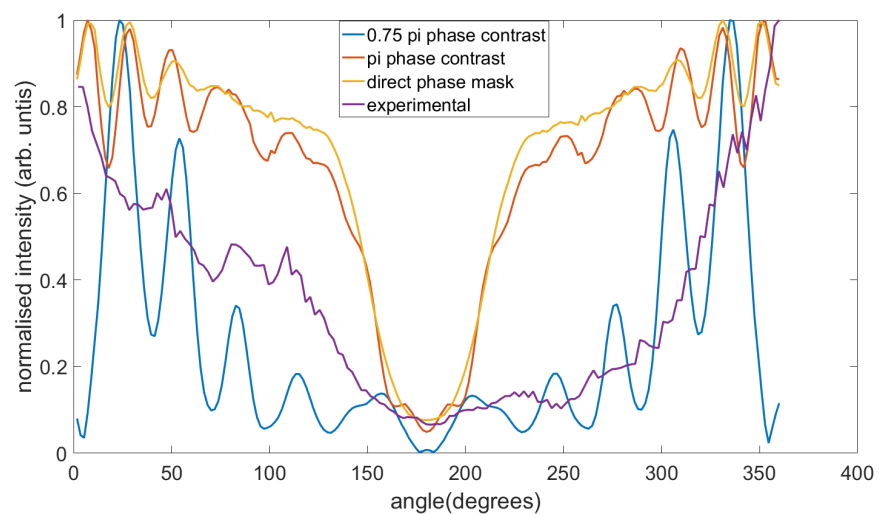


Figure 5.28: A comparison between the simulated azimuthal intensity distribution and the experimental azimuthal intensity oscillations. For a direct phase mask, a phase contrast CGH mask with  $\pi$  and  $0.75\pi$  phase contrasts.

Simulating a phase contrast mask with the ideal  $\pi$  phase shift produces a diffraction pattern without zeroth order intensity. This matches well with the relative intensities predicted by a simple direct phase mask only producing an isolated C shape. However when a phase contrast of  $0.75\pi$  is used the intensity is reduced around the C. The experimental intensity suffers from overlap with zeroth order intensity and as such the intensity profile is more like the non ideal phase contrast. However this zeroth order intensity could be due to other imperfections in the mask such as bar widths. The peaks do align approximately with both the phase contrasts of an ideal  $\pi$  and a reduced  $0.75\pi$ , suggesting the phase profile of the experimental C is as expected and different OAM modes

interfere to produce these fringes. The propagation of the first order from the diffraction mask is also shown in figure 5.27 where the presence and rotation of the gap are shown. This matches what is expected from the theory of chapter 4 and gives evidence that the beam produced has the phase characteristics the experiment aimed to create.

### 5.3.2 Phase contrast for a C with $\alpha = 45^\circ$

For the values of  $m = 6.11$  and  $c = 3.89$  the half opening angle is predicted to be  $45^\circ$ . Using these values the CGH mask produced the experimental electron Fourier plane intensity shown in figure 5.29. When compared to the previous 22.5 mask the higher orders have a higher intensity relative to the first diffraction order. This can be seen by a comparison with figure 5.27. This is related to the bar width ratio between thick and thin sections of the mask. As can be seen from figure 5.29 the mask produced has uneven widths compared to the input CGH.

By making the ratio uneven one section has more intensity than the other, thus one thickness dominates and the destructive interference does not reduce the intensity as much. This means more intensity is found in the previously missing second order compared to figure 5.27. The simulated intensity shown in figure 5.29 uses a threshold value of the minimum plus 0.25 of the range, giving uneven bar widths and intensity in the gap which would not be present for even bar widths. The astigmatism present means that a direct comparison to a circular intensity plot cannot be performed for this intensity,

however the opening angle is clearly larger, showing the successful control of the opening angle via the control equations in section 4.1.2. Qualitatively the experimental intensity is recreated well in the simulation even without astigmatism. The simulated intensity shows peaks of intensity in the center and the tips of the C shape with fringes in the gap due to overlap with a neighbouring C shape of a higher order. When counting the fringes in the opening there appears to be an extra fringe in the experimental image potentially caused by astigmatic deformation of the C shape. Even with the experimental distortions the through focus series still shows a robust gap which slowly rotates with propagation as shown in figure 5.30, the green volume encloses the C-shaped intensity whilst the red volumes

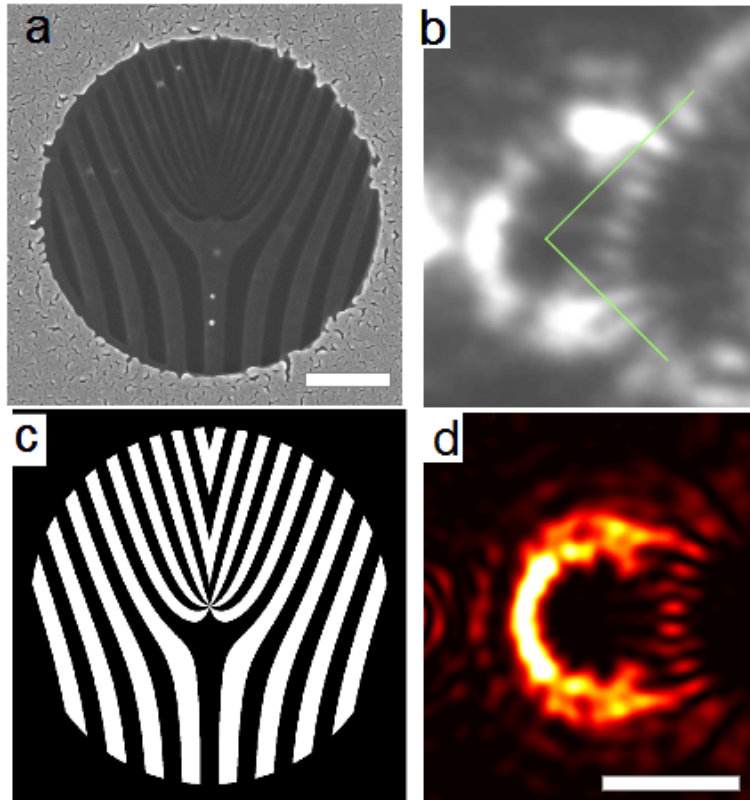


Figure 5.29: A) (scale bar  $1 \mu\text{m}$ ) An SEM image of a phase mask designed to produce an  $\alpha = 45^\circ$  C shape. B) the recorded intensity in the first diffraction order C) the CGH used to produce the mask. D) the simulated intensity from the mask including uneven barwidths. (scale bar  $5 \mu\text{rad}$ )

show the tips and center of the C curve which have higher brightness than the rest of the curve. The astigmatism breaks up the high intensity red region into three sections. The two red sections closest to the camera in figure 5.30 are the tips and the foremost gap is the opening. The back red volume is the central intensity opposite the opening. This is similar to previous renderings with the gap rotating however there are two extra breaks around the C shape. These results show that it is difficult to produce even bar widths however the mask did successfully produce C-shaped electron vortex states with a controlled opening angle.

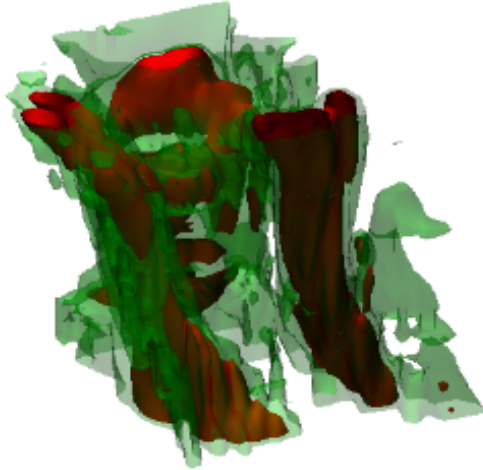


Figure 5.30: *Rendering of recorded intensity defocus series of the first diffraction order C shape from phase contrast mask for  $\alpha = 45^\circ$ . There are 3 main columns of high intensity shown in red, the left and right at the front of the image, correspond to the top and bottom of the C shape and the central red column at the back is the section of the C closest to the zeroth order. The gap between the front two red sections is the gap of the C shape and shows slow rotation as expected.*

### 5.3.3 Phase contrast mask for a C defined with an angular co-ordinate rotation

In addition to the C shapes described previously there is another degree of freedom when producing these C states, namely the relative orientation of the C shape. This is achieved by using a different angle definition in equation 4.1 of chapter 4. If a definition of  $\phi = \text{atan}(Y/X)$  instead of  $\text{atan}(X/Y)$  a diffraction pattern where the openings point up and down can be produced. A phase mask designed to produce this along with its Fourier plane intensity, is shown in figure 5.31. As can be seen from both experiment and simulation the openings for orders on opposite sides must be related by a rotation of  $180^\circ$ , in this case the openings are up and down instead of left and right. This shows the reflection symmetry plane cuts the discontinuity line in the phase mask. The experiment shows the same intensity distribution as the simulation with many of the fringing effect

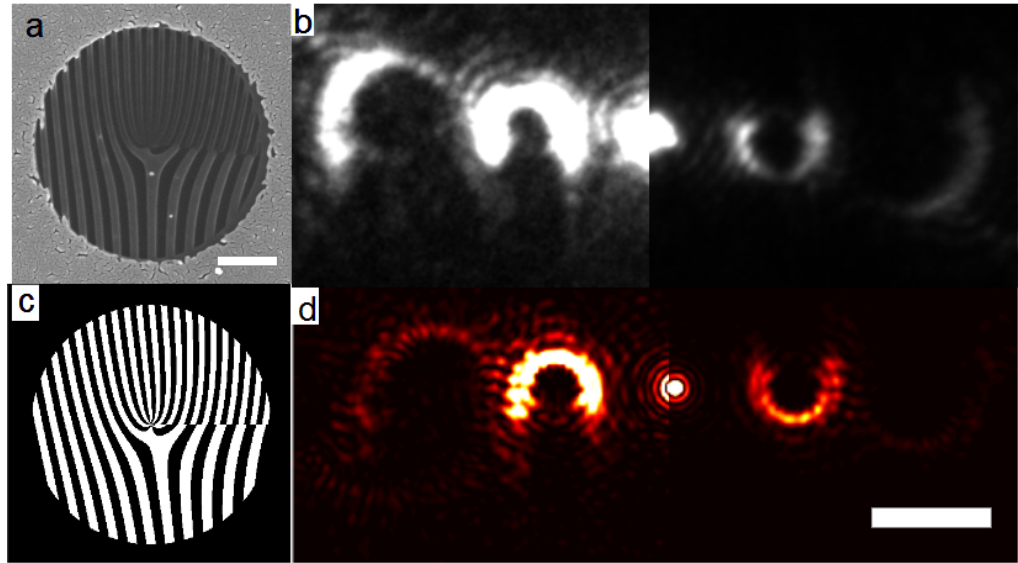


Figure 5.31: a) (scale bar  $1 \mu\text{m}$ ) SEM image(left) of a phase mask designed to produce a C shape with the opening along the vertical line perpendicular to the diffraction axis. b) The diffraction pattern of the mask in (a). Due to symmetry of the measured pattern the experimental intensity is shown with two different contrasts for the left and right side.c) the CGH pattern used to produce the mask d) simulated diffraction pattern from such a mask, also shown with two different contrasts for the left and right sides. Scale bar in d applies to both b and d , and is  $10\mu\text{rad}$

reproduced. There is again an issue with low intensity in the right order at the base of the C. The propagation of the first three orders either side of the central beam is shown in figure 5.32, the grey volume outline the regions of high intensity with the green volume being the highest intensity inside this. This experimental data shows the openings are maintained with slow rotation and that they occur on opposite sides of the propagation volume. The size of the opening also appears to follow the predicted opening angle of  $45^\circ$  well.

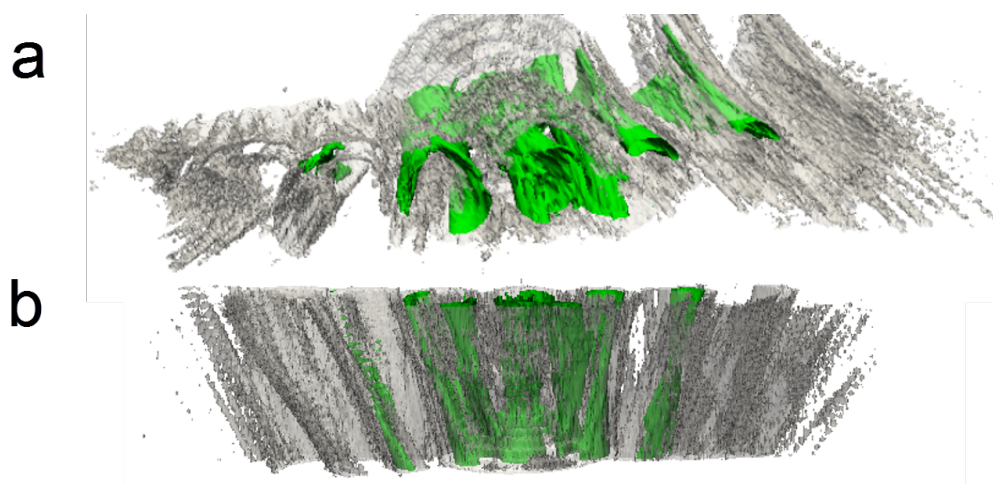


Figure 5.32: Experimental results: *a) a view along the propagation of the first 3 diffraction orders from the mask shown in figure 5.31 showing 6 C shapes and the zeroth order. Grey regions are of medium intensity and green volumes enclose the high intensity regions. b) a side on view of the same set of diffraction orders as in (a).*

### 5.3.4 C shapes produced with a blazed phase contrast mask

The phase contrast masks can also be altered to include a blazing phase ramp from one side of the mask to the other. This means the height follows a path similar to a saw tooth function. This acts to divert intensity preferentially into one sign of diffraction order as shown in figure 5.33. This mask was produced by starting with the interference CGH (from section 3.2) instead of a step function the left hand sides of the bars in the binarised mask were then used to define the start of individual phase ramps in the x direction (perpendicular to the phase discontinuity). The experimental intensity distribution shows that the right order is brighter than the left, however the C structure is less well defined than the other masks in this chapter. The intensities for the at focus image in figure 5.33 are 59.8% in  $0^{th}$  order 25.74% in the right order and 14.47% in left order, as percentages of the total intensity of the 3 orders. So, whilst the blazing did not make the right order the most intense, it did increase the intensity above the left order. This suggests that a different phase gradient may redirect more intensity into the right order, if it is matched to the wavevector of the first diffraction order.

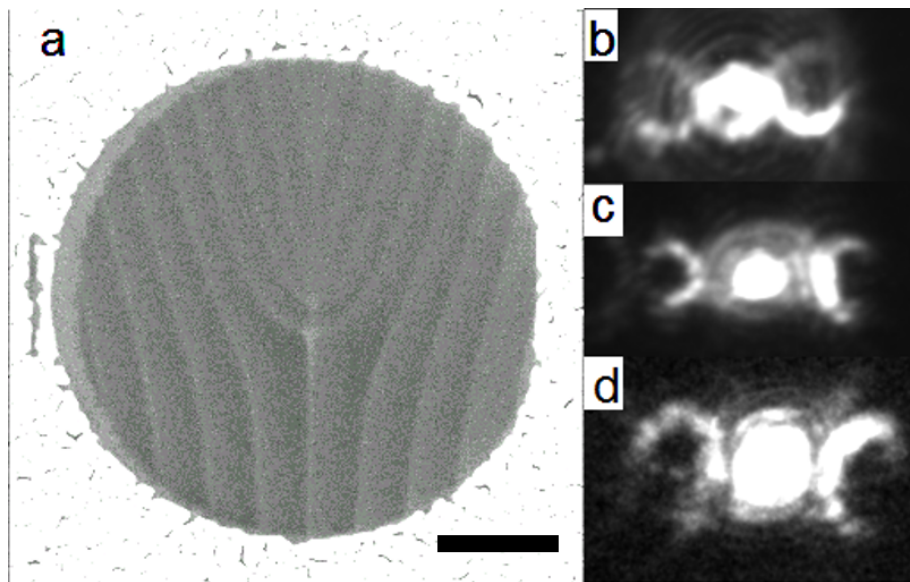


Figure 5.33: *a)*(scale bar  $1\mu m$ ) a SEM image of a blazed phase mask designed to produce a C shape. (contrast has been altered to improve visibility of pattern) *b-d)* the recorded diffraction pattern at 3 different intermediate lens voltages giving a defocus before (*b*), at (*c*) and after (*d*) focus.

## 5.4 A C-shaped electron produced by a direct phase mask

An alternative method is to use the transparent Silicon nitride to directly imprint the desired phase onto the electron beam ([53]). This was done using the mask shown in figures 5.34 . The drawback of this method is the presence of usually unwanted zeroth order. This unwanted order lead to interference patterns in the intensity as shown in figures 5.34 and 5.35. The C-shape is now split into prominent segments after interference with the unwanted order. There is also internal structure inside the arc when at defocus. These can be used to asses the presence of phase singularities as it is essentially performing a sort of in line holography between the C shape beam and the unaffected beam. These intensity distributions can be modelled with interference between the C wavefunction and a spherical wave. Close to focus the spherical wave component causes a bright spot to appear along with the C shape (see figure 5.34 d). Upon propagation close to focus this dots forms a 'bullet' of high intensity as can be seen in figure 5.35 and at larger defocus there is a large amount of fringing and distortion present in the C shape, compared to just the C on its own. Simulations can recreate the experimental intensity seen when defocusing the C-shaped beam, by using a phase contrast of  $0.75\pi$  and by including astigmatism with  $A = 0.5$  (figure 5.34 columns 3 and 4), yet the at experimental at focus intensity is reproduced by simulations with no astigmatism. This suggests that the experimental procedure for varying the defocus also added astigmatism into the beam. This experimental data shows C-shaped electrons can be made via direct phase alterations allowing them to be produced by methods other than CGH masks.

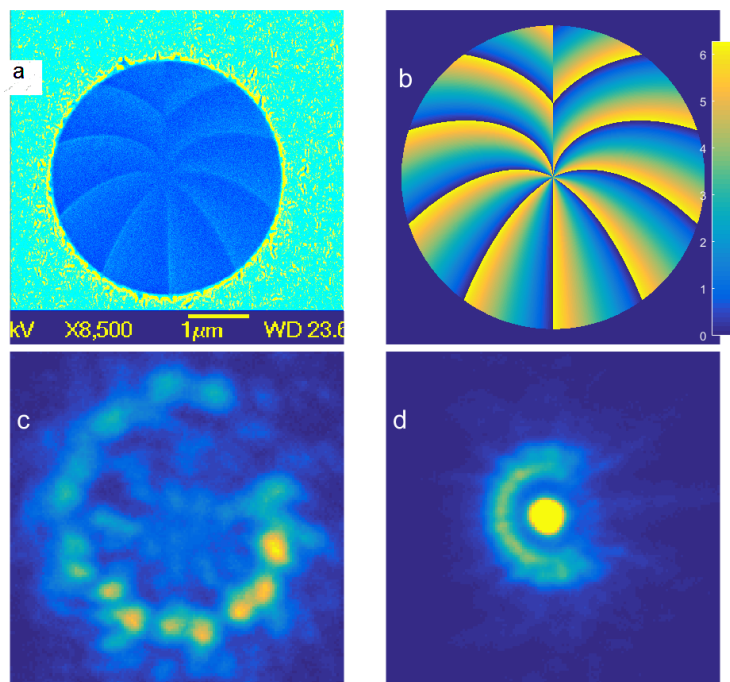


Figure 5.34: a) SEM image of the direct phase mask.(contrast has been altered to improve visibility of pattern) b) the input phase distribution used to produce the mask.c) defocused experimental intensity.d) at focus experimental intensity

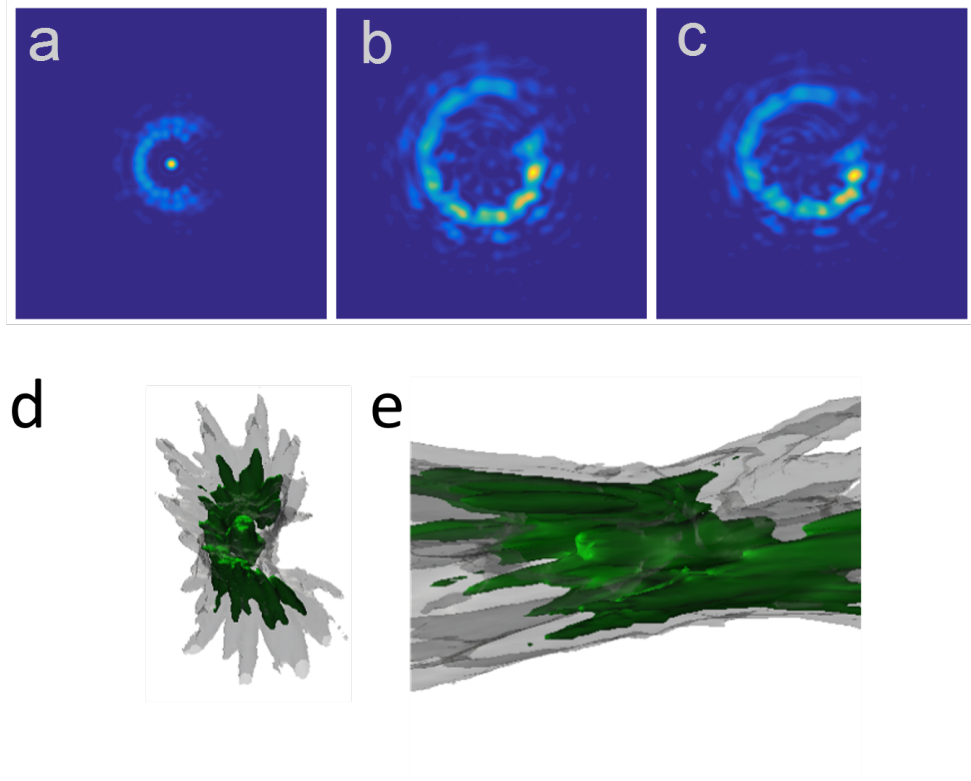


Figure 5.35: (a,b,c): *Simulated intensity distributions for a mask with phase distribution  $0.75 \times \text{mod}(\text{ideal phase}, 2\pi)$  (mod is remainder function) for a) at focus b) defocused with no astigmatism (middle) and c) defocused with astigmatism coefficient  $A = 0.5$ . (d,e) recorded intensity propagation of C-shaped electron formed by a direct phase mask d)view along propagation e) view side on to propagation. Grey regions are medium intensity and green regions are high intensity.*

## 5.5 Chapter summary

This chapter has detailed the experimental production of the C-shaped vortex states described in chapter 4. The intensity produced by an amplitude Pt foil mask placed in the condenser aperture was shown for both TEM mode and NBD mode (see section 3.1 for ray diagrams). An estimate for the phase of the electron was retrieved from the recorded amplitude using iterative methods. Vortex trajectories were then plotted from the retrieved phase of images recorded for different defocus values. These showed a clear set of vortices within the C arc with additional vortices outside the arc, not present in simulation suggesting the non uniform aberrations of the physical environment in the microscope cause distortions and extra vortices to appear. One benefit of using an amplitude mask is that the edges of the binarised image can be more clearly defined, allowing a C shape closer to the ideal simulation. The results from direct write lithography with the C shape produced in TEM mode was then shown. The  $AlF_3$  resist did show patterning in the shape of a C but to improve the reproduction of the C other resists with high resolution could be explored.

The intensity produced in low mag mode from sample plane Silicon Nitride phase masks was then shown for two different opening angles, a blazed phase mask and a direct phase mask. Improvements to these masks mostly rely on the nanofabrication procedure where it may be possible to use smaller ions such as Helium to pattern higher resolution masks. Processes other than FIB could also be investigated to see if a less random procedure could produce more equal thickness variations. Within the JEOL 2200FS microscope, using the condenser aperture in TEM mode produces C shapes which are much brighter than the sample plane phase masks used in low magnification mode. If phase masks could be made to fit the smaller condenser aperture then the intensity falling on the mask could be increased and the phase masks should show higher intensity C-shaped electrons than the equivalent amplitude masks. This is the first time such C-shaped vortex states have been produced for photons or electrons, applying the techniques developed for integer vortex electron shaping to a separate state with fractional OAM. The C-shaped electron states produced here highlight the flexibility of the phase shaping method and provide a new experiment where the wave model of electron interference is useful for predicting experimental results.

# Chapter 6

## Simulation of 2D chiral plasmon vortex modes

STEM EELS has proven itself a useful tool for characterising plasmon modes [148], a useful review has been produced by Colliex et al [149]. This has mostly been for two dimensional structures but some studies have measured interactions with three dimensional plasmon modes, such as those in nanocubes. In 2D, the bound waves measured so far have been modes reflected from either flat surfaces or circular boundaries. An interesting situation arises when the radius of the boundary is nonuniform. As discussed by Kim et al. [45], in this case reflections from the edge will add up to give a wave travelling at an angle to the radial direction, adding a circulation to the plasmon oscillation. The increasing distance from the central region gives a phase delay proportional to angle, as is required for a vortex mode. Initially this chapter will review the plasmon modes which have been found for nanodisks, previously discussed in the literature. It will then be shown that the eigenmodes of the nanodisk can be transformed by adding spiral steps, breaking the circular symmetry. This causes the contributions from OAM modes of  $\pm l$  to become unequal, giving the plasmon eigenmode OAM.

## 6.1 Nanodisk simulations with COMSOL

Simulations of a nanodisk have been performed in COMSOL to compare with previously published modes found [148]. Hobbs et al. used a line current excitation and the frequency domain solver, the solutions shown in this thesis used no excitation and the eigenvalue mode solver. The modes of oscillation should be similar in nature regardless of the solution method. It was found that both the edge 'SP' solutions and centered 'CP' solutions were found by the eigenvalue mode solver, matching the amplitude and phase distributions found by Hobbs et al. The energies of these modes are higher than reported by Hobbs et al, the simulations which produced figure 6.1 used an ideal cylinder of aluminium and used the built in Aluminium and Silicon nitride materials. The modes distributions corresponding to this plot are shown in figure 6.2.

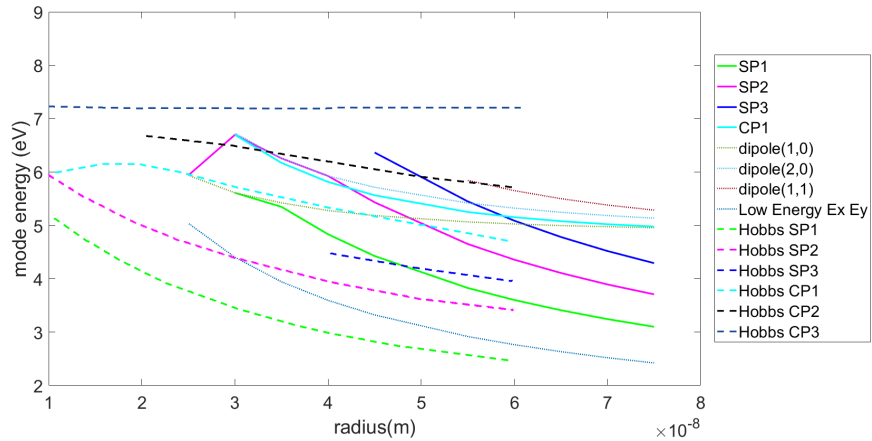


Figure 6.1: A comparison between the modes found via the eigenvalue solver method and the published modes from a frequency domain solver [148]. For Aluminium nanodisks of different radii.

The Hobbs et al. paper uses a 2.6nm aluminium oxide shell, curved corners with 3nm curvature radius and constant dielectric values for Silicon Nitride and Aluminium Oxide of 2.4 and 1.88 respectively. Including these conditions the eigenvalue solver finds a CP1 mode at very similar energies to the published results as shown in figure 6.3. However, when using these conditions the eigenvalue solver did not find any SP modes. Simulations of a 30nm silver nanodisk on 100nm Silicon nitride have also been performed, when comparing to the published values report by Schmidt et al.[92], the centered breathing modes were found at similar

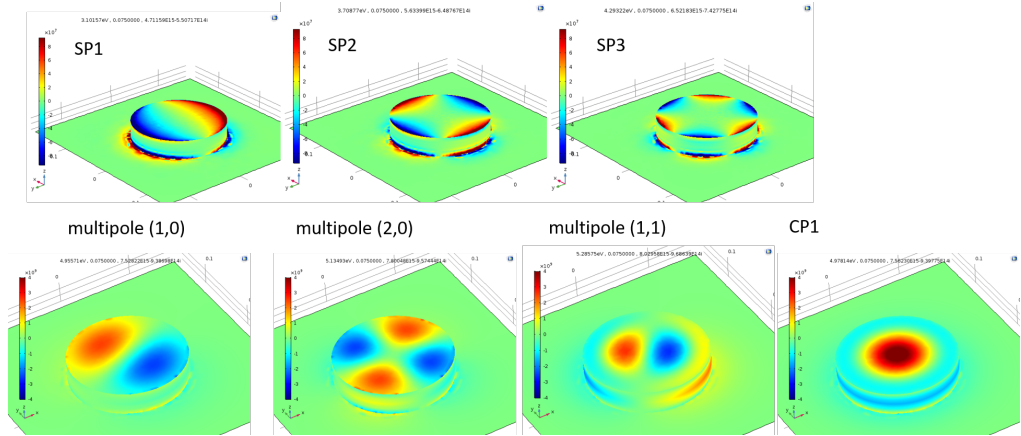


Figure 6.2: The mode distributions of  $E_z$  field for the SP, CP and multipole modes in figure 6.1.  $(l,p)$  nomenclature signifies the number of azimuthal nodes  $l$  and radial nodes  $p$ .

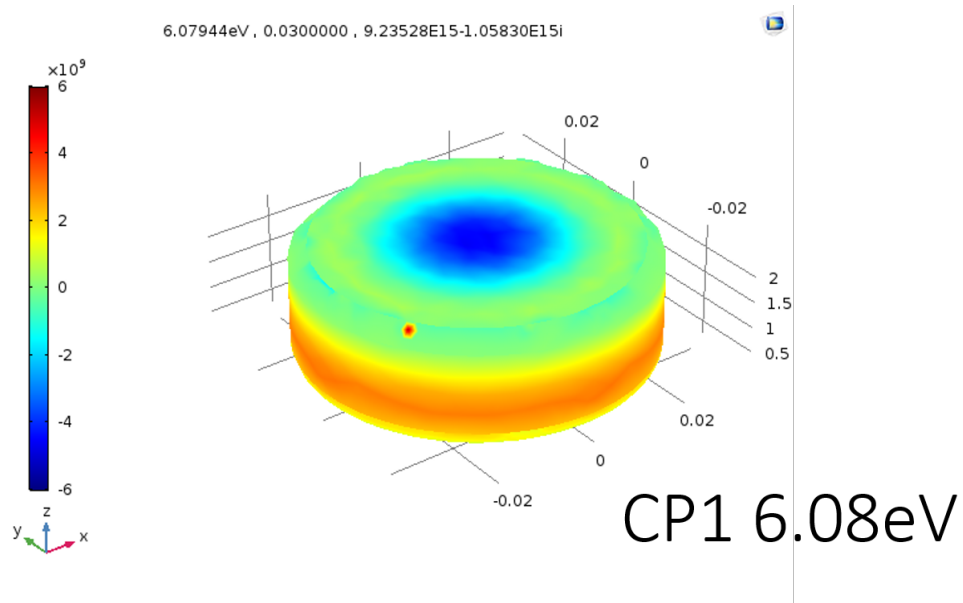


Figure 6.3: A simulated mode for a 30nm radius disk including a 2.6 nm AlO shell, 3nm curvature rounded edges and a constant Silicon nitride and aluminium oxide dielectric values of 1.88 and 2.4 respectively. The energy of the CP1 mode energy matches that of Hobbs et al. Dimensions are in  $\mu\text{m}$ .

energies, however the edge modes (similar to the SP modes of Hobbs et al) were not found. Whilst it is unclear what the cause of these discrepancies are, it is likely due to the use of perfect conductor boundary conditions during the eigenvalue solver, adding a certain amount of confinement, rais-

ing the energies. Whilst the energies only match the published values for some modes, the discussion in this chapter is only concerned with the mode distributions of amplitude and phase which all match the published modes. As such the exact energies calculated do not effect the conclusions of this chapter.

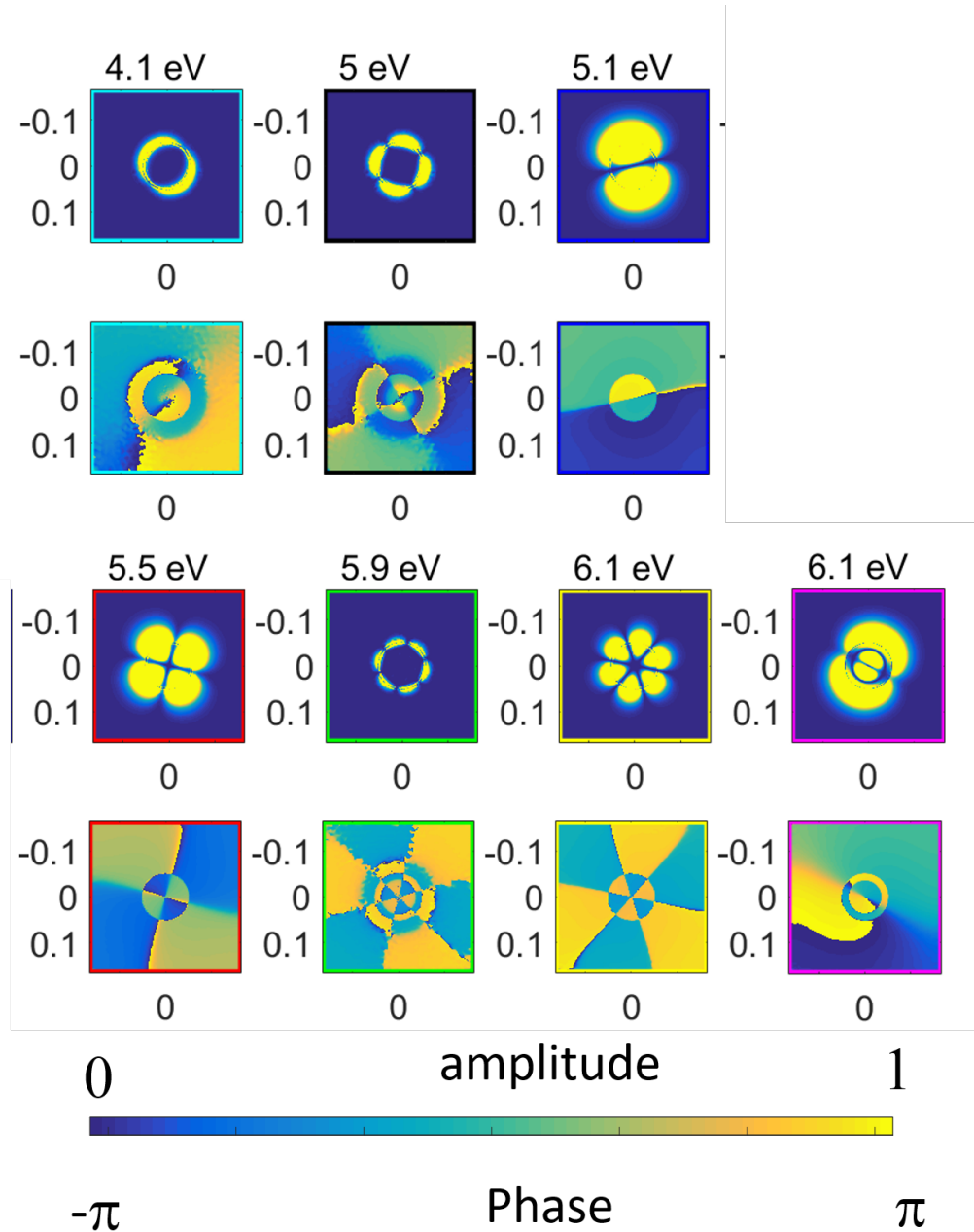


Figure 6.4: Rows 1 and 3 show  $E_z$  amplitude whilst rows 2 and 4 show  $E_z$  phase. The modes found via the eigenvalue modes solver for a 30 nm thick, 100 nm diameter cylinder of Aluminium on a 100 nm Silicon nitride membrane.

The localised plasmon modes have already been theoretically and experimentally discussed for nanodisks [92]. These studies have shown dipole like modes where there are multiple intensity lobes with a  $\pi$  phase shift between different sections. Figure 6.4 shows the calculated eigenmodes for a  $100nm$  Al disk, with modes showing an increasing number of intensity lobes and azimuthal phase discontinuities with increasing energy. The TBB mode decomposition of these modes is shown in figure 6.5, showing these can be considered as combinations of equal amounts of OAM modes of equal and opposite topological charges. This is shown in the approximately symmetric mode distributions.

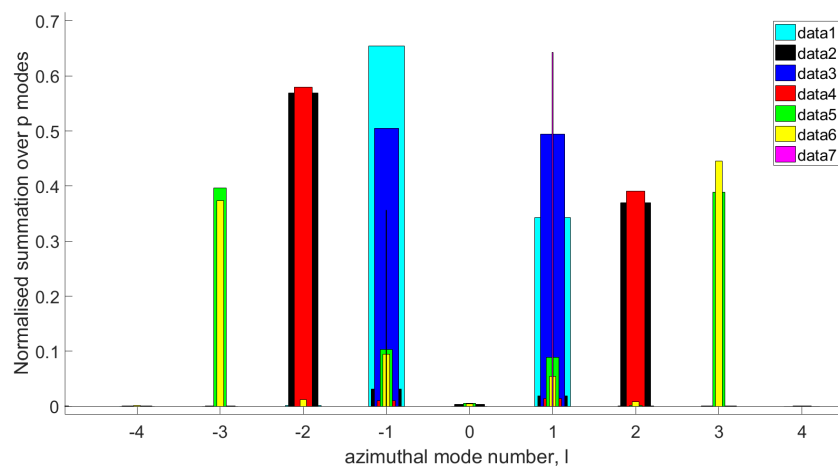


Figure 6.5: *OAM mode decompositions using a TBB basis set for a 100nm diameter nano disk . The colours match the modes shown in figure ??, as such data1 to data 7 are the modes from left to right in figure ?? . The outer radius of the spiral was set to a maximum in the bessel function.*

## 6.2 Chiral plasmon spiral simulations with COMSOL

To view the effect of adding a spiral step to a nanodisk, an  $l = 1$  spiral of  $135nm$  inner radius and  $50nm$  step size was simulated. The eigenmodes for this structure are solely at the edge boundary as can be seen in the modes of figure 6.6. The decompositions of these modes (shown in figure 6.7) shows a larger range of  $l$  values and increased asymmetry compared to the the nanodisk in figure 6.5. This shows evidence for the spiralling

boundary breaking the symmetry of the mode decomposition. To confirm this a further set of simulations were conducted, gradually increasing the spiral step radius for smaller structures to reduce the computation time.

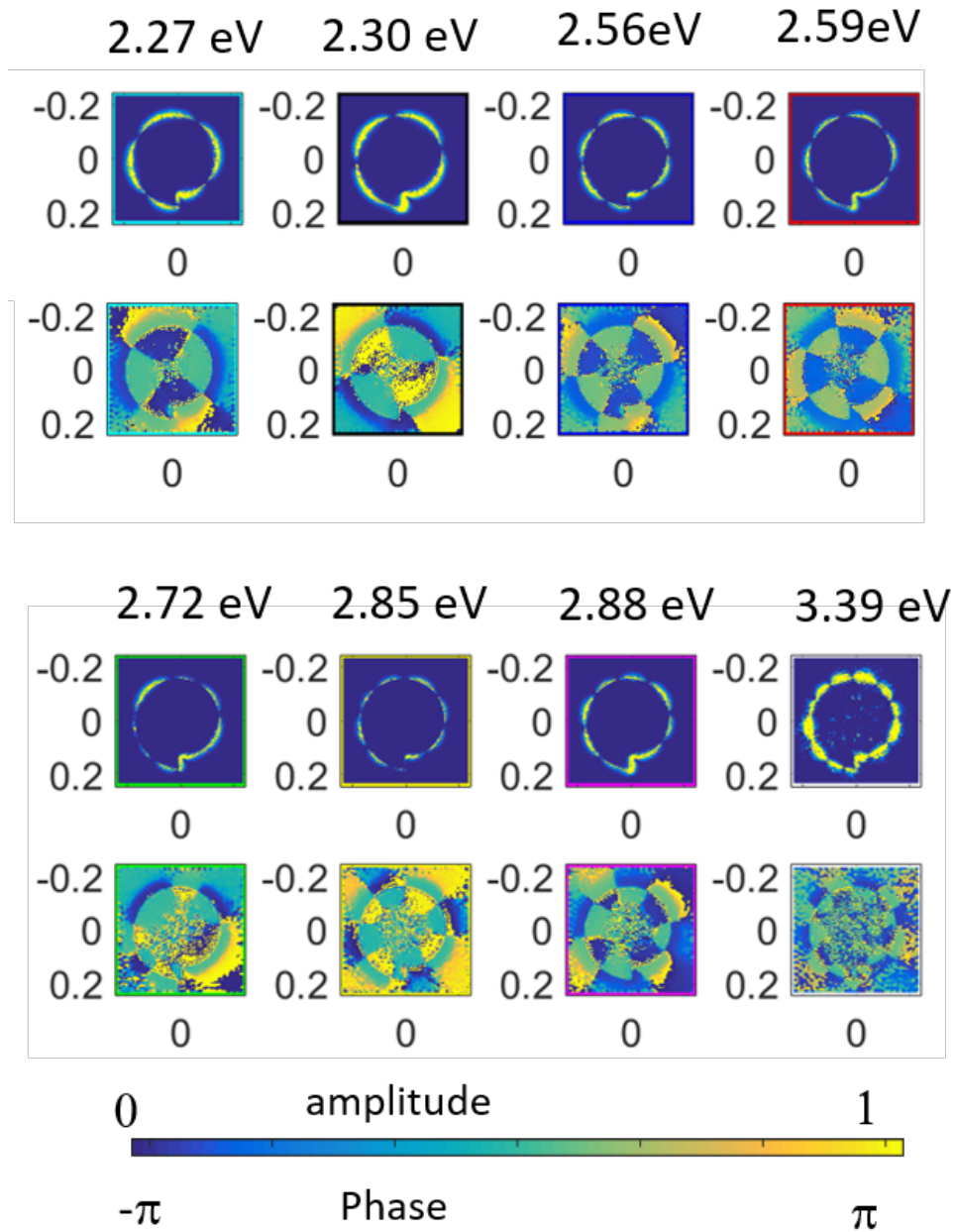


Figure 6.6: *The  $E_z$  eigenmodes found for an  $l = 1$  spiral structure of Aluminium. Rows 1 and 3 show amplitudes rows 2 and 4 show phase distributions.*

It can be seen in figure 6.8 that the dipole mode produced by  $l = \pm 1$  is still present for large spiral stepsizes however the mode energy increases. When looking at the TBB mode decomposition of these modes it

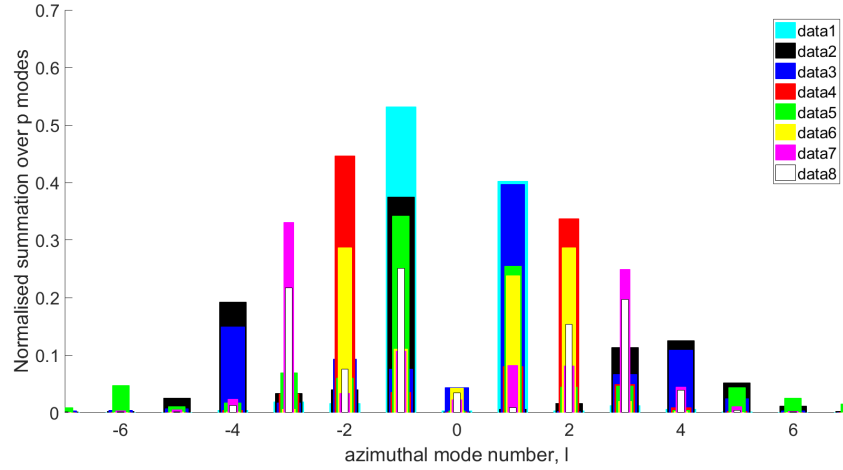


Figure 6.7: *Decomposition into TBB modes of eigenmodes shown in figure 6.6. Summations for radial mode numbers 0 to 20. The outer radius of the spiral was set to a maximum in the Bessel function.*

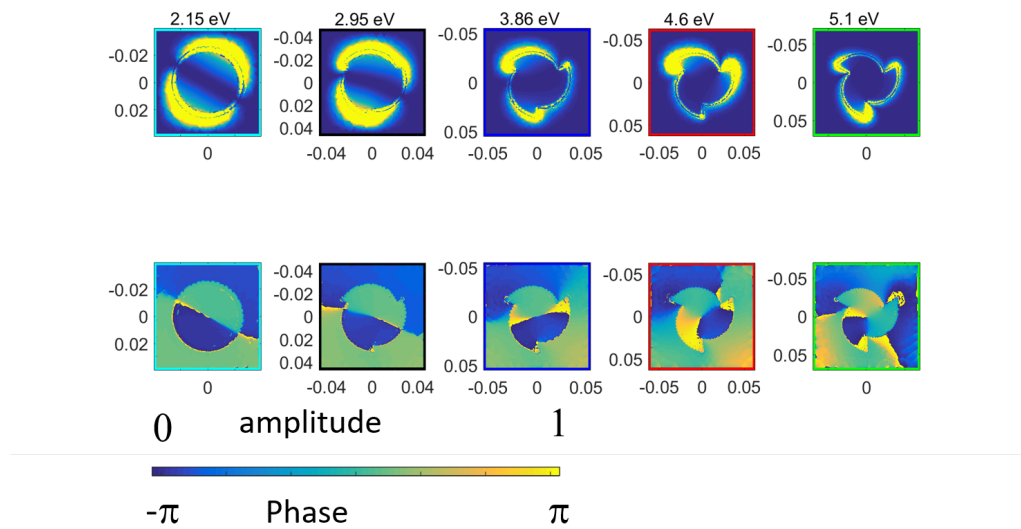


Figure 6.8:  *$E_z$  Amplitude(top) and  $E_z$  phase( bottom) for the  $p=0$ ,  $l=1$  dipole eigenmodes found for an  $l = 3$  spiral with increasing spiral step height left to right: 0,5,10,15,20 in nm.*

can be seen from figure 6.9 that the contribution from the  $l = +1$  increases relative to the  $l = -1$ , this has been calculated using TBB modes with the inner radius ( $25nm$ ) being set to a maximum of the bessel function, however similar results are found for the inner radius being a minimum. When using the outer radius as a maximum or minimum there is a difference but not as pronounced as for the inner being the limiting boundary. The same trend

is seen for the dipolar like mode of a spiral with 4 steps, see figures 6.10 and 6.11. The  $l = 4$  spiral also shows quadrupolar like modes (figure

These decompositions show that the steps in spiral structures break the symmetry of the dipolar modes associated with a disk and confer OAM to the plasmon eigenmodes. It can be seen that the field intensity of these modes is located at the center as well as the edges, supporting the interpretation of these modes as surface plasmon oscillations propagating over the top surface. These results show that adding a spiral step to an otherwise circularly symmetric disk, breaks the asymmetry of the plasmon modes supported at the surface of that structure, allowing eigenmodes containing increased net OAM. This COMSOL method finds the eigenmode solutions to maxwells equations for the structures. In the next section the boundary element method will solve for the energy dependent field and energy loss for an electron, which can be formed from a weighted combination of eigenmodes.

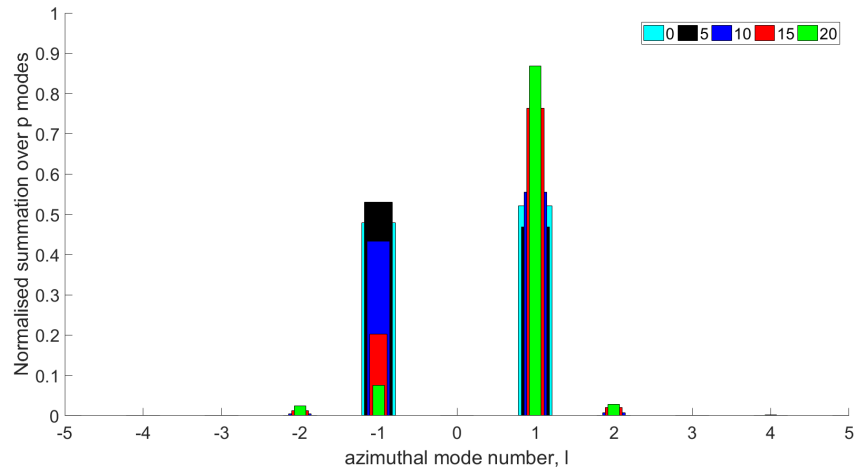


Figure 6.9: *Decompositions into a TBB basis set for the  $E_z$  modes shown in figure 6.8. Using the inner radius as a maximum of the bessel function and summing radial mode numbers from 0 to 20 .*

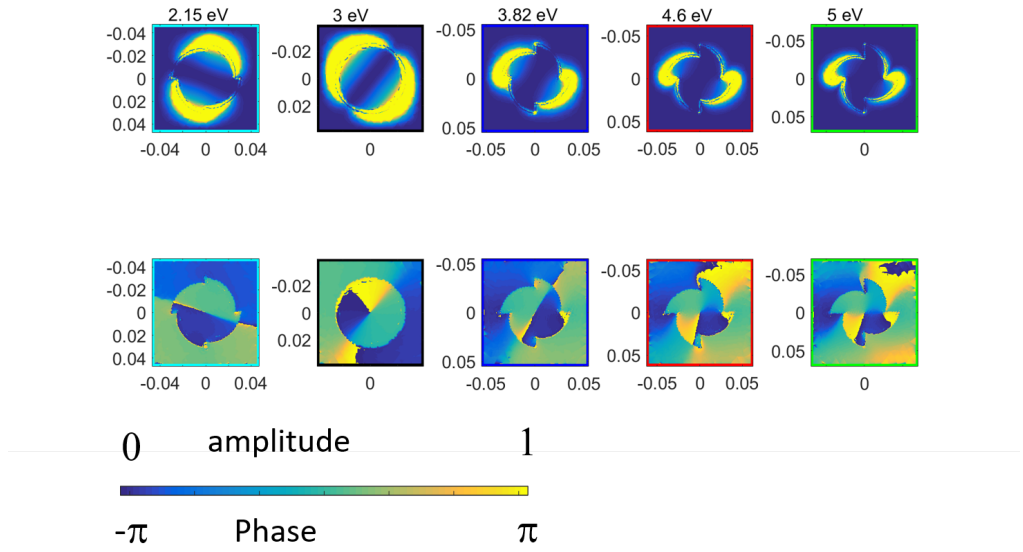


Figure 6.10:  $E_z$  Amplitude(top) and  $E_z$  phase( bottom) for the  $l=1, p=0$  eigenmodes found for an  $l = 4$  spiral with increasing spiral step height.

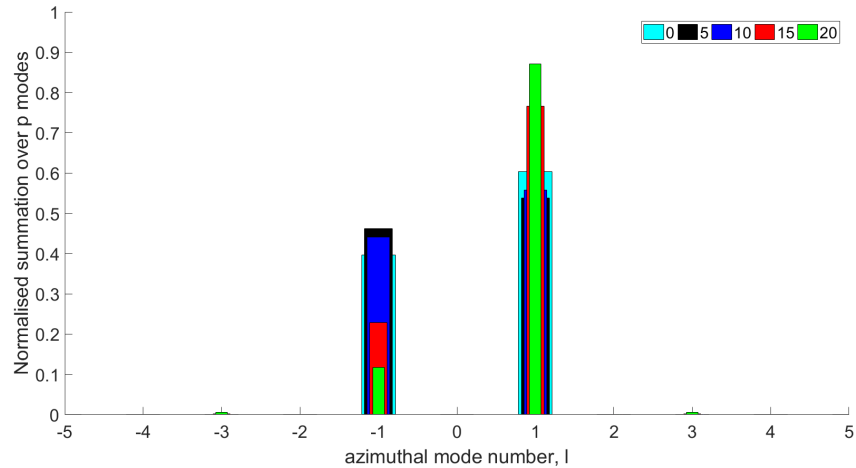


Figure 6.11: . Decompositions into a TBB basis set for the  $E_z$  modes shown in figure 6.10. Using the inner radius as a maximum of the bessel function and summing radial mode numbers from 0 to 20 .

### 6.3 MNPBEM simulations

The boundary element method MATLAB code MNPBEM was used to simulate the EELS spectra and induced  $E_z$  field in a set of spiral structures of 30nm thick aluminium. The inner radius was 25nm and the stepsize was varied between 0 nm, 5 nm, 10 nm, 15 nm and 20 nm . As can be seen in

figure 6.12 the EELS spectra has two main sets of peaks one at low energies (2-2.4eV ) and one at higher energies (3-3.7eV). The higher energy modes are from bessel like modes with different radial mode numbers as can be seen by a comparison of figure 6.13 and figure 6.14.

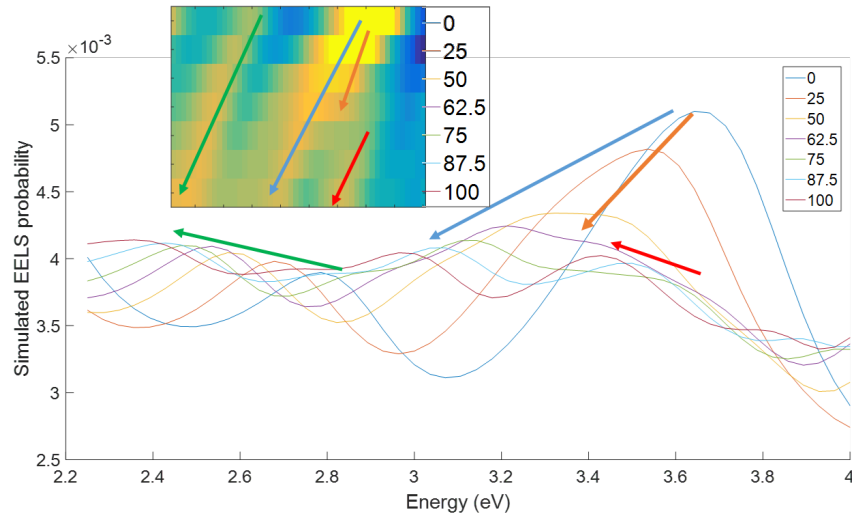


Figure 6.12: *Calculated EELS for spirals with an inner radius of 200 nm and different stepsizes as shown in the inset legends. Beam impact parameter is centered on the spiral center , i.e. at the origin, at a radius of 0.*

As can be seen in figure 6.12 there are initially two main modes for the nanodisk, which are bessel modes with different radial quantum numbers. As the step size is increased the lower energy mode (green arrow, figure 6.13) peak moved to lower energies but the higher energy mode (blue arrow, figure 6.14), peak broadens (blue arrow and orange arrow, figure 6.15) and there is an appearance of a third higher energy peak (red arrow, figure 6.16). This higher energy third mode (red arrow) has outer edge intensity mostly around the base of the step and the broader lower energy mode has a more even intensity around all of the edge.

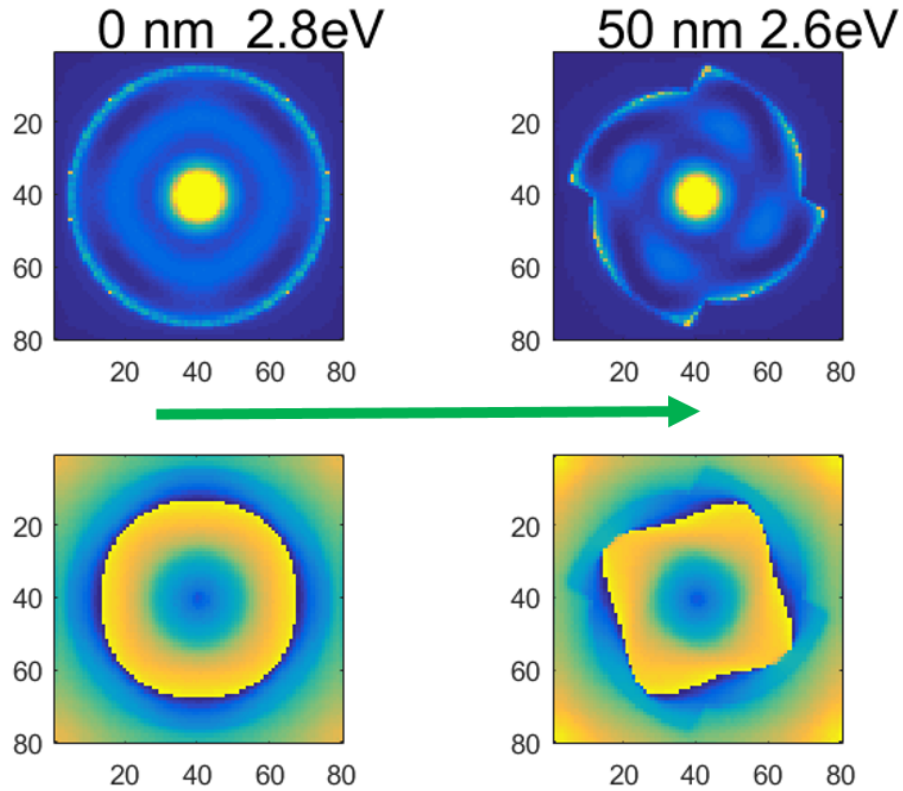


Figure 6.13: *Examples of the  $E_z$  amplitude (top) and  $E_z$  phase (bottom) for the lower energy peaks (green arrow) in the EELS spectra of figure 6.12.*

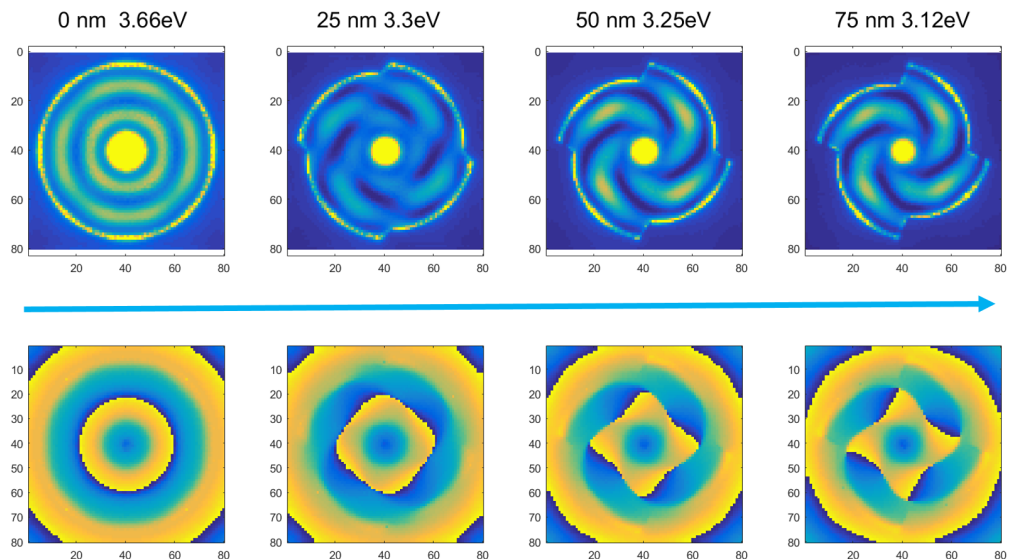


Figure 6.14: *Examples of the  $E_z$  amplitude (top) and  $E_z$  phase (bottom) for the mid energy peaks (blue arrow) in the EELS spectra of figure 6.12.*

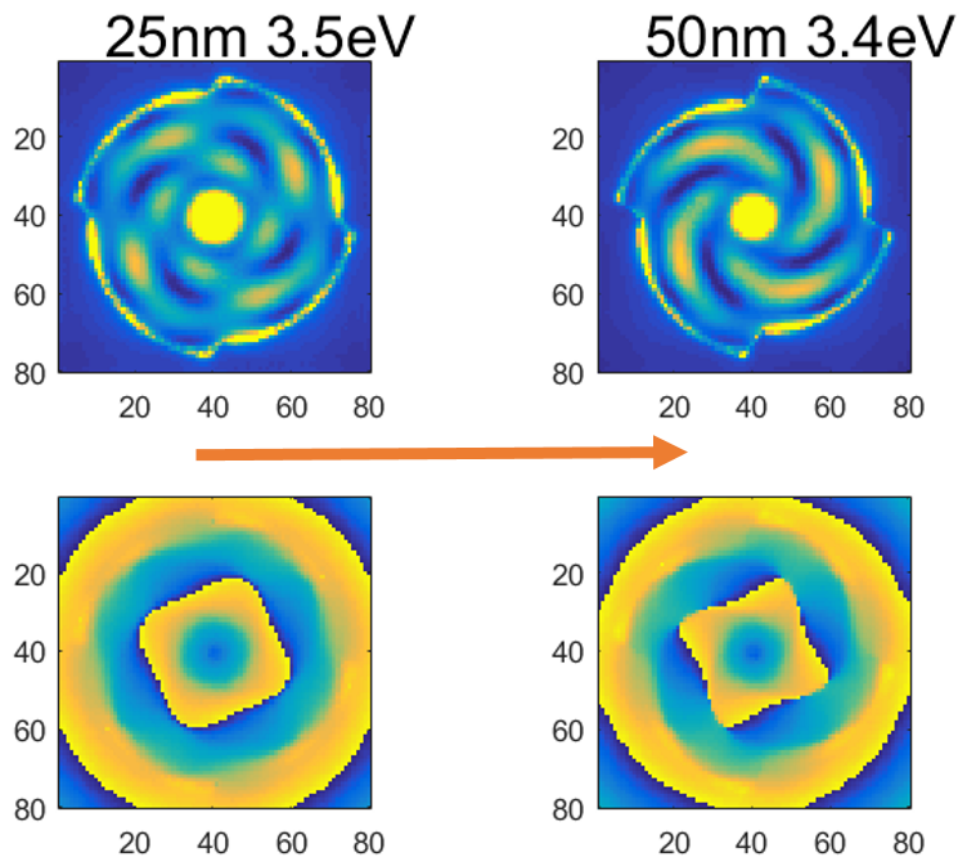


Figure 6.15: *Examples of the  $E_z$  amplitude (top) and  $E_z$  phase (bottom) for the mid energy peaks (orange arrow) in the EELS spectra of figure 6.12.*

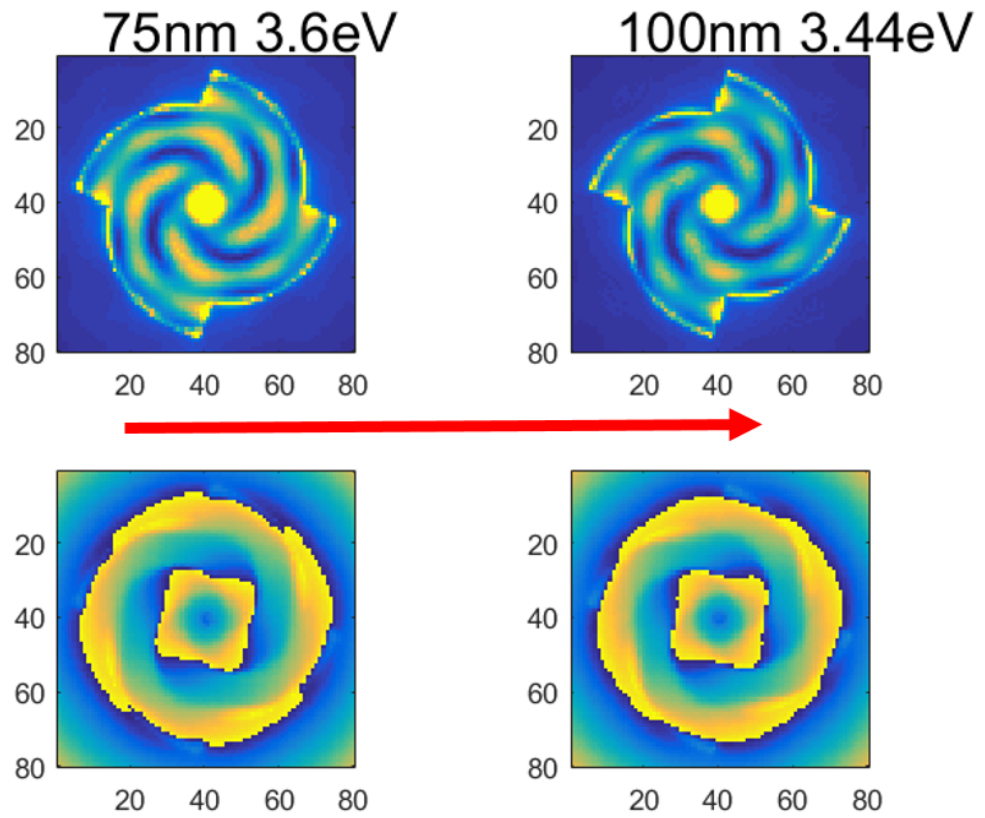


Figure 6.16: Examples of the  $E_z$  amplitude (top) and  $E_z$  phase (bottom) for the high energy peaks (red arrow) in the EELS spectra of figure 6.12.

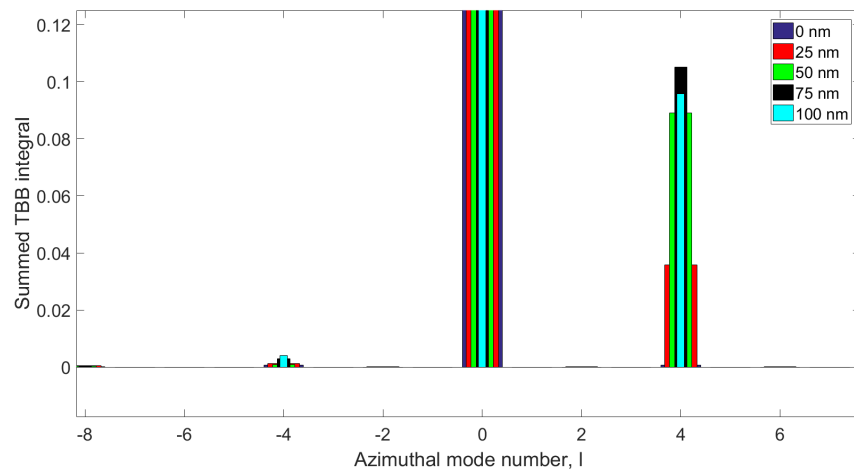


Figure 6.17: A decomposition into TBB modes using the inner radius as a maximum for the blue arrow mid energy  $E_z$  modes from figure 6.12. Colour represents different step sizes.

Larger step sizes show larger numerical OAM (calculated as described in chapter 4 section 4.1.9), for lower energy peak field in upper energy range. The mid energy EELS peak (blue arrow) E field shows an increased contribution from the  $l=4$  and a higher numerical OAM for larger stepsizes, as shown in figure 6.17. Increasing the step size breaks up the ring of constant phase present for the disk, producing pairs of vortices of opposite charge. Vortices of one sign are pushed to smaller radii meaning the OAM decompositions of the modes gain a contribution from one  $l > 0$  mode, along with higher harmonics of that mode. Shifting the phase singularities to different radii means that the numerical integral for the induced  $E_z$  field increases, as is shown in figure 6.18.

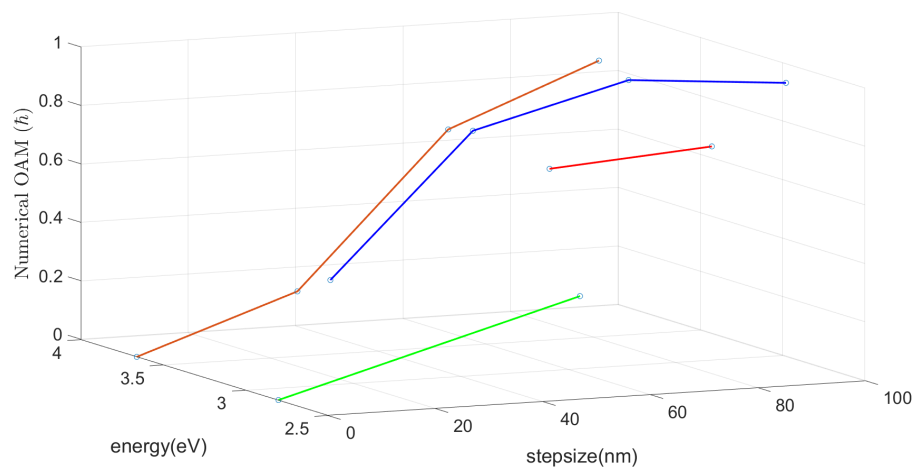


Figure 6.18: Numerically calculated OAM for the  $E_z$  modes in figure 6.12. Line colour corresponds to arrow colour in figure 6.12.

A larger structure was simulated to model a spiral with 400nm inner radius and 100nm step size, the results are shown in figure 6.20. This shows the EELS has two prominent modes between 2.5 eV and 4 eV, one at 2.98 eV and one at 3.44 eV. The simulated field distributions for these are shown in figure 6.19 and show the presence of a groove in the E field induced by a centered probe.

These simulated modes suggest that in the recorded EELS maps (which will be shown in chapter 7), the fields being induced have some off center phase singularities and are of a similar type to those simulated. The phase singularities caused by the spiralling edge appear to occur close to the edge, in pairs of alternating sign as can be seen in figure 6.19 with the phase increasing around the base of the spiral steps and also in the opposite

direction at a point removed from this. This second position can be seen by following the line separating the minimum and maximum colours on the figure. The simulated fields presented here show that in contrast to coupling photons to plasmon modes at the outer edges, a centred electron probe does not induce a centred vortex in the phase structure of the  $E_z$  field, however it does produce off center vortices which will give the plasmon mode some OAM.

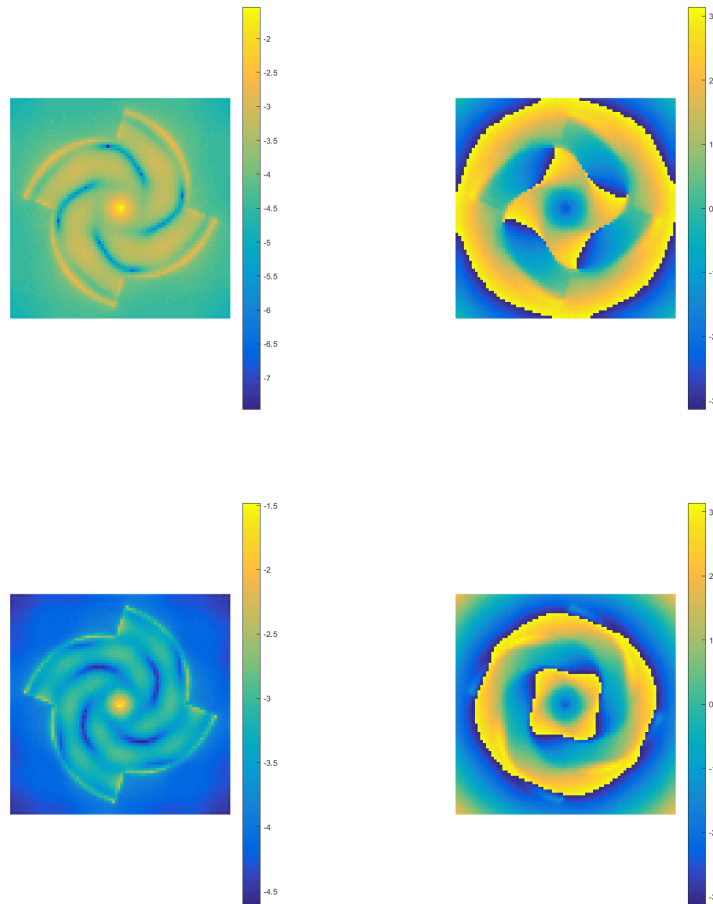


Figure 6.19:  $\text{Log}(|E_z|^2)$  (left) and phase (right) for modes at 2.98eV (upper) and 3.44eV (lower) for inner radius 200nm, stepsize 100. Modelling a 30nm Al layer on a 100nm  $\text{Si}_3\text{N}_4$  substrate. For central impact parameter  $(0,0)$

Even for small structures the simulated induced E field shows no central vortex for both on axis and off axis excitation. An example is shown for a small  $l = 3$  spiral with an inner radius of 25nm and a

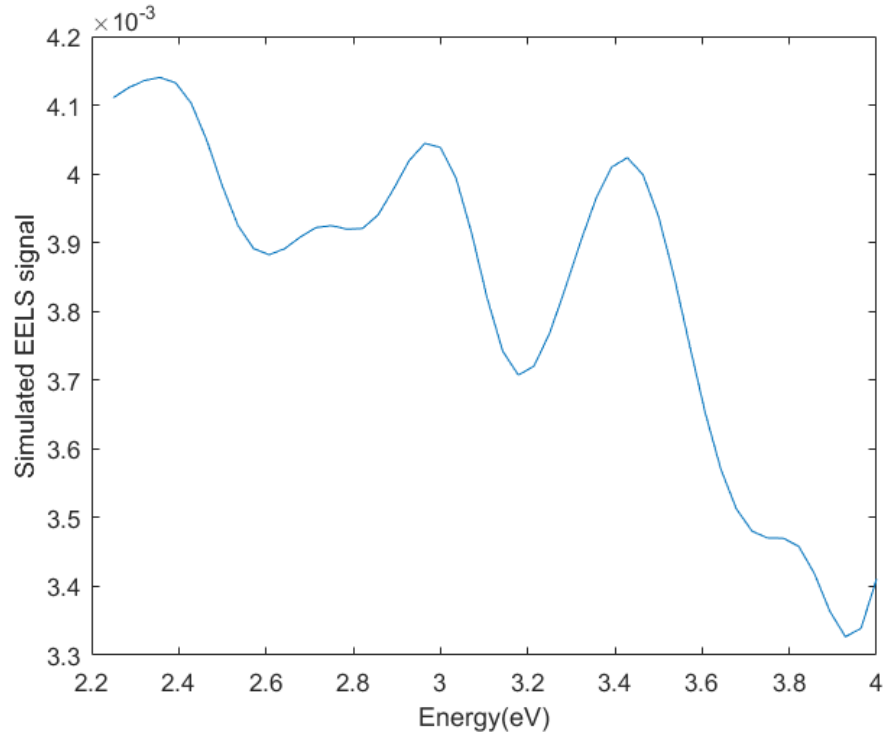


Figure 6.20: A simulated EELS spectra for an  $l = 4$  spiral with diameter  $400\text{nm}$  and stepsize  $100\text{nm}$ . For  $30\text{nm}$  Al film on a  $100\text{nm}$  silicon nitride substrate. The impact parameter is centered at the origin.

stepsize of  $25\text{nm}$  in figures 6.21 and 6.22. These suggest that excitation with a single point beam cannot excite plasmon modes with OAM, however a vortex electron beam with a radius similar to the outer edge may be able to launch plasmons inwards which are in phase at the boundary and form a vortex in the center.

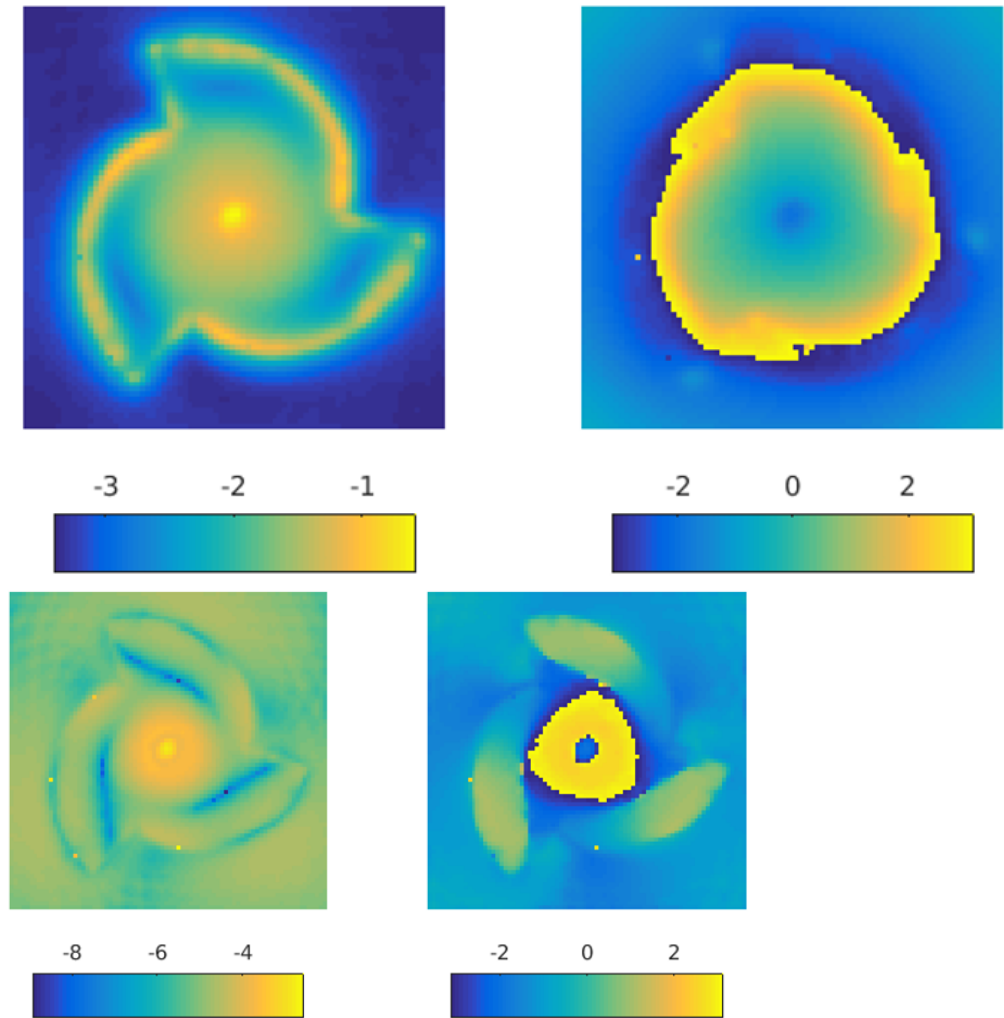


Figure 6.21:  $\text{Log}(|E_z|^2)$  (left) and phase (right) of the induced field in an  $l = 3$  spiral with an inner radius of 25nm and a stepsize of 25nm. For energies of 5eV (upper) and 10eV (lower).

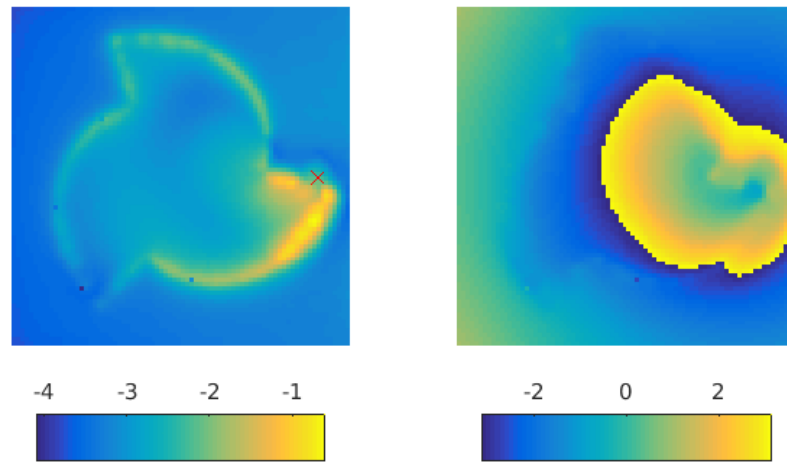


Figure 6.22:  $\text{Log}(|E_z|^2)$  (left) and phase (right) of the induced field in an  $l = 3$  spiral with an inner radius of  $25\text{nm}$  and a stepsize of  $25\text{nm}$ . For an energy of  $5\text{eV}$  with an off axis incident beam position, represented in the left image by a red cross.

## 6.4 Chapter summary

This chapter has presented simulated eigenmodes and induced electric fields initially for a nanodisk and then for sets of spiral structures with an increasing stepsize. As the stepsize increases, both the normal electric field eigenmodes found by COMSOL and induced normal electric fields found by Matlab, show an increasing asymmetry to the TBB mode decomposition. This shows that structures with a spiralling boundary can support plasmon modes with OAM. It was also shown that higher energy modes in these structures have a larger amount of radial nodes similar to ideal Bessel functions. These induced fields with OAM offer a potential mechanism through which chiral electron beams containing OAM could couple selectively to thin metallic films depending on whether the electron chirality matches the induced fields. The transfer of OAM could be thought of as via a virtual photon containing OAM. Alternatively it could be due to the induced field of the plasmon containing some OAM, due to reflections from the spiral boundary thus also exchanging momentum with the metal structure .

# Chapter 7

## EELS experimental

### 7.1 EELS studies

To experimentally excite vortex plasmons with a TEM beam electron, chiral structures such as those introduced in chapter 6 were produced via EBL. As shown schematically in figure 7.1, these were produced on 100 nm thick silicon nitride membranes, which were  $500\mu m \times 500\mu m$  in a substrate  $200\mu m$  thick. These were bought from Silson as a  $4 \times 4$  grid and were separated after the patterning procedure. The input design for the EBL tool was a grid of various shapes, including spiral structures (similar to the upper image of figure 7.1), with inner diameters of  $100nm$  to  $1000nm$  in steps of  $100nm$ , the step size was varied from  $50nm$  to  $350nm$  in steps of  $50nm$ . This  $10 \times 7$  grid was produced for  $l = 1, 2, 3, 4, 5, 10$  and  $11$ . In addition to this a set of nanosquares and nanodisks with width  $50nm$  to  $225nm$  in steps of  $25nm$  were present in the input design however most of the structures below an outer radius of  $100nm$  were not successfully reproduced. The plasmon modes of similar shapes have been mapped by scanning nearfield optical microscopy (SNOM) however, due to the size of the shapes relative to the wavelength of plasmon, the analysis has focused on the central field structure and not the structure near the edge.

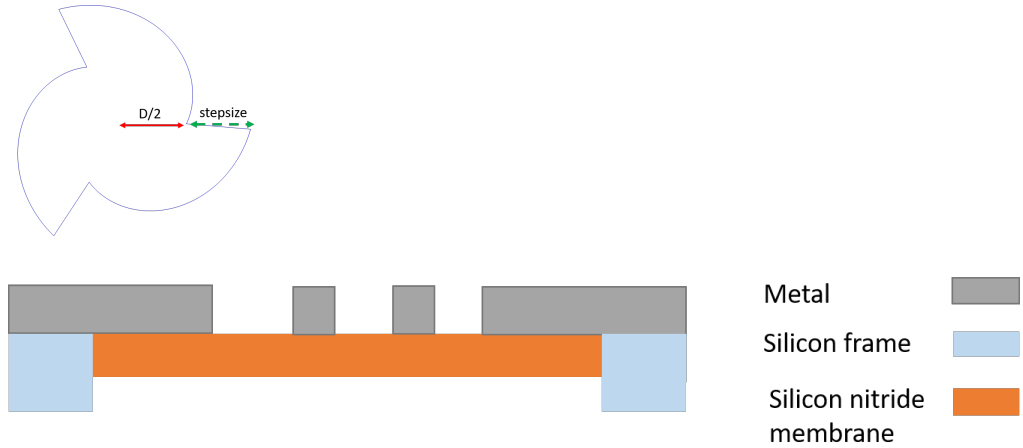


Figure 7.1: A schematic of a single  $l = 3$  spiral island shape (upper) and a cross section schematic (lower) of the array of multiple spiral islands shapes. In the experiments the metal layer was 30 nm or 20nm Al and the Silicon nitride membrane was 100nm thick

### 7.1.1 STEM EELS of nanoshapes

As an initial test of the procedure STEM EELS maps were gained for a nanodisk, nanorods, and a nanosquare produced on the sample array. Figure 7.2 shows STEM images at different energy ranges. The presence of maxima and minima can be seen in figure 7.2, for example the corners of the nanosquare, an inner ring of the disk and the ends of the nanorods all show reduced intensity. The patterns are indicative of interference occurring within bound plasmon modes which have been reported for rods [150], disks [148][92] and squares [151].

When considering localised surface plasmon modes on a nanodisk the cylindrical symmetry means that solutions follow the function form of Bessel modes where the radial oscillation is determined by a Bessel function. The zeros and maxima of Bessel functions do not occur at arguments with even  $\pi$  intervals like a sin function, as such the gap predicted between the arguments of an edge maxima and the preceding minima will not be  $\pi/4$ . The Bessel functions  $J_m$  for  $m > 0$  give gaps which are larger than  $\pi/2$  as such the distances predicted for the minima to the edge will be larger than would be predicted by a  $\pi/4$  gap. Figure 7.3 plots the predicted difference in argument for the first 5 maximum-minimum gap for Bessel modes  $J_i$  for  $i = 1$  to  $i = 5$ . These are all larger than  $\pi/4 = 0.78539$ . This means

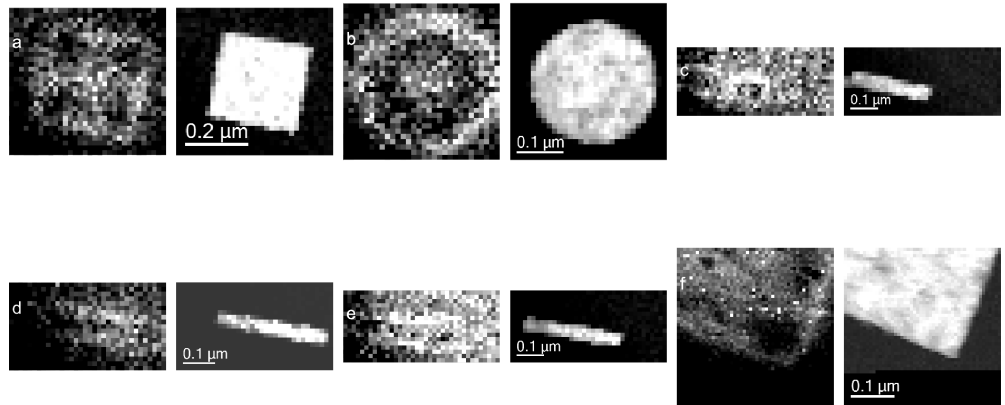


Figure 7.2: *STEM EELS maps for various shapes with 2.5eV on the left images and 15eV on the right images for: A) Nanosquare, B) Nanodisk C, D, E) Nanorods, F) the corner of a large cross structure*

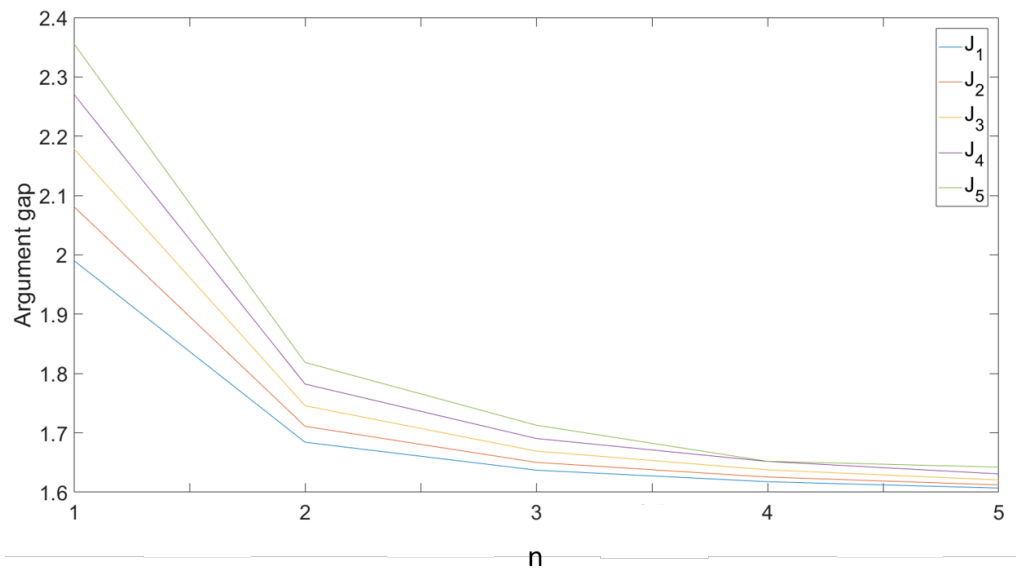


Figure 7.3: *Difference in argument required between  $(n + 1)^{th}$  maxima and  $n^{th}$  minima for Bessel functions of order larger than 0. Colours show different bessel functions and the x axis is the index n.*

later on it will be possible to rule out the higher order bessel modes as the cause of the measured gaps, which will be shown to all be lower than  $\pi/4$ . However the experimentally recorded minima for a 275nm diameter nanodisk show smaller gaps than predicted by either the  $\pi/4$  or a Bessel  $J_1$  function.

The scale of the distance from maxima to minimum is the same size as the Bessel  $J_0$  but the radius required to match the outer maximum argument does not match the experimental  $137.5nm$  radius. This was calculated to be  $3.83/3.5 \times 10^7 = 109nm$  or  $7.0156/3.5 \times 10^7 = 200nm$  using a wavevector of  $3.5 \times 10^7 m^{-1}$  calculated for an energy of  $3eV$  from the standard surface plasmon travelling wave dispersion, thus meaning the experimental intensity is not due to a pure  $J_0$  Bessel plasmon mode.

### 7.1.2 STEM EELS of spiral island structures

The measured EELS signal for a structure depend upon the local density of states (determined by the material) and the supported geometric modes (determined by the shape). It was unclear at which energy the electron beam in the TEM would couple to the spiral structures so a collection of spirals were made. This collection allowed the investigation of how the energy loss spectra vary when the dimensions of the shape, in particular the curvature of the boundary which depends upon the ratio of the step size to the angle per step . A grid of structures were produced following the equation  $s = r_{in} + \lambda_{spiral} mod[(l\phi/2\pi)]$ , where  $s$  is the radius of the shape,  $mod$  denotes the remainder,  $r_{in}$  is the inner radius and  $\lambda_{spiral}$  is the designed step size. This produces shapes similar to those shown in figure 7.1 which, due to their isolated nature, will be referred to as 'spiral island' structures. For the set of produced spiral islands the parameters used were  $r_{in}(nm) = (50, 100, 150, 200, 250, 300, 350, 400, 450, 500)$  and  $\lambda_{spiral}(nm) = (50, 100, 150, 200, 250, 300, 350)$ . A selection of these shapes were analysed by taking EELS maps with a dwell time of 0.32 seconds per pixel. The recorded dm3 files were then read into MATLAB where the zero loss peaks were aligned and intensities were scaled. The intensity maps at energy cross sections show a low intensity groove close to the edge of the spiral island structures as shown for  $l = 1$  in figure 7.5 . This occurs for energies of between 2-5eV with the gap, measured between the intensity minimum and the bright edge maximum, reducing for higher energies.

This is similar to a maxima-minima gap in a standing wave pattern as the wavelength decreases. To model the experimental data shown in section 7.1.2 the MNPBEM toolkit for matlab was used to simulate the EELS maps across the structures. To characterise the experimental STEM

EELS maps and compare with simulations with angular-averaged gap size was measured between the bright edge and closest radial minimum .

In figures 7.5 to 7.13 , each experimental and simulated EELS intensity map has been analysed with the algorithm below.

For each energy analysed :

1. The 15eV image is used to set a binary mask outlining areas of high intensity to outline the Al metal structure. Multiply STEM EELS slice image by this binary mask.
2. sample image to transform to circular polar coordinates
3. for all angles;
  - 3.1. find maximum intensity along radius
  - 3.2. find minimum intensity within a selected region at lower radii than maximum from previous step
  - 3.3. measure maximum-minimum separation
4. find the average gap from all results of step 3.3.

The STEM images are low resolution due to experimental stability limiting the imaging time. Due to the low signal to noise ratio and low resolution of the images some error checking sections were added into the code, to ensure the assigned position of the maxima and minima made sense. One of which was to ensure the minima was at a smaller radius than the maximum and to ensure that the minimum found was the minimum which can be assigned to the groove by eye and not a minimum due to noise. The overall radial minimum was not always the groove minimum due to the low signal to noise ratio. The results for all l values are summarised in figure 7.4, whilst the outputs of this algorithm for individual values are shown for 3eV in figures 7.5 to 7.13.

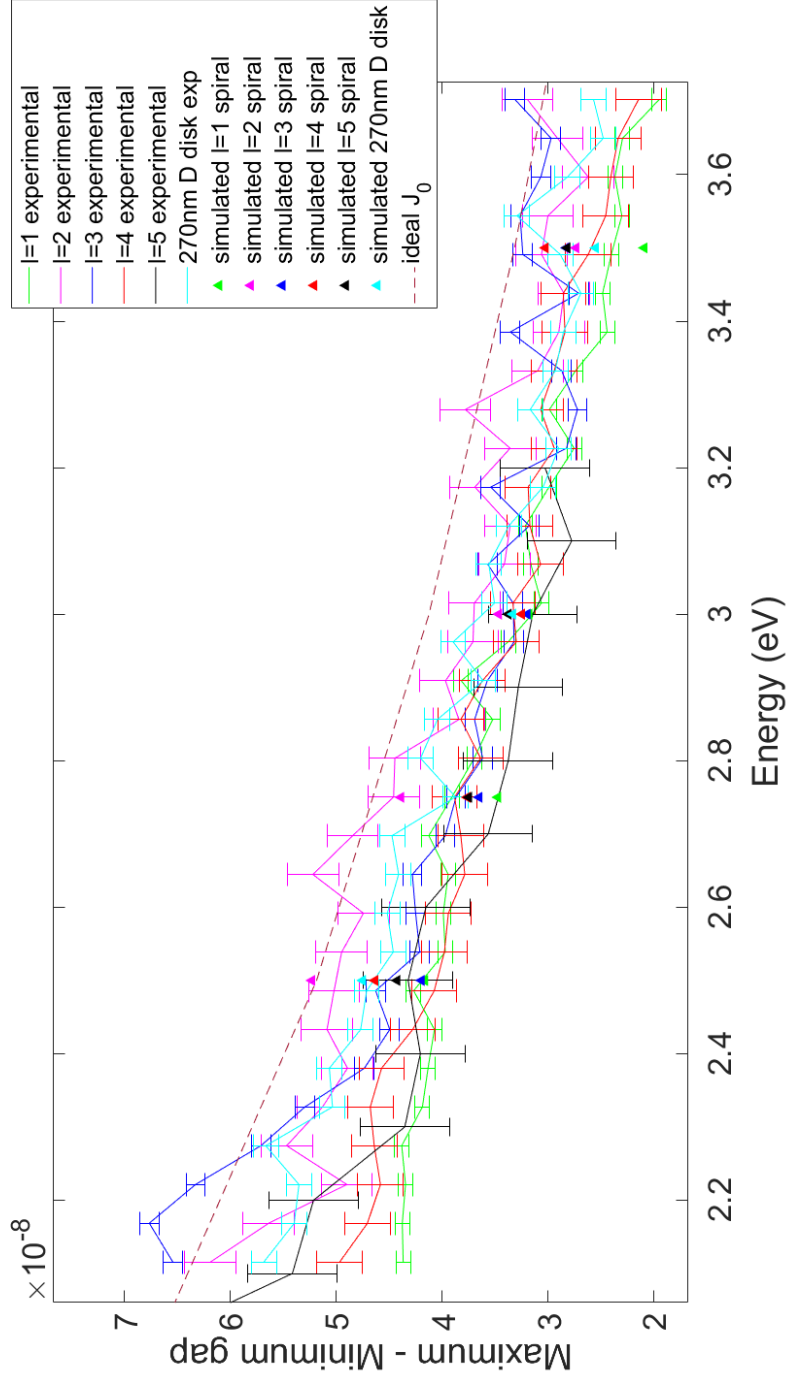


Figure 7.4: A comparison of the maximum-minimum gap from experimental and simulated EELS maps. Error bars represent half of the pixel spacing, above and below the calculated gap value.

Figures 7.5 to 7.13 contain the polar plot with the measured minima (red line) and maxima (green line) overlain. Figure 7.5 shows the  $l = 1$  which was the smallest structure tested.

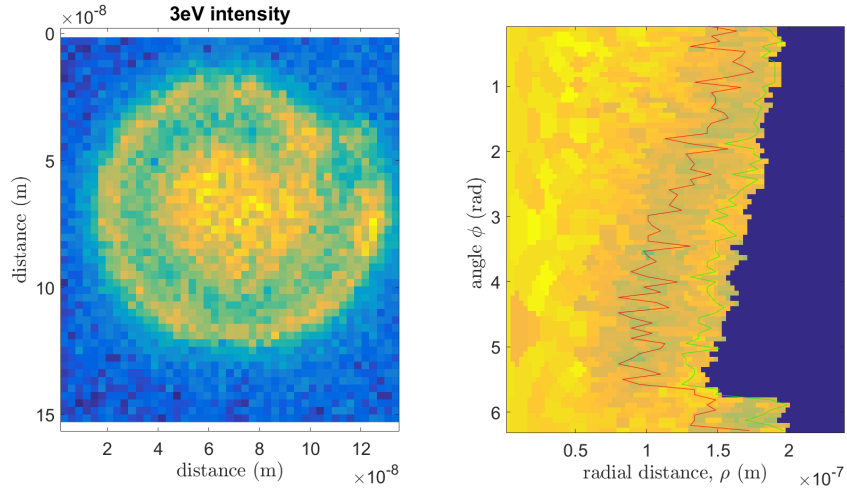


Figure 7.5: *Left is an intensity slice at 3eV for the  $l=1$  spiral and right is a  $(\rho, \phi)$  azimuthal plot of the left image with the measured maxima (green line) and minima (red line) overlain.*

The STEM EELS map at 3eV shows a prominent minimum close to the edge which is also predicted in the simulation in figure 7.6, in addition the minimum by the flat step edge is predicted by simulation and visible in the experimental data.

However the fine structure of the central minimum is not seen in the low resolution experimental data. For the  $l = 2$  structure in figure 7.7 there is also a minimum close to the edge and edge step minimum found in both simulation (figure 7.8) and experiment.

There are 4 main intensity spots in the simulation which are actually roughly visible in the experimental data, a pair at the base of the steps and a pair in the central region. The  $l = 3$  structure is slightly larger again and both experiment (figure 7.9) and simulation (figure 7.10) shows edge minima near the boundary and minima near the step edges.

The simulation also shows a detailed internal interference structure with 3 bright spots and spiralling intensity peaks, these are not seen in the experimental data. The  $l = 4$  structure shown in figures 7.11 and 7.12 show once again clear minima close to the boundary and flat step edges.

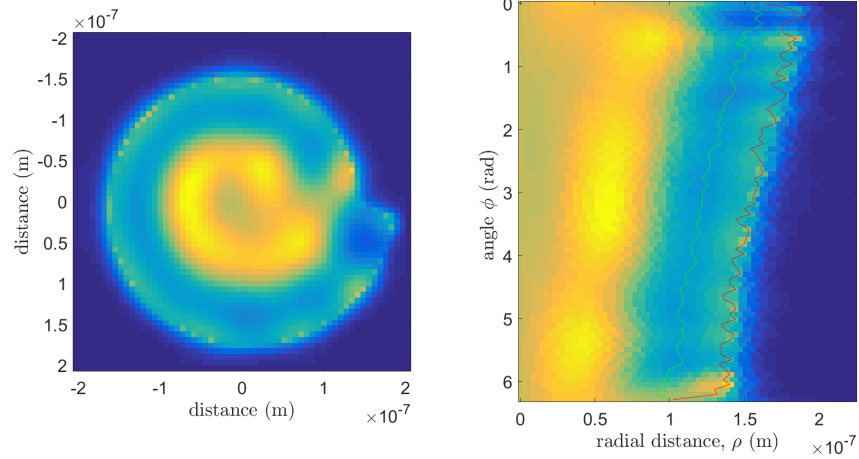


Figure 7.6: *The simulated EELS map at 3 eV for the dimensions of the experimental  $l = 1$  structure, shown in cartesian coordinates (left) and polar co ordinates (right). The measured positions of the radial minima and maxima are shown with the green and red lines respectively on the polar plot image.*

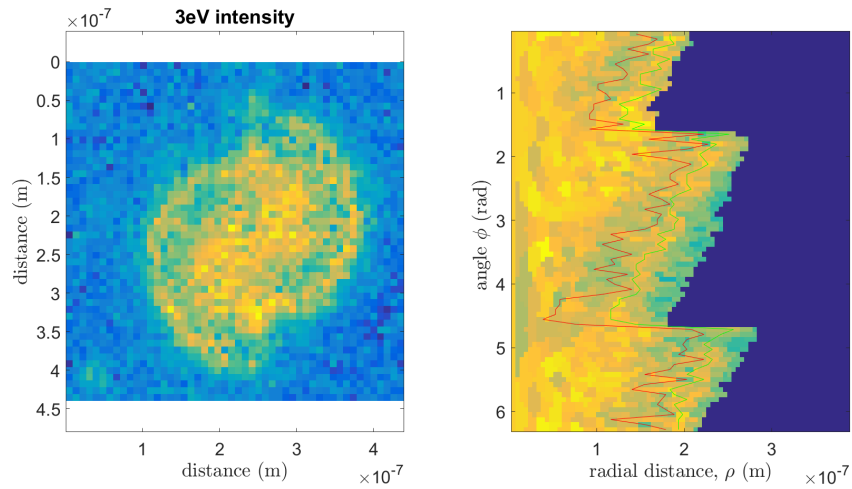


Figure 7.7: *Left is an intensity slice at 3eV for the  $l=2$  spiral and right is a  $(\rho, \phi)$  azimuthal plot of the left image with the measured maxima (green line) and minima (red line) overlain.*

The simulation now shows oscillations in intensity around the curved boundary which were present but not as prominent in the lower  $l$  value structures. This along with the fine central detail, like the previous structures was not visible in the experimental data. The  $l = 5$  structure

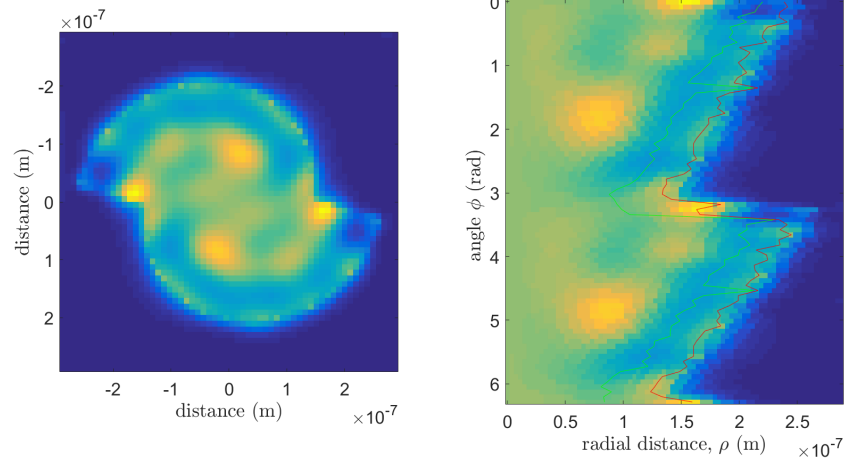


Figure 7.8: *The simulated EELS map at 3 eV for the dimensions of the experimental  $l = 2$  structure, shown in cartesian coordinates (left) and polar co ordinates (right). The measured positions of the radial minima and maxima are shown with the green and red lines respectively on the polar plot image.*

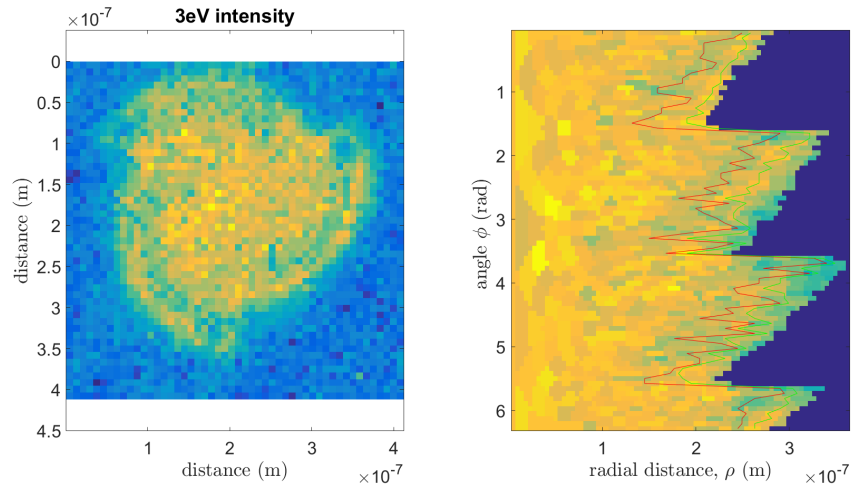


Figure 7.9: *Left is an intensity slice at 3eV for the  $l=3$  spiral and right is a  $(\rho, \phi)$  azimuthal plot of the left image with the measured maxima (green line) and minima (red line) overlain.*

is the largest structure and as such only a portion of the structure was simulated (figure 7.14) due to computational constraints. The experimental data (figure 7.13) only shows a narrow minimum close to the boundary edge and the resolution is not high enough to see any minima close to the

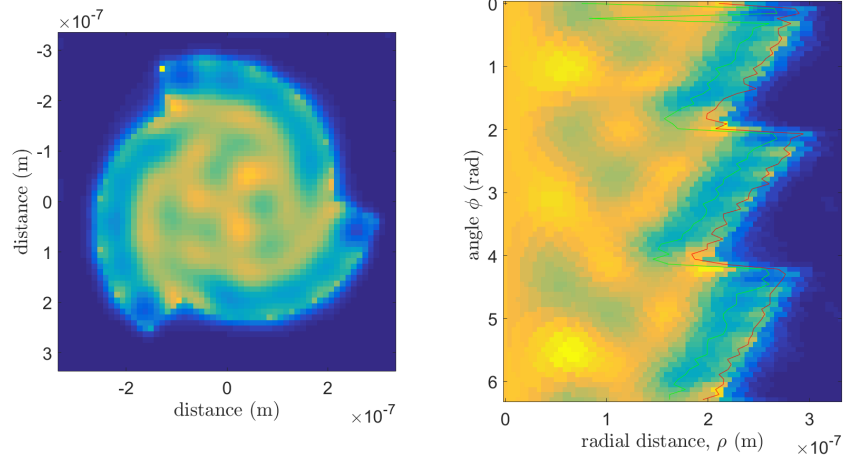


Figure 7.10: *The simulated EELS map at 3 eV for the dimensions of the experimental  $l = 3$  structure, shown in cartesian coordinates (left) and polar co ordinates (right). The measured positions of the radial minima and maxima are shown with the green and red lines respectively on the polar plot image.*

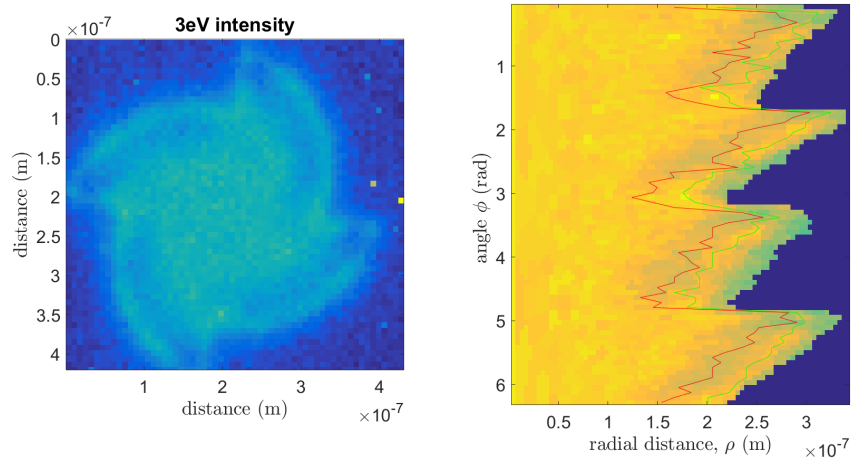


Figure 7.11: *Left is an intensity slice at 3eV for the  $l=4$  spiral and right is a  $(\rho, \phi)$  azimuthal plot of the left image with the measured maxima (green line) and minima (red line) overlain.*

step flat edges, even though these are predicted in the simulation.

Whilst the error in finding the correct minima is large for this computational analysis the measured gap sizes are in general good agree-

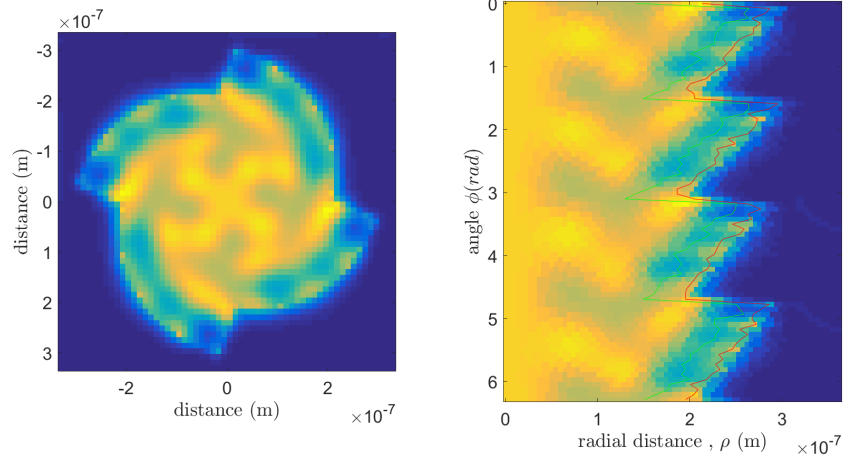


Figure 7.12: *The simulated EELS map at 3 eV for the dimensions of the experimental  $l = 4$  structure, shown in cartesian coordinates (left) and polar co ordinates (right). The measured positions of the radial minima and maxima are shown with the green and red lines respectively on the polar plot image.*

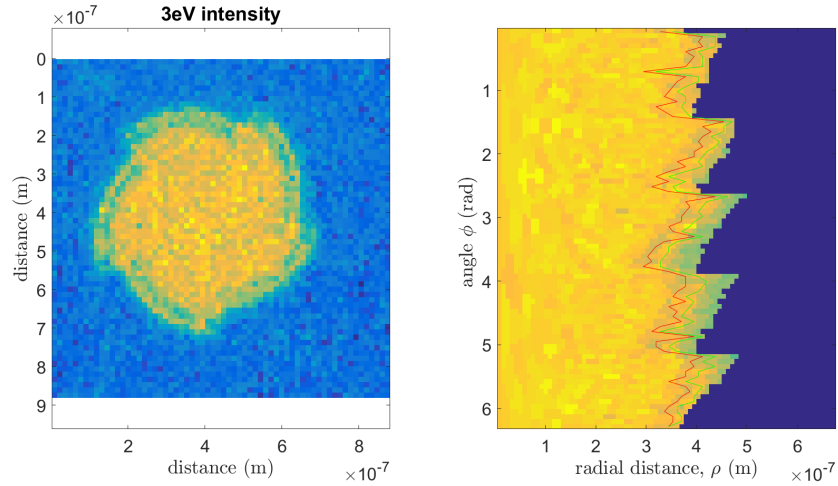


Figure 7.13: *Left is an intensity slice at 3eV for the  $l=5$  spiral and right is a  $(\rho, \phi)$  azimuthal plot of the left image with the measured maxima (green line) and minima (red line) overlain.*

ment with the simulated EELS maps as is shown in figure 7.4. However the resolution of the experimental data was limited by the limited acquisition time possible, due to beam stability and sample drift. For the smaller structures a higher resolution dataset could potentially reveal these details.

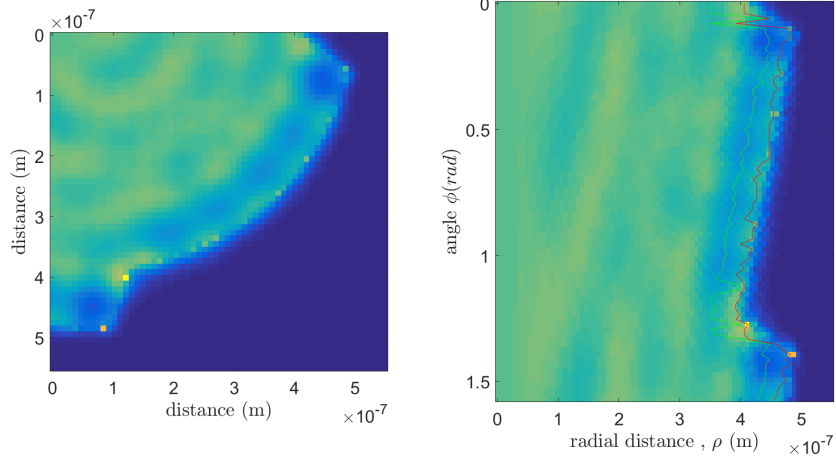


Figure 7.14: *The simulated EELS map at 3 eV for the dimensions of the experimental  $l = 5$  structure, shown in cartesian coordinates (left) and polar co ordinates (right). The measured positions of the radial minima and maxima are shown with the green and red lines respectively on the polar plot image.*

However for the larger structures there was no sign of internal structure and it appears this is more a limitation of the sample itself. This could be related to inherent damping in the metal film or the quality of the film, roughness and crystallinity, both of which would require future experiments to investigate and are left open as a future direction of research. The broad match between simulation and experiment shows the structures produced successfully support the electromagnetic fields predicted by simulation, at least close to the boundary. The maximum-minimum gaps measured are all lower than would be predicted from a  $\pi/4$  gap on the standard dispersion, this agrees with the findings of Schmidt [93] that edge modes formed by reflection from boundaries have lower energies than the standard dispersion curve. The angular distance of step size per angle per step  $\lambda_{spiral}/(2\pi/l)$  can give a measure of the spiralling nature of the boundary. A larger angular distance means that the boundary normal is directed at higher angles to the radial unit vector. A surface plasmon wave directed at an angle to the inwards radial unit vector would show a smaller gap in the interference pattern than one travelling along the radius. This is because when compared to a wavevector along the radial unit vector, a wavevector with an azimuthal component will suffer the same phase delay when travelling a shorter radial distance. The results for  $l = 2, 3, 4, 5$  shown in figure 7.4 support this idea with the modes having angular distances of 39.8, 47.7, 63.7, 71.6nm/rad re-

spectively. The  $l = 2$  has the smallest angular distance of 39.8 and shows the largest gaps next the  $l = 3$  and  $l = 4$  have similar ratios and show similar gap sizes, finally the  $l = 5$  has the largest angular distance and shows mostly the smallest gaps (above 2.5eV). However, the  $l = 1$  measured and simulated gaps do not follow this trend and despite having the lowest angular distance it shows gaps closer to the  $l = 5$  smaller than the other  $l$  values. The trend of  $l = 2 > l = 3 > l = 4 > l = 5$  is not always followed and it is unclear why. This trend would support the idea that the gaps are due to surface plasmon modes determined by the boundary geometry. Future experiments would be required with higher spatial and energy resolution STEM images to check these initial findings.

### 7.1.3 Cathodoluminescence experimental results

To produce structures which support plasmon modes with OAM both FIB and EBL have been used to produce a variety of spiral slit and spiral island structures. Figure 7.15 shows a collection of 11 structures for which the cathodoluminescence signal was recorded in an SEM, this figure can be used for reference when looking at the subsequent spectra to see which shape gave which spectrum. Due to noise, to improve the visibility of the key trends, 4 point moving averages of the CL spectra are shown in figures 7.16 and 7.17. The structures were of 30nm thick Al film which had been FIB milled to produce a spiral boundary to reflect plasmons inward. The CL spectra in figure 7.16 show that there is extra intensity around 350 nm above the background. This shows there is some coupling to a dipole mode around 3.5 eV for these structures in the Al film. There is an even more prominent peak at this energy for samples 8,9 and 10 which is likely due to the increased efficiency of emission via coupling to cavity modes in the closed slits. Sample 11 showed a very large peak around 420nm (approximately 3 eV). As shown in figure 7.18 the cathodoluminescence shows the same groove structure as the EELS intensity around 3 eV showing it is not an artefact of the EELS apparatus and is most likely some form of plasmon mode which can couple to photon emission to some extent. The structures produced by FIB clearly shows strong visible coupling to radiative modes in the metal film, which can be most easily explained by low energy surface plasmons.

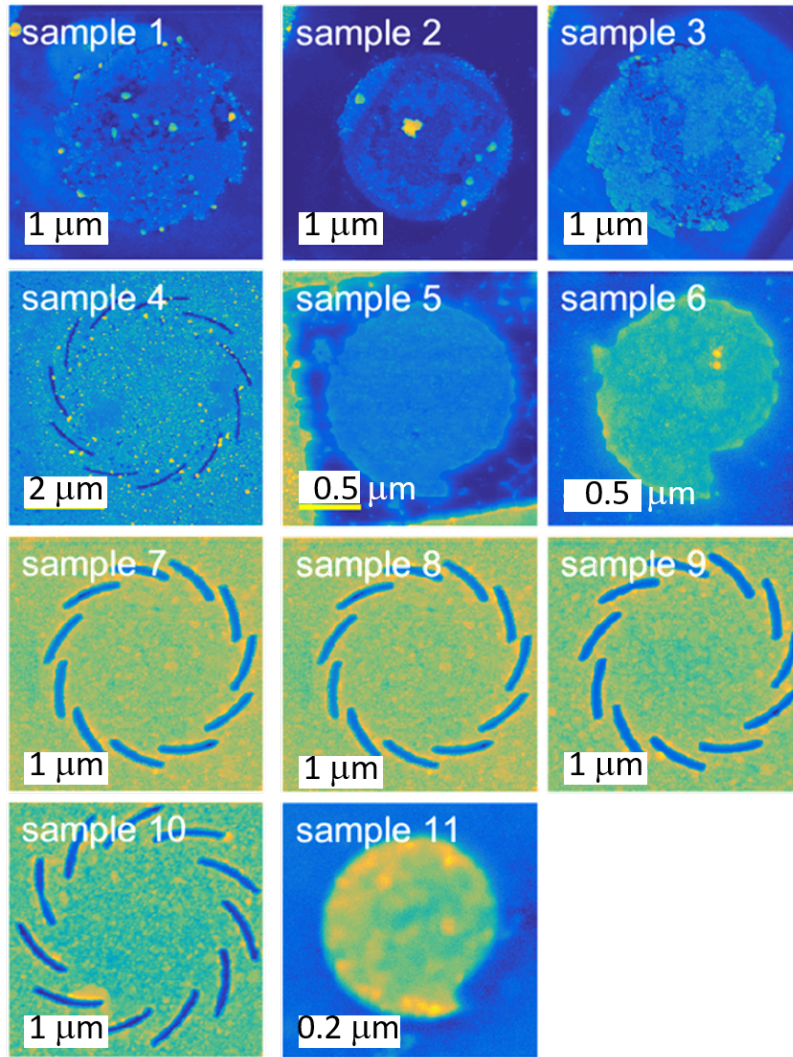


Figure 7.15: SEM images of the 11 structures produced by FIB and tested by CL, the results of which are shown in figures 7.16 and 7.17. Scale bars are 1)  $1\mu m$ , 2)  $1\mu m$ , 3)  $1\mu m$ , 4)  $2\mu m$ , 5)  $0.5\mu m$ , 6)  $0.5\mu m$ , 7)  $1\mu m$ , 8)  $1\mu m$ , 9)  $1\mu m$ , 10)  $1\mu m$ , 11)  $0.2\mu m$ .

As discussed in the appendix section A.4 EBL was also used to produce spiral island structures and was much more efficient than the FIB process, allowing a collection of different shapes to be produced in one batch. Examples of  $l=1$  spirals produced by this procedure are shown in figure 7.19, these include both Al film and Ag film. Figures 7.20 to 7.22 show the four point moving averages (the mean of four sequential counts) of the spectra from the Al film structures produced by EBL. These show large intensity above the background between 350nm to 550nm with a peak around 420-450 . By comparison to figure 7.16 it can be assumed that there is likely a mode around 350nm and around 420nm. The Ag struc-

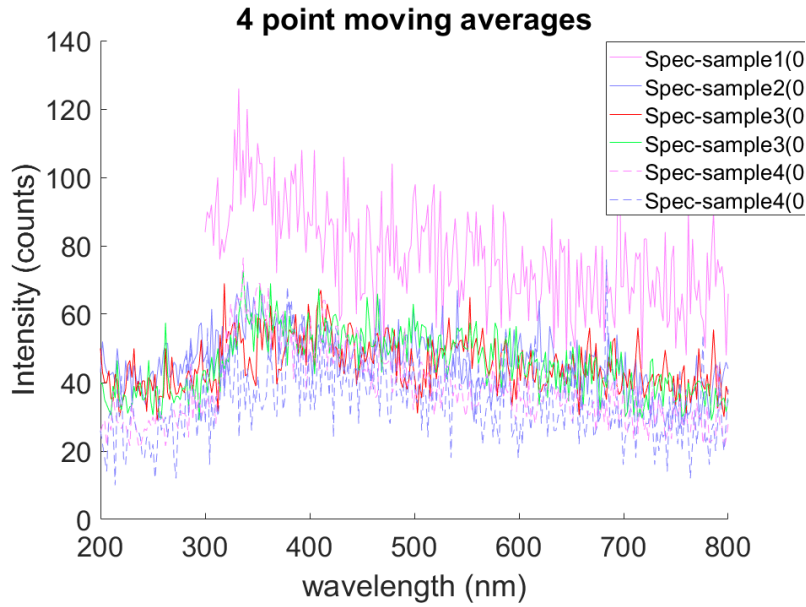


Figure 7.16: *CL spectra for the samples indicated in the legend. The Al film shows peak around 350nm above the background.*

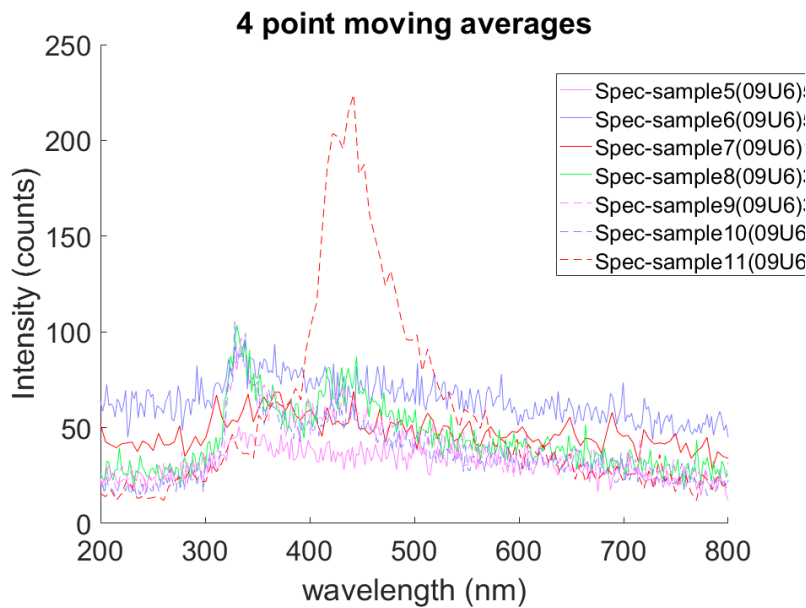


Figure 7.17: *CL spectra for the samples indicated in the legend. A strong peak at 440nm is seen for the small  $l=1$  spiral of sample 11. The samples with slits (7,8,9,10) show a prominent 350nm mode (possibly the cavity mode of the slit gap).*

tures showed a more pronounced peak between 300-400nm indicative of low energy plasmon modes, showing these structures can support plasmon modes in the energy range 2-5eV ( 620nm-245nm). The results from both

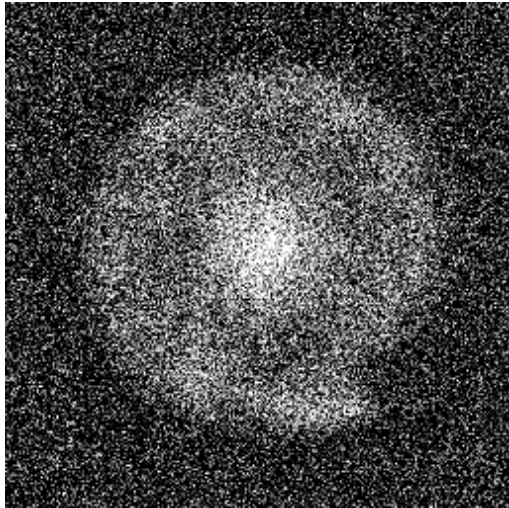


Figure 7.18: A cathodoluminescence image for sample 11 from figure 7.15

the FIB milled spiral islands and those produced by EBL gives weight to the interpretation of the chiral EELS signals which will be discussed later on in this chapter as being related to sample interactions and not artefacts.

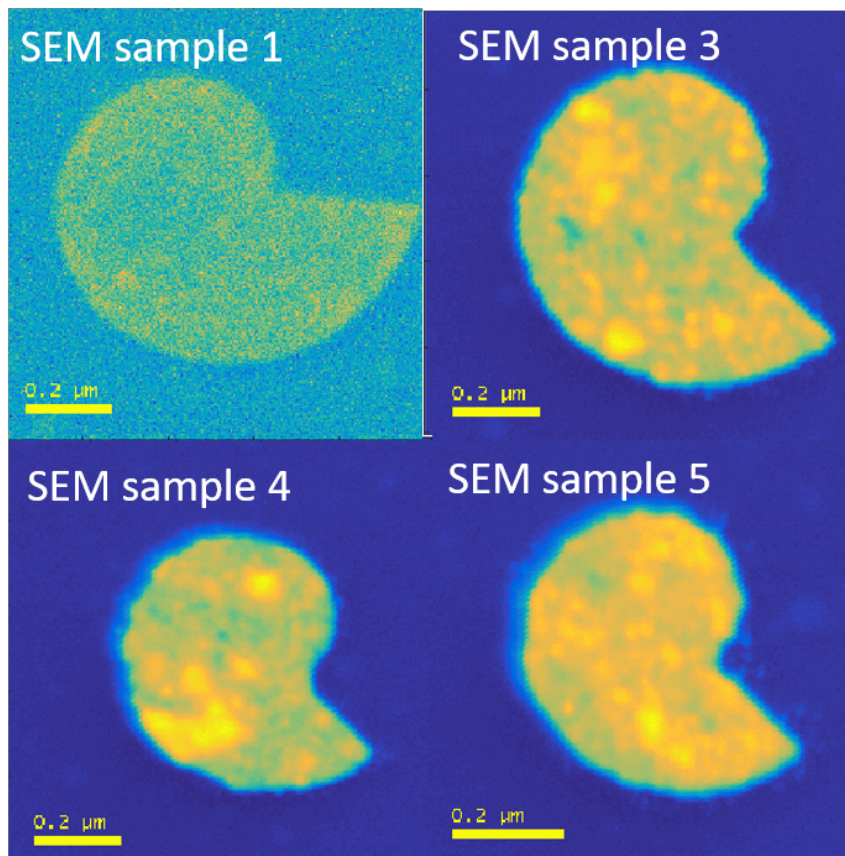


Figure 7.19: SEM images of the Aluminium structures produced by EBL and tested with CL. All scale bars are 200nm

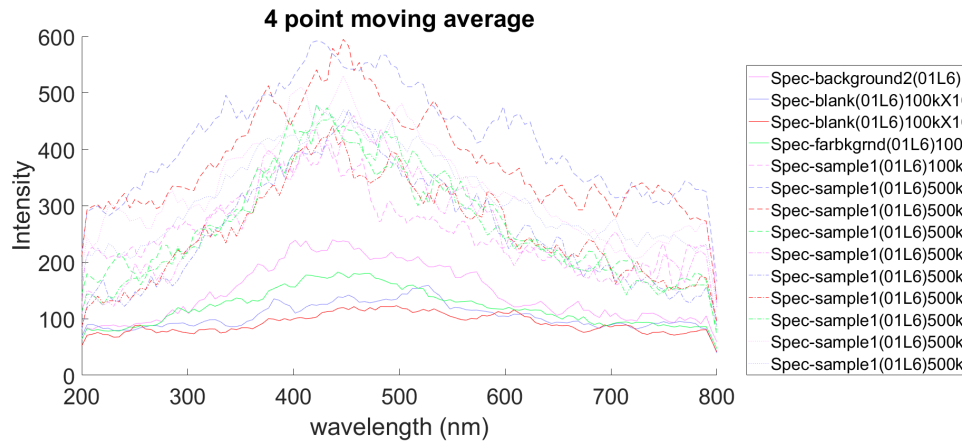


Figure 7.20: Cathodoluminescence of structures produced by EBL. Peaks can be seen around 420nm with intensity from 350nm to 600nm. The intensities for the background samples are much weaker but Silicon Nitride shows some intensity around 400nm to 600nm.

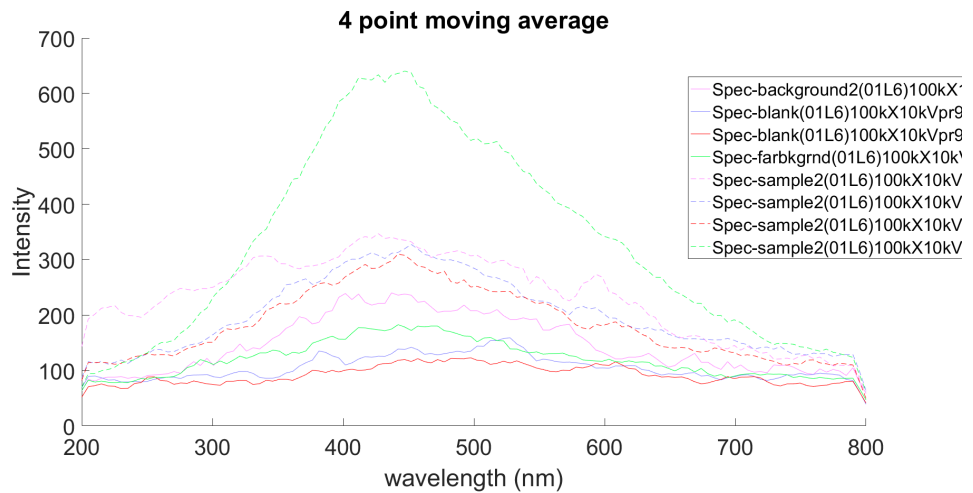


Figure 7.21: Cathodoluminescence of structures produced by EBL. A large peak is seen when an increased sensitivity is used, there are also some higher intensity peaks above the background intensity, between 350nm and 400nm.

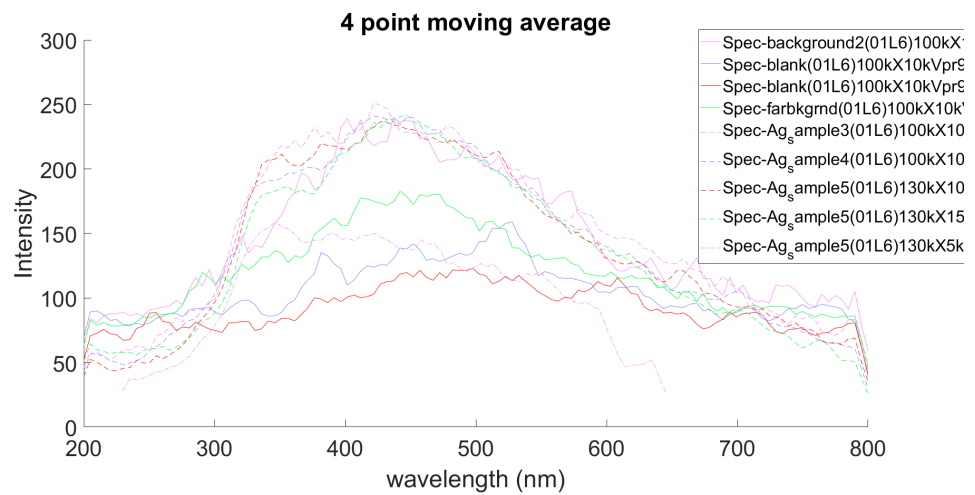


Figure 7.22: *Cathodoluminescence of silver structures. Ag shows some clear peaks around 400-500nm with a prominent second peak around 350nm. These show that small spirals can support low energy modes.*

### 7.1.4 Atomic force microscopy of spiral structures

The lack of structure in the central region of the STEM EELS intensity maps of figures 7.5 to 7.13 is most likely due to strong damping of plasmon mode oscillations leading to a loss of coherence when reflections travel to the center. This strong damping could be related to the surface roughness, even though the surface plasmons match the dispersion for the  $Si_3N_4/Al$  interface, roughness on the Al/vacuum interface could lead to variations in coupling between the two surfaces and this inhomogeneity could ultimately cause scattering. Figures 7.23 and 7.24 show atomic force microscopy images and line plots of surface height across example spiral structures showing a surface with a height which varies by approximately 10nm for the FIB structure and 5nm for the EBL structure. Future experiments may benefit from improvements to the production procedure to create films which are of a more uniform thickness, to offer less potential scattering centres for travelling plasmon waves. A study of the surface roughness effect and metal layer deposition techniques is left open as a area to be explored in future research projects.

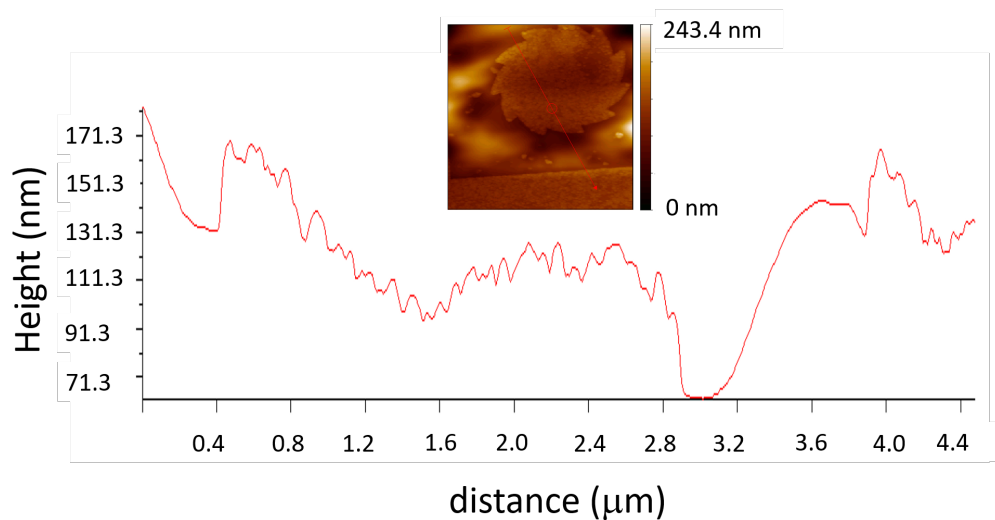


Figure 7.23: Results of an AFM line scan across a spiral island structure produced by FIB in thermally deposited Al film. The lower line chart plots the height measured along the red arrow in the top AFM image.

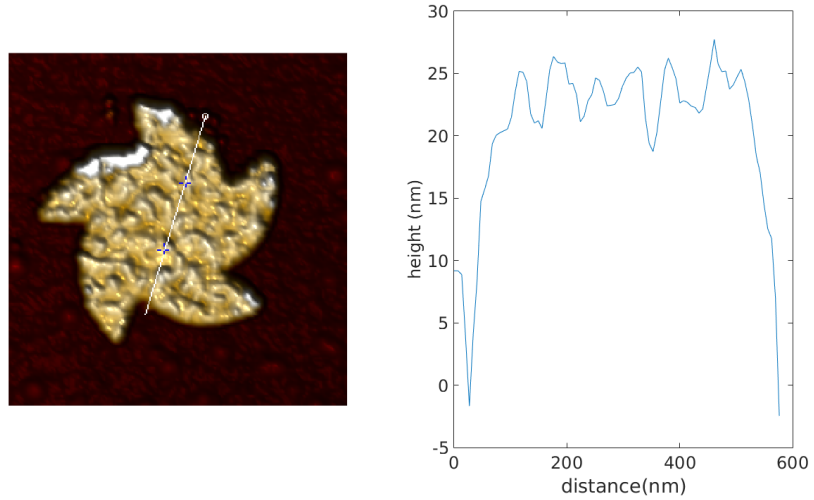


Figure 7.24: Results of an AFM line scan across a spiral island structure produced by EBL. Left is an AFM images of the  $l = 5$  structure and right is the depth linescan along the white line in the left image. Distances are in nm.

### 7.1.5 The nature of the recorded energy losses

The structure shown in the recorded energy loss intensity is most likely due to coupling of the beam electron with surface plasmon modes at the  $Al/Si_3N_4$  interface. The EELS intensity is proportional to the local density of states from all allowed eigenmodes in the structure. Away from the edge, at the center the reflected plasmon waves have been scattered and the amplitude is reduced too much to see any of the the struture which is predicted by the MNPBEM code. The lack of interference and short decay length can explain both the central intensity in the EELS maps at 2.5-5eV and the lack of difference in the TEM EELS of section 2.1.11. If there are waves being reflected from the curve boundary then there must be some inherent circulation of the plasmon mode close to the edge. However it is unclear if this circulation is solely due to exchange of momentum with the boundary upon reflection or if the electron is transferring any OAM into this circulation. The experimental and simulated data show that in order to create structures supporting plasmon modes containing OAM which travel to the center of the shape, improved fabrication techniques would be required to either produce smaller structures (less than 50nm) or produce a metallic film with a larger decay length (higher purity or fewer surface imperfections). Hobbs et al [148] show surface plasmon occuring

only at the edges of  $12nm$  diameter nano disks and volume plasmon in the center. For the structured considered here the dimensions are much larger and there is prominent intensity in the central region even at  $3.5eV$ . In the following section the interaction between these spiral structures and C-shaped vortex electrons is discussed and EELS analysis is presented.

### 7.1.6 Chirality dependent EELS signals

EELS spectra have been recorded with C-shaped electrons after interaction with the flat spiral island structures produced by electron beam lithography (EBL) described in section A.4. These were placed in the sample plane of the JEOL 2200 microscope whilst in TEM mode and electron energy loss spectra (EELS) were recorded whilst the energy filter entrance aperture was used to post select intensity coming from one diffraction order of the condenser aperture mask described in chapter 5 section 5.1. The two experimental set ups used are shown in Figure 7.25, in A a hologram mask produces diffraction orders separated in the transverse plane, whilst in B the mask is a pinhole interference mask producing diffraction orders separated along the beam propagation direction. In both cases the entrance aperture (EA) is used to select the intensity entering the filter however it only excludes most intensity from unwanted orders for figure 7.25A. In figure 7.25 B there is some intensity allowed through the on axis filter from diffraction orders focused above or below the sample plane, however these vortex rings will be larger away from their focus and less intensity will be present within the EA.

For the aluminium samples used in this experiment there are 4 key regions of interest in the energy loss spectra. The first being from 3 to 5eV which can be assigned to low energy localised surface plasmon modes [152][43], secondly, around 7eV which can be assigned to travelling surface plasmon modes [153] thirdly a prominent peak around 15eV which is produced by loss to the bulk Al plasmon oscillation[154]and finally 23eV which is the bulk Silicon Nitride substrate plasmon mode and is also close to the 22eV of the  $Al_2O_3$ [155]

There are also some multiple losses seen at 30eV, equivalent to an electron losing energy twice to two 15eV plasmon oscillations. Additionally this means some intensity could also be present, due to surface plasmons

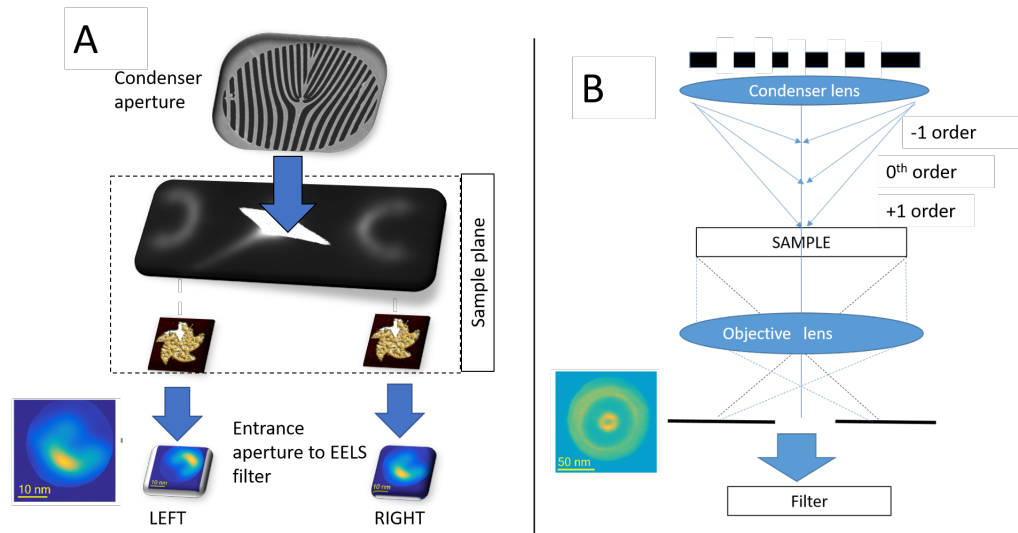


Figure 7.25: *The two type of amplitude mask EELS experiments conducted. A) The mask is an interference of angled plane waves and diffraction orders are dispersed transverse to propagation direction, travelling at different angles. B) The mask is an interference of spherical waves, diffraction orders are dispersed along the propagation direction with different curvatures and so different focal points. Also shown in the bottom left insets of each section is the experimental intensity of the C-shaped or integer vortex diffraction order in the entrance aperture shadow.*

at the sum energies of from a combination of  $3\text{-}5\text{eV}+7\text{eV}=10\text{-}12\text{eV}$  ,  $7\text{eV}+15\text{eV}=22\text{eV}$  and  $15\text{eV}+3\text{to}5\text{eV}=18\text{ to }20\text{eV}$ . However these will be low intensity compared to the main peaks.

### 7.1.6.1 EELS from a pinhole mask integer vortex

Electrons with OAM could potentially interact with chiral samples differently, leading to a measurable difference in observables. In general this can give more information about the sample. Specifically comparisons of EELS with electron beams of different chirality can potentially give information about the allowed magnetic transitions. Initial experimental results of the chirality dependent interaction with iron film has been shown by Verbeeck [55]. The equivalent results for interaction which chiral plasmon modes in 2 dimensional structures has not yet been published. If chiral dependent interactions are possible this opens the way for plasmon OAM based

sensing techniques, which has potential applications in the development and optimisation of future plasmonic devices utilising OAM. With this in mind, EELS was used to see if there are any chiral interactions with the Al thin film structures the far field of a spiral sieve mask was used (figure 7.26 a). This had been previously designed and produced by the electron vortex group at the University of York [156]. This pinhole mask was of the type shown in figure 7.25B, and producing  $l=11$  vortex beams in the first diffraction orders above and below the  $l=0$  diffraction order. An example of this vortex beam is shown in figure 7.26 b, and shows the central vortex surrounded by interference patterns from other defocused diffraction orders. The condenser lens was varied to bring the desired diffraction order into focus on the sample plane, in an identical experimental set up to chapter 5 section 5.1. However the variation of topological charge is achieved by varying the defocus and not by shifting the beam.

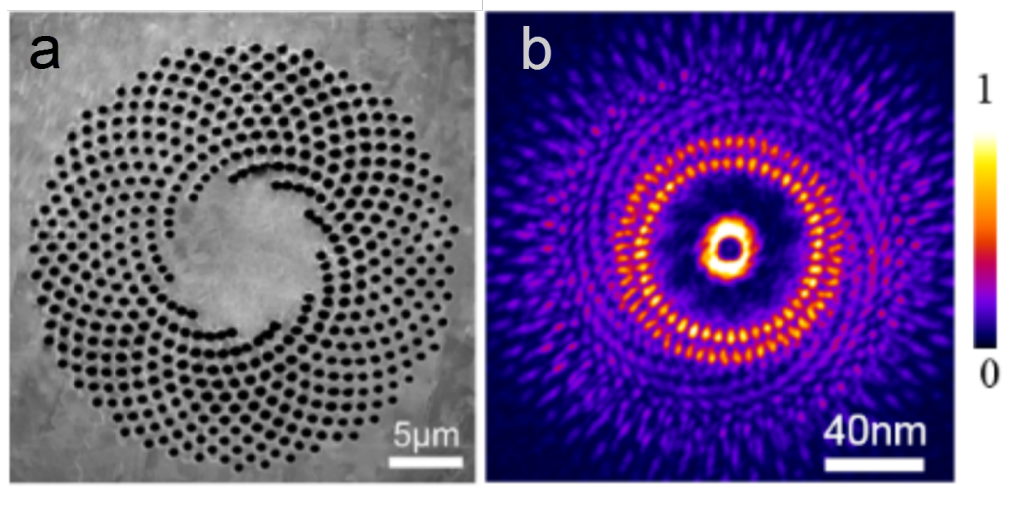


Figure 7.26: (adapted from reference [156]) a) an SEM image of the pinhole mask used. b) A TEM image of one of the first diffraction orders produced by the pinhole mask in (a).

For many shapes on the grid described in section A.4, the orders above and below focus produced the same EELS spectra. However there was one instance where one order showed increased intensity at approximately 3.5eV, this is shown in figure 7.27. These EELS were recorded from 50 spectra at 0.1 second exposure. At energies of 15eV and 23eV it is the alternate order which has a higher intensity, showing the 3-5eV difference is not due to any tails from broadening of peaks from higher energies.

When normalised to the integrated counts up to  $27\text{eV}$ , the fact that a loss of bulk intensity occurs which appears to compensate for the gain at  $3.5\text{eV}$  suggests the difference in EELS intensity is related to a surface state. It was also tested defocusing the diffraction order such that only the inner intensity is selected by the EA, excluding as much of the unwanted diffraction orders as possible. However this reduced the signal to noise ratio and did not show any clearer difference signal.

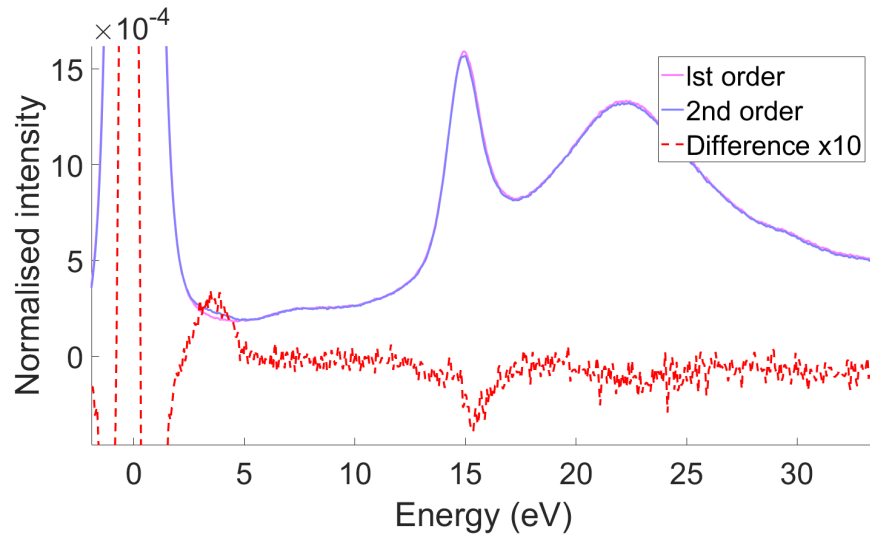


Figure 7.27: Recorded EELS spectra, the 2nd order is the opposite opposite side of focus along the propagation direction of the 1st order. A difference in EELS intensity can be seen between  $3\text{-}5\text{eV}$  when comparing diffraction orders either side of focus for a pinhole vortex mask.

### 7.1.6.2 EELS using a C-shaped electron

Based upon the initial pinhole mask result, the condenser aperture from section 5.1 was used to create C-shaped diffraction orders in an EELS experiment as shown in figure 7.25A. The EELS were compared when using the EA to post select intensity in the left ('-C') and right('+C') C-shaped diffraction orders (an example is shown in the inset of figure 7.25 a ). The resulting energy loss spectra (summations of  $10 \times 0.1\text{sec}$  exposures) can then give information on differences between the probability of interaction between the two C-shaped intensities and the sample. The left order ('negative') has a higher intensity , as such all spectra need to be normalised to be compared. The method chosen to normalise the intensities was by

dividing by the summation of electron counts up to  $27\text{eV}$ , this gives a representation of the percentage of the electrons out of the beam which lose energy and is not affected by different interaction strengths when multiple loss mechanisms are present.

By overlapping the C shapes onto the central region of the chiral aluminium structures the interaction of C beams and the film plasmon modes can be examined. It was found that there are repeatable differences between vortex probe and C beams of opposite chirality, as shown in figures 7.28 and 7.29. However, whilst the difference was initially pro-

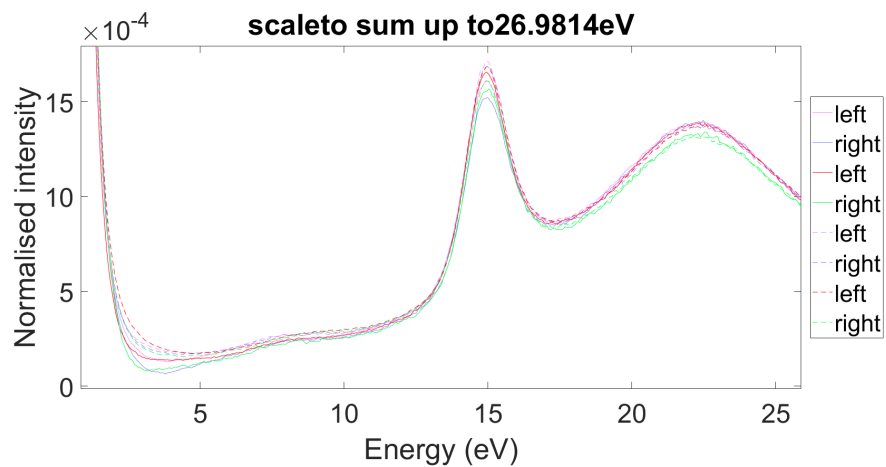


Figure 7.28: A large difference signal was measured for the Al spiral

nounced it quickly reduced when subsequently repeating the measurement. The reduction in the difference signal suggests there is some contamination (potentially carbon based) of the sample which causes intensity at 3-5eV which is not due to plasmon modes or chiral interactions. Under the same conditions the  $l=0$  bright dot gave a low intensity around 3-5eV showing that it was only the -C which had a high intensity in the EELS spectra. This would be consistent with a chiral coupling between the -C and a chiral plasmon mode. However in later measurements the  $l=0$  mode also gave high intensities, and as will be shown the lack of repeatability of a large signal suggests the coupling is weak and at least shows it is extremely difficult to measure with the experimental set up used in this study.

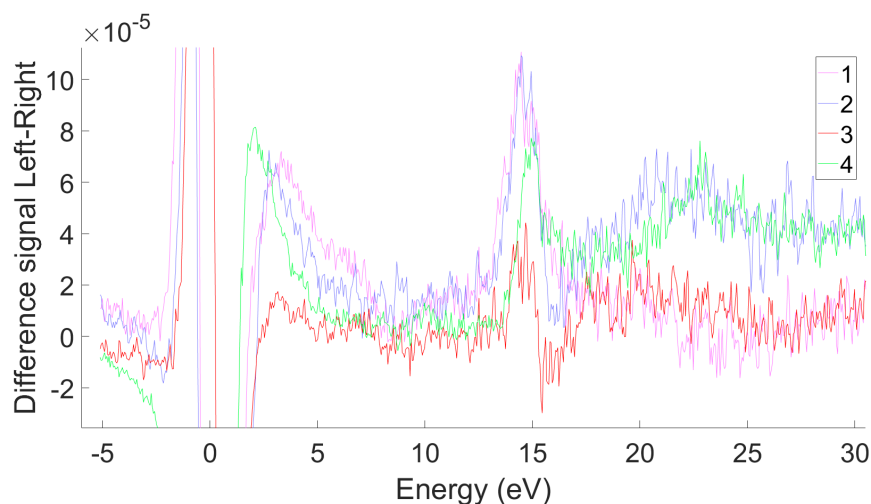


Figure 7.29: *The large difference signals measured on an Al spiral from the spectra in figure 7.28. Different colours are for different repetitions of the same measurement.*

### 7.1.6.3 Background difference signals

As a background comparison measurement the apertured EELS for +/- C were compared for the background Silicon nitride (figures 7.32 and 7.33) and large areas of Aluminium (figures 7.30 and 7.31). All of these figures show a difference signal with the -C being higher intensity around 3.5eV however the size of the signal was reduced when compared to the spiral structures. The presence of a difference for the large aluminium structure shows the difference in energy loss is not solely due to a localised surface plasmon mode which should only occur for small structures with a defined boundary. A nanodisk 225nm diameter was also tested (figure 7.32) and showed a large difference signal, showing the difference cannot be solely due to a chiral interaction related to the spiralling boundary.

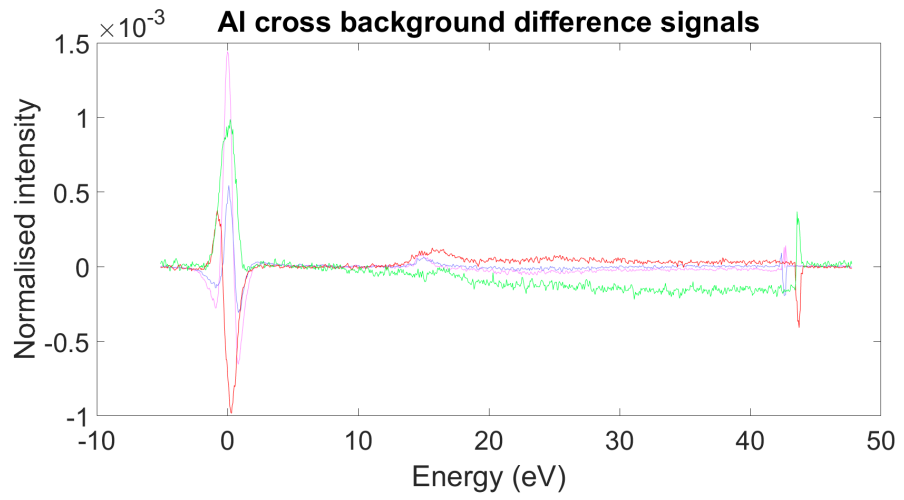


Figure 7.30: *Difference signals (left order-right order) recorded for a large Aluminium structure. The intensities were scaled to sum of intensities up to 27eV. Different colours are for different repetitions of the same measurement.*

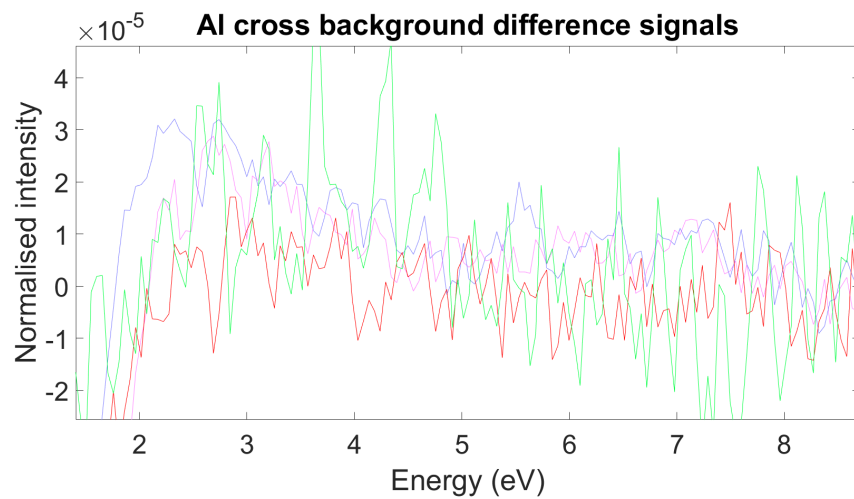


Figure 7.31: *A zoomed in version of figure 7.30*

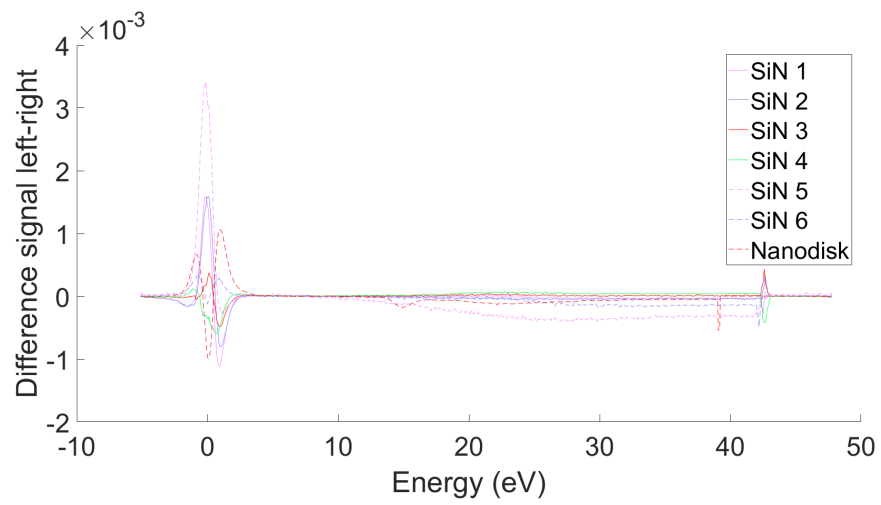


Figure 7.32: *The difference signal measured for a nanodisk (diameter 225 nm) and multiple sets with just the Silicon nitride substrate (used as a background).*

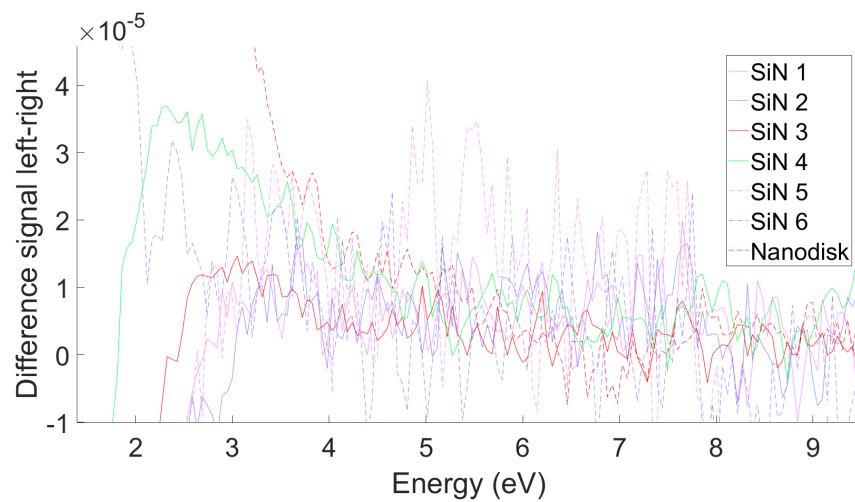


Figure 7.33: *A zoomed in view of the graph shown in figure 7.32*

#### 7.1.6.4 Point spread function recorded without a sample

There is still a large difference in the EELS from the diffraction orders without any sample in the beam path (see figures 7.34 and 7.35). The zero loss peak (ZLP) shows some asymmetry which occurs to different amounts for the positive or negative diffraction orders. This could be related to the different orientations of the opening angle, which may cause electrons of opposite topological charge to produce different intensity distributions when the filter lenses collect them to a line along the energy dispersive axis. It should be noted that all of the spectra recorded contain low intensity variations with multiple spectra showing identical structure showing this is a systematic error due to the CCD rather than an experimentally produced variation.

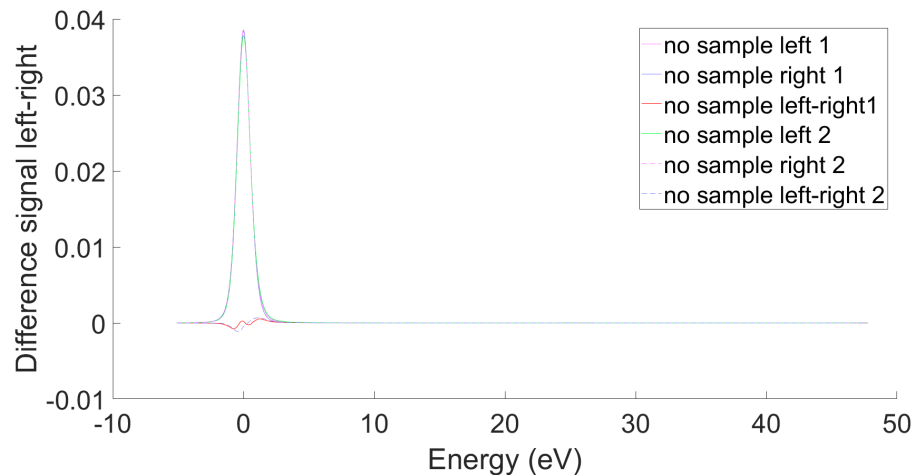


Figure 7.34: *EELS spectra recorded for both right and left diffraction orders with an empty sample holder.*

After multiple attempts to recreate the difference signals seen in figures 7.27 and 7.29 it was not possible to do so. The left C was consistently higher in intensity however other parts of subsequent spectra were different in intensity. By comparison with the background difference signals the later differences are not significantly above the noise level and as such cannot be considered as a clear chiral interaction signal. Figure 7.36 and 7.37 shows the integrated difference signal between 3eV and 4eV for spiral structures as well as the background. It shows there are only a few sets of data which show a difference larger than the background levels, some of these have higher intensity related to the zero loss peak tail.

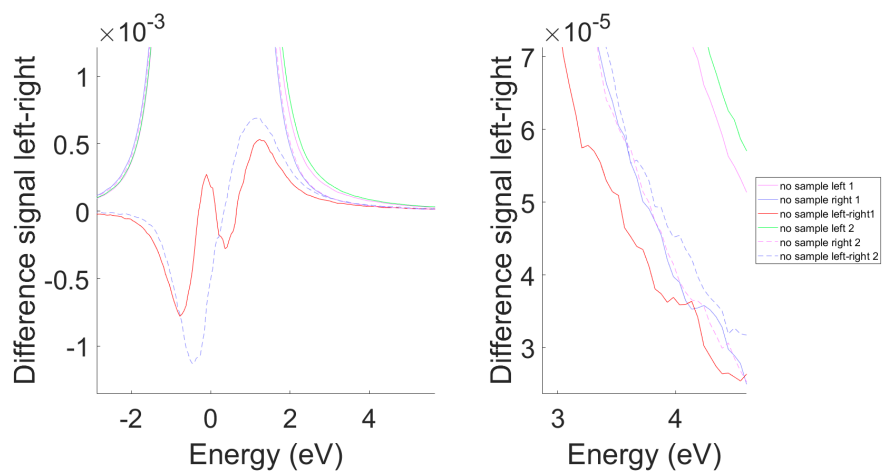


Figure 7.35: A zoomed in view of the graph shown in figure 7.34

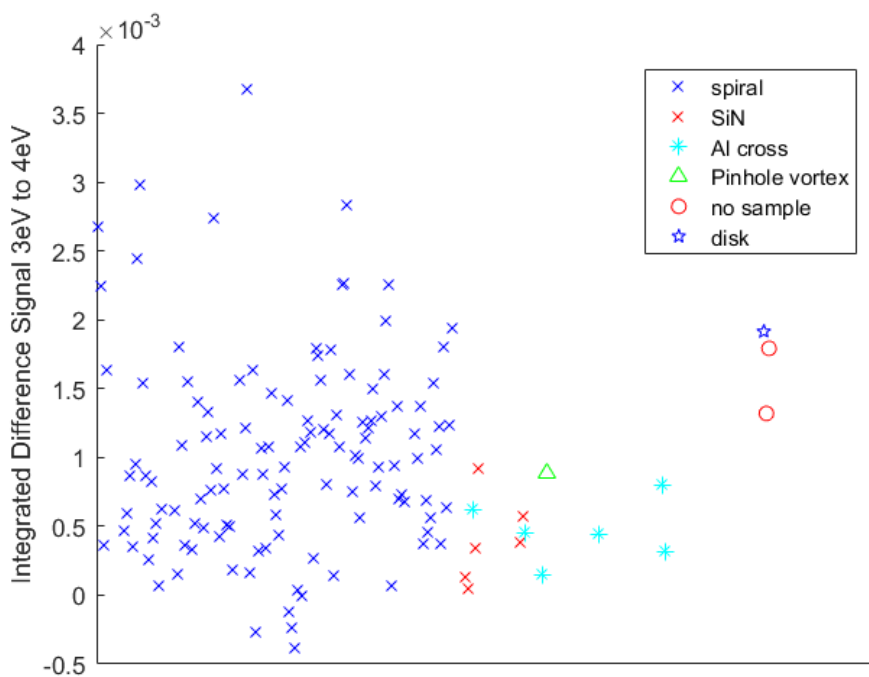


Figure 7.36: A plot of the measured difference signal integrated between 3eV and 4eV of EELS spectra, normalised to  $zlp$  under different experimental conditions, as shown in the legend.

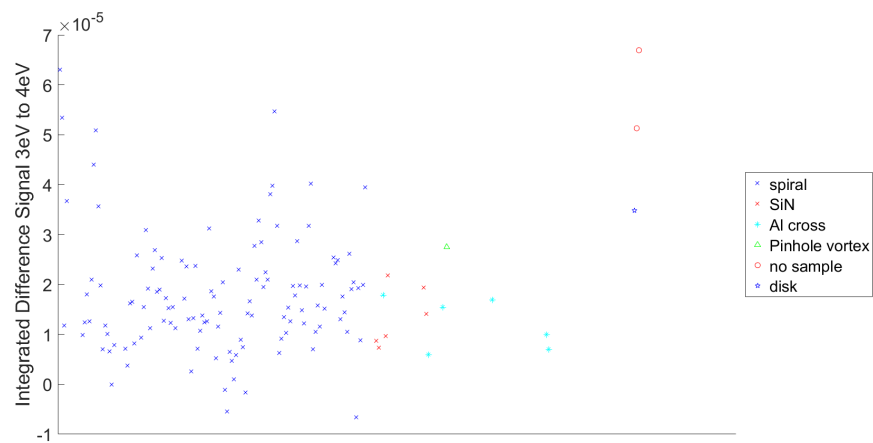


Figure 7.37: A plot of the measured difference signal integrated between 3eV and 4eV of EELS spectra, under different experimental conditions. The spectra were normalised to the sum of intensities up to 27eV

## 7.1.7 Chapter summary

This chapter has detailed the experimental investigation of energy loss between electron beams and spiral structures in thin metal films for plane wave and C-shaped electrons. This is the first time such flat chiral spiral island structures have been investigated, looking at their interaction with a TEM electron beam. STEM EELS mapping showed interesting structure near to the objects boundary edge, suggesting interference between incident and reflected surface plasmon modes. The central region of the spiral structures did not show a vortex minima. Both cathodoluminescence and EELS show energy loss between 3-5 eV, which has been attributed to localised surface plasmon modes. The interaction of C-shaped electrons of opposite chirality showed an initial difference signal. Whilst this is a very exciting result, the inability to reproduce this and the presence of similar level differences caused by experimental effects mean this cannot be unequivocally attributed to a chiral transfer of energy between the electron and plasmon mode. If the initial signal was a chiral interaction the subsequent results show this is a weak interaction and difficult to repeat with the experimental set up used. Future research could calculate the trajectories of electron beams with OAM travelling through an energy filter, and future experiments could investigate this signal further, improving the signal to noise ratio and discovering the source of the background signal difference. Whilst the analysis of the experimental results was ultimately unclear, for completeness, section A.1 of the appendix presents a discussion of potential causes of the measured difference in the EELS signal.

# Chapter 8

## Conclusions

This thesis has added to the experimental data for electron beam shaping experiments which has been lacking behind the theory developed to describe such states. For the first time it was shown how a C-shaped beam can be produced by combining fractional topological charge and radial phase gradients. Local phase gradient analysis was used to derive control equations to predict the size and opening angle of the C produced. The OAM content has been analysed theoretically by numerical and analytical methods and the C shape is found to be made of a contributions from integer vortices from a narrow spread of topological charge. The control of the vortex C-shape is new and applicable to both photon and electron optics. The theoretical control of the opening angle derived in chapter 4 was experimentally verified in a transmission electron microscope in chapter 5, highlighting the versatility of electron beam shaping methods. This is the first time a C-shape with controlled size and opening has been produced either with photons or electrons.

The electromagnetic modes of small metallic spiral were then simulated, it was found that by adding a spiralling step to a nanodisk the eigenmode solutions gained an increased asymmetry in their OAM mode decompositions, showing that spiral structures can support electromagnetic oscillations containing OAM. Following this, in addition to furthering the field of experimental electron beam shaping, this thesis investigated the possibility of chirally selective OAM transfer to 2D chiral plasmon modes, a subject as yet unexplored for electron vortices. Flat metal structures were produced and EELS maps were recorded, showing a match to simulated EELS. These EELS maps contain patterns characteristic of standing

waves caused by interference of incident and reflected wave components near the edge. Comparison with Bessel mode functions suggests that the edge boundary conditions are that the electric field is a maximum. Future work could involve using near field measurement techniques such as SNOM to probe the electric field directly to test this hypothesis.

Phase structured electron probes were used to gain EELS of the chiral structures collecting signals from probes of one chirality at a time. A difference signal was then measured to see if there was any interaction similar to the chiral interactions observed between light and 2D chiral metal structures. This is the first time such an experiment has been tried with electrons. Whilst there was some evidence of a CD like signal the results in this thesis show it is not possible to show EMCD with 2D plasmon structures under the experimental conditions available. This suggests either the transfer of OAM to 2D plasmon modes is forbidden or requires much finer control of experimental conditions than is currently possible.

### 8.0.8 Future prospects

The work in this thesis has the potential to be expanded and furthered in many different ways. Due to spatial light modulator technology one of the easiest experiments would involve producing C-shaped lasers and applying some of the optical trapping applications mentioned in chapter 4. In addition to the 'low hanging fruit' of optical trapping with silicon microparticles, interactions of C-shaped beams with more exotic forms of matter such as Bose-Einstein condensates could be explored, with the possibility to investigate a vast range of fundamental interactions in quantum physics, such as OAM transfer or tunnelling through the potential barrier of the gap in the C.

The theory behind single and multiple C-shapes could be applied to the development of fast electron beam lithography of split ring structures for metamaterial production. More broadly the possibility of having OAM without circular symmetry could be explored by producing other states with phase singularities but intensities other than a ring structure.

Whilst our understanding of free space and idealised electron vortices provides a solid foundation, there needs to be more work in understanding the interactions of electron vortex probes with samples and how to extract

information once the interaction has taken place. The simulations of electromagnetic modes with COMSOL could be furthered by trialling different boundary conditions, to match the energies with previously published values and simulating different materials to test if the effect of increasing the spiral stepsize is present for other materials.

The theory behind OAM transfer to 2D chiral plasmons still needs to be fully developed, this would improve our understanding of the experimental results presented in this thesis and aid the future design and further experiments to record an EMCD signal proving chirality specific OAM transfer from free space electrons carrying OAM. Modelling the effect of external magnetic fields on C-shaped probes could expand our understanding of these non integer OAM carrying states, and a detailed simulation of the effect of an EELS spectrometer on C-shapes and indeed integer vortices would be beneficial to the field. The interactions and transfer of OAM with other quanta of energy such as magnons or spin waves offers a vast potential to explore the unique magnetic properties of phase structures electrons carrying OAM. These interactions offer the potential to gain further insight into the processes governing spin transport or magnetic properties, both key properties underpinning current computer memory technologies. Electrons are one of our most accessible tools for investigating materials on the nanoscale and, as this thesis has shown, there is wide scope for the application of phase control to further our fundamental understanding of electrons and provide distinctly new tools with which to probe matter.

# Appendix A

## Appendix

### A.1 Discussion of potential causes of STEM EELS signal

The possibility of the repeatable but small difference signal being due to a chiral interaction appears to be low. Below the potential causes of this difference signal are considered. During this analysis the abbreviation psf is used for point spread function.

#### A.1.1 Ruled out causes of intensity difference between 3eV and 5eV

By comparison with the central order ( $l=0$ ) and illumination from a circular aperture (labelled CA# 2 in the spectra keys) some possible causes of the difference can be ruled out.

##### peak intensity

Variations in the peak intensity between the two orders could potentially cause a stronger interaction for the more intense order, however the highest intensity of  $l=-1,0,+1$  is the  $l=0$  central diffraction order. This does not always show a higher intensity around 3-5eV (see figure A.1) and shows the variation in the counts at 3-5eV is not caused by intensity variations.

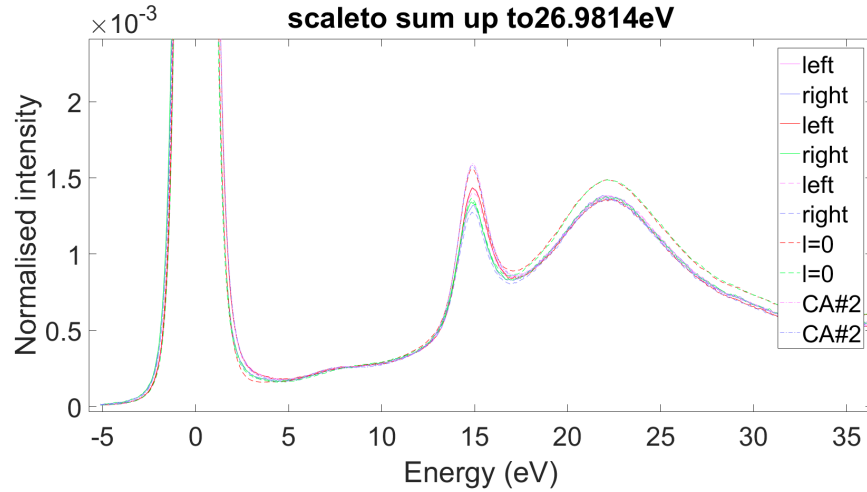


Figure A.1: A comparison of EELS recorded with left and right C-shaped beams, the central  $l=0$  beam and a circular CA#2 aperture. These show that the difference was not due to variations in the brightness or intensity differences between the C shapes.

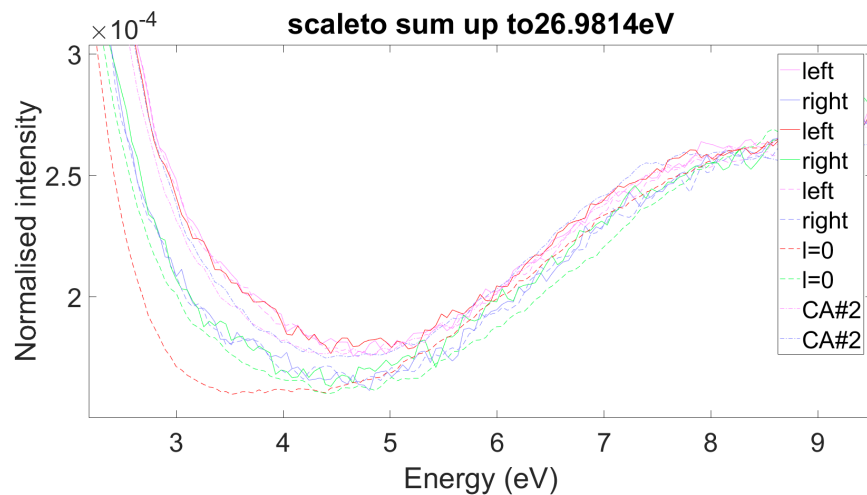


Figure A.2: A zoomed in view of the graph in figure A.1.

### astigmatism

The holographic mask and lens system may introduce different amounts of astigmatism in  $\pm 1$  orders. Differences in astigmatism could potentially alter the trajectory the beams take through the energy filter producing a higher signal for one C than the other. This was checked by purposefully adding in astigmatism in different directions (figure A.3). The difference did not change senses with the -C remaining at higher intensity for both directions of astigmatism. This rules out astigmatic variation as a cause of the  $\pm$  C intensity differences.

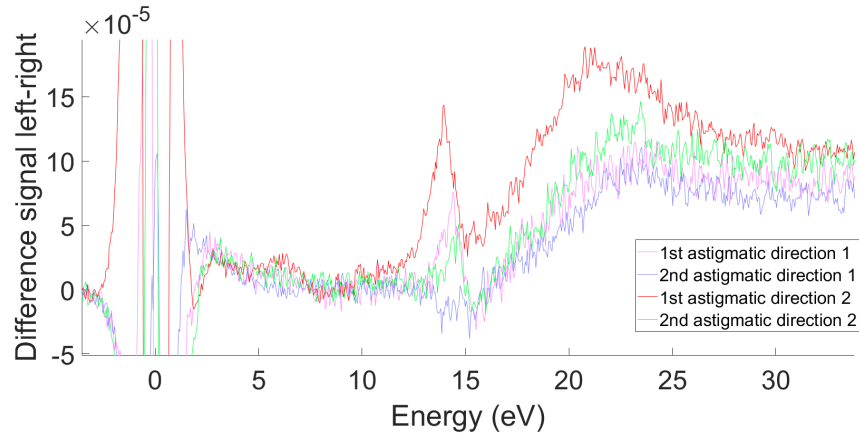


Figure A.3: *The difference in EELS intensity between left and right C shapes when applying astigmatism in 2 opposite directions. These show that the difference is not due to any astigmatic effect.*

### Defocus

In a similar way to the astigmatism the effect of varying defocus was tested by collecting spectra using purposefully defocused beams such that the spiral fills the EA. The -C shows higher 3eV intensity even when defocused in both directions (figure A.4) , as such it is unlikely that variations in the defocus of -C and +C could explain the difference signal.

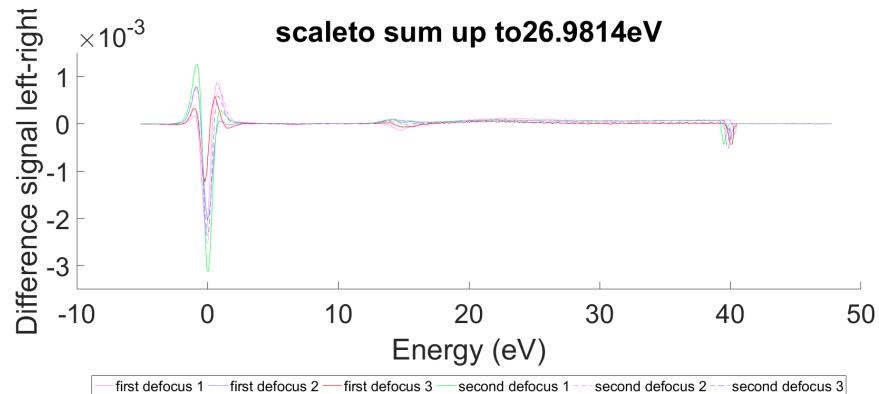


Figure A.4: *Difference signals (left -right) for varying defocus conditions, intensities have been scale to the zero loss peak.*

### Tilt

Differences in tilt of the +/-C diffraction orders relative to the sample could be a cause of the intensity difference. The +/-C EELS difference

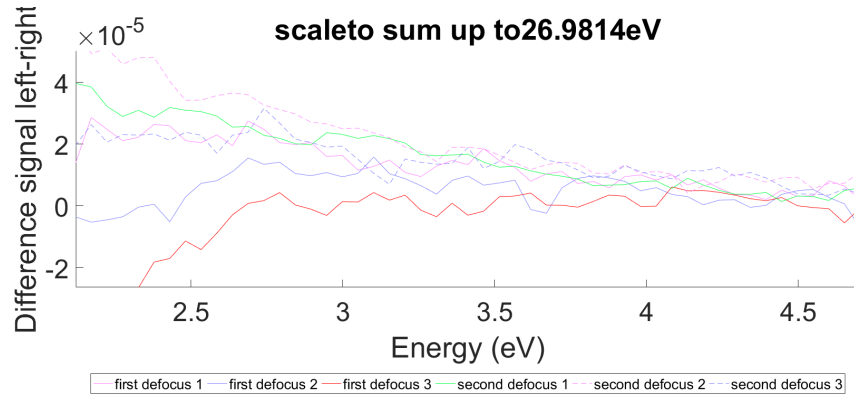


Figure A.5: *Difference signals (left -right) for different defocus conditions, intensities have been scaled to the sum of intensities up to 27eV.*

was recorded at different tilts (figure A.6) and did not show inversion of the difference signal. This shows varying tilt angles cannot account for the difference in EELS intensities. The reduction in signal intensity between 3-5eV could be related to the three dimensional structure of the mode intense region of the C spiral , tilting the sample reduces the overlap of the sample plane with the high intensity region. This appears to affect both C shapes EELS the same and cannot explain the differences seen.

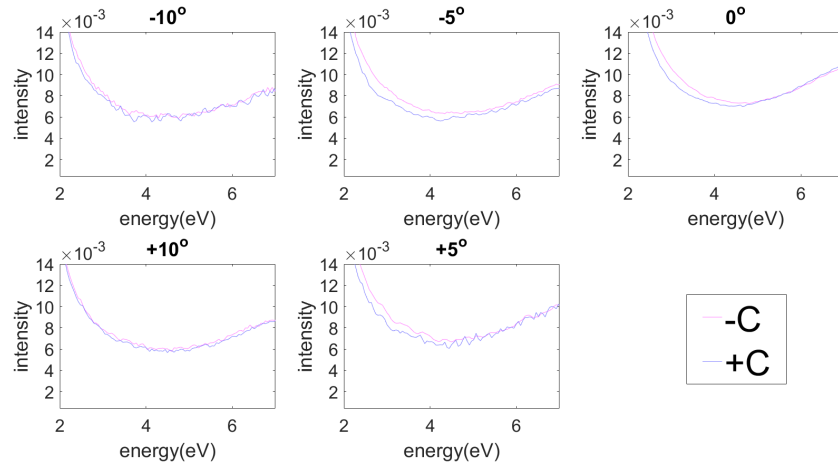


Figure A.6: *EELS recorded for +C and -C at different values of sample tilt.*

#### Other peaks and FWHM of zero loss

A comparison of intensities at 3-5eV, 15eV and 23eV shows that there is no correlation between the intensities. As such spectra showing the highest intensity at 15eV does not necessarily show the highest intensity at 3-5eV.

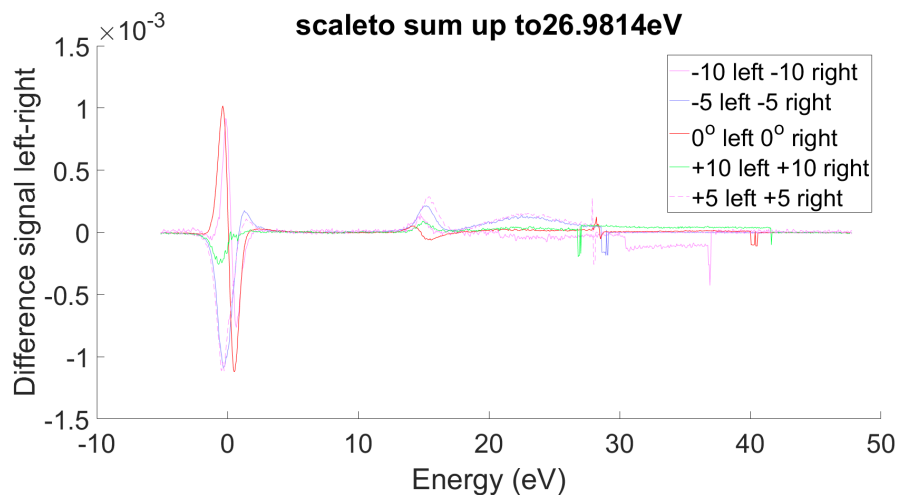


Figure A.7: *Difference signals left-right (from figure A.6 for different values of tilt with sample 'upside down', with the electron interacting with Silicon nitride membrane first.*

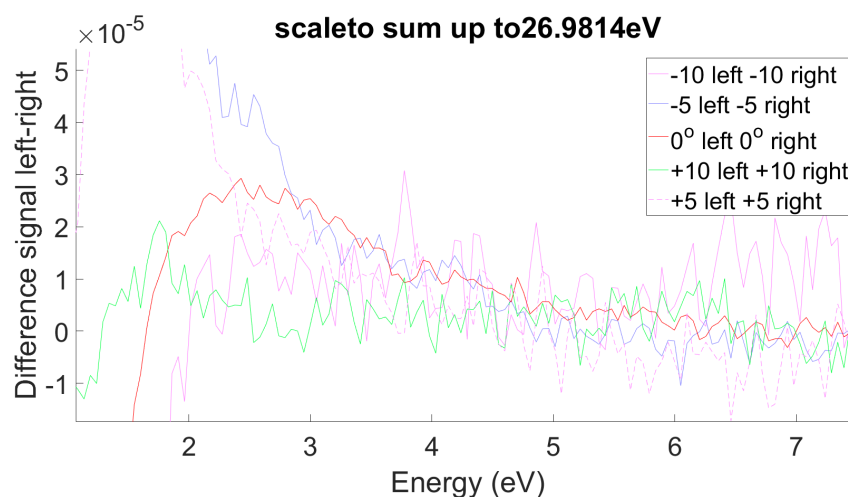


Figure A.8: *A zoomed in view of the graph in figure A.7*

This shows the difference in intensities at 3-5eV is not due to the tail of the bulk plasmon 15eV and 23eV peaks. When comparing +/-C spectra there is some variation of the full width half maximum (FWHM) and asymmetric shape of the zero loss peak. However as shown in figure A.9 there is no correlation between either size of FWHM or symmetry of the peak which would explain the difference in intensity as a simple artefact of the spectra ZLP shape.

When flipping the sample over such that the electron beam is incident from the opposite side the EELS intensity from the -C shape re-

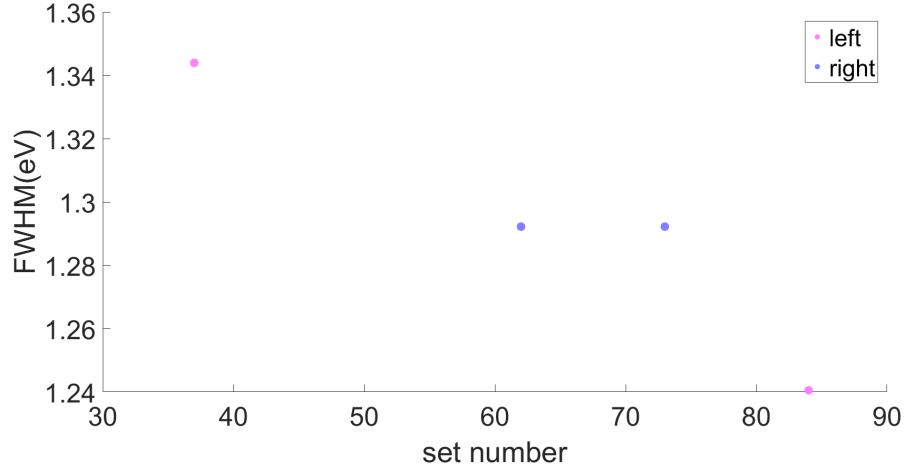


Figure A.9: Measured full width half maximum values for zero loss peaks of different  $C$  orders.

mains the highest when compared to that of the +C. This shows that if the 3eV-5eV intensity is due to a chiral interaction then the Silicon nitride ( $Si_3N_4$ )/Al structure has some 3D chirality to it, due to the interface  $Si_3N_4$ /Al having a sense of direction from Al to  $Si_3N_4$ . This would mean that the sample would still lose more energy to the -C electron.

#### A.1.1.1 Potential explanations of EELS

Whilst the largest difference was seen for a patterned spiral structure as shown in figure 7.29, there were also differences recorded for the  $Si_3N_4$  background and the larger Al cross. The difference between the +/-C EELS intensities was smaller for the background tests showing that the initial difference signal was due to interaction with the Aluminium spiral structure. This could be due to chiral interaction with bound plasmon modes. However subsequent lower difference signals are not appreciably above the size of the background differences.

The energy loss for the spiral is not due to a localised bound mode, which is supported by the STEM images in section 7.1.2 showing a lack of any nodes close to the central region of the Aluminium shape. This implies that the plasmon mode decays before reaching the center of the spiral shape, as such any chiral interaction at the center cannot be due to the chiral boundary shape.

This leaves a chiral transverse plasmon with an energy between 3-5eV as a likely explanation for the differences seen on the Aluminium film. This could be due to an uneven surface producing a chiral arrangements of bumps with which there is a chiral specific interaction. Similar to an arrangement of nanosphere surfaces Any smaller differences seen without a sample or with the silicon nitride membrane could be due to different trajectories caused by the asymmetrical nature of the C shapes. This in turn leads to different shapes being formed by rays entering the aperture with large angles. This effect is much less pronounced at smaller angles however a small difference could be caused by this effect for rays entering the spectrometer close to the entrance aperture edge.

#### **A.1.1.2 Direct background subtraction**

In an attempt to remove the ZLP background intensity a fitting function 'logfit', available for MATLAB was used to fit a power law ,  $y = 10^{int}x^{sl}$  (*int* is the intercept , *sl* is the slope of a log log best fit line) , to the low energy tail of the ZLP. This fit was then extended to the 2-10eV range and subtracted from the normalised spectra. The results are shown in figure A.10, this is the clear evidence that there is some energy loss peak around 3eV. By performing this ZLP subtraction it is clear that the difference in intensity is not caused by differing shapes of the ZLP, otherwise the differences would all be very similar. Interestingly high intensity around 3eV is seen for both C shapes and so the high intensity cannot be due to an experimental artefact only affecting one shape. This double hump structure is also seen for the Al cross spectra (825, 836), suggesting it is not a localised plasmon mode.

#### **A.1.1.3 Richardson-Lucy Matlab**

To further analyse the spectra taken from the +/-C diffraction orders deconvolution techniques have been applied to look for peaks in the low energy region and assess the presence of differences in these peaks.

Initially a background spectra taken on the silicon nitride substrate was used as the point spread function (PSF) as in input for the Richardson lucy algorithm in matlab "deconvlucy". Figure A.11 shows the

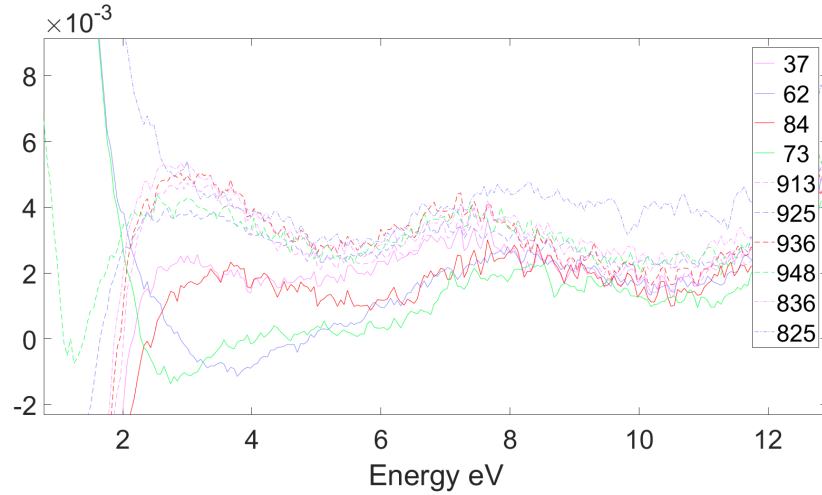


Figure A.10: *The results of direct subtraction of the Silicon Nitride background, red or pink are -C blue or green colours are for +C. sets 836 and 825 are for a large aluminium cross, all other sets are for an  $l = 4$  spiral. Both 3eV and  $y=7eV$  show peaks however these are both present in Al cross too*

result of the psf with itself with iterations 1 to 5 ('Data 1' to 'Data 5'). As more iterations are performed the spectra peaks become narrower and after 5 iterations there is only some intensity around the Silicon Nitride bulk plasmon peak (23eV) and either side of the zero loss peak (-5eV to -1eV and 1eV to 10eV). When applying the deconvolution with the psf to the initial spectra '37' which has a high intensity around 3.5eV (figure A.12) there remains a peak shape between 2-5eV after 5 iterations.

However the intensity at 15eV reduces too much to be useful, as such the first 3 iterations are compared in figures A.13,A.14 and A.15. With 1 and 2 iterations there is distinct peak like structure between 2-5eV for the first 4 spectra, however in subsequent spectra the deconvolution leaves low intensity peaks and small differences between +/-C EELS. After 3 iterations the spectra are very distorted however there are 2 distinct shapes for the +/- C spectra with only the +C retaining a peak at 0eV however this is also present in the Silicon Nitride background and as such is a characteristic of the probes and not the sample modes.

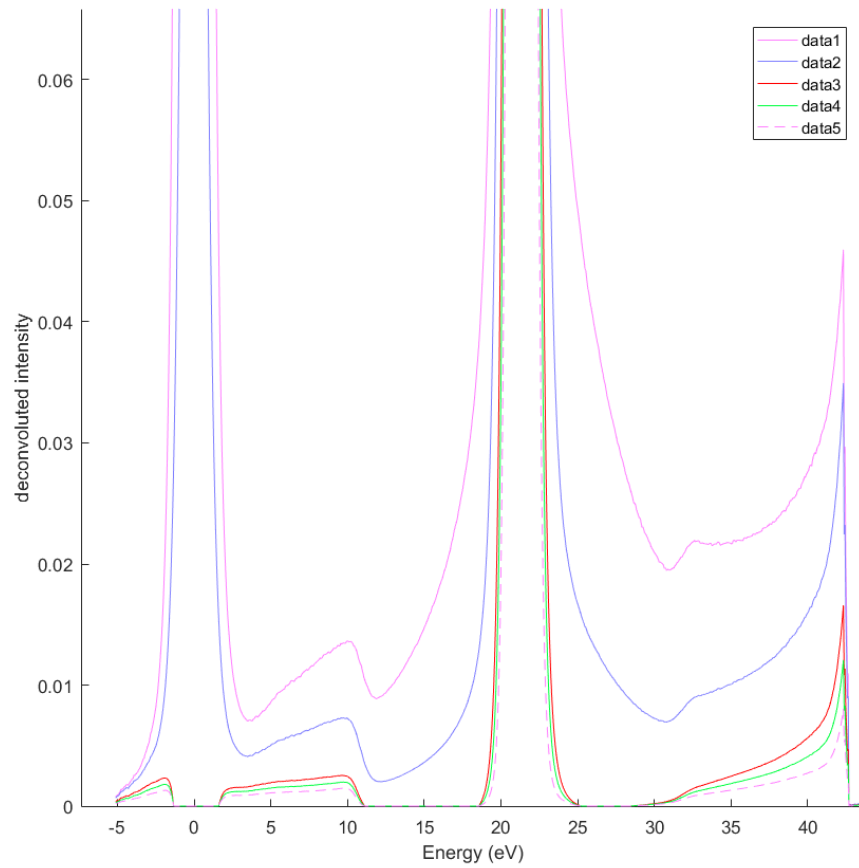


Figure A.11: *RL deconvolution of psf from no sample with psf 781 (from only Silicon nitride) in matlab with data 1 to data 5 corresponding to 1 to 5 iterations respectively.*

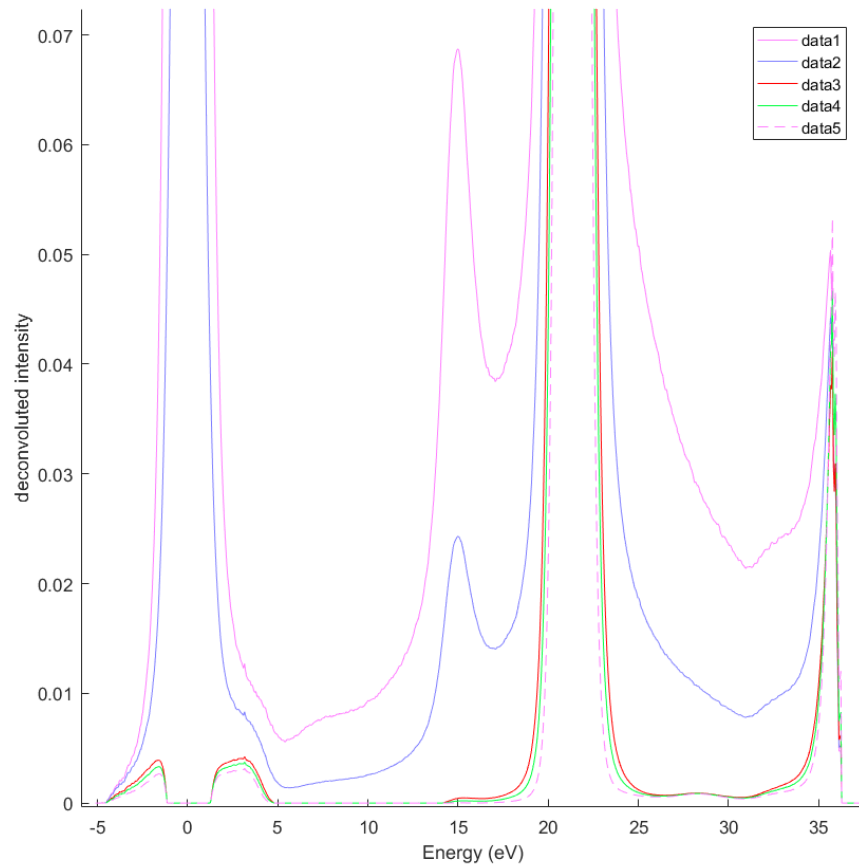


Figure A.12: *RL deconvolution of 12sept 37 (-C on  $l = 4$  spiral) with psf 781 (only Silicon nitride) in matlab with data 1 to data 5 corresponding to 1 to 5 iterations respectively.*

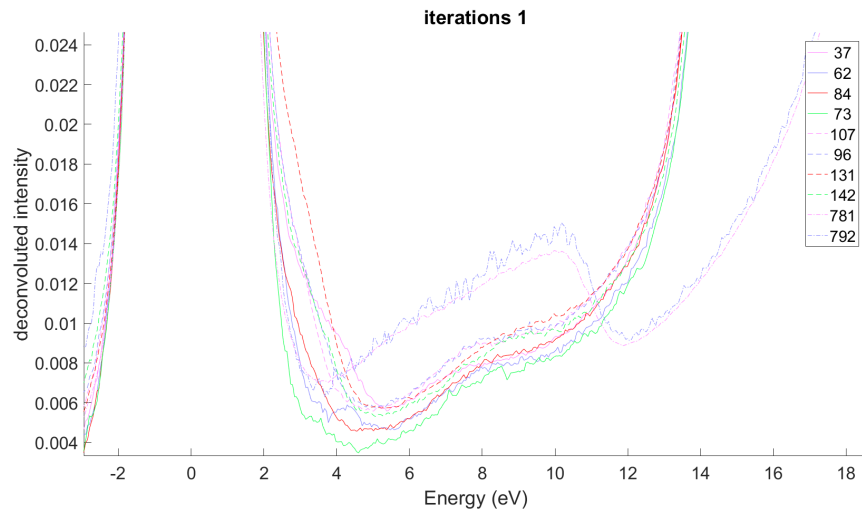


Figure A.13: *RL deconvolution of 12sept sets with a psf taken without a sample, in matlab for 1 iteration. Pink and red colours are  $-C$  blue and green are  $+C$ . 781 and 792 are for the silicon nitride substrate background all others are for an  $l = 4$  spiral.*

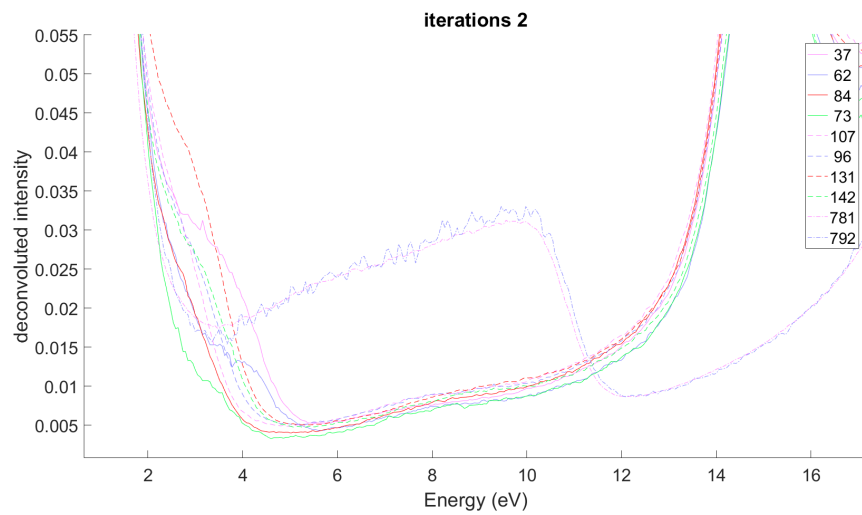


Figure A.14: *RL deconvolution of 12sept sets with a psf taken without a sample, in matlab for 2 iterations. Pink and red colours are  $-C$  blue and green are  $+C$ . 781 and 792 are for the silicon nitride substrate background all others are for an  $l = 4$  spiral.*

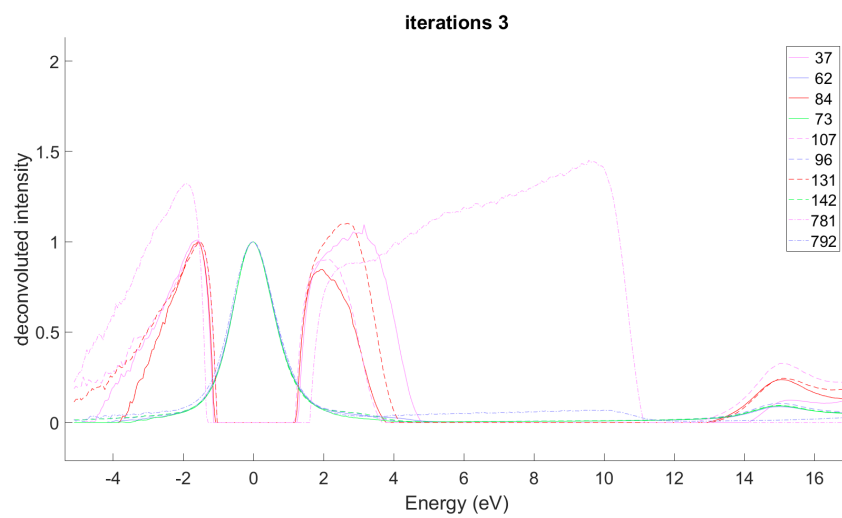


Figure A.15: *RL deconvolution of 12sept sets with a psf taken without a sample, in matlab for 3 iterations. Pink and red colours are -C blue and green are +C. 781 and 792 are for the silicon nitride substrate background all others are for an  $l = 4$  spiral.*

Deconvolution in matlab was also performed using a background spectra recorded with no sample in the holder. This only contains a zero loss peak. As is shown in figure A.16, a similar trend to before is seen as the iteration number increases the spectra peaks get narrower, the 15eV bulk plasmon Al peak is reduced relative to the bulk  $Si_3N_4$  and AlO peaks around 20-23eV. There is once again a peak in the range 2-5eV which gains intensity with more iterations, as figures A.17, A.18 and A.19 show. Using the MATLAB function deconvlucy there is some extra intensity around 3-5eV which appears as a peak after deconvolution but there is no clear difference between +/-C so it cannot be ascribed to a chiral interaction. It could potentially be caused by loss to a low lying plasmon mode, however given the weak signal this is unclear.

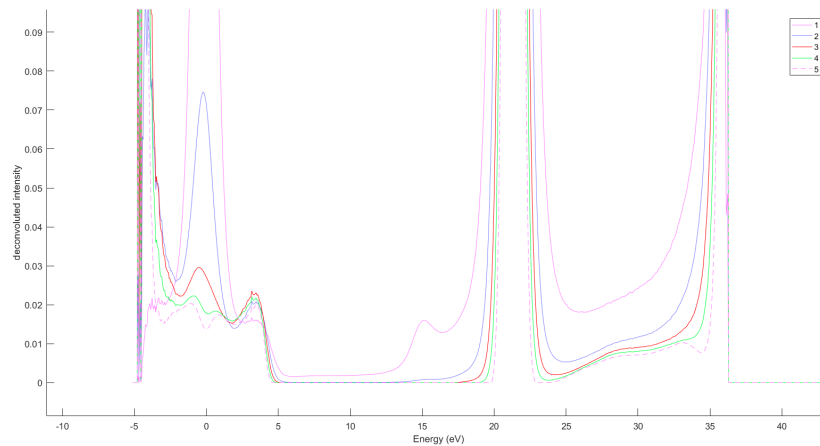


Figure A.16: *RL deconvolution of 12sept set 37 (-C on  $l = 4$  spiral) with 11 oct no sample PSF shows that increasing the number of iterations distorts the relative intensities*

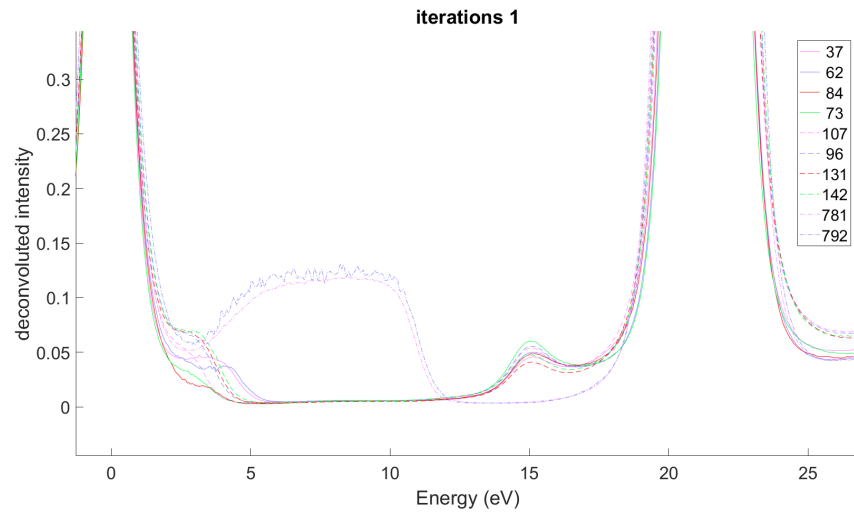


Figure A.17: *RL deconvolution with 1 iteration. Pink and red colours are -C blue and green are +C. 781 and 792 are for the silicon nitride substrate background all others are for an  $l = 4$  spiral.*

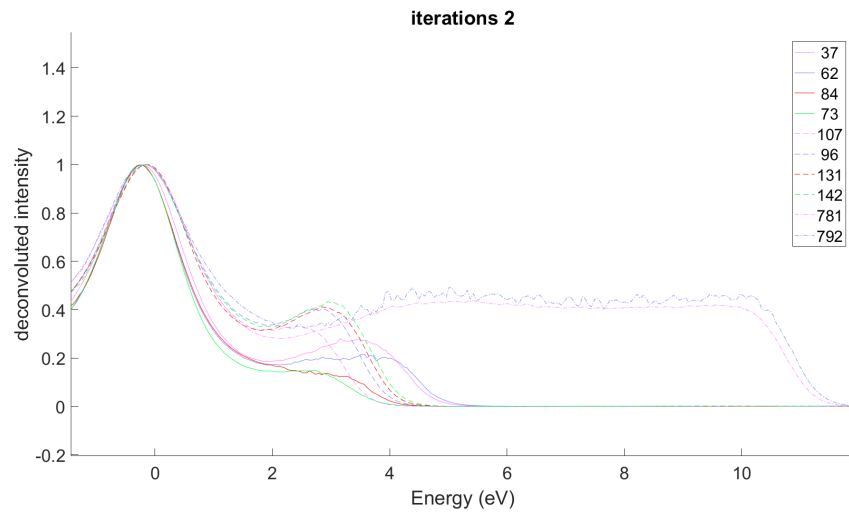


Figure A.18: *RL deconvolution with 2 iterations. Pink and red colours are -C blue and green are +C. 781 and 792 are for the silicon nitride substrate background all others are for an  $l = 4$  spiral.*

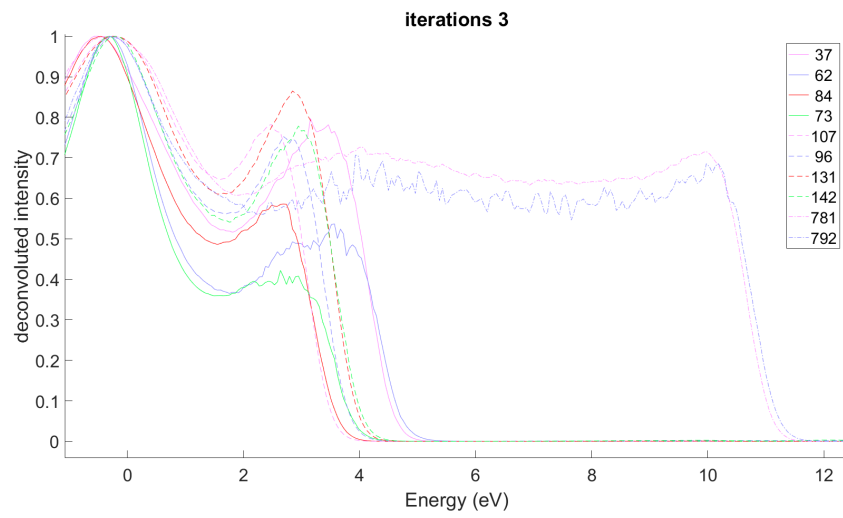


Figure A.19: *RL deconvolution with 3 iterations. Pink and red colours are -C blue and green are +C. 781 and 792 are for the silicon nitride substrate background all others are for an  $l = 4$  spiral.*

#### A.1.1.4 Richardson lucy hyperspy

In addition to MATLAB code , Richardson-Lucy deconvolution has also been performed in the software Hyperspy. This deconvolution algorithm appears to distort the spectra less than for the same number of iterations as MATLAB. Shown in figure is a deconvolution with the no sample psf with 5 iterations. A peak around 7eV is present in all spectra however there is no clearer structure present in the 2-6eV range. The relative intensities are still higher for the -C spectra showing that the difference seen in the experiments are not simply due to a convolution of different PSFs due to spectrometer optics. Figure A.21 is the same as figure A.20 but for the spectra from a flipped sample. The -C is still higher and there is no clear peak structure between 2eV and 6eV. Again this suggests the sample requires three dimensional chirality if the difference is related to chiral interactions.

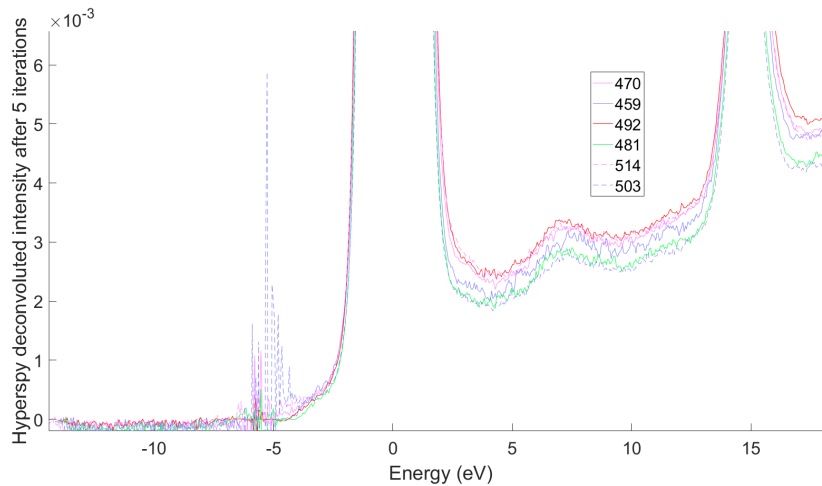


Figure A.20: *Hyperspy deconvolutions using RL 5 iterations 11th oct psf ,pink and red colours are -C blue and green are +C, all sets are for an  $l = 4$  spiral.*

#### A.1.2 Fourier Deconvolution reconvolution

As a comparison to the Richardson Lucy deconvolution a reconvolution technique has also been used. This involves deconvolution by division of the Fourier components from a spectra and by the fourier components of a PSF then a reconvolution with a gaussian spectra to limit high frequency noise.

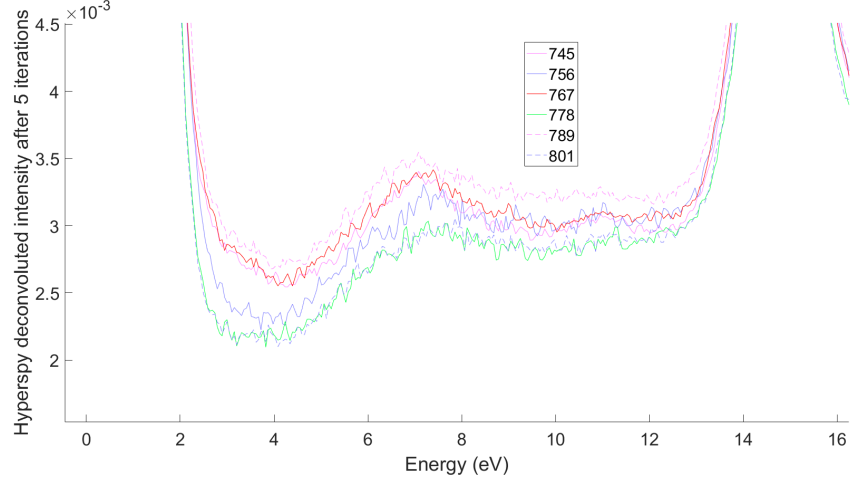


Figure A.21: *Hyperspy deconvolutions using RL 5 iterations 11th oct psf on flipped substrate, pink and red colours are -C blue and green are +C, all sets are for an  $l = 4$  spiral.*

The background spectra of +C/-C silicon nitride can be used as point spread functions (PSF's), deconvoluted out of the signals which are then reconvoluted with a gaussian. This accounts for any experimental artefacts related to the optical set up when no Aluminium is present which could account for the large difference seen in figure 7.28. Figure A.22 shows the result of a reconvolution of spectra '37' using varying gaussian width values,  $w_g$ , following the equation  $\exp(-x^2/w_g)$  for  $-512 < x < 512$ . As can be seen the first width value produces a spectrum which still shows high frequency oscillations. However by the fifth width the spectra has been smoothed out. To maintain any low intensity features whilst also removing high frequency noise the 2nd and 3rd widths were chosen to further analyse the spectra. The results from these widths are shown in figures A.23 and A.24. A similar pattern to previous deconvolutions is seen, whilst there may be some secondary peak character around 3-4eV in some spectra, this shape is not repeated in later spectra and no clear assignment can be made to explain the reconvoluted shape. The reconvoluted spectra still show a large difference between +/- C spectra suggesting the differences recorded are related to interaction between the beam and the Al film. Furthermore the reconvoluted spectra for the large Al cross structures show lower intensity between 4-11 eV suggesting these interactions are only strong when the structures are small, what would be expected for localised surface plasmons or interferences between reflected surface plasmons.

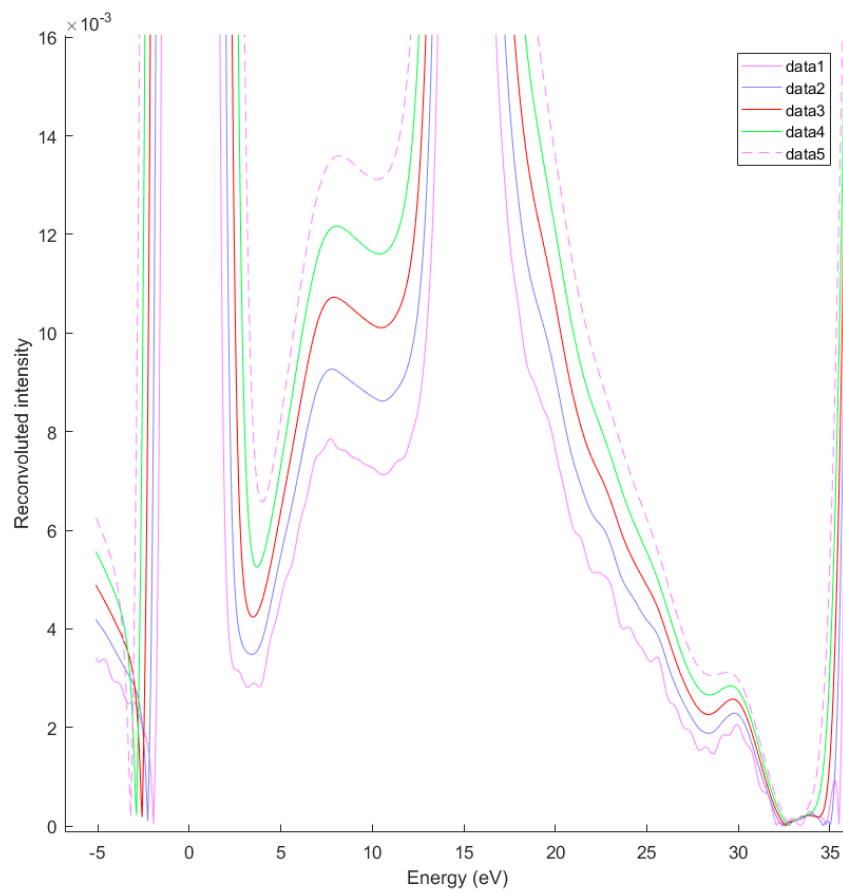


Figure A.22: *reconvolutions with gauss widths 25,30,35,40,45 . No extra low energy details were gained*

When reconvoluting the spectra with the 3rd gaussian width using the psf from no sample, the difference between the results for '37' and '62' (-C and +C) is more pronounced but again there is no consistent structure repeated in the spectra.

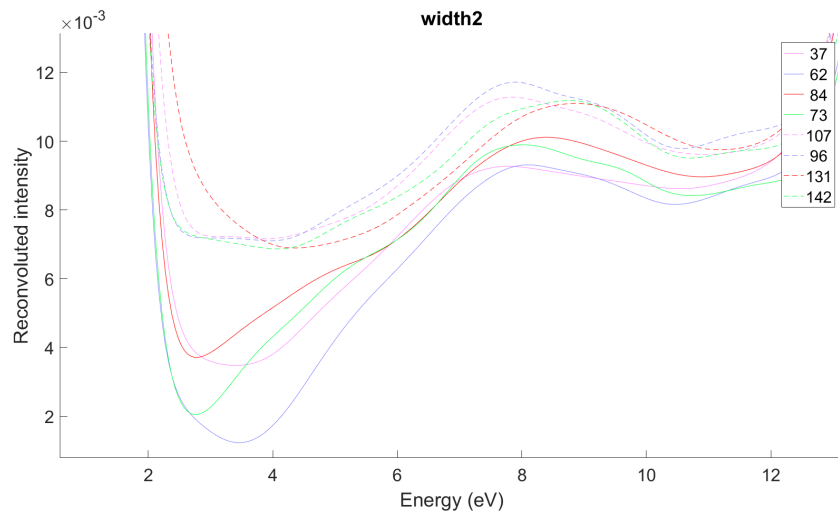


Figure A.23: *Reconvolutions using the second gaussian width (equivalent to 30 in figure A.22) and using the 12th sept psf. The results do not show any clear peaks*

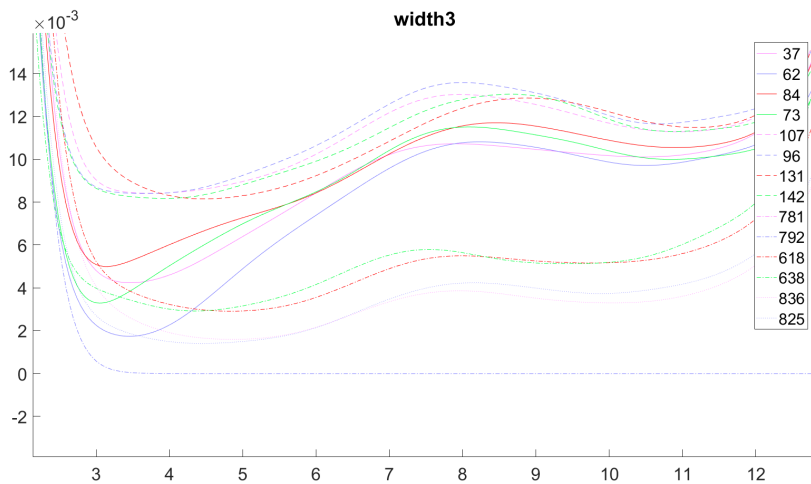


Figure A.24: *Reconvolutions from 12th sept psf do not show any clear peaks. Pink and red colours are -C blue and green are +C, sets 37-142 are for an  $l = 4$  spiral, 781, 792 are the PSFs used, 825, 836 are for a large Al cross and 618, 638 are for the same  $l = 4$  spiral but recorded during a later TEM session.*

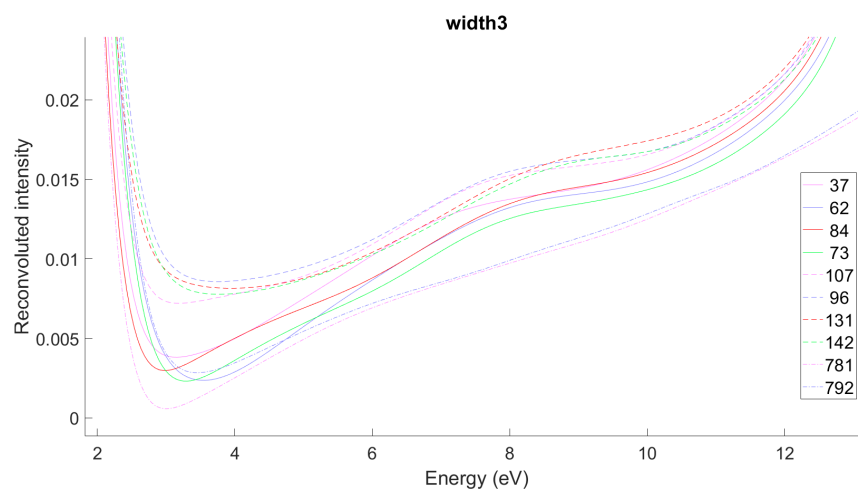


Figure A.25: *reconvolutions from 11th oct no sample psf do not show any clear peaks. Pink and red colours are -C blue and green are +C. 781 and 792 are for the silicon nitride substrate background all others are for an  $l = 4$  spiral.*

## A.2 IFTA implementation for beam shaping

The IFTA algorithm used in this thesis and is as follows:

### IFTA algorithm

1. Define a target intensity distribution (figure 4.14)
2. Perform a Fourier transform on this distribution to produce an initial guess at the mask wavefunction
3. Form an updated guess by setting the amplitude of the mask function to a binary value defining an aperture. The phase is kept from the initial guess in step 2.
4. Perform a Fourier transform of the updated guess from step 3 to define a new resultant intensity.
5. Compare the resultant intensity with the target intensity from step 1 and calculate a fitting parameter
6. Compare the fitting parameter to a desired condition or criteria. If the fitting parameter does not meet the pass criteria Replace the amplitude of the resultant intensity with the target intensity, but keep the phase producing an input wavefunction. If the fitting parameter meets the pass criteria then stop the iterations.
7. Repeat steps 2.-6. using the new input from step 6. instead of the target in step 1.
8. Stop if the number of iterations is above a pre determined cut off value

This procedure is also shown in figure A.26. The final complex field in the mask plane can then be used as a phase mask to produce an approximation to the input intensity. The results of applying this algorithm to producing a C-shaped focal plane intensity are shown in section 4.1.5. There are multiple functions which can be used as the fitting parameter of step 5., all of which seek to quantify the match between the target intensity and the current result. The parameter used in this thesis was  $\sum |I_{res} - I_{tar}|$  where  $I_{res}$  and  $I_{tar}$  are the squared amplitudes of the complex fields in the current result field and the target field respectively.

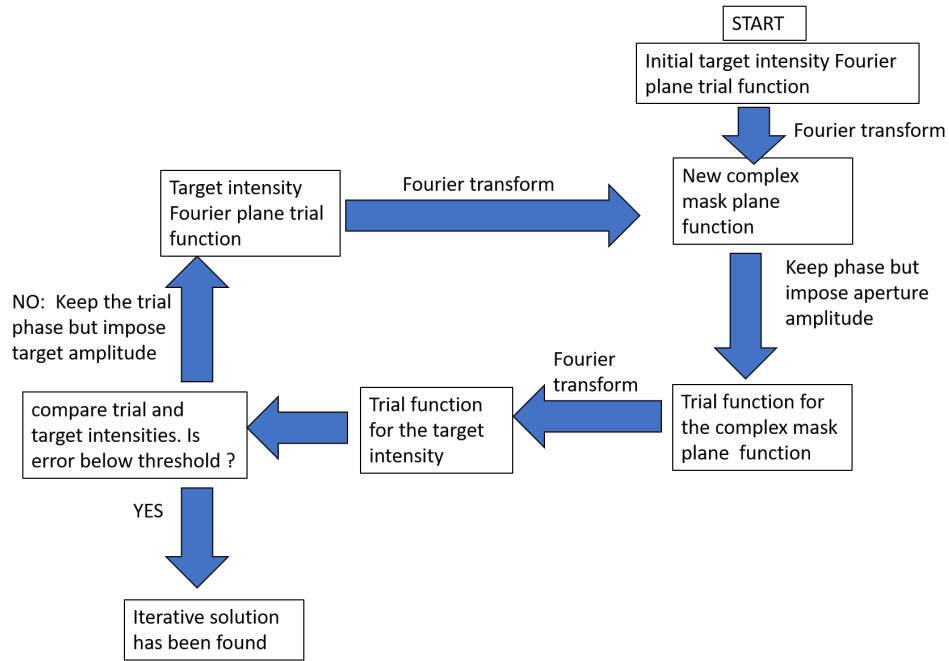


Figure A.26: *The beam shaping method shown in a flow chart.*

### A.3 Iterative phase retrieval with function seeding

A similar algorithm to the IFTA can be used to calculate an estimate of the phase of a wavefunction for which the amplitude has only been recorded from an intensity measurement. This can be improved if the target phase or an estimate is known beforehand, then the initial guess used to seed the algorithm is the ideal case and the algorithm will converge on the best fit with the experimental data.

#### Phase retrieval algorithm

1. Use the square root of the recorded experimental intensity distribution as the amplitude for the initial guess. Use the ideal, simulated phase distribution as the phase of the initial guess.
2. Perform a Fourier transform on the initial guess function to produce an initial Fourier wavefunction
3. Form an updated Fourier wavefunction by setting the amplitude of the results of step 2. to a value defined by an aperture. The phase is kept from the initial Fourier function in step 2..

4. Perform a Fourier transform of the updated Fourier function from step 3 to define a new resultant intensity.
5. Compare the resultant intensity with the experimental intensity from step 1 and calculate a fitting parameter
6. Compare the fitting parameter to a desired condition or criteria. If the fitting parameter does not meet the pass criteria Replace the amplitude of the resultant intensity with the target intensity, but keep the phase producing an input wavefunction. If the fitting parameter meets the pass criteria then stop the iterations.
7. Repeat steps 2.-6. using the new input from step 6. instead of the target in step 1.
8. Stop if the number of iterations is above a pre determined cut off value

This method is shown in the flow chart of figure A.27.

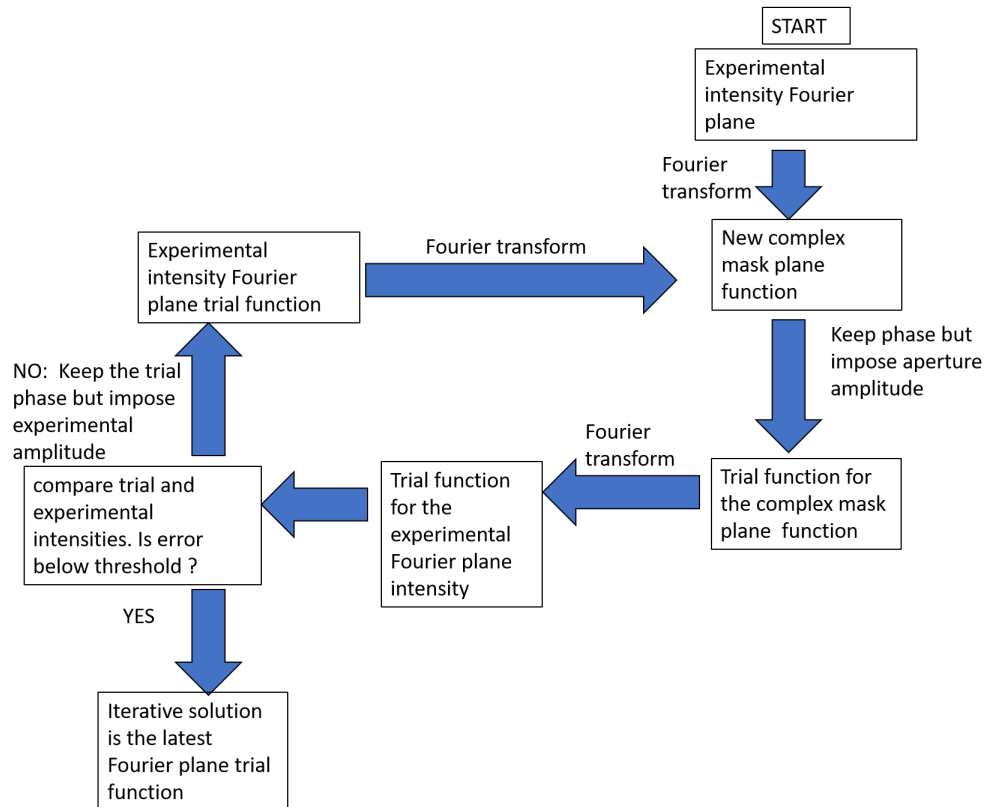


Figure A.27: *The phase retrieval method shown in a flow chart.*

## A.4 EBL of Al structures

A collection of spiral structures shown by the schematic of figure 7.1 were produced by EBL. The EBL was conducted with Dr Mark Rosamond and the method was as follows:

1. ZEP520A resist (ZEON CORPORATION) was diluted 1:1 by volume in anisole
2. The resist mixture was spin coated onto a 4x4  $Si_3N_4$  membrane array (Silson) at 4,000 rpm to give an approximate resist film thickness of 150 nm.
3. The membrane was baked at  $180^\circ C$  for 3 minutes
4. The EBL tool JEOL JBX-6300FS , used a beam current of  $400pA$ , in mode EOS6 (this means 5 lens (high resolution mode) was used at 100 kV. In this mode, the field size  $62.5 \times 62.5\mu m$  and minimum step  $0.125nm$ ). The shot pitch (actual distance between exposure shots) was 2.5 nm and the exposure dose was  $343\mu C/cm^2$
5. The exposed sample was developed in ZED N-50 (n-Amyl acetate) at room temperature for 1 minute.
6. The sample was rinse in propan-2-ol for 20 s and  $N_2$  dried

Once the membranes had been patterned they were transferred to an electron beam evaporator( Oerlikon Univex 350 with Cryo pump) and a metal layer was added following the method:

1. The pressure before evaporation was  $< 1.0e-6$  mbar
2. Aluminium was evaporated at a rate of 2.5 A/s to a thickness of 30 nm (the pressure during evaporation was  $1.4e-6$  mbar)  
OR Aluminium was evaporated at a rate of 1.7 A/s to a thickness of 20 nm (the pressure during evaporation was  $1.5e-6$  mbar)
3. Finally the ZEP resist was dissolved by immersing the samples in cyclopentanone at  $70^\circ C$ , the samples were then rinsed in propan-2-ol and  $N_2$  dried

## A.5 ImageSurfer visualisation

To produce the 3D visualisations used in this thesis the free software ImageSurfer2 was used. To achieve this the dataset to be plotted was saved as a tiff stack of images. It was then opened by ImageSurfer2 using the load option. The tool 'transform' was used to stretch the data in the z direction such that the variations could be easily seen. The images used were produced by the 'contour' tool as shown in figure A.28. Occasionally the 'clip' tool was also used to focus on one section of the data (e.g. for highlighting individual vortex trajectories).

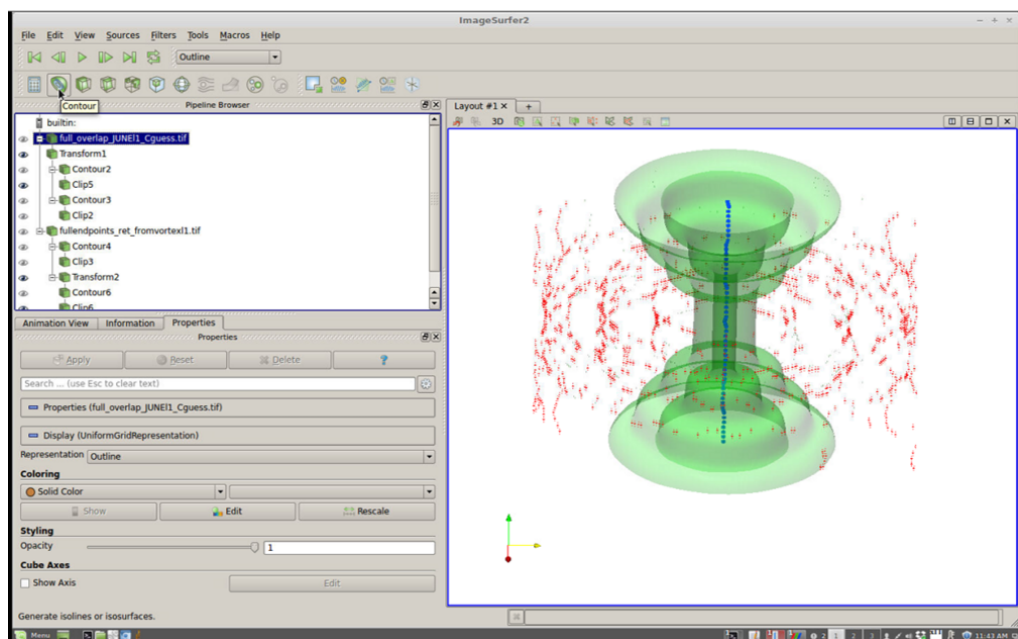


Figure A.28: An example of the ImageSurfer2 software being used to produce a contour plot.

# Bibliography

- [1] E Ruska and M. Knoll. Concentration coil for rapid electron beams. *Zeitschrift fur Technische Physik*, 12(8):389–399, 1931.
- [2] Tore Frangsmyr. *Physics 1981-1990*. World Scientific, Singapore River Edge, N.J, 1993.
- [3] [https://www.nobelprize.org/nobel\\_prizes/physics/laureates/1986/ruska-lecture.pdf](https://www.nobelprize.org/nobel_prizes/physics/laureates/1986/ruska-lecture.pdf).
- [4] A. V. Crewe, J Wall, and J. Langmore. Visibility of Single Atoms. *Science*, 168(3937):1338–1340, 1970.
- [5] M. Haider, P. Hartel, H. Muller, S. Uhlemann, and J. Zach. Current and future aberration correctors for the improvement of resolution in electron microscopy. *Philosophical Transactions of the Royal Society A: Mathematical, Physical and Engineering Sciences*, 367(1903):3665–3682, 2009.
- [6] SuperSTEM- [www.superstem.org/instrumentation](http://www.superstem.org/instrumentation).
- [7] P. Z. El-Khoury, P. Abellan, Y. Gong, F. S. Hage, J. Cottom, A. G. Joly, R. Brydson, Q. M. Ramasse, and W. P. Hess. Visualizing surface plasmons with photons, photoelectrons, and electrons. *The Analyst*, 141:3562–3572, 2016.
- [8] Brett Barwick and Ahmed H. Zewail. Photonics and Plasmonics in 4D Ultrafast Electron Microscopy. *ACS Photonics*, page 150924080031000, 2015.
- [9] A Ryabov and P Baum. Electron microscopy of electromagnetic waveforms. *Science*, 353(6297):374–377, 2016.

- [10] P a Midgley and M Weyland. 3D electron microscopy in the physical sciences: the development of Z-contrast and EFTEM tomography. *Ultramicroscopy*, 96(3-4):413–31, sep 2003.
- [11] Jakob B. Wagner, Filippo Cavalca, Christian D. Damsgaard, Linus D L Duchstein, and Thomas W. Hansen. Exploring the environmental transmission electron microscope. *Micron*, 43(11):1169–1175, 2012.
- [12] C. A. Bennett. *Principles of physical optics*. Wiley, Hoboken, N.J, 2008.
- [13] Christophe Kopp and Patrick Meyrueis. Near-field Fresnel diffraction: improvement of a numerical propagator. *Opt. Comm.*, 158(1-6):7–10, 1998.
- [14] S Feng and H G Winful. Physical origin of the Gouy phase shift. *Optics letters*, 26(8):485–7, apr 2001.
- [15] JC Wyant and K Creath. Basic wavefront aberration theory for optical metrology. *Applied optics and optical engineering*, XI, 1992.
- [16] Carlo Alonzo, Peter John Rodrigo, and Jesper Glückstad. Helico-conical optical beams: a product of helical and conical phase fronts. *Optics express*, 13(5):1749–1760, mar 2005.
- [17] G Thirunavukkarasu, M Mousley, M Babiker, and J Yuan. Normal modes and mode transformation of pure electron vortex beams. *Philosophical Transactions of the Royal Society A: Mathematical, Physical and Engineering Sciences*, 375(2087):20150438, 2017.
- [18] Sacha Kocsis, Boris Braverman, Sylvain Ravets, Martin J Stevens, Richard P Mirin, L Krister Shalm, and Aephraim M Steinberg. Observing the average trajectories of single photons in a two-slit interferometer. *Science (New York, N. Y.)*, 332(6034):1170–3, jun 2011.
- [19] A. Tonomura, J. Endo, T. Matsuda, T. Kawasaki, and H. Ezawa. Demonstration of singleelectron buildup of an interference pattern. *American Journal of Physics*, 57(2):117–120, 1989.
- [20] Hannes Lichte. Electron Holography: phases matter. *Microscopy (Oxford, England)*, 62 Suppl 1(0):S17–28, jun 2013.

- [21] J F Nye and M. V. Berry. Dislocations in Wave Trains. *Proceedings of the Royal Society of London A: Mathematical, Physical and Engineering Sciences*, 336(1605):165–190, 1974.
- [22] L. Allen, M. W. Beijersbergen, R. J C Spreeuw, and J. P. Woerdman. Orbital angular momentum of light and the transformation of Laguerre-Gaussian laser modes. *Physical Review A*, 45(11):8185–8189, 1992.
- [23] Miles Padgett and Richard Bowman. Tweezers with a twist. *Nature Photonics*, 5(6):343–348, 2011.
- [24] G C G Berkhout and M W Beijersbergen. Using a multipoint interferometer to measure the orbital angular momentum of light in astrophysics. *Journal of Optics A: Pure and Applied Optics*, 11(9):094021, 2009.
- [25] Mitchell A. Cox, Carmelo Rosales-Guzmán, Martin P. J. Lavery, Daniel J. Versfeld, and Andrew Forbes. On the resilience of scalar and vector vortex modes in turbulence. *Optics Express*, 24(16):18105, 2016.
- [26] Konstantin Bliokh, Yury Bliokh, Sergey Savel’ev, and Franco Nori. Semiclassical Dynamics of Electron Wave Packet States with Phase Vortices. *Physical Review Letters*, 99(19):190404, nov 2007.
- [27] A. Ashkin. Acceleration and Trapping of Particles by Radiation Pressure. *Physical Review Letters*, 24(4):156–159, 1970.
- [28] Steven Chu, J. E. Bjorkholm, a. Ashkin, and a. Cable. Experimental observation of optically trapped atoms. *Physical Review Letters*, 57(3):314–317, 1986.
- [29] A Ashkin, JM Dziedzic, JE Bjorkholm, and S Chu. Observation of a single-beam gradient force optical trap for dielectric particles. *OPTICS LETTERS*, 11(5):288–290, MAY 1986.
- [30] N. B. Simpson, L. Allen, and M. J. Padgett. Optical tweezers and optical spanners with LaguerreGaussian modes. *Journal of Modern Optics*, 43(12):2485–2491, 1996.
- [31] V S Letokhov, V G Minogin, and B D Pavlik. Cooling and capture of atoms and molecules by a resonant light field. *Zeitschrift Fur Physik*, 45(1949):698, 1977.

- [32] a. Ashkin. Trapping of atoms by resonance radiation pressure. *Physical Review Letters*, 40(12):729–732, 1978.
- [33] Steven Chu. The manipulation of neutral particles. *Rev. Mod. Phys.*, 70(3):685–706, 1998.
- [34] Ludwig Reimer. *Transmission Electron Microscopy Physics of Image Formation*. Springer Verlag, City, 2008.
- [35] R F Egerton. Electron energy-loss spectroscopy in the TEM. *Reports on Progress in Physics*, 72(1):016502, 2009.
- [36] R H Ritchie. The interaction of swift electrons with surface excitations. *Journal of Physics: Condensed Matter*, 5(33A):A17–A24, 1999.
- [37] Stefan a Maier. *Plasmonics: Fundamentals and Applications*, volume 0. Springer New York, 2007.
- [38] M. Dragoman and D. Dragoman. Plasmonics: Applications to nanoscale terahertz and optical devices. *Progress in Quantum Electronics*, 32(1):1–41, 2008.
- [39] J. M. Pitarke, V. M. Silkin, E. V. Chulkov, and P. M. Echenique. Theory of surface plasmons and surface-plasmon polaritons. 1:54, 2006.
- [40] Edward D Palik. *Handbook of optical constants of solids*. Orlando: Academic Press, 1985.
- [41] a. Archambault, T. V. Teperik, F. Marquier, and J. J. Greffet. Surface plasmon Fourier optics. *Physical Review B*, 79(19):195414, may 2009.
- [42] Lian Ming Tong and Hong Xing Xu. Frontiers of Plasmonics. *Frontiers of Physics*, 9(1):1–2, 2014.
- [43] Mark W Knight, Nicholas S King, Lifei Liu, Henry O Everitt, Peter Nordlander, and Naomi J Halas. Aluminum for plasmonics. *ACS nano*, 8(1):834–40, jan 2014.
- [44] R H Ritchie. Plasma Losses by Fast Electrons in Thin Metal Films. *Physical Review*, 106:874–881, 1957.

- [45] Hwi Kim, Junghyun Park, Seong-Woo Cho, Seung-Yeol Lee, Minsu Kang, and Byoung-ho Lee. Synthesis and dynamic switching of surface plasmon vortices with plasmonic vortex lens. *Nano letters*, 10(2):529–36, feb 2010.
- [46] Guillaume Boudarham and Mathieu Kociak. Modal decompositions of the local electromagnetic density of states and spatially resolved electron energy loss probability in terms of geometric modes. *Physical Review B - Condensed Matter and Materials Physics*, 85(24):1–15, 2012.
- [47] Feng Ouyang and Michael Isaacson. Surface plasmon excitation of objects with arbitrary shape and dielectric constant. *Philosophical Magazine Part B*, 60(4):481–492, 1989.
- [48] Jaysen Nelayah, Mathieu Kociak, Odile Stéphan, F. Javier García de Abajo, Marcel Tencé, Luc Henrard, Dario Taverna, Isabel Pastoriza-Santos, Luis M. Liz-Marzán, and Christian Colliex. Mapping surface plasmons on a single metallic nanoparticle. *Nature Physics*, 3(5):348–353, apr 2007.
- [49] a. Asenjo-Garcia and F.J. García de Abajo. Dichroism in the Interaction between Vortex Electron Beams, Plasmons, and Molecules. *Physical Review Letters*, 113(6):066102, aug 2014.
- [50] Tyler R Harvey, Jordan S Pierce, Jordan J Chess, and Benjamin J. McMorran. Demonstration of electron helical dichroism as a local probe of chirality. *ArXiv*, 97403(2), 2015.
- [51] Daniel Ugarte and Caterina Ducati. Controlling multipolar surface plasmon excitation through the azimuthal phase structure of electron vortex beams. *Physical Review B*, 93(20):1–9, 2016.
- [52] Masaya Uchida and Akira Tonomura. Generation of electron beams carrying orbital angular momentum. *Nature*, 464(7289):737–9, apr 2010.
- [53] Roy Shiloh, Yossi Lereah, Yigal Lilach, and Ady Arie. Sculpturing the electron wave function using nanoscale phase masks. *Ultramicroscopy*, 144:26–31, oct 2014.

- [54] A. Béch e, R. Winkler, H. Plank, F. Hofer, and J. Verbeeck. Focused electron beam induced deposition as a tool to create electron vortices. *Micron*, 80:34–38, 2016.
- [55] J Verbeeck, H Tian, and P Schattschneider. Production and application of electron vortex beams. *Nature*, 467(7313):301–4, sep 2010.
- [56] Koh Saitoh, Yuya Hasegawa, Nobuo Tanaka, and Masaya Uchida. Production of electron vortex beams carrying large orbital angular momentum using spiral zone plates. *Journal of electron microscopy*, 61(3):171–7, jun 2012.
- [57] J Verbeeck, H Tian, and P Schattschneider. Production and application of electron vortex beams. *Nature*, 467(7313):301–4, sep 2010.
- [58] J. Verbeeck, P. Schattschneider, S. Lazar, M. Stoger-Pollach, S. Löffler, A. Steiger-Thirsfeld, and G. Van Tendeloo. Atomic scale electron vortices for nanoresearch. *Applied Physics Letters*, 99(20):203109, 2011.
- [59] Koh Saitoh, Yuya Hasegawa, Nobuo Tanaka, and Masaya Uchida. Production of electron vortex beams carrying large orbital angular momentum using spiral zone plates. *Journal of electron microscopy*, 61(3):171–7, jun 2012.
- [60] J. Verbeeck, H. Tian, and a. B ech e. A new way of producing electron vortex probes for STEM. *Ultramicroscopy*, 113:83–87, feb 2012.
- [61] Benjamin J McMorran, Amit Agrawal, Ian M Anderson, Andrew a Herzing, Henri J Lezec, Jabez J McClelland, and John Unguris. Electron vortex beams with high quanta of orbital angular momentum. *Science (New York, N.Y.)*, 331(6014):192–5, jan 2011.
- [62] T. Schachinger, S. L offler, M. St oger-Pollach, and P. Schattschneider. Peculiar rotation of electron vortex beams. *Ultramicroscopy*, 158:17–25, 2015.
- [63] Konstantin Y. Bliokh, Peter Schattschneider, Jo Verbeeck, and Franco Nori. Electron Vortex Beams in a Magnetic Field: A New Twist on Landau Levels and Aharonov-Bohm States. *Physical Review X*, 2(4):041011, nov 2012.

- [64] Giulio Guzzinati, Peter Schattschneider, Konstantin Bliokh, Franco Nori, and Jo Verbeeck. Observation of the Larmor and Gouy Rotations with Electron Vortex Beams. *Physical Review Letters*, 093601(March):1–5, 2013.
- [65] Colin Greenshields, Robert L Stamps, and Sonja Franke-Arnold. Vacuum Faraday effect for electrons. *New Journal of Physics*, 14(10):103040, oct 2012.
- [66] Vincenzo Grillo, Gian Carlo Gazzadi, Ebrahim Karimi, Erfan Mafakheri, Robert W. Boyd, and Stefano Frabboni. Highly efficient electron vortex beams generated by nanofabricated phase holograms. *Applied Physics Letters*, 104(4):043109, jan 2014.
- [67] Amir Hossein, Tavabi Forschungszentrum, Vincenzo Grillo, Italian National, E. Mafakheri, A. H. Tavabi, P. H. Lu, R. Balboni, F. Venturi, C. Menozzi, G. C. Gazzadi, S. Frabboni, A. Sit, R. E. Dunin-Borkowski, E. Karimi, and Vincenzo Grillo. Realization of electron vortices with large orbital angular momentum using miniature holograms fabricated by electron ... *Applied Physics Letters*, 110(December), 2016.
- [68] Vincenzo Grillo, Ebrahim Karimi, Gian Carlo Gazzadi, Stefano Frabboni, Mark R. Dennis, and Robert W. Boyd. Generation of Non-diffracting Electron Bessel Beams. *Physical Review X*, 4(1):011013, jan 2014.
- [69] M Mazilu, D James Stevenson, F Gunn-Moore, and K Dholakia. Light beats the spread: non-diffracting beams. *Laser Photonics Reviews*, 4(4):529–547, sep 2009.
- [70] L. Clark, a. Béch e, G. Guzzinati, a. Lubk, M. Mazilu, R. Van Boxem, and J. Verbeeck. Exploiting Lens Aberrations to Create Electron-Vortex Beams. *Physical Review Letters*, 111(6):064801, aug 2013.
- [71] Armand B ech e, Ruben Van Boxem, Gustaaf Van Tendeloo, and Jo Verbeeck. Magnetic monopole field exposed by electrons. *Nature Physics*, 10(1):26–29, dec 2013.
- [72] Koh Saitoh, Yuya Hasegawa, Kazuma Hirakawa, Nobuo Tanaka, and Masaya Uchida. Measuring the Orbital Angular Momentum of Electron Vortex Beams Using a Forked Grating. *Physical Review Letters*, 111(7):074801, aug 2013.

- [73] Giulio Guzzinati, Laura Clark, Armand Béch e, and Jo Verbeeck. Measuring the orbital angular momentum of electron beams. *Physical Review A*, 89(2):025803, feb 2014.
- [74] L. Clark, a. B ech e, G. Guzzinati, and J. Verbeeck. Quantitative measurement of orbital angular momentum in electron microscopy. *Physical Review A*, 89(5):053818, may 2014.
- [75] L Clark, G Guzzinati, A Lubk, and J Verbeeck. Symmetry-constrained electron vortex propagation. 063840:1–11, 2016.
- [76] Jo Verbeeck, He Tian, and Gustaaf Van Tendeloo. How to manipulate nanoparticles with an electron beam? *Advanced materials (Deerfield Beach, Fla.)*, 25(8):1114–7, feb 2013.
- [77] T Gnanavel, J Yuan, and M Babiker. Observation of gold nanoparticles movements under sub-10 nm vortex electron beams in an aberration corrected TEM ( a ) ( c ). In *Proceedings of the 15th European Microscopy Congresss*, number ii, Manchester, UK, 2012. Royal Microscopy Society.
- [78] Roeland Juchtmans and Jo Verbeeck. Orbital angular momentum in electron diffraction and its use to determine chiral crystal symmetries. *Cleo*, 134108(October):1–10, 2015.
- [79] Roeland Juchtmans, Armand B ech e, Artem Abakumov, Maria Batuk, and Jo Verbeeck. Using electron vortex beams to determine chirality of crystals in transmission electron microscopy. *Physical Review B*, 91(9):1–11, mar 2015.
- [80] Roeland Juchtmans, Giulio Guzzinati, and Jo Verbeeck. Extension of Friedel’s law to Vortex Beam Diffraction. *Arxiv preprint*, 033858(August):1–7, 2016.
- [81] P Schattschneider, S L offler, M St oger-Pollach, and J Verbeeck. Is magnetic chiral dichroism feasible with electron vortices? *Ultramicroscopy*, 136:81–5, jan 2014.
- [82] Giulio Guzzinati, A. B ech e, Hugo Lourenco-Martins, Jerome Martin, Mathieu Kociak, and Jo Verbeeck. Probing the symmetry and phase of localised surface plasmon resonances with singular electron probes. *submitted to Nature Physics*, pages 1–21, 2016.

- [83] T Niermann, J Verbeeck, and M Lehmann. Creating arrays of electron vortices. *Ultramicroscopy*, 136:165–70, jan 2014.
- [84] Sophia Lloyd, Mohamed Babiker, and Jun Yuan. Quantized Orbital Angular Momentum Transfer and Magnetic Dichroism in the Interaction of Electron Vortices with Matter. *Physical Review Letters*, 108(7):74802, feb 2012.
- [85] P. Schattschneider, S. Löffler, and J. Verbeeck. Comment on Quantized Orbital Angular Momentum Transfer and Magnetic Dichroism in the Interaction of Electron Vortices with Matter. *Physical Review Letters*, 110(18):189501, may 2013.
- [86] S. M. Lloyd, M. Babiker, and J. Yuan. Mechanical properties of electron vortices. *Physical Review A*, 88(3):031802, sep 2013.
- [87] J. Yuan, S. M. Lloyd, and M. Babiker. Chiral-specific electron-vortex-beam spectroscopy. *Physical Review A*, 88(3):031801, sep 2013.
- [88] Stefan Löffler and Peter Schattschneider. Elastic propagation of fast electron vortices through crystals. *Acta Crystallographica Section A Foundations of Crystallography*, 68(4):443–447, may 2012.
- [89] Axel Lubk, Laura Clark, Giulio Guzzinati, and Jo Verbeeck. Topological analysis of paraxially scattered electron vortex beams. *Physical Review A*, 87(3):033834, mar 2013.
- [90] Huolin L Xin and Haimei Zheng. On-column 2p bound state with topological charge 1 excited by an atomic-size vortex beam in an aberration-corrected scanning transmission electron microscope. *Microscopy and microanalysis : the official journal of Microscopy Society of America, Microbeam Analysis Society, Microscopical Society of Canada*, 18(4):711–9, aug 2012.
- [91] Roeland Juchtmans and Jo Verbeeck. Local orbital angular momentum revealed by spiral phase plate imaging in transmission electron microscopy. *Phys. Rev. A*, 023811(2):1–7, 2015.
- [92] Franz Philipp Schmidt, Harald Ditlbacher, Ulrich Hohenester, Andreas Hohenau, Ferdinand Hofer, and Joachim R. Krenn. Dark plasmonic breathing modes in silver nanodisks. *Nano Letters*, 12(11):5780–5783, 2012.

- [93] Franz-Philipp Schmidt, Harald Ditlbacher, Ulrich Hohenester, Andreas Hohenau, Ferdinand Hofer, and Joachim R Krenn. Universal dispersion of surface plasmons in flat nanostructures. *Nature communications*, 5:3604, 2014.
- [94] J.-C. Weeber, J. Krenn, A. Dereux, B. Lamprecht, Y. Lacroute, and J. Goudonnet. Near-field observation of surface plasmon polariton propagation on thin metal stripes. *Physical Review B*, 64(4):1–9, 2001.
- [95] Yuri Gorodetski, Aurélien Drezet, Cyriaque Genet, and Thomas W. Ebbesen. Generating Far-Field Orbital Angular Momenta from Near-Field Optical Chirality. *Physical Review Letters*, 110(20):203906, may 2013.
- [96] Z. Shen, Z. J. Hu, G. H. Yuan, C. J. Min, H. Fang, and X.-C. Yuan. Visualizing orbital angular momentum of plasmonic vortices. *Optics Letters*, 37(22):4627, nov 2012.
- [97] Xi-Feng Ren, Guo-Ping Guo, Yun-Feng Huang, Chuan-Feng Li, and Guang-Can Guo. Plasmon assisted transmission of high dimensional orbital angular momentum entangled state. *Europhys. Lett.*, 76(December):7, 2006.
- [98] Daniel Ugarte and Caterina Ducati. Controlling multipolar surface plasmon excitation through the azimuthal phase structure of electron vortex beams. *Physical Review B*, 93(20):1–9, 2016.
- [99] M V Berry. Optical vortices evolving from helicoidal integer and fractional phase steps. *Journal of Optics A: Pure and Applied Optics*, 6(2):259–268, feb 2004.
- [100] Jonathan Leach, Eric Yao, and Miles J Padgett. Observation of the vortex structure of a non-integer vortex beam. *New Journal of Physics*, 6:71–71, jul 2004.
- [101] I V Basistiy, V a Pas ko, V V Slyusar, M S Soskin, and M V Vasnetsov. Synthesis and analysis of optical vortices with fractional topological charges. *Journal of Optics A: Pure and Applied Optics*, 6(5):S166–S169, may 2004.

- [102] J. B. Götte, S. Franke-Arnold, R. Zambrini, and Stephen M. Barnett. Quantum formulation of fractional orbital angular momentum. *Journal of Modern Optics*, 54(12):1723–1738, aug 2007.
- [103] Jörg B Götte, Kevin O’Holleran, Daryl Preece, Florian Flossmann, Sonja Franke-Arnold, Stephen M Barnett, and Miles J Padgett. Light beams with fractional orbital angular momentum and their vortex structure. *Optics express*, 16(2):993–1006, jan 2008.
- [104] T Fadeyeva, C Alexeyev, a Rubass, and a Volyar. Vector erf-Gaussian beams: fractional optical vortices and asymmetric TE and TM modes. *Optics letters*, 37(9):1397–9, may 2012.
- [105] Julio C Gutiérrez-Vega and Carlos López-Mariscal. Nondiffracting vortex beams with continuous orbital angular momentum order dependence. *Journal of Optics A: Pure and Applied Optics*, 10(1):015009, jan 2008.
- [106] S Tao, X-C Yuan, J Lin, X Peng, and H Niu. Fractional optical vortex beam induced rotation of particles. *Optics express*, 13(20):7726–31, oct 2005.
- [107] Cheng-Shan Guo, Ya-Nan Yu, and Zhengping Hong. Optical sorting using an array of optical vortices with fractional topological charge. *Optics Communications*, 283(9):1889–1893, may 2010.
- [108] Nathaniel P. Hermosa and Christine O. Manaois. Phase structure of helico-conical optical beams. *Optics Communications*, 271(1):178–183, mar 2007.
- [109] Jinsong Li, Xiumin Gao, Shuqin Zhang, and Songlin Zhuang. Focusing properties of Gaussian beam with mixed screw and conical phase fronts. *Optik - International Journal for Light and Electron Optics*, 121(19):1794–1798, oct 2010.
- [110] Vincent R Daria, Darwin Z Palima, and Jesper Glückstad. Optical twists in phase and amplitude. *Optics express*, 19(2):476–81, jan 2011.
- [111] Sunil Vyas, Rakesh Kumar Singh, and P. Senthilkumaran. Fractional vortex lens. *Optics & Laser Technology*, 42(6):878–882, sep 2010.

- [112] T a Fadeyeva, a F Rubass, I S Valkov, and a V Volyar. Fractional optical vortices in a uniaxial crystal. *Journal of Optics*, 15(4):044020, apr 2013.
- [113] C. Bennett. *Principles of Physical Optics*. Wiley, 2008.
- [114] Steve Reyntjens and Robert Puers. A review of focused ion beam applications in microsystem technology. *Journal of Micromechanics and Microengineering*, 11(4):287–300, 2001.
- [115] Vitor R. Manfrinato, Lihua Zhang, Dong Su, Huigao Duan, Richard G. Hobbs, Eric A. Stach, and Karl K Berggren. Resolution limits of electron-beam lithography toward the atomic scale. *Nano Letters*, 13:1555–1558, 2013.
- [116] a E Grigorescu and C W Hagen. Resists for sub-20-nm electron beam lithography with a focus on HSQ: state of the art. *Nanotechnology*, 20(29):292001, jul 2009.
- [117] Paul R Edwards and Robert W Martin. Cathodoluminescence nano-characterization of semiconductors. *Semiconductor Science and Technology*, 26(6):064005, 2011.
- [118] R W Gerchberg and W O Saxton. A practical algorithm for the determination of phase from image and diffraction plane pictures. *Optik*, 35(2):237–246, 1972.
- [119] Gábor Oszlányi and András Sütó. The charge flipping algorithm. *Acta Crystallographica Section A: Foundations of Crystallography*, 64(1):123–134, 2008.
- [120] Ulrich Hohenester and Andreas Trügler. MNPBEM - A Matlab toolbox for the simulation of plasmonic nanoparticles. pages 1–26, 2011.
- [121] Ulrich Hohenester and Andreas Trügler. MNPBEM A Matlab toolbox for the simulation of plasmonic nanoparticles. *Computer Physics Communications*, 183(2):370–381, feb 2012.
- [122] <https://uk.mathworks.com/help/matlab/ref/mldivide.html>.
- [123] Ulrich Hohenester. Simulating electron energy loss spectroscopy with the MNPBEM toolbox. *Computer Physics Communications*, 185(3):1177–1187, 2014.

- [124] Rossella Zoli, Guido Oliva, Rinaldo Zocca, Giovanni Tartarini, and Paolo Bassi. Propagation of truncated focused astigmatic laser beams. *Online*, 5:315–323, 2003.
- [125] Zoltán L. Horváth and Zsolt Bor. Focusing of truncated Gaussian beams. *Optics Communications*, 222(1-6):51–68, 2003.
- [126] D. Jen, P. Parente, J. Robbins, C. Weigle, Ii Taylor, R.M., a. Burette, and R. Weinberg. ImageSurfer: a tool for visualizing correlations between two volume scalar fields. *IEEE Visualization 2004*, (November), 2004.
- [127] F Ricci, W Loffler, and M P van Exter. Instability of higher-order optical vortices analyzed with a multi-pinhole interferometer. *Optics Express*, 20(20):22961–22975, 2012.
- [128] S M Baumann, D M Kalb, L H MacMillan, and E J Galvez. Propagation dynamics of optical vortices due to Gouy phase. *Optics express*, 17(12):9818–9827, 2009.
- [129] Christian Schulze, Angela Dudley, Robert Brüning, Michael Duparré, and Andrew Forbes. Measurement of the orbital angular momentum density of Bessel beams by projection into a Laguerre-Gaussian basis. *Applied optics*, 53(26):5924–33, 2014.
- [130] Gabriel Molina-Terriza, Juan Torres, and Lluís Torner. Management of the Angular Momentum of Light: Preparation of Photons in Multidimensional Vector States of Angular Momentum. *Physical Review Letters*, 88(1):013601, dec 2001.
- [131] D. R. Smith, Willie J. Padilla, D. C. Vier, S. C. Nemat-Nasser, and S. Schultz. Composite Medium with Simultaneously Negative Permeability and Permittivity. *Physical Review Letters*, 84(18):4184–4187, 2000.
- [132] Cheng-Shan Guo, Xuan Liu, Jing-Liang He, and Hui-Tian Wang. Optimal annulus structures of optical vortices. *Optics express*, 12(19):4625–4634, 2004.
- [133] David McGloin, G Spalding, H Melville, Wilson Sibbett, and Kishan Dholakia. Applications of spatial light modulators in atom optics. *Optics Express*, 11(2):158–166, 2003.

- [134] Stephen Eckel, Jeffrey G Lee, Fred Jendrzejewski, Noel Murray, Charles W Clark, Christopher J Lobb, William D Phillips, Mark Edwards, and Gretchen K Campbell. Hysteresis in a quantized superfluid 'atomtronic' circuit. *Nature*, 506(7487):200–3, 2014.
- [135] B.D. Josephson. Possible new effects in superconductive tunnelling. *Physics Letters*, 1(7):251–253, 1962.
- [136] a. Ramanathan, K. C. Wright, S. R. Muniz, M. Zelan, W. T. Hill, C. J. Lobb, K. Helmerson, W. D. Phillips, and G. K. Campbell. Superflow in a toroidal bose-einstein condensate: An atom circuit with a tunable weak link. *Physical Review Letters*, 106(13):1–4, 2011.
- [137] Michael Mousley, Gnanavel Thirunavukkarasu, Jun Yuan, and Mohamed Babiker. C-shaped electron beams: design, experimental production and application. In *Proc. SPIE 9581, Laser Beam Shaping XVI, 95810C*, 2015.
- [138] Albina Borisevich. Fire up the atom forge. *Nature*, 539(7630):485–487, 2016.
- [139] Stephen Jesse, Qian He, Andrew R. Lupini, Donovan N. Leonard, Mark P. Oxley, Oleg Ovchinnikov, Raymond R. Unocic, Alexander Tselev, Miguel Fuentes-Cabrera, Bobby G. Sumpter, Stephen J. Pennycook, Sergei V. Kalinin, and Albina Y. Borisevich. Atomic-Level Sculpting of Crystalline Oxides: Toward Bulk Nanofabrication with Single Atomic Plane Precision. *Small*, 11(44):5895–5900, 2015.
- [140] Marco Esposito, Vittorianna Tasco, Massimo Cuscuna, Francesco Todisco, Alessio Benedetti, Iolena Tarantini, Milena De Giorgi, Daniele Sanvitto, and Adriana Passaseo. Nanoscale 3D chiral plasmonic helices with circular dichroism at visible frequencies. *ACS Photonics*, 2(1):105–114, 2015.
- [141] a. Muray, M. Isaacson, and I. Adesida. AlF<sub>3</sub>A new very high resolution electron beam resist. *Applied Physics Letters*, 45(5):589, 1984.
- [142] VI I. Nikolaichik. Self-developing processes in metal fluorides under a focused electron beam. *Philosophical Magazine A*, 68(August 2014):227–236, aug 1993.

- [143] I. Adesida A. Murray, M. Scheinfein, M. Isaacson. Radiolysis and resolution limits of inorganic halide resists. *J. Vac. Sci. Technol.*, 3(1985):67, 1985.
- [144] A E Grigorescu and C W Hagen. Resists for sub-20-nm electron beam lithography with a focus on HSQ: state of the art. *Nanotechnology*, 20(29):292001, 2009.
- [145] G. S. Chen and C. J. Humphreys. Study of sample thickness dependence in electron-beam irradiation of self-developing inorganic materials. *Journal of Applied Physics*, 85(1):148, 1999.
- [146] <http://www.silson.com/index.html>.
- [147] Roy Shiloh, Roei Remez, and Ady Arie. Prospects for electron beam aberration correction using sculpted phase masks. *Ultramicroscopy*, 163:69–74, 2016.
- [148] Richard G. Hobbs, Vitor R. Manfrinato, Yujia Yang, Sarah A. Goodman, Lihua Zhang, Eric A. Stach, and Karl K. Berggren. High-Energy Surface and Volume Plasmons in Nanopatterned Sub-10 nm Aluminum Nanostructures. *Nano Letters*, 16(7):4149–4157, 2016.
- [149] Christian Colliex, Mathieu Kociak, and Odile Stéphan. Electron Energy Loss Spectroscopy imaging of surface plasmons at the nanometer scale. *Ultramicroscopy*, 162:A1–A24, 2015.
- [150] Mark W. Knight, Lifei Liu, Yumin Wang, Lisa Brown, Shaunak Mukherjee, Nicholas S. King, Henry O. Everitt, Peter Nordlander, and Naomi J. Halas. Aluminum plasmonic nanoantennas. *Nano Letters*, 12(11):6000–6004, 2012.
- [151] Edson P. Bellido, Alejandro Manjavacas, Yue Zhang, Yang Cao, Peter Nordlander, and Gianluigi A. Botton. Electron Energy-Loss Spectroscopy of Multipolar Edge and Cavity Modes in Silver Nanosquares. *ACS Photonics*, page acsphotronics.5b00594, 2016.
- [152] Christoph Langhammer, Zhe Yuan, Igor Zorić, and Bengt Kasemo. Plasmonic properties of supported Pt and Pd nanostructures. *Nano Letters*, 6:833–838, 2006.
- [153] Heinz Raether. Surface plasmons on smooth and rough surfaces and on gratings, Volume 111. page 136, 1988.

- [154] C. J. Powell and J. B. Swan. Origin of the characteristic electron energy losses in aluminum. *Physical Review*, 115(4):869–875, 1959.
- [155] S. D. Berger, I. G. Salisbury, R. H. Milne, D. Imeson, and C. J. Humphreys. Electron energy-loss spectroscopy studies of nanometre-scale structures in alumina produced by intense electron-beam irradiation. *Philosophical Magazine Part B*, 55(3):341–358, mar 1987.
- [156] Yuanjie Yang, G. Thirunavukkarasu, M. Babiker, and Jun Yuan. Orbital-Angular-Momentum Mode Selection by Rotationally Symmetric Superposition of Chiral States with Application to Electron Vortex Beams. *Physical Review Letters*, 119(9):094802, 2017.